AVERTISSEMENT

Ce document est le fruit d'un long travail approuvé par le jury de soutenance et mis à disposition de l'ensemble de la communauté universitaire élargie.

Il est soumis à la propriété intellectuelle de l'auteur. Ceci implique une obligation de citation et de référencement lors de l'utilisation de ce document.

D'autre part, toute contrefaçon, plagiat, reproduction illicite encourt une poursuite pénale.

Contact : ddoc-theses-contact@univ-lorraine.fr

LIENS

Code de la Propriété Intellectuelle. articles L 122. 4
Code de la Propriété Intellectuelle. articles L 335.2- L 335.10
http://www.cfcopies.com/V2/leg/leg_droi.php
http://www.culture.gouv.fr/culture/infos-pratiques/droits/protection.htm

UNIVERSITÉ DE LORRAINE
École Nationale Supérieure des Industries Chimiques
Laboratoire Réactions et Génie des Procédés
École Doctorale SIMPPÉ

THÈSE

Présentée pour obtenir le grade de
Docteur de l'Université de Lorraine

Spécialité: Génie des Procédés, des Produits et des Molécules

Par
Qindan ZHANG

Sujet:

Ecoulements polyphasiques et phénomènes interfaciaux à multi échelles

Soutenue publiquement le 28 September 2020

Membres du jury

Président

Mme Catherine CHARCOSSET, Directrice de recherche au CNRS (Université Lyon 1, Lyon)

Rapporteurs

Mme Marie-Laurence GIORGI, Professeure (CentraleSupélec, Paris)

M. Yuanhai SU, Professor (Shanghai Jiao Tong University, Shanghai)

Examinateurs

Mme Xiaojie JU, Professeure (Sichuan University, Chengdu)

M. Youguang MA, Professeur (Co-directeur de thèse, Tianjin University, Tianjin)

M. Huai-Zhi LI, Professeur (Directeur de thèse, ENSIC-Université de Lorraine, Nancy)

Acknowledgements

I want to express my deepest gratitude to my supervisor at the University of Lorraine, Professor Huai-Zhi LI. He has provided remarkable guidance and great help throughout my research in the French lab. He spent much time and patience on the experimental operations and the further revisions of the manuscripts. His stringent careful attitude towards the scientific works set an outstanding example for me. I also appreciate his generous help in my daily life in France, especially in my early times on arriving.

My heartfelt gratitude also goes to my supervisor at Tianjin University, Professor Youguang MA. I learned a lot from him not only in the academic research, but also benefited from his words and deeds to my life. Prof. MA has offered many practical suggestions and constructive comments, which have contributed greatly to the completion of my PhD thesis. My research works cannot be smoothly accomplished without his extraordinary patience and encouragement.

Many thanks to Souhila PONCIN, David BRUNELLO, Christian BLANCHARD, et al, who have offered great help on my experiments. My gratitude also goes to Taotao FU and Chunying ZHU, who gave valuable guidance in the experiment and manuscript revision. Thanks to all the colleagues in my research groups “Syspol (LRGP-CNRS)” and “Multiple phase process and microchemical technology”, who helped me a lot in the study and research and companied with me for the good times all the way.

The financial support from the China Scholarship Council is gratefully acknowledged as well. I would not be able to pursue and complete my two-year study in France without this solid guarantee.

Many thanks to the invited jury members Catherine CHARCOSSET, Marie-Laurence GIORGI, Xiaojie JU and Yuanhai SU for their kind attendance and beneficial suggestions.

At last but not least, I want to express sincere gratitude to my family who has always respected my decisions and been the strongest support behind me.

Table of Contents

Résumé étendu 1

General introduction.....19

Chapter 1 Literature review 21

1.1 Multiphase flows at the microscale.....22

1.1.1 Droplet (bubble) formation at the microscale 23

1.1.2 Droplet (bubble) breakup at the microscale 31

1.2 Drop coalescence and spreading 36

1.2.1 Drop impact and coalescence on a liquid surface 36

1.2.2 Drop impact and spreading on a solid surface 42

1.3 Passive and active manipulation on multiphase flows.....45

1.3.1 Passive methods 45

1.3.2 Active methods.....47

1.4 Outline.....52

Chapter 2 Experimental section 55

2.1 Experimental devices 55

2.1.1 High-speed camera.....55

2.1.2 Ultra-high-speed DC electrical device 56

2.1.3 High-speed micro-PIV 57

2.1.4 Syringe pump 58

2.1.5 Microfluidic devices.....58

2.2 Experimental liquids 60

2.3 Analytical methods.....62

2.3.1 High-speed images 62

2.3.2 Electrical signals 62
2.3.3 Velocity fields 63
2.3.4 Liquid properties 64
Chapter 3 Droplet formation in T-junction and flow-focusing devices 67
3.1 Introduction 67
3.2 Experimental section 69
3.2.1 Liquid properties for the droplet formation in the T-junction device .71
3.2.2 Liquid properties for the droplet formation in the flow-focusing device 73
3.3 Results and discussion 74
3.3.1 Formation of elastic droplets in a microfluidic T-junction 74
3.3.2 Droplet formation in elastic fluid at a flow-focusing microchannel ...86
3.4 Summary 100
Chapter 4 Stretching and breakup of elastic droplets in consecutive flow-focusing device 101
4.1 Introduction 101
4.2 Experimental section 103
4.3 Results and discussion 106
4.3.1 Breakup regimes of the droplets in the flow-focusing junction 106
4.3.2 Dynamics of the droplet stretch-rebound 108
4.3.3 Dynamics of the droplet stretch-breakup 114
4.4 Summary 116
Chapter 5 Initial coalescence of an aqueous drop at a planar liquid surface 117
5.1 Introduction 117
5.2 Experimental section 118
5.3 Results and discussion 122
5.4 Summary 131

Chapter 6 Drop impact, spreading and breakup on a solid surface.....133
6.1 Introduction.....133
6.2 Experimental section.....134
6.3 Results and discussion.....138
6.3.1 Initial contact and spreading of a pendant drop at solid surface.....138
6.3.2 Filament thinning of the liquid neck.....153
6.4 Summary.....160
Chapter 7 Magnetic manipulation on the coalescence of a ferrofluid drop at its bulk surface.....161
7.1 Introduction.....161
7.2 Experimental section.....163
7.3 Results and discussion.....167
7.3.1 Initial coalescence of a ferrofluid drop without a magnetic field.....167
7.3.2 Initial coalescence of a ferrofluid drop under a magnetic field.....170
7.4 Summary.....177
Chapter 8 Conclusions, innovations and perspectives.....179
8.1 General conclusions.....179
8.2 Innovations.....181
8.3 Perspectives.....182
References.....187
Nomenclature.....209
Publications.....213

Résumé étendu

Les écoulements polyphasiques se concentrent sur l'écoulement, le mélange et la dispersion des phases gazeuse, liquide et solide. Ces écoulements couvrent les très larges champs tels que diphasiques gaz-liquide et liquide-liquide, triphasiques gaz-liquide-liquide et gaz-liquide-solide et encore plus complexes. Les écoulements polyphasiques et les phénomènes interfaciaux associés sont largement impliqués dans la nature, notre vie quotidienne et de nombreux procédés industriels tels que le génie chimique, la cosmétique, la pharmaceutique, l'agroalimentaire ou encore le génie pétrolier. Les recherches fondamentales sur les écoulements polyphasiques et les phénomènes interfaciaux permettent d'approfondir la compréhension des mécanismes élémentaires et de fournir des orientations théoriques pour les applications industrielles.

Dans le domaine du génie chimique, une grande variété de phénomènes se produit dans une gamme étendue d'échelles tant spatiales et que temporelles. L'approche multi-échelles intégrée triple "Processus moléculaires – Produit - Procédé (3P)" a été définie pour décrire les phénomènes pluridisciplinaires non linéaires et hors équilibre. Cette approche spatio-temporelle à multi-échelles moderne répond à la demande de la compréhension des écoulements polyphasiques et des phénomènes interfaciaux. À la fin du 20e siècle, le nouveau concept de "Lab on a Chip" a été proposé pour répondre à la tendance à la miniaturisation et à la demande pressante de sécurité et de protection de l'environnement. La micro-technologie présente d'appréciables avantages en termes de contrôlabilité, de sécurité, d'efficacité, d'économie, de compacité et de respect de l'environnement dans l'espace confiné des dispositifs microfluidiques. Mis à part des écoulements polyphasiques dans des microcanaux confinés à des micro-échelles, l'impact de la goutte à surface libre est un autre domaine de recherche essentiel. Catalogué selon la vitesse d'approche de la goutte tombante et l'état de la surface, l'impact de la goutte comprend deux comportements distincts : contacter, rebondir, coalescence ou éclabousser sur une surface liquide et rebondir, coalescence ou étaler sur une surface solide.

Pour les écoulements polyphasiques dans des espaces confinés ou non confinés,

la gestion de ces écoulements pourrait être réalisée par des méthodes passives ou actives, où la première est menée à bien sans aucune force externe tandis que la seconde repose sur des forces supplémentaires ou des propriétés intrinsèques des liquides. Les deux méthodes sont utiles pour une meilleure compréhension des phénomènes interfaciaux complexes et répondent aux exigences des applications industrielles : le contrôle passif de la formation ou de la rupture des gouttelettes pourrait être obtenu en modifiant la géométrie du dispositif, ce qui implique la jonction en T, la jonction en Y et également l'introduction de nouvelles géométries telles que des obstructions, des pentes et des configurations d'émulsification par étapes. L'introduction d'une force externe s'avère efficace pour réaliser le contrôle actif des écoulements polyphasiques et des comportements de gouttes liquides. Les techniques de pointe reposent principalement sur le champ magnétique, le champ électrique, la force centrifuge, l'onde acoustique, le laser de puissance et la lumière visible ou UV, etc. En fonction des différentes propriétés intrinsèques, des liquides peuvent être classés en fluides newtoniens, fluides non newtoniens, ferrofluides, dispersions et liquides ioniques, suspension, émulsion, etc. Des fluides rhéofluidifiants dépendant du cisaillement et viscoélastiques sont les solutions aqueuses non newtoniennes typiques, et la manipulation active sur la goutte de ferrofluide est souvent combinée avec un champ magnétique externe. Des fluides complexes sont très souvent rencontrés dans notre vie quotidienne et dans des applications industrielles.

Les écoulements polyphasiques et les phénomènes interfaciaux à plusieurs échelles ont été expérimentalement étudiés par des méthodes tant passives et qu’actives dans cette thèse de doctorat. L’approche multi-échelle aborde l'échelle de longueur du micromètre au millimètre et l'échelle de temps de la microseconde à la seconde. Les travaux de recherche de cette thèse ont été menés à l'aide de liquides aqueux non newtoniens et ferrofluides, y compris la formation et la rupture de gouttelettes dans des dispositifs microfluidiques, l'impact de gouttes sur une surface liquide ou solide ainsi que la manipulation magnétique de gouttes de ferrofluide. La thèse comprend 8 chapitres au total. Le premier chapitre commence par la revue de la littérature comprenant le contexte de la recherche et l'état de l’art sur les écoulements polyphasiques et les phénomènes interfaciaux à différentes échelles. Au chapitre 2, une brève introduction des dispositifs expérimentaux, des liquides de travail et des

méthodes analytiques générales est donnée. Les chapitres 3 à 7 présentent une collection d'articles déjà publiés dans des revues ou des manuscrits à soumettre : au chapitre 3, la formation de gouttelettes dans les dispositifs de jonction en T et de flow-focusing a été étudiée expérimentalement par la visualisation à grande vitesse et la technique micro-PIV. Au chapitre 4, la dynamique de la déformation et de la rupture des gouttelettes élastiques dans un dispositif de flow-focusing a été étudiée. Le chapitre 5 vise à étudier la coalescence initiale de la goutte de liquide non newtonien sur une surface liquide plane de la même nature et le chapitre 6 traite du contact initial et de l'étalement d'une goutte pendante sur une surface solide. Ces deux parties ont été conjointement étudiées par un système électrique ultra-rapide à courant continu développé par nos soins, une caméra à grande vitesse et un système micro-PIV à grande vitesse. L'amincissement et la rupture du filament du cou de gouttes ont été étudiés à des échelles du temps très courtes grâce aux signaux électriques par l'acquisition ultra-rapide de la conductimétrie électrique. Au chapitre 7, l'accent est mis sur le contrôle actif des gouttes de ferrofluide par un champ magnétique externe. Le dernier chapitre 8 donne lieu aux conclusions générales, aux innovations réalisées et à quelques perspectives pertinentes. Le contenu principal est le suivant.

- Chapitre 1

Le contexte de la recherche et l'état de l'art sur les écoulements polyphasiques et les phénomènes interfaciaux à différentes échelles sont présentés dans cette section. Les comportements d'écoulements polyphasiques dans des dispositifs microfluidiques sont affectés par divers paramètres, notamment des conditions de fonctionnement, des propriétés du fluide ainsi que des géométries de dispositifs. Les écoulements diphasiques gaz-liquide et liquide-liquide dans le microcanal sont à la base de la technologie microfluidique. Le principal contenu de recherche concerne le diagramme d'écoulement, la formation et la rupture de gouttelettes (ou bulles), des corrélations de taille, etc. progressivement étendu aux solutions aqueuses non newtoniennes. En combinaison avec les méthodes expérimentales classiques de la caméra à grande vitesse, une technique avancée de vélocimétrie par image de particules à micro-échelle (micro-PIV) a été introduite pour obtenir un aperçu approfondi du champ de vitesses dans un écoulement diphasique.

En plus des écoulements polyphasiques dans des microcanaux confinés à des micro-échelles, l'impact de la goutte à une surface liquide ou solide est un autre domaine de recherche essentiel. Catalogué par l'état de la surface, l'impact de la goutte comprend deux phénomènes distincts que ce soit sur une surface liquide ou sur une surface solide. Les travaux de la littérature sur la coalescence non confinée d'une goutte sur une surface liquide et d'une goutte s'étalant sur une surface solide sont également présentés. De plus, les méthodes de contrôle passif et actif des écoulements polyphasiques et certains phénomènes interfaciaux associés sont présentés en détail.

- Chapitre 2

Une brève introduction à la description des différents dispositifs expérimentaux, à la préparation des liquides et aux méthodes analytiques générales est reprise dans cette partie.

Dans les expériences, trois différentes techniques, y compris une caméra à grande vitesse, un système d'acquisition ultra-rapide de la conductimétrie électrique à courant continu (CC) et un micro-PIV à grande vitesse ont été utilisées. La caméra à grande vitesse peut atteindre une vitesse de capture de 6000 images par seconde (fps) dans les dispositifs microfluidiques et de 84054 fps pour la coalescence et l'étalement des gouttes en pleine résolution. La tension électrique de la goutte liée à la grandeur surfacique de contact avec le temps a été mesurée avec une vitesse d'échantillonnage de 1,25 x 10^6 Hz. Ainsi l'intervalle de temps entre deux signaux électriques successifs est descendu à 0,8 µs. Le micro-PIV à grande vitesse pourrait atteindre une vitesse de capture de 10^4 champs de vitesse par seconde dans les dispositifs microfluidiques et de 5000 champs de vitesse par seconde pour la coalescence et l'étalement des gouttes. Les dispositifs microfluidiques de jonction en T et de flow-focusing sont en polyméthacrylate de méthyle (PMMA), la largeur du canal varie de 200 à 600 micromètres.

Les fluides utilisés dans cette thèse sont constitués des fluides newtoniens et des fluides complexes. Les fluides newtoniens sont de différente viscosité. Les fluides complexes comprennent les fluides rhéofluidifiants de carboxyméthylcellulose (CMC), les fluides viscoélastiques de polyacrylamide (PAAm) et d'oxyde de polyéthylène (PEO) ainsi que le ferrofluide. Dans ce travail, trois types de particules d'ensemencement ont été utilisés, qui sont des sphères de verre creuses revêtues

d'argent, des particules de fluorescence et des particules de latex respectivement. Des sphères de verre creuses revêtues d'argent et des particules de fluorescence ont été utilisées pour explorer le champ de vitesses pendant la coalescence et l'étalement d'une goutte. Des particules de latex ont été utilisées pour suivre les champs de vitesse pendant la formation de gouttelettes dans les dispositifs microfluidiques. En outre, les propriétés du liquide telles que la densité, la viscosité, la tension superficielle, l'angle de contact, la conductivité électrique, la densité de flux magnétique sont mesurées par les appareils de mesure correspondants.

- Chapitre 3

Dans ce chapitre, les écoulements diphasiques liquide-liquide et la formation de gouttelettes dans les dispositifs microfluidiques ont été expérimentalement étudiés par une caméra à grande vitesse et un micro-PIV à grande vitesse. Deux configurations microfluidiques comprenant la jonction en T et le flow-focusing ont été utilisées.

Dans la première partie, le dispositif de jonction en T avec une section de 200 μm x 200 μm a été utilisé. Des solutions de PEO-glycérol avec différentes masses moléculaires de PEO et une solution de glycérol à 50% en masse ont été utilisées comme phase dispersée pour des gouttelettes. De l'huile minérale avec un tensioactif a été utilisée comme phase continue. La solution de PEO-glycérol est un fluide de Boger avec une viscosité indépendante de la vitesse de cisaillement. L'élasticité du fluide de Boger est normée pour former un nombre d'élasticité.

Quatre régimes d'écoulement ont été observés sous divers rapports des débits diphasiques lorsque l'élasticité de la phase dispersée était fixée : bouchon, goutte à goutte, perles-sur-corde et stratifié, comme le montre la figure I. En comparaison avec le régime d'écoulement observé dans un fluide newtonien dans la jonction microfluidique en T, l'élasticité conduit à l'émergence d'un écoulement perles-sur-corde. Plus l'élasticité du fluide est importante, plus la longueur du filament est grande au moment de la rupture. La dynamique de la formation des gouttelettes dans le fluide élastique et le fluide newtonien est étudiée et comparée dans un cycle. L'ensemble du processus peut être divisé en trois étapes : l'expansion, la compression et l'étirement respectivement. Pour les fluides élastiques, le col du filament de la phase dispersée subit une étape d'étirement après l'étape de compression. La largeur minimale du filament reste constante tandis que la longueur augmente. Dans l'étape

d'étirement, le col du filament évolue en un fil fin de largeur minimale constante et s'allonge sous l'étirement de la gouttelette en aval. La longueur adimensionnelle du filament augmente linéairement avec le temps adimensionnel. Le maximum de la longueur adimensionnelle du filament à la rupture est positivement corrélé à l'élasticité de la phase dispersée mais inversement proportionnel au débit de la phase continue.

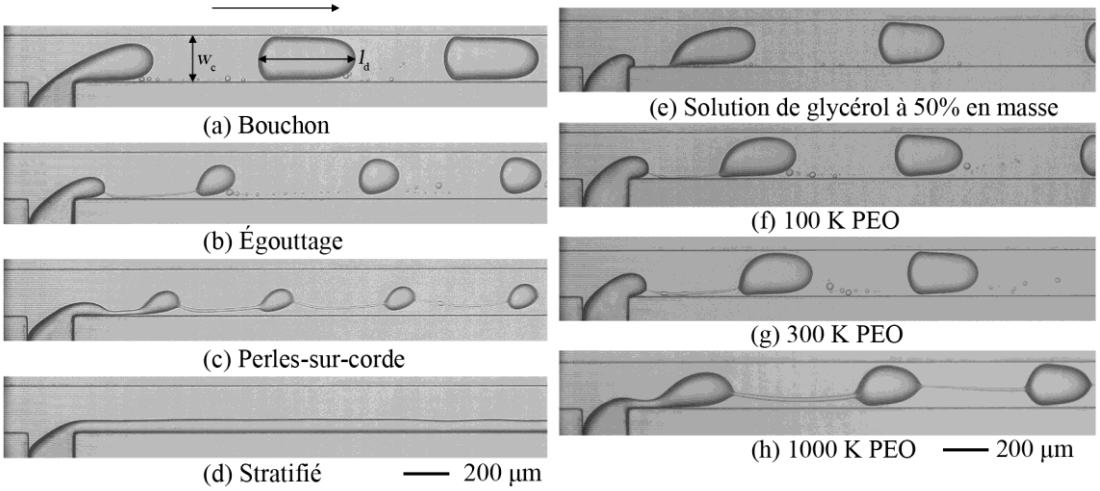


Fig. I (a-d) Régimes d'écoulement avec les débits diphasiques. (a) Bouchon. (b) Égouttage. (c) Perles-sur-corde. (d) Stratifié. (e-h) Régimes d'écoulement avec l'élasticité de la phase dispersée. (e) Solution de glycérol à 50% en masse. (f) Solution de PEO à 100 K. (g) Solution de PEO à 300 K. (h) Solution PEO à 1000 K.

Ensuite, l'influence des débits diphasiques, du nombre de capillarité et du nombre d'élasticité sur la taille des gouttelettes a été étudiée. La taille des gouttelettes augmente avec le débit de la phase dispersée et le nombre d'élasticité, tandis que diminue avec le débit de la phase continue, le rapport des débits diphasiques et le nombre de capillarité de la phase continue. En combinaison avec les mécanismes de compression et de cisaillement, les corrélations prédictives de la littérature pour la taille des gouttelettes newtoniennes ont été modifiés en tenant compte du rapport des débits diphasiques, du nombre de capillarité et du nombre d'élasticité. En comparant les exposants des trois paramètres, il a été démonté que l'effet de l'élasticité du fluide est plus prononcé sur la dynamique de formation des gouttelettes que la taille finale des gouttelettes.

La deuxième partie du chapitre 3 s'est concentrée sur la formation de gouttelettes

dans un fluide élastique dans un flow-focusing microfluidique, où de l'huile de silicone était utilisée comme phase dispersée et des solutions élastiques de PEO de différente masse moléculaire comme phase continue. Le modèle de Carreau a été utilisé pour décrire les propriétés rhéologiques des solutions de PEO. A des débits fixes de la phase dispersée, trois régimes d'écoulement: bouchon, égouttage et jet ont été observés en augmentant le débit de la phase continue, comme illustré dans la figure II. Le nombre de capillarité et le nombre de Weber sont considérés comme les principaux paramètres permettant de distinguer divers régimes d'écoulement. Les lignes de transition entre divers régimes d'écoulement ont également été étudiées.

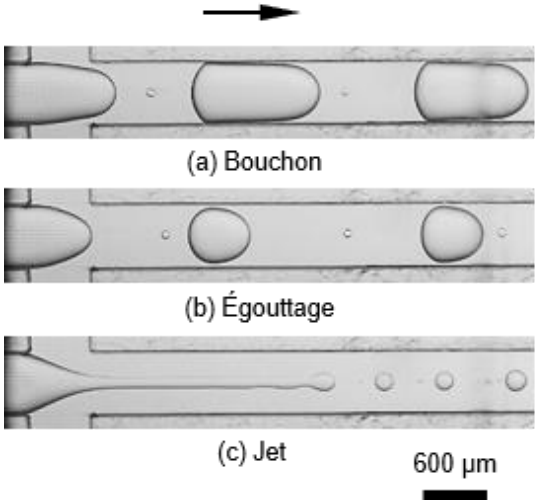


Fig. II Régimes d'écoulement de la solution d'huile de silicone-PEO dans le flow-focusing microfluidique.

La dynamique de la formation d'une gouttelette de bouchon dans un cycle entier comprend les étapes d'attente, d'expansion, de compression et de pincement. La variation de la largeur minimale du filament avec le temps suit une loi de puissance durant l'étape de pincement. Les exposants de 1/3 à divers débits de la phase continue et des concentrations de PEO indiquant que le mécanisme de pincement dans les liquides viscoélastiques est le même que celui de la formation de bulles, également dominé par la force d'inertie.

Pour fournir des informations approfondies sur le champ de vitesses pendant la formation des gouttelettes, la technique micro-PIV à grande vitesse a été appliquée dans ce travail. Ici, les champs de vitesse dans la phase dispersée pendant la formation

de gouttelettes correspondant à trois régimes d'écoulement ont été mesurés expérimentalement à 10^4 Hz. Dans l'écoulement de bouchons, deux situations ont été observées en fonction du fait si l'écoulement inverse a été observé ou non en amont dans la phase dispersée au point de la rupture. Dans le régime d'égouttage, un écoulement inverse et les gouttelettes satellites sont également apparus dès la rupture du col. Dans le régime de jet où le débit de la phase continue était beaucoup plus grand que le débit de la phase dispersée, le filament de la phase dispersée se situe au milieu du microcanal et est allongé dans la direction axiale vers l'aval.

L'effet de différents paramètres sur la taille de la gouttelette de bouchon a également été étudié. La taille des gouttelettes augmente avec le débit de la phase dispersée et le rapport des débits diphasiques, tandis que diminue avec le débit de la phase continue, le nombre de capillarité de la phase continue et le nombre d'élasticité. Sur la base des corrélations prédictives de la taille des bulles dans les fluides viscoélastiques, les corrélations pour prédire la taille de la gouttelette de bouchon ont été proposées dans deux gammes de la taille des gouttelettes en prenant en compte le rapport des débits diphasiques, le nombre de capillarité et le nombre de Reynolds de la phase continue.

- Chapitre 4

Dans cette partie, l'étirement et la rupture des gouttelettes élastiques dans un dispositif microfluidique de flow-focusing ont été étudiés expérimentalement par une caméra à grande vitesse. Des solutions de PEO-glycérol avec différentes masses moléculaires de PEO et une solution aqueuse de glycérol à 50% en masse ont été utilisées comme phase dispersée Ll. De l'huile minérale avec un tensioactif a été utilisée comme phases continues L2 et L3. Le nombre élasto-capillaire *Ec* a été choisi pour décrire l'élasticité de la solution PEO-glycérol, où *Ec* varie de trois ordres de grandeur.

Trois régimes typiques ont été observés à la deuxième jonction de flow-focusing en ajustant les conditions opératoires et l'élasticité de la phase dispersée : étirement-rebond sans queue, étirement-rebond avec queues et étirement-rupture, comme le démontre la Fig. III. Pour les phases dispersées à faible élasticité, trois régimes sont apparus consécutivement avec le débit de L3. A élasticité moyenne, l'augmentation du débit de L3 n'a abouti qu'à l'émergence de deux régimes

d'étirement-rebond sans rupture de gouttelettes. A une élasticité extrêmement forte, seul le régime d'étirement-rebond sans queue a été observé dans les conditions opératoires. L'évolution interfaciale pendant les régimes d'étirement-rebond des gouttelettes pourrait être divisée en trois étapes : le déplacement, l'étirement et le rebond. Les tendances étaient similaires dans les étapes de déplacement et d'étirement. La différence se reflète dans l'étape de rebond : en régime I sans queue, la largeur minimale du col de la gouttelette augmente progressivement jusqu'à ce que la gouttelette retrouve sa forme d'origine. En régime II avec queue, la largeur minimale du col de la gouttelette est restée quasiment inchangée et la longueur de la gouttelette a diminué dans l'étape de rebond.

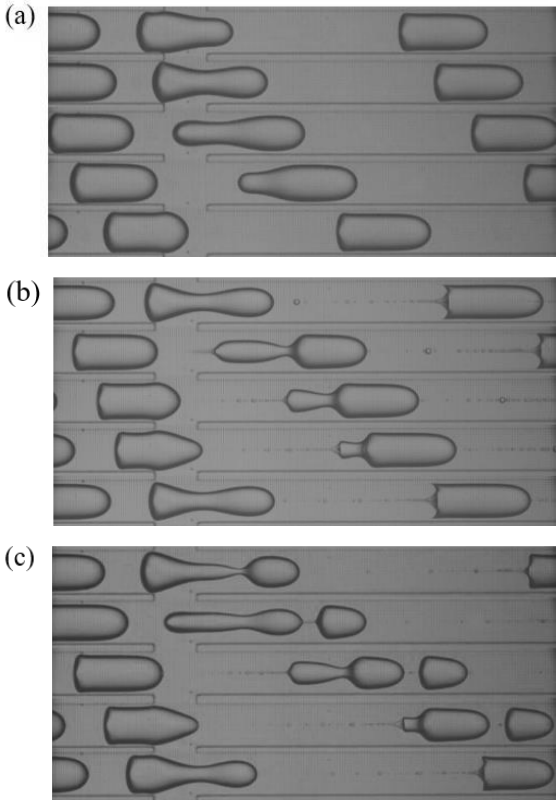


Fig. III Régimes d'écoulement de l'étirement élastique et de la rupture active des gouttelettes élastiques dans une jonction microfluidique de flow-focusing. (a) Étirement-rebond sans queue (régime I) ; (b) Étirement-rebond avec queue (régime II) ; (c) Etirement-rupture (régime III).

Pour les fluides à faible élasticité, la valeur de crête de la longueur maximale des gouttelettes pourrait atteindre 2,2 fois la longueur initiale des gouttelettes. Pour les fluides à élasticité élevée, la gouttelette continuerait à s'étirer et pourrait atteindre 9

fois la longueur initiale dans nos conditions expérimentales. La loi de puissance pour la longueur maximale adimensionnelle de la gouttelette pourrait être exprimée en deux gammes.

En régime III de rupture par étirement, les tailles de la gouttelette mère et de la gouttelette fille 1 étaient moins affectées par l'élasticité du fluide. Le rapport de taille a diminué avec le temps jusqu'à ce que la “gouttelette fille 2” atteigne un asymptote stable. Pour les gouttelettes de différente élasticité, le rapport de taille était plus petit avec le nombre élasto-capillaire plus important.

- Chapitre 5

Dans les chapitres précédents, l'écoulement liquide-liquide et le comportement des gouttelettes ont été étudiés dans les dispositifs microfluidiques. Dans les chapitres présent et suivants, l'échelle de longueur des gouttes est étendue et varie de plusieurs centaines de micromètres à millimètres.

Le chapitre 5 s'est concentré sur la coalescence initiale d'une goutte aqueuse sur une surface liquide plane de la même nature en utilisant trois techniques. Les séquences de coalescence ont été enregistrées par une caméra à grande vitesse depuis une vue frontale. Le circuit électrique à courant continu (CC) a été développé dans ce travail sur la base d'une source de courant Howland améliorée, où une goutte liquide coalescente sert de la résistance électrique qui reflète la taille de la zone de coalescence. Les champs de vitesses pendant la coalescence ont été mesurés par le micro-PIV à grande vitesse pour la première fois tant dans la goutte qu’à la surface initialement plane du liquide. Les liquides de travail sont étendus aux liquides non newtoniens très visqueux avec des viscosités à cisaillement nul variant de près de cinq ordres de grandeur.

Pendant la coalescence initiale durant les premiers 4 ms, il n'y a pas de différence notable entre les liquides de travail de différente viscosité selon les images prises par la caméra à grande vitesse, comme le montre la Fig. IV. Ensuite, nous nous concentrons sur la variation de la résistance électrique avec le temps lors de la coalescence initiale.

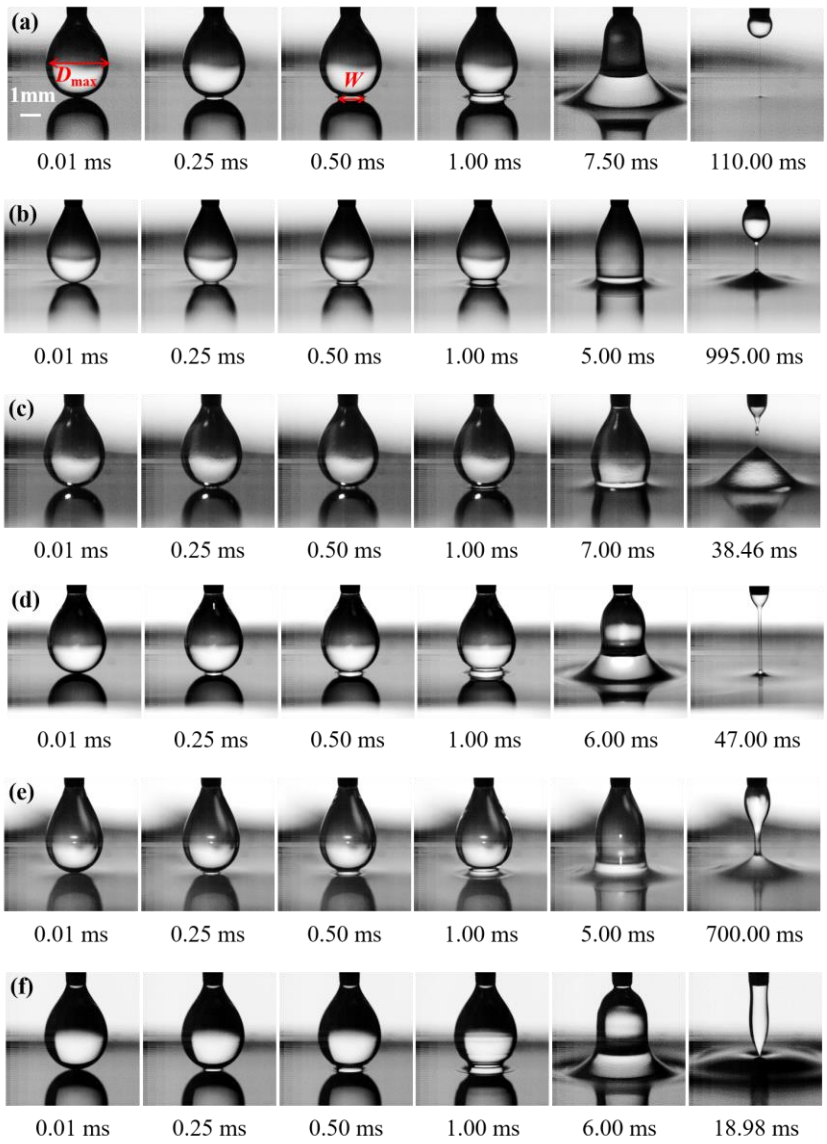


Fig. IV Séquence pour la coalescence initiale d'une goutte pendante à la surface plane du liquide. v_0 = 0,29 mm.s^{-1}. (a) 0,5% en masse de PAAm avec 10% en masse de NaCl. (b) 2% en masse de PAAm avec 10% en masse de NaCl. (c) 2% en masse de HV CMC avec 5% masse de NaCl. (d) 1% en masse de MM PEO avec 5% en masse de NaCl. (e) 1% en masse de HM PEO avec 5% en masse de NaCl. (f) De l'eau avec 5% en masse de NaCl. D_{max} et W représentent respectivement la largeur de goutte maximale à la coalescence initiale et la largeur de coalescence. La barre d'échelle indique 1 mm.

En seulement 0,1 ms, la résistance diminue de près de deux ordres de grandeur. La conductance de la goutte n'est rien d'autre que l'inverse de la résistance: une intégration par le logiciel électrostatique révèle que la conductance dominante se situe dans la section de la coalescence S d'une manière linéaire lorsque celle-ci est

inférieure à 2,5% de la section minimale de liquide à la sortie de la buse. Cela conduit à une loi de puissance entre la largeur de coalescence et la conductance avec un exposant de 1/2. La relation entre la largeur de coalescence normée par le diamètre maximum de la goutte et le temps normé par le temps inertiel confirme les régimes distincts pour la configuration goutte à goutte : linéaire dans le régime visqueux à limitation inertielle (ILV); racine carrée dans le régime inertiel; éventuellement un régime visqueux transitoire entre les deux avec une correction logarithmique. L'appareil électrique CC ultra-rapide a permis de suivre l'évolution de la largeur de coalescence jusqu'à 7,4 μm sur une durée de 10 μs.

Le champ de vitesses dans la goutte et à la surface plane du liquide lors de la coalescence initiale est assez similaire quels que soient les liquides utilisés dans ce travail. Dès que la goutte pendante coalesce avec la surface plane du liquide, la libération brutale d'énergie surfacique provient de la pression de disjonction de Laplace due à l'évolution de la courbure locale. La diminution progressive de l'amplitude de la vitesse avec le temps révèle que la transformation de l'énergie surfacique en énergie cinématique est plus prononcée au début de la coalescence. Lorsque la section de coalescence s'élargit, la vitesse radiale se développe à la base de la goutte et la vitesse axiale s'infléchit pour former un vortex dans le coin à mesure que la goutte rétrécit progressivement.

- Chapitre 6

Ce chapitre a porté sur l'impact d'une goutte pendante suivi de l'étalement et de la rupture du cou sur une surface solide. Le dispositif expérimental était similaire à celle de la coalescence des gouttes, une électrode est également reliée à la buse métallique tandis que l'autre sur la surface sous forme du disque en acier inoxydable. Le disque a été minutieusement poli avant utilisation. Le microscope électronique à balayage (SEM) et la microscopie à force atomique (AFM) permettent de caractériser avec grande précision l'état de la surface du disque en acier inoxydable et démontrent que la rugosité maximale de la surface est seulement de 1 μm.

Pendant le contact initial et l'étalement d'une goutte sur la surface solide durant les premiers 4 ms, il n'y a pas non plus de différence notable entre les liquides de travail de différente viscosité selon les images prises par la caméra à grande vitesse, comme le montre la figure V. Ensuite, nous utilisons la même approche que la

coalescence de gouttes sur la variation de la résistance électrique avec le temps lors de l'étalement initial. En 0,5 ms, la résistance diminue de près de deux ordres de grandeur. Le retard d'apparition de la résistance minimale est essentiellement attribué à des effets plus prononcés de friction liquide-solide et de dissipation visqueuse par rapport à la coalescence. Dans la phase initiale d'étalement, l'exposant était de 3/4 à une grande vitesse de la goutte approchant la surface solide et passait à 2/3 à une petite vitesse d'approche, quelle que soit la viscosité de différents liquides non newtoniens. A 0,8 μs, le rayon d'étalement sur la surface solide variait entre 8,4 et 23 micromètres pour tous les liquides de travail, ce qui diminue un ordre de grandeur pour la largeur minimale observée par rapport à la méthode de visualisation par la caméra à grande vitesse.

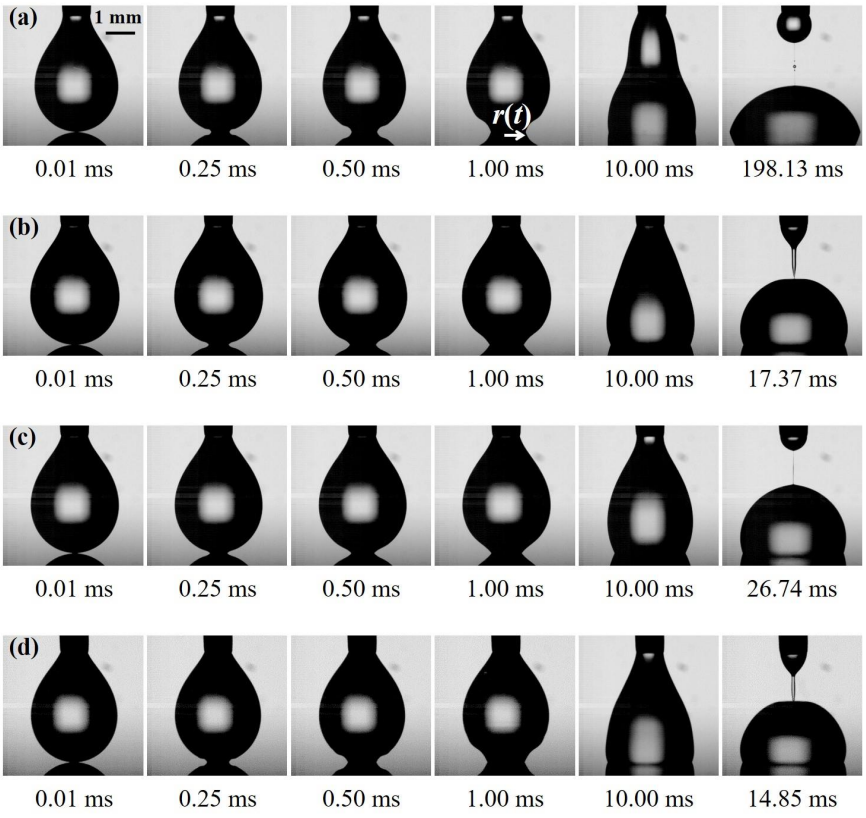


Fig. V Séquence pour le contact initial et l'étalement d'une goutte pendante sur une surface en acier inoxydable. v_0 = 0,29 mm.s^{-1}. (a) 1% en masse de LM PEO solution avec 5% en masse de NaCl. (b) Solution de CMC LV à 2% en masse avec NaCl à 5% en masse. (c) Solution de CMC à 2% en masse de MV avec 5% en masse de NaCl. (d) De l'eau avec 5% en masse de NaCl. *r(t)* est le rayon temporel d'étalement. Toutes les images partagent la même barre d'échelle de 1 mm.

Les champs de vitesses dans la goutte lors du contact initial et de l'étalement ont été obtenus pour la première fois par le micro-PIV jusqu'à 5000 champs de vitesse par seconde. Un phénomène intéressant d'amortissement dans la direction axiale a attiré notre attention. Si l'on met les champs de vitesses tous ensemble, on a pu constater que le phénomène oscillatoire était plus marqué à des vitesses d'approche plus élevées et des viscosités liquides plus faibles. Dans les champs de vitesses mesurés par le micro-PIV, la vitesse de rebond dans la direction axiale a mis en évidence une diminution des exposants de la loi de puissance à l'instant initial par rapport à la relation linéaire de la coalescence des gouttes sur une surface liquide plane.

Après le contact initial suivi de l'étalement de la goutte, le col liquide passerait par le processus d'amincissement du filament jusqu'à la rupture finale. Ensuite, une analyse plus approfondie a été effectuée sur la variation des signaux électriques durant le pincement du filament. De manière surprenante, des pics réguliers ont été observés dans l'évolution de la résistance électrique. Le nombre de pics augmentait à la fois avec masse moléculaire et la concentration du polymère. De plus, on constate que l'intervalle de temps entre deux pics successifs était quasiment identique de 20 ms, à la fois dans la courbe évolutive principale et le plateau de saturation des signaux électriques. En menant les expériences de référence, il a été démontré sans ambiguïté que les pics réguliers n'apparaissaient que lors de l'amincissement du filament des solutions de polymère. Le filament d'une solution de polymère servirait d'interrupteur qui ajuste régulièrement le transport de la macromolécule chargée électriquement. Une étude plus approfondie sera nécessaire pour bien comprendre ce mécanisme.

- Chapitre 7

Dans les chapitres précédents, tous les écoulements polyphasiques et les comportements de gouttes sont étudiés par les méthodes passives. Au chapitre 7, le contrôle actif sur les gouttes de ferrofluide a été réalisé par un champ magnétique externe. Le ferrofluide à base d'huile a été utilisé dans ce travail. Lorsque l'aimant permanent se déplace verticalement vers la buse qui génère une goutte, la densité de flux magnétique exercée sur le ferrofluide devient plus forte.

La coalescence initiale d'une goutte pendante de ferrofluide à la surface du même ferrofluide a d'abord été étudiée en l'absence de champ magnétique externe. La goutte pendante de ferrofluide et la surface se déplaceraient l'une vers l'autre sous l'attraction

magnétique mutuelle entre les particules ferromagnétiques dans le ferrofluide, ce qui est évidemment différent en comparaison avec une goutte pendante de forme ronde et la surface liquide plane d'un liquide newtonien ou non newtonien. L'angle conique de la surface du ferrofluide est de 158° au premier contact. Parmi la plage couverte des vitesses d'approche dans ce travail, l'angle du cône est indépendant de la vitesse d'approche de la goutte de ferrofluide.

Lorsque le champ magnétique est appliqué, la goutte et la surface du ferrofluide se déforment en cônes plus pointus en se rapprochant du point de la coalescence, comme illustré dans la Fig. VI. L'angle conique de la goutte pendante de ferrofluide au premier contact diminue de 18° à 13° avec la densité de flux magnétique, tandis que l'angle du pic de ferrofluide dans le ferrofluide initialement à la surface plane augmente de 32° à 50° avec la densité de flux magnétique appliquée.

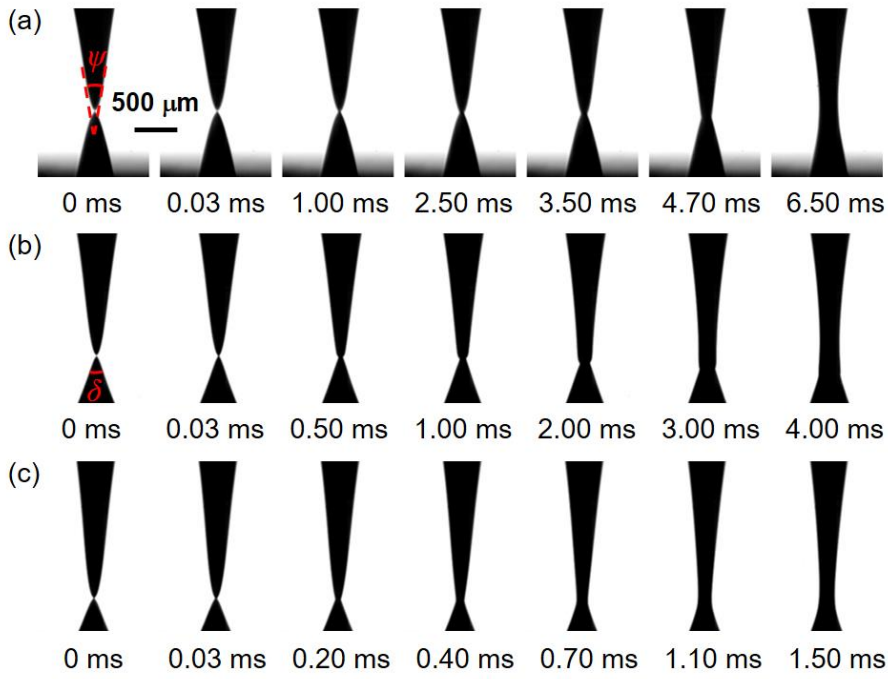


Fig. VI Séquences pour la coalescence initiale d'une goutte de ferrofluide à la surface du même ferrofluide sous divers champs magnétiques. (a) B = 73,10 mT, $v_{0,s}$ = 8,97 mm.s^{-1}, ψ = 18°, δ = 32°. (b) B = 85,54 mT, $v_{0,s}$ = 62,82 mm.s^{-1}, ψ = 16°, δ = 42°. (c) B = 95,25 mT, $v_{0,s}$ = 83,58 mm.s^{-1}, ψ = 13°, δ = 50°. Toutes les images partagent la même barre d'échelle de 500 μm.

Pour découvrir le mécanisme de la coalescence initiale, une technique de micro-PIV à grande vitesse a été appliquée à un liquide modèle newtonien transparent

de solution glycérol-eau à viscosité comparable au ferrofluide. Dès que la goutte a touché la surface du liquide, un phénomène intéressant d'amortissement dans la direction axiale a apparu. Par rapport aux liquides très visqueux, l'oscillation des vitesses axiales est principalement causée par la faible traînée sur la goutte pendante dans ce liquide beaucoup moins visqueux.

En l'absence d'un champ magnétique, la section de coalescence suit une loi de puissance avec le temps. L'exposant est de 0,64 indépendamment de la vitesse d'approche de la goutte de ferrofluide. La largeur de coalescence varie avec la racine carrée du temps et se situe dans le régime inertiel. A faible densité de flux magnétique, la section de coalescence augmente jusqu'à 0,1 mm suivant une loi de puissance avec un exposant de 0,59. Ensuite, la coalescence est accélérée avec un exposant de 3,02 lorsque l'inertie et l'attraction magnétique devenaient progressivement dominantes. Une seule tendance à caractère transitoire à faible vitesse d'approche sous un champ magnétique moyen a été observée. Dans d'autres cas de champ magnétique moyen et élevé, la largeur de coalescence de la goutte de ferrofluide se situe dans le régime inertiel.

La largeur maximale de coalescence diminue avec la densité de flux magnétique, indiquant un effet opposé sur la coalescence des gouttes de ferrofluide par le champ magnétique. Les cycles auto-entretenus de coalescence-rupture des gouttes de ferrofluide ont été observés pour la première fois au-dessus d'un champ magnétique critique. Une modélisation a été développée pour prédire la largeur de coalescence maximale décroissante et la fréquence d'oscillation croissante avec le champ magnétique appliqué.

- Chapitre 8

Pour conclure, les écoulements polyphasiques et les phénomènes interfaciaux à différentes échelles ont été systématiquement étudiés dans le présent travail, ce qui pourrait jeter une base solide sur la conception et l'optimisation des dispositifs d'écoulement polyphasique et faciliter ainsi le développement des modèles théoriques. Les conclusions générales, les innovations et les points pertinents des travaux sont présentés et résumés. Cependant, il existe encore de nombreux domaines d'intérêt qui nécessitent une investigation plus approfondie. Par exemple, nous pourrions effectuer la simulation numérique par les approches de la dynamique moléculaire et de Lattice

Boltzmann, ce qui pourrait acquérir plus de précisions entre l'approche par conductimétrie ultra-rapide à courant continu et la caméra à grande vitesse. La dynamique de la coalescence et de l'étalement d'une goutte pourrait être étudiée plus en détail en faisant varier la vitesse d'approche de la goutte ou les propriétés de la surface liquide et solide. En outre, le sillage négatif derrière un "micro-nageur" manipulé par la mobilité d'un champ magnétique dans des fluides viscoélastiques pourrait être étudié par le micro-PIV à grande vitesse, afin de faire la jonction avec les travaux antérieurs à l'échelle macro- et méso-échelle de notre équipe. Les renseignements qualitatifs obtenus autour du micro-nageur pourraient ainsi compléter l'approche multi-échelle.

General introduction

Multiphase flows and interfacial phenomena are widely involved in the natural world, our daily life, and numerous industrial processes such as chemical engineering and petroleum engineering. The fundamental researches on the multiphase flows and interfacial phenomena could deepen the understanding on the internal mechanisms and provide theoretical guidance for the practical applications. By employing three different techniques including a high-speed camera, an ultra-high-speed Direct Current (DC) electrical device, and a high-speed micro-Particle Image Velocimetry (micro-PIV), the multiphase flows and interfacial phenomena at multiscale were investigated experimentally by both passive and active methods. The multiscale indicates the length scale from micrometer to millimeter and the time scale from microsecond to second. The main contents are as follows:

The flow behaviors of the elastic non-Newtonian liquid-liquid two-phase flow in both T-junction and flow-focusing devices were investigated. The fluid elasticity affected the dynamics of droplet formation, stretching and breakup. During the droplet formation, the peculiar beads-on-string flow was observed and the flow pattern map as well as the transition lines were also plotted. The influences of both the fluid elasticity and the two-phase flow rates on the minimum neck width, the maximum length of the dispersed thread and the droplet size were studied. The predicting models for the droplet size were optimized by introducing the dimensionless parameters to characterize the fluid elasticity. For the stretching and breakup of elastic droplets, the influences of elasticity on the transition from droplet stretching to breakup, the dynamics of droplet stretching and breakup as well as the size ratio of the daughter droplets were also investigated. The power-law models were proposed to predict the maximum stretching length.

Subsequently, the initial coalescence of a pendant drop at a liquid surface and the initial spreading on a solid surface were investigated. The ultra-high-speed DC electrical device with the sampling speed of 1.25×10^6 Hz allows to monitoring the dynamics of coalescence and spreading within 10 μs. The coalescing width expands linearly with time in the inertially limited viscous regime and follows a power law in

the inertial regime. The evolutions of the velocity fields during the initial coalescence and spreading were measured and computed by the high-speed micro-PIV with a capturing rate up to 5000 velocity fields per second, revealing the transformation of surface energy to kinetic energy. Besides, the consecutive electrical peaks with a regular interval of 20 ms were observed during the filament thinning of the polymer liquid neck.

In addition, the active manipulation of the ferrofluid drop was realized by introducing an external magnetic field. Evident deformations of both the pendant ferrofluid drop and the bulk surface were observed prior to the contact even in the absence of a magnetic field. The dynamics of ferrofluid drop coalescence were investigated at various magnetic fields. The exponential laws were proposed to predict the increasing coalescing width with time and the decreasing maximum coalescing width with the magnetic field. A high-speed micro-PIV technique was employed with a transparent model fluid to reveal the flow fields during the ferrofluid drop coalescence. The self-sustained coalescence-breakup cycles of ferrofluid drops were observed for the first time. The exponential model was proposed to predict the increasing periodic frequency with the applied magnetic field.

Chapter 1 Literature review

Multiphase flows and interfacial phenomena are of both academic and industrial interest and widely involved in the dispersed systems. The multiphase flows cover the basic gas-liquid and liquid-liquid two-phase flows, the gas-liquid-liquid and gas-liquid-solid three-phase flows and even more complex flows [1-5]. The emphasis is put upon the mechanisms and dynamics governing the gas-liquid and liquid-liquid two-phase flows. The understanding of the interfacial phenomena and in particular the fundamental mechanisms of spatio-temporary deformation dynamics are of key importance for developing and optimizing the industrial technologies such as emulsification, chemical synthesis, mass transfer and chemical reaction between the gas-liquid and liquid-liquid two phases.

In the field of chemical engineering, a huge variety of phenomena occur in a wide range of both spatial and temporal scales, as shown in Fig. 1-1. The triplet "molecular Processes-Product-Process (3PE)" integrated multiscale approach was defined to describe the multidisciplinary non-linear and non-equilibrium phenomena [6]. This modern multiscale spatiotemporal approach suits the demand for understanding the multiphase flows and interfacial phenomena.

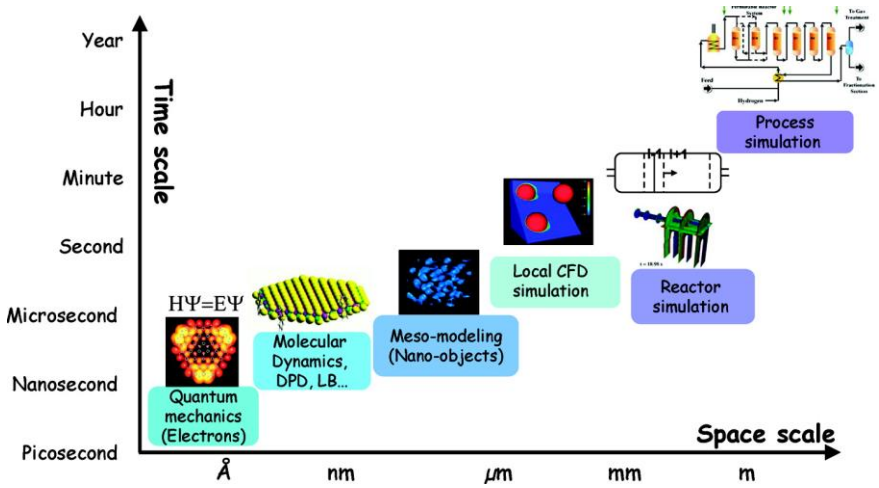


Fig. 1-1 Multidisciplinary non-linear and non-equilibrium phenomena occurring on different length and time scales [7].

1.1 Multiphase flows at the microscale

In the late 20th century, the new concept of "Lab on a Chip" was proposed to meet the trend of miniaturization and the urgent demand for safety and environment protection. Since the microfluidic technology appeared, it has received widespread attention from the researchers around the world and became an attractive alternative to the conventional-scale systems. The microfluidic technology is showing excellent advantages of the controllability, safety, efficiency, economy, compactness and environmental friendliness in the confined space in the microfluidic devices. In the past decade, the micro-mixer, micro-reactor, micro-heating, micro-emulsification and micro-analysis developed rapidly in combination with the microfluidic technology [8-11]. It is worth noting that the most difficult challenge in Chemical Engineering – scale-up could be avoided by the parallelized use of the above-mentioned microtechnology.

Gas-liquid and liquid-liquid two-phase flows in the microchannel are the basis of the microfluidic technology. The main research content involves flow patterns, droplet (or bubble) formation, and the size correlation, etc. The study on the droplet or bubble behaviors in the microfluidic devices is conducive to enrich the theoretical basis of microfluidic technology. The development of microfluidic technology to generate and manipulate monodispersed droplets or bubbles has attracted numerous attention for a wide range of practical applications, including the fields of chemical engineering, bioengineering, agriculture, daily chemical industry, such as the emulsification, crystallization, extraction, synthesis [12-15], the heat and mass transfer [16-18] and the chemical reaction [19, 20].

The multiphase flow behaviors in the microfluidic devices are affected by various parameters, including the operating conditions (two-phase flow rates, temperature and pressure, etc), the fluid properties (viscosity, elasticity, and magnetism, etc) and also the device geometries. The fluids could be classified into two broad categories of the Newtonian fluids and the non-Newtonian fluids with elasticity, shear-thinning or shear-thickening properties. The common geometries of the microfluidic devices include the T-junction, flow-focusing, co-flowing, Y-junction, step junction, etc [21-24], as displayed in Fig. 1-2. The droplet (bubble)

motion, formation, breakup and coalescence could be passively or actively realized and manipulated using the above-mentioned fluids and device geometries.

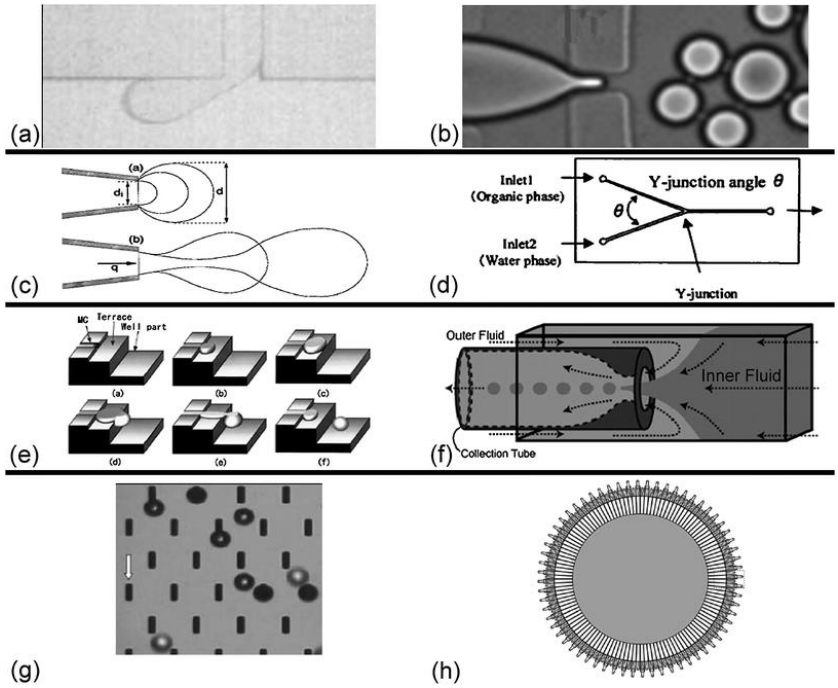


Fig. 1-2 Common geometries of the microfluidic devices [25]. (a) T-junction. (b) Flow-focusing. (c) Co-flowing. (d) Y-junction. (e) Step-junction. (f) Microcapillary device. (g) Straight-through microchannel. (h) Parallelized cross-flow junction.

1.1.1 Droplet (bubble) formation at the microscale

The droplet and bubble based microfluidic technology, based on the liquid-liquid and gas-liquid two-phase flows at the microscale, involves the formation, motion, breakup, distribution/filtration and coalescence of droplets and bubbles [26-28]. Accurate and effective control of the droplets or bubbles in the microfluidic devices has great potential and extensive application prospects in the fields of chemical analysis, medicine, biology and materials synthesis et al. [29-32]. The dynamics of the droplet and bubble formation in the microchannels are affected by the fluid properties (such as the viscosity, surface tension and viscoelasticity), the features of microfluidic devices (such as the wetting with various chip material, configuration and size of the cross section) and the operating conditions (such as the two-phase flow rates, temperature and pressure).

From the perspective of the fluid properties, the research on the droplet or bubble formation in the microchannels goes first from the Newtonian two-phase flows. The production of monodisperse microbubbles in a flow-focusing configuration was firstly reported by Gañán-Calvo et al. [33]. Both experimental and theoretical analyses were performed to propose the scaling law on the bubble size in function of the fluid properties, device geometries and the flow parameters. Their contribution laid a foundation for the application of the microfluidic technology in a vast range of practical processes.

Then a T-junction microchip was designed to generate water-in-oil droplets in pico/nanoliter size [34]. The microchannels with rectangular cross sections of 100 μm × 100 μm (width × depth) for the inlet of the dispersed phase and 500 μm × 100 μm for the continuous phase were fabricated on a polymethyl methacrylate (PMMA) plate. The manipulation of the size and production rate of droplets could be realized by changing the flow rates of both phases.

A comprehensive study on the bubble and droplet formation in various junctions was carried out by Garstecki et al. [35, 36]: The necessary conditions for the quasistationary collapse of the droplet at a narrow orifice was revealed, including the stable geometry and the slow thinning rate of the dispersed thread. The squeezing mechanism made it clear that the pressure drop across the droplet or bubble dominated the breakup of the dispersed neck. The size of a droplet or bubble was exclusively dependent on the two-phase flow rate ratio.

Three types of micromixers with various junction angles of 60°, 90°, and 180° were employed on the bubble formation [37]. The bubble size increased with the liquid viscosity and surface tension while decreased with the junction angle, indicating the cross-shaped junction was able to form the smaller bubbles than those in the convergence shapes. Moreover, the correlations were established to predict the bubble length under all the circumstances.

Then the two stages of the bubble pinch-off before the breakup point were paid attention [21, 38]. The data for the minimum width of the gas thread in function of the remaining time collapsed on a power-law master curve. In the first stage, the scaling exponent of 1/3 indicated the dominant filling effect with a pressure-driven flow through a liquid layer rather than the capillarity. In the final stage where the axial

length scale of the bubble neck decreased faster than the radial one, the exponent of 2/5 could be derived from the less slender neck due to the liquid inertia.

Fu et al. [39-42] conducted a series of works on the bubble and droplet formation in microfluidic flow-focusing and T-junction devices. For the case of bubble formation in Newtonian liquids, the effects of the viscosity, flow rate of the continuous phase and the channel geometry on the bubble size were discussed. The correlations for the pinch-off dynamics and the bubble size were also quantified. As for the droplet formation, six typical patterns of the liquid-liquid two-phase flows in a flow-focusing device were observed and the flow pattern map was plotted by the Weber number *vs.* the capillary number. The scaling laws for the droplet size in the dripping and jetting regimes were established with the two-phase flow rate ratio and the capillary number. In the jetting regime, the length and width of the stable jet could be predicted with the liquid properties and flow rates.

The droplet or bubble formation was also expanded to the highly viscous Newtonian liquids. The breakup mechanism of high-viscosity thread for droplet formation in a flow-focusing device was investigated [43], where 89.5 wt% glycerol aqueous solution was used as the high-viscosity dispersed phase. Two breakup types of the symmetrical and asymmetrical rupture were observed and each could be divided into the squeezing and the pinch-off stage, owing to the disparity of the strain field at the detachment point in the pinch-off stage.

On the bases of the two-phase flows concerning the Newtonian liquids, the research interests of the two-phase flow in microfluidic devices gradually extended to the non-Newtonian aqueous solutions, including the shear-thinning liquids of xanthan gum and carboxymethyl cellulose sodium (CMC), the viscoelastic liquids of polyacrylamide (PAAm) and polyethylene oxide (PEO), etc.

Chiarello et al. [44] conducted the formation of oil drops in the shear-thinning xanthan gum solutions in a T-junction microchip. The channel walls made of PDMS were hydrophilic after the surface treatment, thus stable linseed oil droplets could be realized without the addition of surfactant into the continuous phase. When the shear-thinning liquids served as the continuous phase, the differences in the droplet size could be explained in terms of the liquid viscosity that varies with the velocity gradient according to its flow rate. Rostami et al. [45, 46] performed the formation of xanthan gum droplets at a microfluidic cross-junction. The presence of the

non-Newtonian dispersed phase resulted in longer dispersed thread and satellite droplets which increased the polydispersity of the system. The monodispersed emulsions could be obtained at low flow rate ratios when the capillary numbers of the continuous phase are larger than 0.05.

The bubble formation in the viscoelastic PAAm liquids in both the flow-focusing and T-junction devices was focused [47-49]. The rheological property of the polymer liquids showed significant effects on the breakup dynamics of bubble formation and the bubble size. The minimum width of the gas thread before the breakup in function of the remaining time exhibited a power-law relationship with an exponent around 1/6 in the flow-focusing device and 1/5 in the T-junction. Modified scaling laws for the bubble size were proposed to describe the effect of the PAAm concentration. For the case of droplet formation in PAAm solutions [50], numerous sub-satellite droplets were frequently formed with interdependent sizes of the primary satellite droplet.

Another viscoelastic liquid of PEO also received a lot of attention on the droplet formation: Husny and Cooper-White [51] investigated the droplet formation in PEO-glycerol solutions in a microfluidic T-junction, they divided the stretching process of the dispersed thread into the pre-stretch stage and exponential self-thinning stage. In addition, it was found that the droplet size was nearly independent of the PEO molecular weight within the experimental range, which implies that the effect of elasticity on the droplet size is negligible. Steinhaus et al. [52] investigated the elasticity effects of PEO aqueous solutions with various molecular weights on the droplet formation. It was found that the PEO solutions would exhibit stronger elasticity and viscosity at higher molecular weights. The dispersed thread grew longer and the time required for the neck rupture increased. The formation of the dispersed thread was systematically studied by Lee et al. [53]. The PEO-glycerol aqueous solutions and the mineral oil with the addition of the surfactant Span 80 were employed as the dispersed phase and the continuous phase, respectively. A stable region dominated by the viscoelasticity and the migration of surfactant would result in the appearance of long threads. Du et al. [54, 55] focused on the breakup dynamics of viscoelastic PEO thread for the droplet formation in the flow-focusing device. Four breakup regimes of the viscoelastic thread including two unique regimes in the viscoelastic fluid where the breakup could occur at the upstream end were observed. For the flow-focusing devices with an additional orifice, it was demonstrated that the

breakup of the viscoelastic thread exhibited the self-similarity at the microscale and the finite-time singularity at microscale was inhibited by the viscoelasticity.

In combination with the classical experimental methods by the high-speed camera, an advanced technique of Particle Image Velocimetry (PIV) was introduced to gain deep insight into the flow field during the multiphase flows [56].

For the bubble formation in a co-flowing microfluidic device [57], the velocity fields were computed by adding the fluorescence seeding particles into the continuous phase. The results indicated that the bubble formation was accelerated by the velocity components perpendicular to the direction of the inlet gas flow.

A high-speed confocal micro-PIV system was constructed and applied to the flow of a moving droplet in the microchannel [58], which enabled the acquisition of the cross-sectional velocity distributions in a region of 228 μm × 171 μm at 2000 frames per second. Then the three velocity components in a three-dimensional domain (3D3C) were measured by this system, indicating that the fluid inside a micro-droplet circulated intricately in a closed volume due to the drag force as the droplet moved in the square channel.

For the liquid-liquid system, the velocity fields around the generated droplet gave further understandings on the role of the continuous phase in a whole cycle of droplet formation [42]: In the collapse stage, the droplet neck evolved from convex into concave in the radial direction under the continuous feeding of the continuous phase. Numerous velocity vectors in the radial direction around the dispersed neck confirmed the inertial effect of the continuous phase. Before the final pinch-off, a short viscous tail connecting the dispersed phase and the generated droplet in the downstream formed. Velocity vectors around each end of the tail were in opposite directions in the axial direction. After the pinch-off, the tail derived into a sphere-shaped satellite droplet under the control of the surface tension. The retraction flow disappeared as soon as the satellite droplet with a stable profile formed.

The two-color micro-PIV technique and the high-speed bright field micro-PIV technique were developed by Chinaud et al. [59] to follow the flow field during the plug formation at a microfluidic T-junction. The flow patterns varied with the two-phase flow rate ratios and a large vortex formed at the plug tip when the flow rate ratio equaled to unity. The increase in the interface curvature at the rear of the plug

accelerated the drainage of the continuous phase between the plug and channel wall and caused the meniscus breakup and plug detachment.

The two-color micro-PIV method was also performed to investigate the flow fields in both phases [60], where the shear-thinning xanthan gum served as the non-Newtonian continuous phase. The area of the plug flow, the plug length and velocity as well as the front plug edge curvature increased with the polymer concentration. As shown in Fig. 1-3, the horizontal component of the velocity developed along the flow direction. The maximum velocity emerged in the middle of both phases and decreased toward the liquid-liquid interface and the side walls.

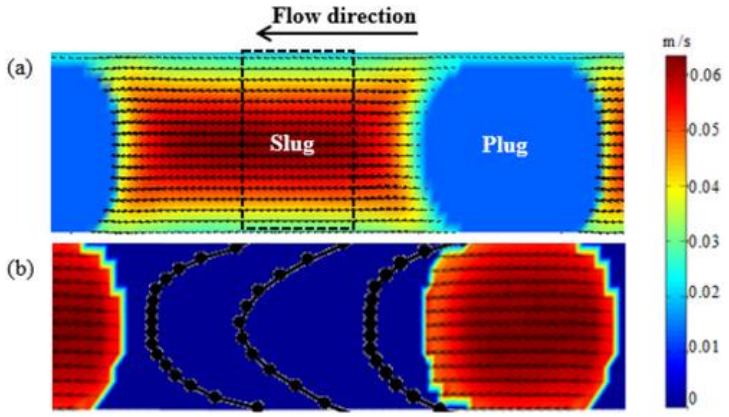


Fig. 1-3 Average velocity fields in both phases obtained by the two-color micro-PIV system [60]. (a) Velocity fields in the slug. The dotted rectangle shows the area of fully developed laminar flow. (b) Velocity fields in the plug.

The high-speed bright field micro-PIV was also employed by Tsaoulidis et al. [61] to obtain the velocity profiles within the plugs of the dispersed aqueous phase. The plug length decreased with the mixture velocity, while the plug velocity showed an opposite trend. The correlation for the plug length of all channel sizes was proposed making use of the capillary number and the Reynolds number. Both the predicting models for the film thickness and pressure drop were established based on the literature model and the experimental data.

A large number of results can be acquired by the above-mentioned experimental methods. However, there are limitations such as the instrument errors of microfluidic devices and the difficulties in the data measurement under some extreme conditions. Thus the numerical methods are widely used to provide accurate information of the

droplet formation, such as the concentration field, velocity field and pressure distribution, etc. With the development of the numerical approaches, the simulation method has become a powerful tool and plays a considerable role in the comparison between the theoretical and experimental investigation of droplet formation at the microscale.

Sang et al. [62] developed a three-dimensional volume of fluid (VOF) model to explore the viscosity effect on the droplet formation at a T-junction. The droplet size decreased with both the consistency and flow index of the non-Newtonian power-law liquid. The analytical model based on the force balance showed a satisfactory prediction of the droplet size. As for Bingham fluids, size prediction based on the analytical model showed an acceptable error within 15%.

Qiu et al. [63] conducted a numerical study on the droplet formation from a micro-aperture in the non-Newtonian cross-flow. Distinct droplet formation regimes including the dripping and jetting regimes were observed and characterized by the capillary number. The simulation results were in good agreement with the experiments and showed that the liquid rheology greatly affected the formation and size of the droplets.

Shi et al. [64] performed the Newtonian and non-Newtonian dispersed droplet formation in the non-Newtonian continuous phase by the lattice Bhatnagar-Gross-Krook (BGK) model. The lattice BGK model could act as an alternative to the lattice gases or the lattice Boltzmann equation for the numerical simulation of fluid dynamics [65, 66]. It was found that the apparent viscosity of the continuous phase increased with the power-law index of the continuous phase. Thus the growth of the droplet was hindered and the droplet length decreased as a result.

Sontti et al. [67] presented a three-dimensional VOF based model on the computational study of the formation of the Newtonian droplets in non-Newtonian liquids at a microfluidic T-junction. Both the rheological parameters and interfacial tension had significant effects on the droplet length and the formation regimes including the squeezing, dripping and jetting regimes.

Taassob et al. [68] investigated the droplet formation of the non-Newtonian xanthan gum in a co-flow device with the InterFoam solver based on the VOF method within the framework of OpenFOAM. The simulated dripping and jetting regimes were observed, where the droplet volume was less dependent on the viscosity of the

xanthan gum and the flow rate of the continuous oil phase significantly affect the droplet formation in the jetting regime.

The effect of viscoelasticity on the drop formation was numerically investigated in various geometries. In a co flowing configuration where the viscoelastic bulk fluid was employed as the continuous phase [69], the viscoelasticity played a similar role as decreasing the two-phase flow ratio. Among the three regimes, the effect of viscoelasticity on the droplet size was most pronounced in the dripping regime. In a microfluidic cross junction [70], the plots for the effective force in a matrix viscoelasticity case where the viscoelastic liquid served as the continuous phase are displayed in Fig. 1-4. The elastic boundary layer was observed, which promoted the extra forces towards the downstream of the liquid thread of the dispersed phase and the deformation of the thread as well.

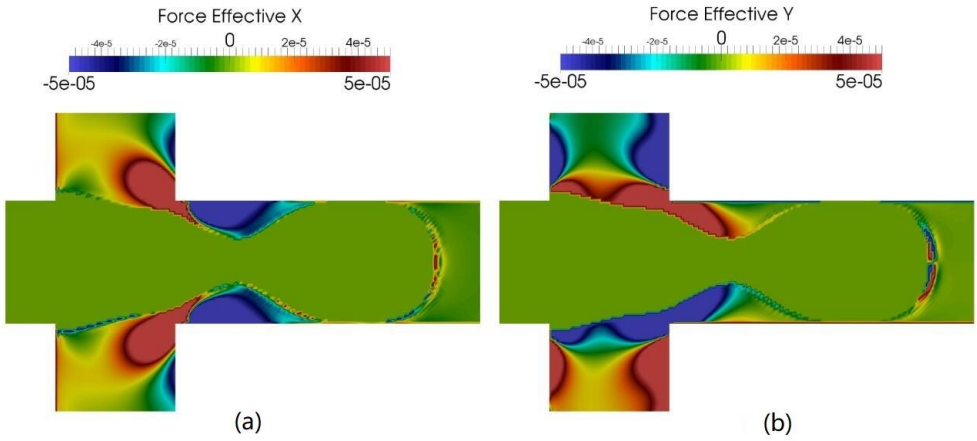


Fig. 1-4 Two distinct plots for the effective force of a matrix viscoelasticity case [70]. (a) *x* component. (b) *y* component.

A bilayer microfluidic device with a bifurcating junction was designed and proposed by Ren et al. [71]. A three-dimensional VOF model was implemented to characterize the shear-thinning effect on the formation of CMC droplets in silicone oil. as well as breakup dynamics when droplets flow through a three-dimensional bifurcating junction. It was demonstrated that the deformation and breakup of the mother droplets were significantly affected by the shear-thinning property and the confined space.

In summary, the elastic properties of the liquids and in particular the triple line contact dynamics at the walls of the microdevices remain still challenging and open

problems in all numerical approaches.

1.1.2 Droplet (bubble) breakup at the microscale

The droplet (bubble) breakup into two or more daughter droplets (bubbles) proves a valid way to improve the production efficiency. It requires systematic research on the complex mechanisms encountered in the droplet (bubble) breakup. Common geometries for the droplet (bubble) breakup include the T-junction, Y-junction and flow-focusing junction, etc.

The droplet breakup was firstly investigated by Link et al. [72] in a microfluidic T-junction and an obstruction-mediated geometry at large capillary numbers. Based on the Rayleigh-Plateau instability, a model for the critical capillary number was proposed to characterize the transition between the breakup and non-breakup regimes in the T-junction, as shown in Fig. 1-5(a-j). For the breakup design with obstruction, the sizes of the resulting daughter drops were sensitive to the precise placement of the obstacle, as displayed in Fig. 1-5(k-m). Each breakup technique mentioned above showed advantages and disadvantages, where the precise control on the droplet size distribution could be realized in a T-junction, while the production efficiency could be obtained in the space-saving design with obstructions.

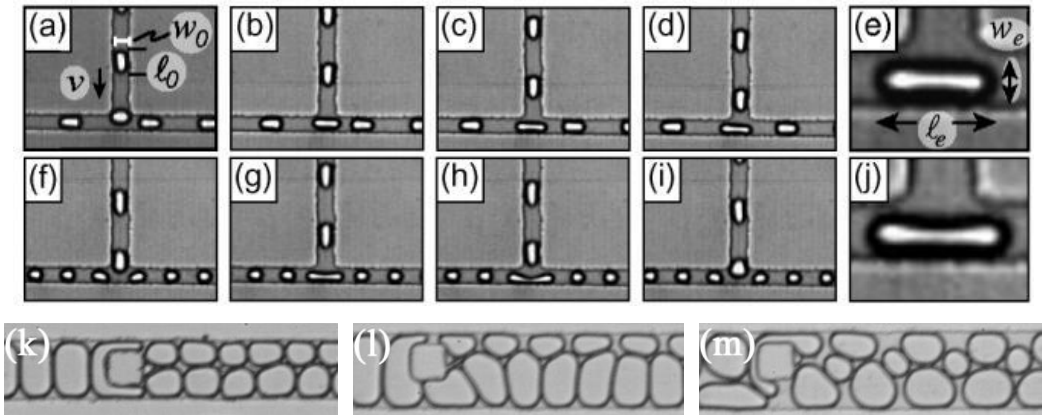


Fig. 1-5 Regimes of droplet breakup [72]. (a-e) Non-breakup in a T-junction. (f-j) Breakup in a T-junction. (k-m) Breakup in an obstruction-mediated geometry with distinct obstacle placement.

Extended to moderate values of the capillary number, the theoretical prediction for the critical condition determining the droplet breakup in a symmetric T-junction was improved by Leshansky and Pismen [73]. The surface tension competed with the

viscous force in the narrow gap between the droplet and the channel wall. It should be noted that this theory could not be directly applied for the droplet breakup in an asymmetric T-junction, where the breakup process producing daughter drops with unequal sizes was intrinsically dynamical and dominated by the flow direction.

Jullien et al. [74] also performed the droplet breakup in a symmetric T-junction where the capillary number varied in three orders of magnitude. Three regimes were observed included the non-breakup, breakup with gaps and breakup with permanent obstruction. A critical droplet length for breakup, independent of the capillary number, was proposed by the physical arguments.

An improved asymmetric T-junction with branch arms of identical lengths and distinct cross sections was employed to form unequal-sized daughter droplets [75]. The power-law correlation in function of the capillary number showing the transition line between the breakup and non-breakup regimes was given. Among the range of the capillary number, the volume of the droplets with unequal sizes was merely affected by the branch width ratios and independent of the capillary numbers. The device could be optimized by using higher branch width ratios and lower capillary numbers to further decrease the droplet size and improve the production efficiency.

Apart from the breakup regimes and size distribution of the daughter droplets in a T-junction, the emergence of satellite droplets during the droplet breakup was paid attention and explored as well [76]. The thread underwent the stretching, fluid drainage and bounce back processes prior to the formation of satellite droplets. It was revealed that both the superficial velocity of the mother droplet and the droplet viscosity exhibited a positive effect on the size of the satellite droplets. A critical capillary number of 0.03 was observed, where the size of the main satellite droplet kept constant below this value and increased with the capillary number above this value.

The deformation and breakup of droplets were also investigated in a symmetric focusing junction. For droplets of low viscosities [77, 78], the phase diagrams were plotted to characterize the critical transition conditions between various regimes including the non-breakup, single breakup and double breakup. The number and size of the daughter droplets were jointly determined by the flow rate and the length of the mother droplet. The critical lengths of the mother droplet and the first daughter droplet showed excellent agreements between the theoretical and experimental results. In the highly viscous systems [79, 80], stable viscous stratifications and a series of

daughter droplets could be observed when the liquid of high viscosity served as the second continuous phase. The size difference between the first two daughter droplets was dominated by the capillary number and the thickness of the liquid film between the droplet and channel wall. Under the circumstance where the highly viscous liquid was employed as the dispersed phase, the non-breakup together with the convective and absolute breakup were observed. The scaling law of the maximum droplet elongation as a function of the initial droplet size and the capillary number was established.

Besides the Newtonian and non-Newtonian aqueous liquids referred above, the ferrofluid was also employed to investigate the droplet breakup at both the T-junction and Y-junction, as exhibited in Fig. 1-6. In a symmetric T-junction [81, 82], three breakup types with permanent, partly obstruction and without obstruction were observed. Both regimes with obstruction could be divided into the squeezing, transition and pinch-off stages. In the regimes with obstruction, the power-law exponents of the minimum neck width with time increased with the magnetic flux density in the squeezing and transition stages and kept constant in the pinch-off stage. The sizes of the daughter droplets and breakup dynamics could be actively controlled by the non-uniform magnetic field. For the breakup of ferrofluid droplets in a Y-junction [83], the size distribution could be manipulated by varying the flow rates and the strength of the magnetic field. A fitted correlation incorporating the magnetic Bond number was attained to predict the volume ratio between two daughter ferrofluid droplets.

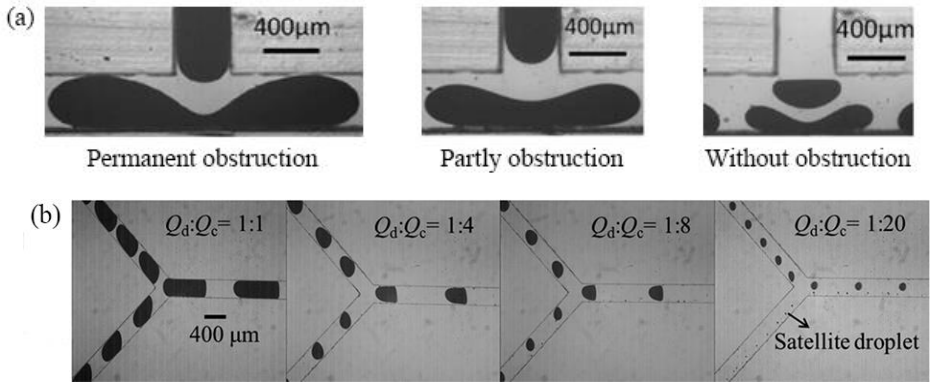


Fig. 1-6 Breakup regimes of ferrofluid droplets. (a) In a symmetric T-junction [81]. (b) In a Y-junction [83].

In addition to the above-mentioned droplet breakup under various circumstances, the bubble breakup also attracted extensive attention to figure out the similarities and differences in comparison with the droplet breakup. Common regimes of a bubble moving through a T-junction involves the breakup with permanent and partly obstruction, breakup with gaps, non-breakup with partly obstruction and gaps [84-86]. For the breakup regimes with partly and permanent obstructions, the critical length of the mother bubble was characterized by the head and rear velocities of the bubble to describe the transition between the two regimes. The breakup dynamics of a bubble corresponding to the regimes with partly and permanent obstructions were also investigated systematically, including the evolution of the minimum neck width, superficial velocity and pressure difference in each sub-stages. The breakup time decreased with the superficial velocity of the mother bubble while nearly independent of the liquid viscosity and the length of the mother bubble.

The T-junction divergences within a symmetric and asymmetric loop were also employed to induce the bubble breakup. In the symmetric loop with two branches of the same length [87, 88], the bubbles could break or do not break at the first T-junction. The breakup regimes were the same as those in the simple T-junction without a loop. The transition model between the breakup and non-breakup regimes was described by a power-law relationship, showing that the extension of the bubble was related to the capillary number and the viscosity ratio between the gas and liquid phases. Furthermore, the critical dimensionless width of the bubble neck was determined as 0.5-0.6: the bubble breakup was irreversible and fast below the critical value while reversible and slow above the value. In the asymmetric loop where two branches with different lengths were divided at the first T-junction, the bubble breakup was affected by the hydrodynamic feedback from the daughter bubbles in the downstream [89]. The size ratio between two bubbles in the branches exhibited a nonmonotonic relationship with the two-phase flow rate ratio and liquid viscosity. The resistance effect of the downstream bubble was related to the capillary number of the longer bubble. While the representative resistance induced by the shorter bubble required further experimental and theoretical studies.

As supplementary to the experimental results, the numerical simulations were also conducted to carry out thorough studies on the droplet (bubble) breakup. The asymmetric breakup of droplet in a novel T-junction with a valve in one of the

branches was investigated by the VOF based numerical algorithm [90]: In the side branch with a valve, daughter droplets with smaller sizes could be acquired by decreasing the capillary number. It was found that the breakup time of droplet was independent of the valve ratio. The pressure drop decreased linearly with the valve ratio in the absence of the tunnel, while irrelevant to the valve ratio with the formation of a tunnel.

With the multiphase Lattice Boltzmann method, the droplet breakup in microfluidic T-junctions was simulated, where the channel walls in one branch were smooth and inhomogeneous in another [91]: Under the effect of contact angle hysteresis, the daughter droplets with smaller sizes always appeared in the nonideal branch. Moreover, the daughter droplet in the nonideal branch moved towards the outlet in a relatively low velocity or maintained blocked near the junction.

The color-gradient model of Lattice Boltzmann method was performed to investigate the asymmetric breakup of droplet in a T-junction [92]: Under a pressure difference at two branches which was expressed by the Darcy-Weisbach equation, the breakup into unequally sized daughter droplets followed two steps of the filling stage and the breakup stage. The volume ratio of droplet in each branch could be adjusted by the asymmetric condition of the T-junction.

The breakup of ferrofluid droplets in a T-junction was also numerically investigated [93]. In the presence of an asymmetric magnetic field, five regimes including the non-breakup and a new splitting in hybrid mode (SHM) were observed. The mother droplet with larger size suppressed the sensibility of the droplet volume ratio to the strength of the magnetic field. A correlation model in function of the capillary number and the magnetic Bond number was built to determine the transition line between the breakup and non-breakup regimes.

The hydrodynamic behaviors of the bubble breakup and deformation were numerically investigated as well. Based on the boundary element model, the interface evolution and flow field of a semi-infinite bubble moving through a Y-junction bifurcation were calculated by Calderon et al. [94]. The splitting ratio was found to increase with the driving bubble pressure and decrease with the angle between the branch arms. The bubble velocity was significantly affected by the viscous loss at the bifurcation. The recirculation zone near the contact line was observed at a higher

pressure and wall shear stress, which laid a foundation for the design of microfluidic devices where fluid mixing was desired.

Chen et al. [95] made use of the interface tracking and finite element methods to investigate the bubble deformation in a symmetric bifurcation. The incompressible Navier-Stokes equation was employed to characterize the effects of the gravity, inertia, and surface tension on the flow pattern and the shear stress gradient. The gravity showed noteworthy influence and led to the changes in the bubble profile and higher pressure and shear stress gradients in the upper branch. The increased pressure gradient near the tip of the bifurcation corner could be observed only in the case of asymmetric bubble breakup.

1.2 Drop coalescence and spreading

Expect for the multiphase flows in confined microchannels at microscales, the free-surface drop impact is another vital research field. Classified by the surface condition below the falling drop, the drop impact comprises two distinct behaviors on a liquid surface and a solid surface.

1.2.1 Drop impact and coalescence on a liquid surface

From the physical point of view, a drop may float, bounce, coalesce or splash at a planar liquid interface according to the initial impact conditions [96, 97] when impinging with a bath of liquid, as shown in Fig. 1-7. Generally speaking, the emphasis is given more to the drop splashing and the drop coalescence, which gain numerous attention in the fields of industrial and engineering applications.

The splashing phenomenon is defined as the ejection of numerous small-sized droplets as a result of the severe deformation of a liquid interface following the drop impact [98]. It's widely encountered in the problems of the industrial and environmental applications [99]. According to the shape, dynamical behavior of the liquid corolla, the splashing could be classified into two categories of the "crown splashing" and the "prompt splashing" [100]. The disintegration of the liquid corolla leads to the ejection of large quantities of droplets. Both the Froude number and the Weber number were employed to determine the splashing behavior, where the deep

liquid splashing was related to both dimensionless numbers while the shallow liquid splashing was only relevant to the Weber number [101-103].

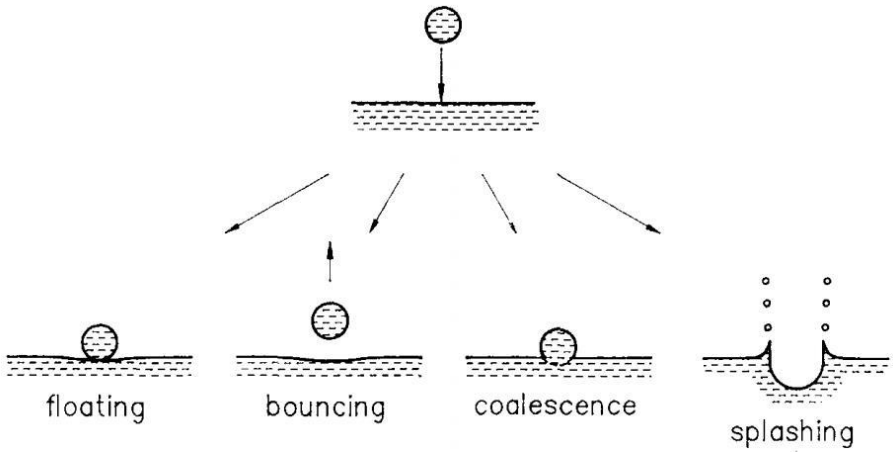


Fig. 1-7 Drop impact on a liquid surface: floating, bouncing, coalescence and splashing [96].

Coalescence is a widely encountered physical phenomenon involving various length scales, such as the formation of solar storms in the universe, raindrop formation, ink-jet printing, oil recovery, emulsification and cell-cell coalescence in micro-biological systems [104-109]. When the gap between two leading edges becomes infinitesimal, an initial liquid bridge forms under van der Waals force [110]. Once the drops come into contact with each other, the neck will rapidly expand due to its lower pressure than the center of the drops. As indicated in Fig. 1-8, the drop coalescence involves the following four types: (1) Drop coalescence at a liquid-liquid interface. (2) Drop coalescence at an air-liquid interface. (3) Coalescence of two spreading drops on a solid substrate. (4) Coalescence of two pendant drops. Each type of drop coalescence will be introduced in detail in the following paragraphs.

Drop coalescence could be observed at a planar liquid-liquid interface in a 2D Hele-Shaw cell, as shown in Fig. 1-8(a). The coalescence of a single glycerol drop at the interface between the glycerol aqueous solution and the silicone oil was jointly investigated by the high-speed camera and the PIV technique [111]. The drop of the water/glycerol mixture was generated through a glass tube and controlled by an electronic valve. As soon as the drop was released from the end of the glass tube, it descended through the superior silicone oil. Prior to the interfacial rupture, the drop was basically motionless on the thin liquid film above the underlying liquid-liquid

interface. After the rupture, the receding free edge of the liquid film was pulled by the capillary force, forming a large opening where the drop sank beneath the bulk liquid. The increasing viscosity of the ambient silicone oil could result in a smaller velocity of the receding free edge and lower vorticity value in the shrinking capillary ring. Then the study on the drop coalescence continued at the glycerol aqueous solution/silicone oil interface [112-114]: The dimensionless Ohnesorge number could distinguish the coalescing regimes. The partial coalescence and a secondary drop were observed in the inertia regime where $Oh < 1$. For the viscous regime where $Oh > 1$, the fully coalescence was observed without any secondary drop. Similarly, the drop coalescence at the liquid-liquid interface between the glycerol aqueous solution and Exxsol D80 oil was also investigated [115]. The 2D PIV system with the maximum frequency of 1000 fps was employed to track the velocity fields inside the coalescing drop. The high concentration of the surfactant Span 80 in the oil phase facilitated the interface deformation before the film ruptured and resulted in a longer time for the film rupture. Immediately after the film rupture, two counter-rotating vortices emerged inside the drop on either side of the rupture point. The intensities of the two vortices significantly decreased with the surfactant concentration. The kinetic energy per unit mass corresponding to various surfactant concentrations was also calculated, indicating that the kinetic energy per unit mass was distributed at the bottom of the drop at the early coalescing stages while distributed near the upper part of the drop at later stages.

Many researchers have also concentrated on the drop coalescence at the air-liquid interface [Fig. 1-8(b)]. The liquid drop might be the same with that in the bath or another miscible liquid [98, 102, 116, 117]. The coalescence of a drop into a pool of liquid can be either instant or delayed [118], complete or partial [119, 120] and affected by various factors including the interfacial tension [121], temperature difference [118], viscosity of the bath liquid and air pressure [98], etc. To be more specific, the drop coalescence could be divided into three stages involving the drainage of the film between the drop and the bulk liquid, the rupture of the film and the growth of the drop neck [121]. In the systems with ultralow interfacial tension, the drainage stage became slow and the film rupture was dominated by the thermal capillary waves. The delayed drop coalescence could be realized in the presence of a temperature difference between the drop and the bath liquid [118]. The critical temperature

difference was determined by the liquid viscosity. Above this critical value, the delayed drop coalescence emerged. The thermal delay of drop coalescence provided a favorable method to levitate drops within the vibrating baths. For the coalescence of a drop with another much more viscous liquid, the mobility was governed by the liquid with a lower viscosity, while the coalescing speed was essentially independent of the viscosity ratio between two phases [116].

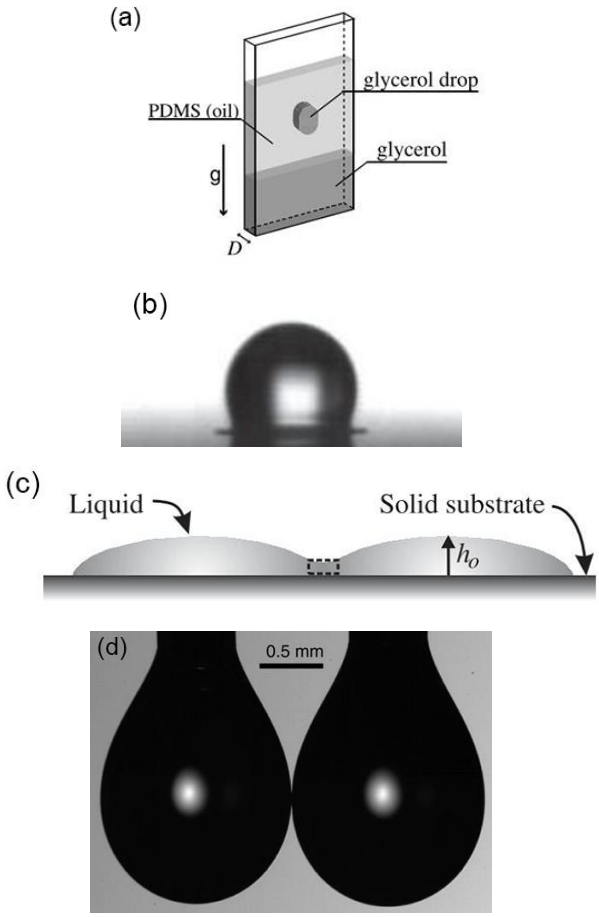


Fig. 1-8 Various types of drop coalescence. (a) Drop coalescence at a liquid-liquid interface [113]. (b) Drop coalescence at an air-liquid interface [98]. (c) Coalescence of two spreading drops on a solid substrate [122]. (d) Side by side coalescence of two pendant drops [123].

In addition to the drop coalescence at the liquid-liquid and the air-liquid interface, the coalescence of two separate drops was also extensively investigated, including the side by side coalescence between two sessile drops on a solid substrate [Fig. 1-8(c)] and two pendant drops [Fig. 1-8(d)]. It was found that the wetting properties of the sessile drops on a substrate could affect the coalescence behavior: (1) For the

coalescence between two silicone oil drops on a highly wettable polystyrene substrate (the contact angle was close to zero) [122], a growing meniscus bridge formed at the early coalescing times and its width expanded as a power-law relationship with an exponent of 1/2. Unlike the coalescence between two freely suspended drops where the width of the meniscus bridge was almost unaffected by the drop sizes, the growth rate was strongly affected by the radius and height of each spreading drop at the initial contact. (2) For the partially wettable substrates [124, 125], the width of the meniscus bridge followed the relationship of the Hoffman-Tanner-Voinov law for the coalescence between two partially wettable drops. The coalescing process involved an early stage with large capillary numbers and the contact line which was almost stationary, and a late stage with small capillary numbers where the meniscus bridge relaxed exponentially until the coalescing drop showed an ellipsoidal shape. The dynamics of asymmetric coalescence between two drops with different contact angles was also studied [126], it was revealed that the growing meniscus bridge was strongly affected by the contact angle and delayed by the Marangoni forces. (3) For the non-wetting superhydrophobic and Leidenfrost surfaces with a contact angle of 180°, the self-propelled jumping phenomenon appeared upon the drop coalescence [127]. The decrease in the total surface area released excess surface energy and activated the larger coalescing drop to jump away from the non-wetting substrate. Scaled by the capillary-inertial velocity, the relatively small jumping velocity was predicted, owing to the non-wetting substrate which could intercept a small part of the oscillating drop. Also, the coalescence between two pendant drops of the identical liquid or different miscible liquids was studied. The effects of the liquid viscosity [128], the initial sizes of the two drops [129, 130] as well as the surface tension [131] on the dynamics of drop coalescence were investigated. The results were similar to those in the drop coalescence at the air-liquid interface.

The majority of research works on the drop impact and coalescence were experimentally visualized by a high-speed camera from the side view. Facing the challenge in determining the coalescing width from the side-view images at the early stages after contact, the bottom-view imaging could provide better spatial clarity. Therefore, in a more optimized manner, the bottom-view images were simultaneously recorded with the side-view images as a supplementary. It was found that the bridge

width evolved faster than the height and verified the two-dimensional model for the prediction of the bridge height [125].

The high-speed images are recorded with a minimum interval of about 0.01 ms, which is far from sufficient to study the dynamics of very initial contact within a typical length of 100 μm. The short dynamics for the drop coalescence in the first few microseconds has never been fully understood. To overcome the limitations of both the capturing rate and spatial resolution, innovative approaches such as the electrical system and the ultrafast x-ray technique were introduced to explore the drop coalescence at a very early stage: (1) The alternating current (AC) electrical measurement technique was firstly utilized by Case et al. [132-134]. This electrical method realized the measurements on the time-dependent electrical resistance and the capacitances of two coalescing drops. The acquisition time interval was three orders of magnitude smaller than that of the high-speed images. (2) Another novel technique using the ultrafast x-ray full-field phase-contrast imaging was reported by Fezzaa et al. [135] to improve the understanding of the initial dynamics of drop coalescence. Taking the advantages of the edge-enhancement capability, the high penetrability and sensitivity, the coalescence singularity and the early coalescing dynamics of two drops could be revisited. This technique proved a feasible method to explore the finite-time hydrodynamic singularities encountered in the drop coalescence.

It's generally acknowledged that the drop coalescence has two typical regimes referred to as the viscous [136] and the inertial regime [136, 137], where the coalescing width exhibited the square root relationship and the logarithmic correction with time, respectively. Previous theoretical and experimental studies by Paulsen et al. [110] revealed an unanticipated "inertially limited viscous" (ILV) regime of drop coalescence at early time stages, where the inertial, viscous, and surface tension forces all take effect [123, 138, 139]. Based on the electrical measurements, the width of the coalescing section, reversely correlated to the electrical resistance, was shown to expand linearly with time in this regime.

Apart from the multiple experimental methods, the numerical simulations were also conducted to gain insight into the initial drop coalescence. Blanchette et al. [117, 120, 140] presented the simulation results on the drop coalescence by solving the Navier-Stokes equations. The shape evolution of the drop and interface as well as the velocity, pressure, concentration fields were tracked during the coalescence. The

velocities in the vertical and horizontal directions verified the accuracy of the simulation results in comparison with the high-speed images. The molecular dynamics (MD) simulation with a still limited number of molecules was introduced to investigate the coalescence between two nanodroplets at extremely small spatiotemporal scales [141]. During the initial coalescence, the multiple local bridges propagated by collective molecular jumps from both droplets, which was defined as the "thermal regime" prior to the classical viscous and inertial regimes. Due to the nanoscale amplitude of the thermal capillary waves, the MD simulation could be considered as the only practical method, which could provide deep insights into the role of thermal motion in the droplet coalescence. Certainly, the MD approach displays currently a dual limitation: one is the time-consuming task; another the number and kind of molecules used. Anthony et al. [142] performed the high-accuracy numerical simulation to reveal the coalescing dynamics of two drops. The inertially limited viscous regime could only be observed when the two drops were initially separated by a finite distance. Otherwise, the coalescence started with the viscous Stokes regime when the two drops touched at the beginning.

1.2.2 Drop impact and spreading on a solid surface

It is worth noting that the review section below concerns essentially the behavior of an individual drop released at some height, this is slightly different from the works performed in the present PhD thesis by making use of pendant drops. Besides the difference in the falling velocity (kinetic energy), pendant drops can slow down the coalescence and spreading dynamics to allow more accurate monitoring for the very initial stage for either the coalescence with a planar liquid surface or the spreading on a solid surface.

Similar to the drop impact and coalescence on a liquid surface, the impact and spreading of a drop on a solid surface compromises three situations of bouncing, coalescence and splashing according to the approaching velocity and the substrate property [96, 143], as shown in Fig. 1-9. To investigate the dynamics of drop spreading can gain deep insight into its further applications in the inkjet printing, coating and spraying, etc [144-146].

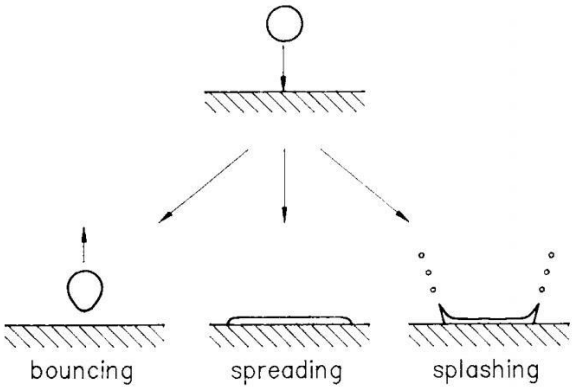


Fig. 1-9 Drop impact on a solid surface: bouncing, spreading and splashing [96].

The properties of the solid substrate could significantly affect the drop impact. The surface could be flat and dry, hydrophilic, hydrophobic, porous, or hemispherical, etc. In general, the majority of studies on the drop impact and spreading were conducted on flat dry surfaces. The dynamics of drop spreading in the final stage was explored at first. The Tanner's law [147] was proposed, where the shape of the spreading drop was assumed as a spherical cap and the radius of the spreading area followed the power law with time with an exponent of 1/10. This slow spreading emerged from the force balance between the surface tension and the viscous force near the triple contact line between three phases. Then the drop spreading in the initial stages was further investigated. For the drops with low viscosities, it was revealed that the spreading radius expanded exponentially with time with an exponent of 1/2 in the inertial regime [148, 149]. For the highly viscous drops, the drop spreading was dominated by the viscous force with an exponent decreasing from 0.8 at the initial contact to 0.1 at the equilibrium state [150]. The drop spreading on a substrate immersed in ambient air and another liquid was also experimentally investigated by the high-speed imaging from both the side and bottom views [151-154]. It was revealed that the spreading dynamics was similar for the substrates kept submerged in the air or the liquid medium: it always began in the initial viscous regime with the exponent of 1, followed by the intermediate inertial regime with the exponent of 1/2 and a final Tanner's regime with the exponent of 1/10.

Inspired by the raindrops on the lotus leaves, the superhydrophobic surface attracted more attention and was employed as one of the substrates of the drop impact and spreading. It was revealed that there existed a low-velocity splashing threshold for

the drop impact on the hydrophobic surface [155]. The three-dimensional numerical simulations were performed to qualitatively reproduce the drop splashing on a superhydrophobic surface [156]. It was shown that the dynamic contact angle was the crucial factor to stimulate the splashing. The drop splashing would not occur when the advancing dynamic contact angle was smaller than 90°. Quetzeri-Santiago et al. [157] used various substrates with distinct wettability, including the hydrophilic, hydrophobic, and superhydrophobic surfaces. The high-speed imaging was applied to investigate the effect of the dynamic contact angle on the splashing behavior. It was found that the splashing behavior could be characterized by the splashing ratio and the maximum dynamic advancing contact angle. The spreading of the aqueous drop with the addition of surfactant on the hydrophobic surface was also investigated: In comparison with the normal anionic surfactant which slowed down the drop spreading, the superspreading surfactant of "trisiloxane" appeared to accelerate the spreading speed. This acceleration could be explained by the strong affinity of the superspreading surfactant molecular on the hydrophobic solid surfaces [158]. The early stage was affected by the addition of surfactants and controlled by the inertia force and the capillary force [159]. For a water drop deposited on the superhydrophobic substrate, the drop spreading was initiated by moving a glass plate from above towards the drop and superhydrophobic substrate. The spreading velocity was similar on a wet or dry surface of the glass plate [148].

Moreover, the porous substrates were introduced for the drop impact. A way to generate monodispersed microdroplets of similar size with that of the individual grid hole was reported [160]. The threshold of the impact velocity was predicted according to the force balance between the inertial force and the capillary force, above which the liquid drop emerged to the other side of the substrate and the microdroplets formed as a result. The non-wettable porous filter membranes were also employed to investigate the impact of suspension drops containing nanoparticles [161]. It was found that the hydrodynamic focusing played a dominant role when the water penetrated into the non-wettable pores at relatively low values of the dynamical pressure associated with drop impact. The VOF method in a two-dimensional solution domain [162] and the 3D lattice Boltzmann method [163] were respectively employed to investigate numerically the drop spreading on flat surfaces with saturated pores. The results showed that the porous structure resisted the liquid edge moving away from the pore and accelerated

the moving towards the pore, which supported the previously proposed concept of the dual action of the saturated pores [164]. Also, the drop spreading was in direct proportion to the total number of pores and the effect of the pores on the liquid drop spreading was enhanced with the surface wettability and the static contact angle.

Apart from the drop impact on the flat solid surfaces, the drop impact on a convex, hemispherical and elastic surface was also investigated through the high-speed imaging technique [165]. The morphologies of the water drop impact were influenced by various factors, including the sizes and elastic modulus of the polydimethylsiloxane (PDMS) hemispherical substrates, the spreading angles, the minimum and maximum lengths of the wetted arc as well as the dynamic contact angles measured by a novel image-processing method. At relatively high Weber numbers, it was found that the oscillation of the dynamic contact angle was inhibited by the size of the substrate and strengthened by the elastic modulus of the substrate. The results on the drop impact laid a solid foundation for further applications in the fields such as the 3D ink-jet printing.

1.3 Passive and active manipulation on multiphase flows

In general, the manipulation on multiphase flows could be realized by passive or active methods [166], where the former is realized without any external force while the latter relies on additional forces or intrinsic properties of the liquids. Both methods are beneficial for a better understanding of complex interfacial phenomena and meet the demands of the practical applications.

1.3.1 Passive methods

The passive control on the droplet formation or breakup could be achieved by modifying the device geometry, which involves the typical T-junction, Y-junction and also the introducing novel geometries such as the obstructions, slopes and step emulsification configurations.

For droplet formation with step emulsification, three regimes including the breakup, step-regime and jet-regime were identified with the two-phase flow rate ratio [167, 168]. The latter two regimes were unique to the step emulsification, where the microdrops with comparable size to the inlet depth formed in the step-regime and the

balloon-shaped droplets formed beyond the step in the jet-regime. High-throughput production of droplets with excellent monodispersity could be realized using the step emulsification.

The obstructions with a circular cylinder and square types, comparable to the principle of static mixers, were adopted to investigate the droplet deformation and breakup [169-171], as shown in Fig. 1-10. The cylinder shape showed better performance on the droplet size control due to the non-trivial satellite droplets observed in the square obstruction. The degree that the circular cylinder deviated from the centerline dominated the distinct patterns of breakup and no breakup. Furthermore, a novel configuration with an array structure of cylinders was proposed to fabricate the Janus particles.

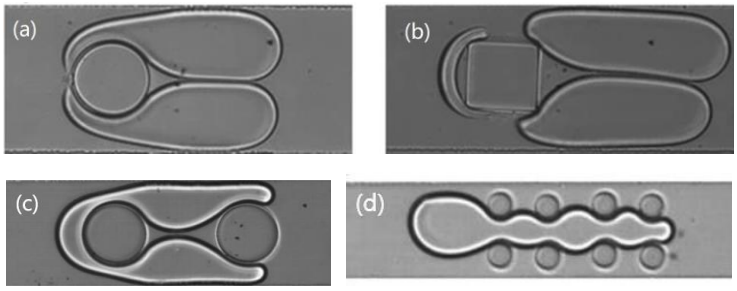


Fig. 1-10 Obstruction-induced droplet breakup in a confined microchannel [169]. (a) Single circular cylinder obstruction. (b) Single square obstruction. (c) two successive cylinder obstructions. (d) An array structure of cylinder obstructions.

The so-called DropChop module with sloped geometry was demonstrated to passively generate monodispersed droplets, as displayed in Fig. 1-11 [172]. In combination with the bypassing channels around the slope, the novel system showed a significant advantage that the droplet volumes depend weakly on the flow rate.

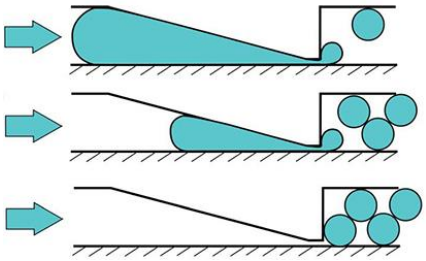


Fig. 1-11 Working principle of the DropChop module [172].

Moreover, the passive methods could also be employed to enhance the process intensification such as the fluid mixing as well the heat and mass transfer. A micromixer with circular, hexagonal and diamond obstructions within a curved microchannel was designed to improve the mixing performance of water and ethanol [173]. The micromixers with circular and hexagonal obstructions showed better performances than that with a diamond obstruction. When the Reynolds number equaled to 0.1 and larger than 15, the curved micromixer with circular obstructions showed the maximum mixing index of 88% at the exit.

The mass transfer intensification of CO_2 into MEA/[Bmim][BF4] aqueous solution was achieved by embedding baffles in the microchannels [174]. The maximum enhancement factor of 1.5 could be realized by increasing the two-phase flow rates, the blockage ratio and decreasing the concentration ratio of MEA to [Bmim][BF4].

The advanced-flow reactor by connecting a serious of heart-shaped cells (Fig. 1-12) behaved excellently on the mass transfer and proves more efficient [175]. In comparison with other common reactors, the mass transfer coefficients and interfacial areas were about one order of magnitude larger with the continuous breakup and coalescence of bubbles between the heart-shaped sections.

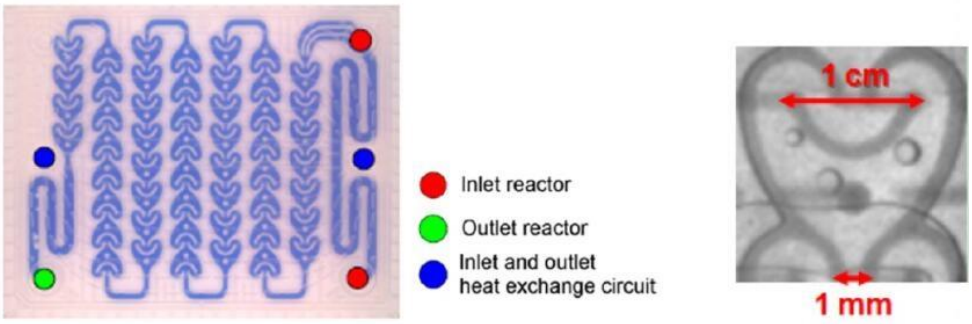


Fig. 1-12 Details of a single heart-shaped cell [175].

1.3.2 Active methods

Introducing an external force proves effective in realizing the active control of the multiphase flows and drop behaviors. The state-of-art techniques mainly rely on the magnetic field [176-182], electric field [183-189], centrifugal force [190, 191], surface acoustic wave [192, 193], focused laser [194] and visible or UV light [195, 196], etc.

Applying a magnetic field is one of the common and contactless methods to realize the active control on the ferrofluid. Ferrofluid is a stable colloidal suspension of ferromagnetic nanoparticles with an average diameter below 10 nanometers [197]. The magnetic particles could be magnetized by an external magnetic field to exhibit magnetic properties, which will vanish immediately after removing the magnetic field and there is no hysteresis observed (without remanent magnetization in the ferrofluid) [198]. Thus the modulation of ferrofluid droplet formation could be easily implemented by applying or removing an external magnetic field. Besides, the intervention of a magnetic field is not confined by the device configuration, which provides a more flexible approach for the droplet manipulation.

Similar to the electric fields, the magnetic fields could also cause ferrofluid drops to stretch oriented in the direction of the field and then coalesce [199, 200]. Placed in an external magnetic field, the ferrofluid drop would deform and divide into a sharp cone and then forms two peaks [201], as shown in Fig. 1-13. The final shapes of ferrofluid drops resulted from the balance of magnetic force and surface tension [198]. The continuous decrease in the vertical distance between the magnet and ferrofluid drop led to a non-linear deformation of the ferrofluid drop into a conelike structure, resulting from a complex combined effect between the polarizing effect and the magnetic attraction caused by an external magnetic field [201-204]. Previous numerical simulation studied the coalescence of ferrofluid drops in a uniform magnetic field and reported the critical separation of the two drops, beyond which the coalescence was inhibited in flat microchannels where the gravity was negligible [205]. The coalescence of two ferrofluid drops attaching to solid supports will form a liquid column. Previous studies focused on the stability of the ferrofluid column in a low gravity environment simulated by the magnetic levitation [206]. The slenderness of the column and the magnetic force co-determined the behavior of the columns [206]. The gravity-compensating or gravity-superimposing magnetic field can affect the initial pinch-off for ferrofluid drops and measure the detachment force [180, 182].

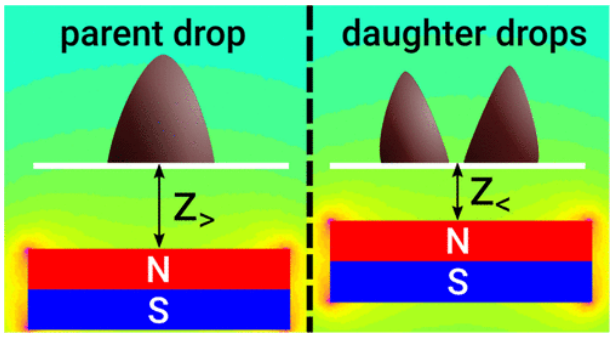


Fig. 1-13 Division of the ferrofluid drop under a magnetic field [201]. *z* indicates the vertical distance between the magnet and the ferrofluid drop.

The combination of ferrofluid and microfluidics has formed a new investigation field known as the micro-magnetofluidics [198], mainly involving researches in the fields of magnetohydrodynamics, ferrohydrodynamics, magnetorheology and magnetophoresis [207, 208]. The micro-magnetofluidics has been widely applied in realizing the precise control of micro ferrofluid droplets in bioanalysis, separation process, catalytic reaction, microfluidic pumps and valves [209-213].

The magnetic modulation of ferrofluid droplet formation is of fundamental importance in the micro-magnetofluidics, and several studies have been devoted to the ferrofluid droplet formation in microfluidic devices. Tan et al. [177] investigated the ferrofluid droplet formation in a T-junction and found that the droplet size could be affected by the magnetization, magnetic field gradient and the position of the magnet. When the magnet was placed upstream to the T-junction, the magnetic force pulled the droplets backward and prevented the droplet formation, which prolonged the droplet formation cycle and accordingly increased the droplet size. Conversely, when the magnet was placed downstream, the magnetic force accelerated the formation process so that smaller droplets could be obtained. Also, the droplet size could be regulated by adjusting the distance between the magnet and the T-junction.

Liu et al. [179] studied the effect of the magnetic field in the flow direction of the dispersed phase fluid on the ferrofluid droplet formation in a flow-focusing device by experimental and numerical methods. It was found that the ferrofluid droplet size increased with increasing the magnetic field strength, and the droplet size was more sensitive to the magnetic field at lower two-phase flow rates.

Tan et al. [214] and Wu et al. [200] also obtained similar conclusions from the experiments. Furthermore, Wu et al. [200] explored the effect of magnetic field in both

axial and radial directions on the ferrofluid droplet formation in a flow-focusing device. The magnetic field in the radial direction accelerated the expansion of the dispersed thread, and the axial magnetic field delayed the thread breakup in the pinch-off stage. The relationship between the minimum width of the dispersed thread and the remaining time could be scaled with a power-law function, the exponent was 0.32 under no existence of a magnetic field, which was consistent with the results in conventional fluids. The exponent increased by increasing the magnetic flux density.

Another active method on the drop manipulation is realized by introducing an electric field. The presence of an applied electric field could affect the coalescence process. Different from the coalescence between two spherical drops without an external force, the leading edges of two oppositely charged drops would deform noticeably into cones before coalescence under the electric field [183, 184], as shown in Fig. 1-14. The cone angle could be adjusted by varying the drop diameter and the electric field strength. In addition, it was revealed that whether or not the drop coalescence depended mainly on the cone angle and the electric field strength. Critical values for both the cone angle and the electric field strength were reported, above which the two drops would recoil after contact [183]. It is then possible to determine whether the drops merged or not by adjusting the cone angle and electric field strength [184].

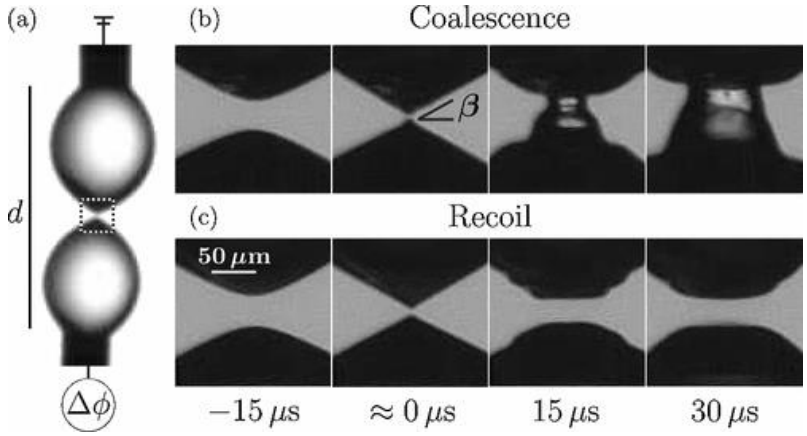


Fig. 1-14 Coalescence of two oppositely charged drops [183]. (a) Schematic diagram of the experimental setup. The voltage $\Delta\phi$ is applied across the two needles. The distance d between the needles is 1.9 mm. (b) The drops coalesce at a low voltage of 815 V. Each drop deforms into a cone with angle β before contact. (c) The drops contact and then recoil at a high voltage of 822 V.

Hamlin et al. [185] reported a critical ionic conductivity below which the partial coalescence of oppositely charged drops occurred. The coalescence between unequal drops tended to be observed at lower electric field strength. The size of the daughter droplet was found to be in coincidence with the established model based on the force balance between the capillary-pressure-driven inertia and the electrophoretic driving force. In terms of the practical application, the electrically tunable partial or complete coalescence could be employed by the on-demand lab chips.

Liu et al [186] observed the non-coalescence of oppositely charged droplets with the pH-sensitive polymeric hydrogel particles acting as the stabilizers. The porous and soft structure of the microgels at the droplet interface led to the unique phenomenon of non-coalescence. It was indicated that the non-coalescence at pH 7 could be switched to coalescence by varying the pH to lower or higher values.

Yun et al [187] provided an electrical method to suppress the rebound of an asymmetric drop from a hydrophobic substrate. The three-dimensional numerical simulation revealed that the consequent kinetic energy transfer was observed between the principal axes of *x* and *y* rather than the vertical *z*-axis.

Huang et al. [188] investigated the filament thinning of the non-Newtonian droplets in a microfluidic flow-focusing device under AC electric fields. The presence of the AC electric field led to smaller droplets with higher formation frequency. Due to the force balance between the hydrodynamic forces and the Maxwell stress induced by the electric field, the flow patterns gradually became dissymmetrical.

Liu et al [189] investigated the coalescence of two and multiple liquid marbles driven by a direct current (DC) electric field. The threshold voltage above which two marbles could be forced to coalesce depended on the stabilizing particles and the surface tension. For the cases of multiple marbles in a chain, the threshold voltage showed a linear relationship with the number of liquid marbles.

In addition to the above-mentioned active methods with the applied electric and magnetic fields, other emerging methods with the centrifugal force, acoustic wave, and focused laser receive extensive attention as well: the rotationally actuated lab-on-a-compact-disk platform was employed to form monodispersed nanodroplets and serpentine-shaped liquid threads at a microfluidic Y-junction [190]. A scaling law of the droplet volume with the input rotation speed was proposed based on the force analysis. It was shown that the droplets could be trapped and merged by the surface

acoustic waves [193]. When the droplet entered the expansion chamber, it was immobilized by the acoustic radiation forces due to surface acoustic wave until the successive droplets arrived. The drag forces were able to overcome the retaining acoustic radiation forces when the total merged volume reached a critical size, thus the merging droplet exited the expansion chamber as a result. The focused laser also acted as an active manner to manipulate the drops by blocking the interface motion [194]. The force balance of a drop in the laser-induced thermocapillary flow was theoretically conducted. Then the predicting model for the droplet size was proposed to favor the miniaturization.

1.4 Outline

With both passive and active methods, the research works were carried out using the non-Newtonian aqueous liquids and ferrofluids, including the droplet formation and breakup in microfluidic devices, the drop impact at a liquid or solid surface as well as the magnetic manipulation of ferrofluid drops.

The thesis comprises 8 chapters in total. The first chapter begins with the literature review including the research background and research status on the multiphase flows and interfacial phenomena at multiscale. In Chapter 2, a brief introduction of the experimental devices, the working liquids and the general analytical methods are given. Chapter 3 to 7 show a collection of the published journal articles and the manuscripts to be submitted with the logical order: In Chapter 3, the droplet formation in both T-junction and flow-focusing devices were investigated experimentally by a high-speed imaging and a micro-PIV. In Chapter 4, the deformation and breakup dynamics of the elastic droplets in a flow-focusing device were studied. Chapter 5 aims to investigate the initial coalescence of the non-Newtonian liquid drop at a planar liquid and Chapter 6 goes for the initial contact and spreading of a pendant drop at a solid surface. Both chapters were jointly investigated by an ultrahigh-speed DC electrical device, a high-speed camera, and a high-speed micro-PIV. The thinning and pinch-off of the polymer filament was studied by analyzing the electrical signals in the dynamical process. In Chapter 7, the emphasis is given to the active control on the ferrofluid drops by an external magnetic

field. The last part of Chapter 8 gives rise to the general conclusions, innovations and some relevant perspectives of interest.

Chapter 2 Experimental section

A brief introduction to the operation of experimental devices, the preparation of liquids, and the general analytical methods are resumed in this part. More details about the experimental procedure and methods will be presented in each relevant chapter below.

2.1 Experimental devices

2.1.1 High-speed camera

The sequences of the focused flow behaviors are recorded by a high-speed camera equipped with a macrolens or a microscope. The high-speed camera Phantom V711 (Vision Research, USA) shown in Fig. 2-1 could reach a maximum capturing speed of 10^6 frames per second (fps) and even 7500 fps at the full resolution of 1280 × 800 pixels. During the experiments, the capturing speed is determined by considering both the characteristics of the process and the spatial and temporary resolutions. When setting a new experimental condition, the image acquisition could be performed after reaching the stability.

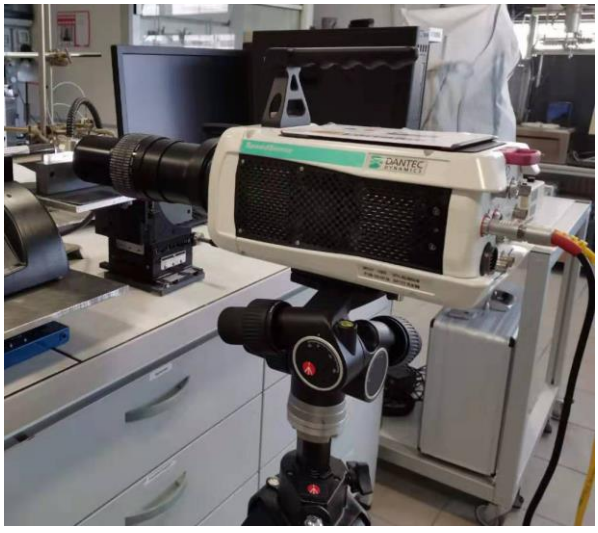


Fig. 2-1 Photograph of the high-speed camera Phantom V711 equipped with a macrolens.

2.1.2 Ultra-high-speed DC electrical device

To push both the spatial and temporary limits further, an ultra-high-speed direct current (DC) electrical device was developed based on an improved Howland current source [215], as shown in Fig. 2-2(a). The device was developed by the "Service of Instrumentation and Electronic in the Laboratory" (SIEL-LRGP) in France. The electrical circuit diagram is illustrated in Fig. 2-2(b). The conducting drop connected with two electrodes serves as a liquid bridge in the circuit. The electrical voltage U of the drop was measured with a sampling speed of 1.25×10^6 Hz. Thus the time interval between two successive electrical signals is down to 0.8 μs. This electrical device was employed to explore the initial coalescence of an aqueous drop at a planar liquid surface, the initial contact and spreading of a pendant drop at a solid surface as well as the thinning and pinch-off of the polymer solutions.

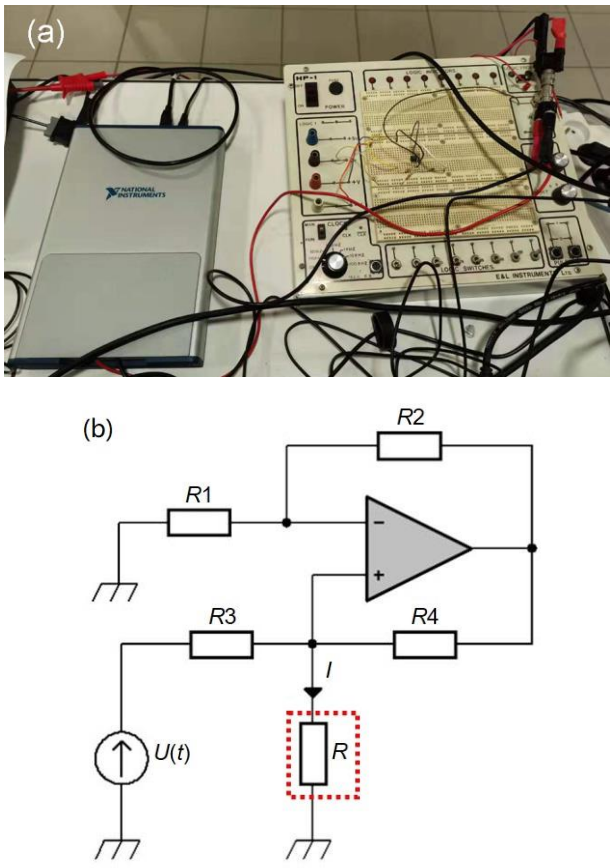


Fig. 2-2 (a) Photograph of the ultra-high-speed DC electrical device. (b) Electrical circuit diagram for the ultra-high-speed DC electrical device. The resistance R represents the pendant drop.

2.1.3 High-speed micro-PIV

A high-speed micro-Particle Image Velocimetry (micro-PIV) technique was developed to obtain the velocity field in flowing liquids. The basic principle is to compute the instantaneous velocities of the seeding particles in the liquids by tracking their motion between every two successive images of a fixed time interval.

In this work, three types of the seeding particles were utilized: (1) Latex particles (Merck Estapor, France) with a mean calibrated diameter of 0.88 μm and a density of 1056 kg m^{-3}; (2) Silver coated hollow glass spheres (S-HGS-10, Dantec Dynamics, Denmark) with an average diameter of 10 μm and a density of 1400 kg m^{-3}; (3) Fluorescence particles (MF-RhB-Partikel-G020, Dantec Dynamics, Denmark) with a diameter of 1-20 μm and a density of 1190 kg m^{-3}.

The latex particles were used to track the velocity fields during the droplet formation in the microfluidic devices. The microfluidic device was placed on the horizontal operation platform of the inversed microscope (Leica, Germany). The images were captured by the high-speed camera Phantom V711 at up to 10000 fps from the bottom view. The fluid velocity can be quantified by tracking the shadow of latex particles in the focus plane.

Both the silver coated hollow glass spheres and fluorescence particles were employed to explore the flow field during the initial coalescence of a drop at a liquid surface and the initial contact followed by spreading of a drop at a solid surface. A suitable number of seeding particles were added and evenly dispersed in the liquids. Two lasers (LaserMax Inc., USA) of 1 mW were placed in opposite directions to illuminate the seeding particles in the laser sheets. The images were captured by the high-speed camera Phantom V711 coupled with a zoom lens (MP-E 65mm f/2.8, Canon, Japan) from the front view. The capturing rate could reach up to 3000 fps for the drop coalescence and even up to 5000 fps for the drop contact and spreading. Then the high-speed images recording the temporary position of the seeding particles in the laser sheets located inside the drop were exported to the software DynamicStudio for further computation.

2.1.4 Syringe pump

The working liquids are injected into the microfluidic devices or the stainless steel nozzle for drop generation by the syringe pump (PHD 2000, Harvard Apparatus, USA) shown in Fig. 2-3 through a syringe connected with a Teflon tube. The inner diameter of the syringe should be defined before starting the injection. The value and unit ($mL \cdot h^{-1}$, $\mu L \cdot h^{-1}$ or $mL \cdot min^{-1}$) of the infuse rate should be consistent with the liquid type and the actual operating conditions.



Fig. 2-3 Photograph of the syringe pump PHD 2000.

2.1.5 Microfluidic devices

All the microfluidic devices used in Chapter 3 were made by Tianjin Micro/Nano Manufacturing Technology Co., Ltd. The microchannels were fabricated on the polymethyl methacrylate (PMMA) chip plate by precision milling. Another PMMA plate with the same size was connected and sealed by bolts and served as the cover plate. The inlets of the dispersed phase and the continuous phase were connected to the syringes with Teflon tubes, respectively.

The microfluidic devices employed in the experiments are shown in Fig. 2-4: (a) The microfluidic T-junction device with a square cross section of 200 μm × 200 μm for the droplet formation in Chapter 3. (b) The microfluidic flow-focusing device with a square cross section of 600 μm × 600 μm for the droplet formation in Chapter 3. (c)

The microfluidic flow-focusing device with a square cross section of 400 μm × 400 μm for the droplet deformation and breakup in Chapter 4.

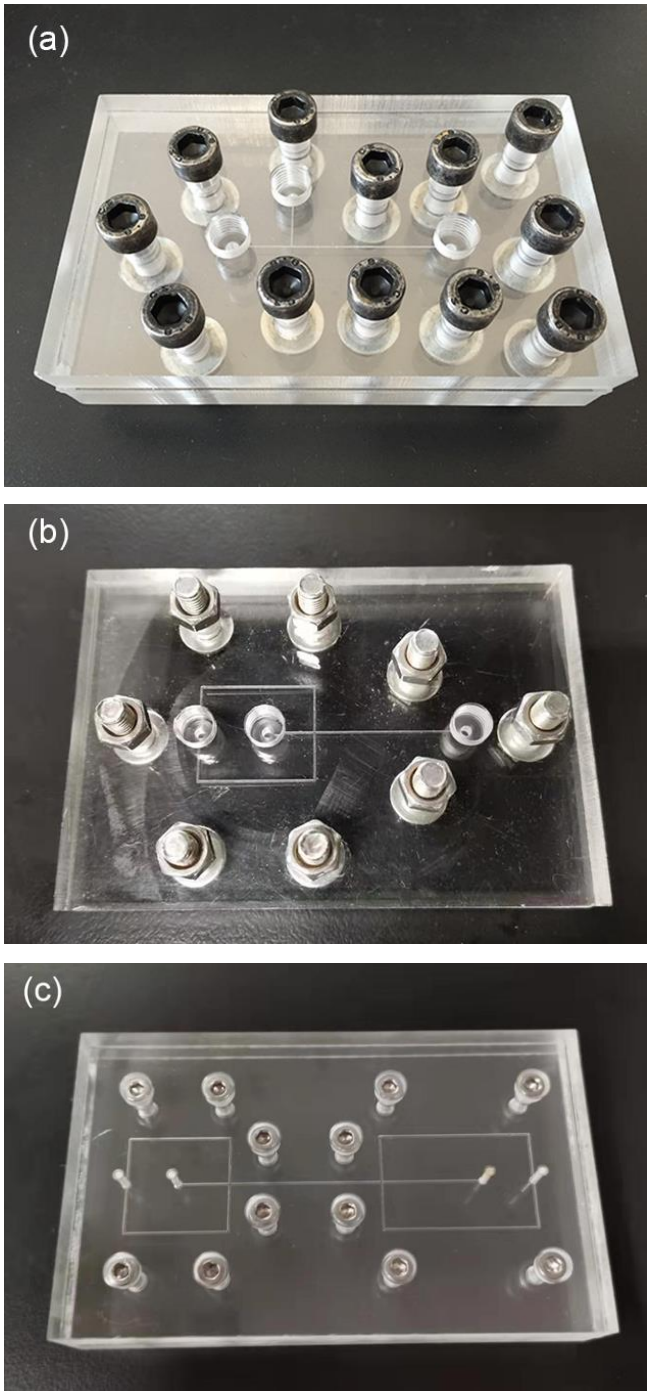


Fig. 2-4 Photograph of the microfluidic devices. (a) Microfluidic T-junction device for droplet formation. (b) Microfluidic flow-focusing device for droplet formation. (c) Microfluidic flow-focusing device for droplet breakup.

2.2 Experimental liquids

In the experiments, the working fluids consist of the Newtonian fluids, non-Newtonian aqueous fluids and ferrofluids.

The Newtonian fluids involve the aqueous liquids with low and high viscosity and the oily liquids: (1) For the Newtonian aqueous fluids with lower viscosity, such as glycerol or sodium chloride (NaCl) aqueous solutions of low concentration: water and the solvents (pure glycerol or NaCl powder) of the required weight are added into the beaker together and then stirs on the magnetic stirrer. (2) For the Newtonian aqueous fluids with higher viscosity, such as the Emkarox aqueous solutions and the glycerol aqueous solutions with higher concentration: the electronic stirrer (RZR 2102 Control, Heidolph, Germany) is employed to avoid the unevenly mixing by the magnetic stirrer. The photograph of the electronic stirrer RZR 2102 is displayed in Fig. 2-5. (3) The oily liquids of silicone oil and mineral oil are directly purchased from the reagent companies.



Fig. 2-5 Photograph of the electronic stirrer RZR 2102.

For non-Newtonian aqueous fluids such as polymer solutions of PEO, PAAm and CMC: The polymer powders are progressively added into the solution with continuous stirring and lasted for at least 12 hours. For liquids used for the

ultra-high-speed DC electrical device, due to the fact that the conductivities for the polymer solutions are too small to detect the voltage, NaCl was added to strengthen the electrical conductivity of the liquids and to improve the sensibility of electrical signals. For polymer liquids with the addition of NaCl, the NaCl powders need to be dissolved firstly in water before polymer granules to enhance their solubility.

The ferrofluids employed in this work were purchased from the company Ferrotech, Germany. Ferrofluid is a stable colloid-liquid system where the ferromagnetic nanoparticles with a nominal diameter of 10 nm are suspended in the carrier liquid [216]. It can be mainly categorized into the oil-based and water-based ferrofluid with the light hydrocarbon oil and deionized water serving as the carrier liquid, respectively. Here, the oil-based ferrofluids EMG 900 was employed. Before each usage of the ferrofluids in the experiments, an ultrasound dispersing device is employed to enhance the dispersion of magnetic particles in the carrier liquid.

For liquids used for micro-PIV measurement, the seeding particles with a reasonable concentration are added and uniformly dispersed in the liquids. Due to the limitation of the mechanical mixing methods, the ultrasound dispersing device is also employed to enhance the dispersion of the seeding particles. The pre-treatment by ultrasound should be conducted before the addition of polymer powders to avoid the breakup of long polymer chains. The liquids with two types of seeding particles are displayed in Fig. 2-6, respectively.

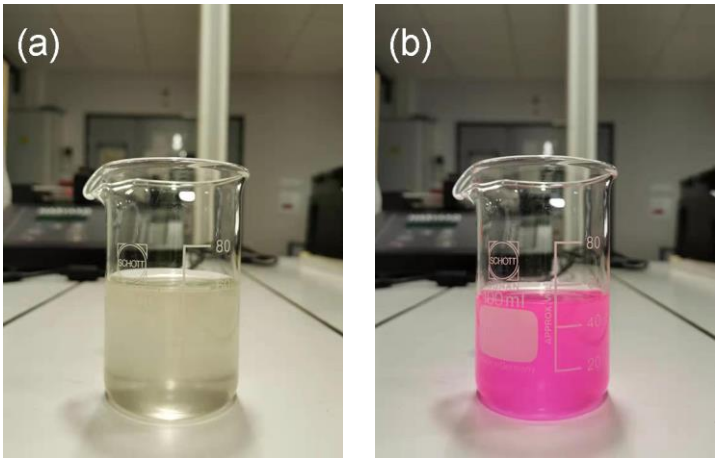


Fig. 2-6 Liquids with seeding particles. (a) Silver coated hollow glass spheres in 1 wt% PAAm solution. (b) Florescence particles in 50 wt% glycerol solution.

2.3 Analytical methods

2.3.1 High-speed images

The accurate calibration of a pixel is based on the outer diameter of the stainless steel nozzle or the width of the microchannel in the visualized images. In combination with the known width and the corresponding pixel number, the actual width of a required section could be directly calculated via the proportional relationship by reading the pixel number in the images. The images captured by the high-speed camera were analyzed one by one through the home-made MATLAB algorithms to acquire the occupied pixels corresponding to the areas we focused, such as the droplet size, the coalescing width and the spreading radius.

2.3.2 Electrical signals

The electrical voltage *U* was acquired by the ultra-high-speed DC electrical device. It's observed that the voltage doesn't increase linearly with the whole resistance range as for all electric circuits, so the voltage needs to be calibrated to resistance. By measuring the voltage corresponding to a wide range of standard resistance *R* from 0 to 800 kΩ in the electrical circuit, the values of electrical current in the electrical circuit were plotted in Fig. 2-7.

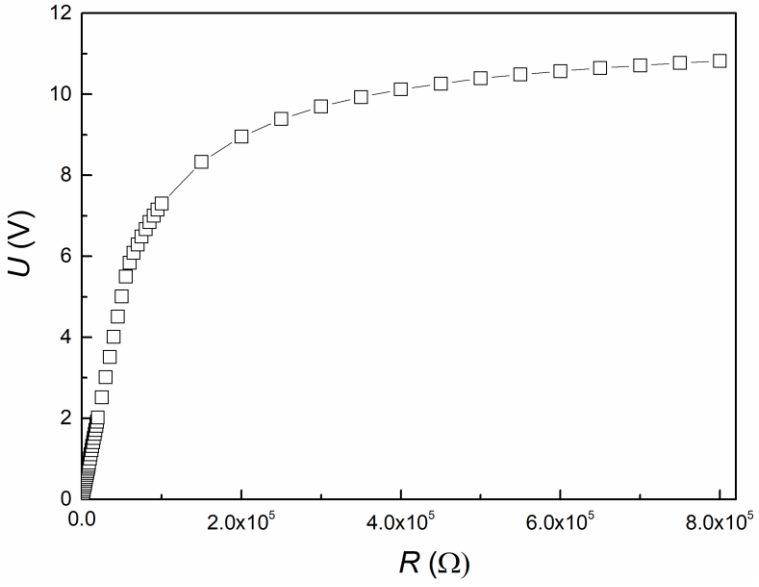


Fig. 2-7 Calibration of the electrical voltage *U* to the resistance *R*.

All the voltage data obtained were analyzed through self-programmed MATLAB algorithms. Firstly, the non-linear curve was fitted by two polynomial functions divided by $U = 6\text{V}$, as shown in Eq. 2-1 and Eq. 2-2.

For $U < 6\text{V}$,

$$f_1(R) = -2.93\times10^{-15}R^3 + 1.65\times10^{-10}R^2 + 9.88\times10^{-5}R \quad (2\text{-}1)$$

For $U \geq 6\text{V}$,

$$f_2(R) = -7.72\times10^{-23}R^4 + 1.64\times10^{-16}R^3 - 1.28\times10^{-10}R^2 + 4.59\times10^{-5}R + 3.73 \quad (2\text{-}2)$$

For each measured value of the electrical voltage *U*, the value of the drop resistance was calculated from the equation $g(R) = U - f(R) = 0$ by the Newton-Raphson method. An initialization of the resistance R_0 was given, where the value depended on the electrical voltage. The equation of the tangent line to $U = f(R)$ at the point $(R_0, f(R_0))$ is $U - f(R_0) = f'(R_0)(R - R_0)$. The tangent line intersects the *x*-axis when $U = 0$ and $R = R_1$, thus $-f(R_0) = f'(R_0)(R_1 - R_0)$. Solving the equation and the value for $R_1 = R_0 - f(R_0)/f'(R_0)$ was obtained. Then the relative deviation $\left|(R_1 - R_0)/R_0\right|$ between R_1 and R_0 was calculated. If the relative deviation is larger than the defined value, the calculation continues, where $R_{n+1} = R_n - f(R_n)/f'(R_n)$. In this work, the calculation convergence was fixed for $\left|(R_{n+1} - R_n)/R_n\right| < 0.01$ for a compromise between the accuracy and the calculating time.

2.3.3 Velocity fields

The velocity field can be computed via the DynamicStudio software (Dantec Dynamics, Denmark) by tracking the motion of each seeding particle between every two successive images of a fixed time interval. The analysis algorithm of “adaptive PIV” was applied to calculate the velocity fields. A 50% window overlap and an optimized interrogation area grid step size of 16 × 16 pixels, 20 × 20 pixels or 24 × 24 pixels were respectively tested to show the most intuitive results. Prior to the calculation, the pre-processing of the high-speed images needs to be performed. Taking the drop coalescence as an example, the pre-processed image with improved contrast and visibility is displayed in Fig. 2-8.

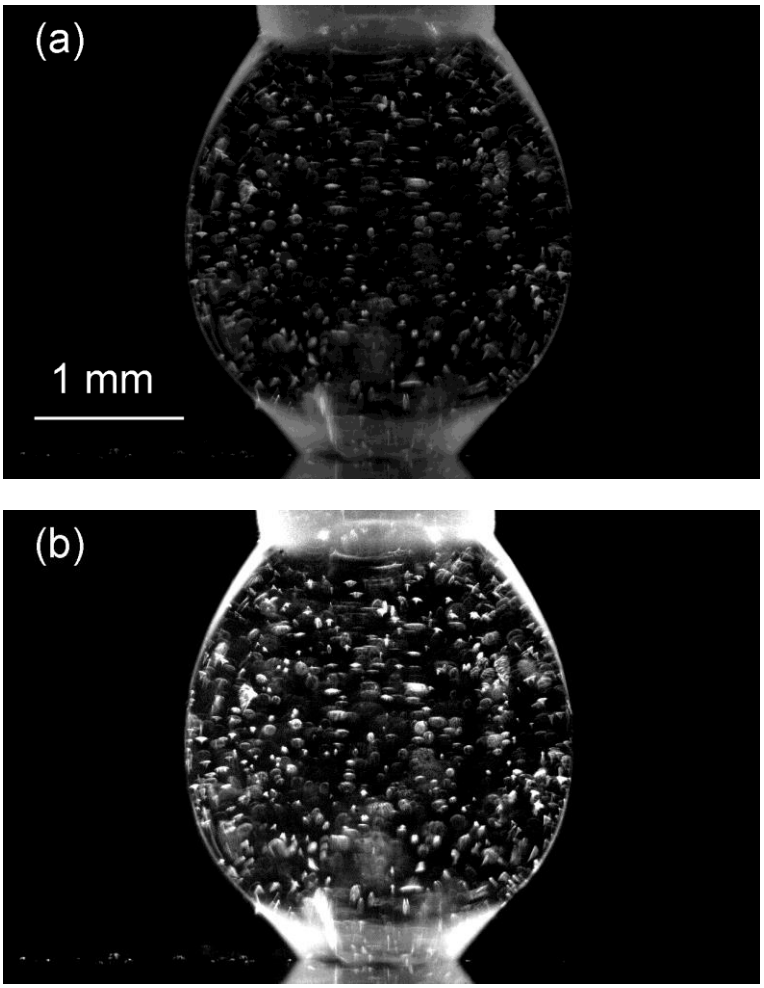


Fig. 2-8 Image analysis for the micro-PIV. Liquid: 2 wt% PAAm + 10 wt% NaCl, seeding particles: silver coated hollow glass spheres with an average diameter of 10 μm. (a) Original image of drop coalescence captured by the high-speed camera. (b) Pre-processed image with improved contrast and visibility. The scale bar indicates 1 mm.

2.3.4 Liquid properties

The densities of liquids were measured using a densimeter (DMA-4500-M, Anton Paar, Austria). The surface tension and contact angle were measured by a dynamical tensiometer (IT Concept, France). The electrical conductivities of the liquids were measured by a multiparameter analyzer (C3030, Consort, Belgium).

The strength of the magnetic field was indicated by the magnetic flux density and determined using a Gaussmeter (GM07, Hirst, U.K.) with an accuracy of 0.01 mT. The magnetic flux density decreases with the distance from the magnet, thus both the

value of the magnetic flux density and the corresponding distance between the probe and magnet should be recorded.

The rheological properties of the working liquids were measured by a rheometer (AR-G2, TA Instruments, USA), as shown in Fig. 2-9. It requires a precise calibration before each measurement, which involves calculating the bearing friction and performing the rotational mapping. Two types of cone-plate geometries are commonly used in the measurement: one with a diameter of 40 mm and a cone angle of 2°, another with a diameter of 60 mm and a cone angle of 1°. The latter with higher precision is suitable for the liquid with lower viscosity. The range of shear rate was determined according to the liquid viscosity based on two distinct considerations: (a) The centrifugal force exerted on the sample liquid in the cone-plate geometry on the rheometer is large under high shear rates. (b) Moreover, to avoid the appearance of the Taylor instability within liquids which affects the rheological measurements. The maximum shear rates at about 200 s^{-1} were applied to the less viscous liquids. For the highly viscous non-Newtonian liquids such as PAAm and PEO, the maximum shear rate could reach up to 1000 s^{-1}.



Fig. 2-9 Photograph of the rheometer AR-G2.

Chapter 3 Droplet formation in T-junction and flow-focusing devices

The liquid-liquid two-phase flows and droplet formation in the microfluidic devices were investigated experimentally by a high-speed camera and a high-speed micro-PIV. Two configurations of the microfluidic devices including the T-junction and the flow-focusing junction were employed. Both the formation of elastic droplets in a T-junction and the formation of silicone oil droplets in aqueous elastic fluids in a flow-focusing junction were studied.

3.1 Introduction

Over the past two decades, microfluidic technology has been rapidly developed and received increasing attention. Due to the excellent controllability, the micro droplets or bubbles with uniform size could be generated in the microfluidic devices, which shows great potential and are frequently encountered in printing, biology, medicine and chemical processes such as emulsification, crystallization, extraction, intensification and synthesis [217-224].

T-junction is one of the most frequently used geometry in microfluidic devices and has been widely employed in realizing the mixing of fluids, the formation, breakup and coalescence of droplets [225-228]. Apart from the above-mentioned T-junction, the flow-focusing junction is another common configuration of the microfluidic devices. The manipulation of the micro droplets could be realized in the microfluidic devices, such as the drop formation, breakup and coalescence.

The liquid-liquid two-phase flow in the microfluidic device is of fundamental importance in the microfluidic technology, which usually involves complex flow pattern, dynamics of droplet formation and droplet size prediction. The slug flow and dripping flow attained extensive applications in many industrial processes such as emulsification, crystallization, etc. Therefore, the dynamics of droplet formation and the droplet size prediction attracted more attention. Garstecki et al. [36] investigated the droplet formation in a microfluidic T-junction in the domination of squeezing

mechanism and proposed the scaling law for the size of slug droplet as $l_d / w_c = 1 + aQ_d / Q_c$, where l_d is the droplet length, w_c is the width of the channel, the pre-factor a depends on the geometry and size of the microfluidic T-junction, Q_d/Q_c represents the two-phase flow rate ratio. Thorsen et al. [229] proposed a shearing mechanism for the droplet formation under the action of both shear stress and interfacial tension. The scaling law for droplet size under the shearing mechanism could be expressed by a power-law with the capillary number Ca [41, 230]. Moreover, the prediction model of droplet size was established as $l_d / w_c \propto (Q_d / Q_c)^{\alpha} Ca^{\beta}$ [231-233], here Q_c/Q_d and Ca represent the role of the squeezing mechanism and shearing mechanism, respectively.

In recent years, a large number of studies have been devoted to the liquid-liquid flows with low-viscosity Newtonian fluid in microfluidic devices. Meanwhile, some complex two-phase flows such as high-viscosity Newtonian fluid, viscoelastic fluid, ionic liquid and ferrofluid also received extensive attention [43, 234-236]. Polyethylene oxide (PEO) solution is a typical viscoelastic fluid, in which both the viscosity and elasticity play an important role in the droplet formation [51, 237]. By adding glycerol into PEO solution, an elastic fluid with shear rate-independent viscosity can be obtained, which is called Boger fluid [238].

Previous studies mainly focused on the two-phase flow using the non-Newtonian fluid as the dispersed phase [52, 53, 68]. It was found that the shear-thinning or viscoelasticity of the non-Newtonian fluids showed an evident impact on the dynamics of droplet formation and the droplet size. While fewer studies concentrated on the configurations where the non-Newtonian fluids are employed as the continuous phase [60, 239]. It's necessary to figure out the influences of the particular characteristics of the non-Newtonian continuous phases on the droplet formation. In addition, the micro-PIV technique could allow the measurement of the velocity fields during the multiphase flows in the microfluidic devices.

To our best knowledge, it requires further investigations on the dynamics and velocity fields of the droplet formation with the non-Newtonian elastic fluids serving as the dispersed phase or the continuous phase. In the present section, the effect of elasticity on the droplet formation was investigated and the predicting models for the droplet size were proposed. The velocity fields during the droplet formation in various flow regimes were measured and computed by the high-speed micro-PIV.

3.2 Experimental section

The scheme of the experimental setup is depicted in Fig. 3-1. Immiscible two-phase liquids were pumped into the horizontal microfluidic device through a polyethylene tube by the syringe pumps (PHD 2000, Harvard Apparatus, USA). The dispersed phase and the continuous phase were injected at the flow rate of Q_d and Q_c, respectively. A high-speed camera (Redlake Motion Pro Y-5, IDT, USA) equipped with a microscopic magnification lens (Non Fine-Focus Zoom 1-6265, Navitar, USA) was used to observe and capture the flow behavior. The images with the spatial resolution of ± 3.1 μm were recorded at 4000 frames per second. A cold fiber illumination (Philips 13629, Philips, Japan), placing at the other side of the microfluidic device, provided sufficient light for the system. When setting a new flow rate, the image acquisition was performed after having reached the stability of droplet formation, which is judged by both the formation frequency of droplets and droplet length. The formation frequency was counted in 30 seconds and repeated three times. The lengths for three individual droplets were also measured.

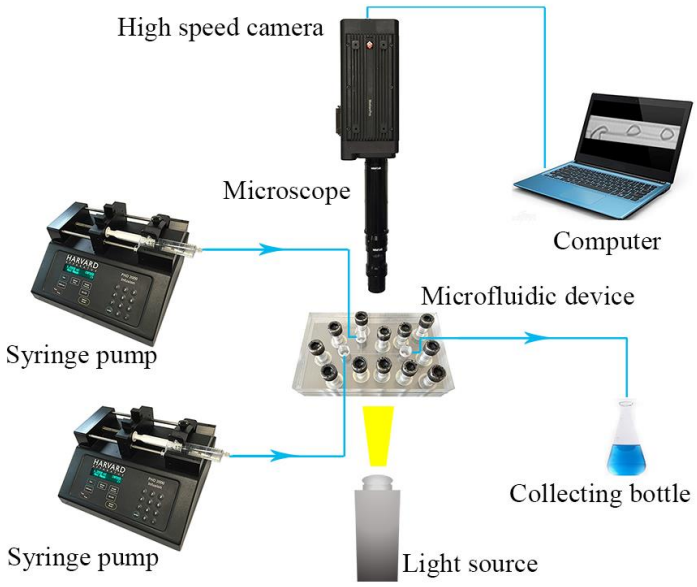


Fig. 3-1 Scheme of the experimental setup.

The microfluidic devices employed in the experiment was obtained by connecting three layers of polymethyl methacrylate (PMMA) plates with bolts. The

channels were fabricated on the chip plate by precision milling. The schematic diagrams of two microfluidic devices are shown in Fig. 3-2. The size of the cross-sections is 200 μm × 200 μm for the T-junction device and 600 μm × 600 μm for the flow-focusing device.

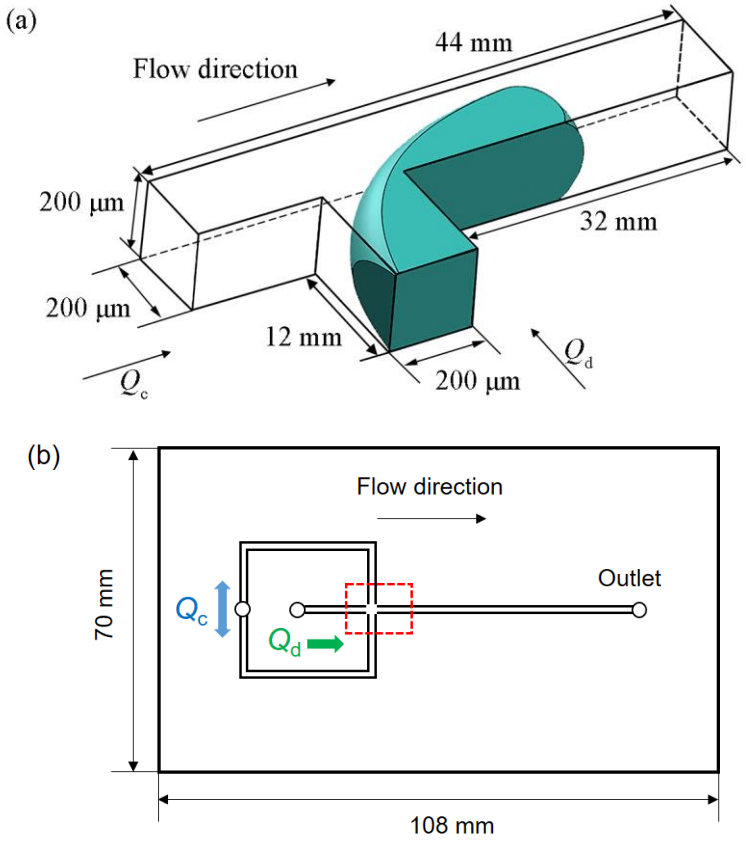


Fig. 3-2 Schematic diagrams of two microfluidic devices. (a) The T-junction device. Size of the cross-section: 200 μm × 200 μm. (b) The flow-focusing device. Size of the cross-section: 600 μm × 600 μm. The focus was given to the flow behaviors at the flow-focusing junction.

A high-speed micro-PIV was utilized to gain deep insight into the velocity fields during the droplet formation at the flow-focusing junction. A small number of latex particles with a diameter of 0.88 μm were added in the dispersed phase. The images were captured by the high-speed camera coupled with a microscope at 10000 fps. By tracking the shadow of the latex particles in the focused plane, the velocity fields were computed through every two successive images by the adaptive PIV algorithm with a grid step size of 16×16.

3.2.1 Liquid properties for the droplet formation in the T-junction device

Mineral oil (Aladdin Industrial Corporation, China, CAS: 8042-47-5) with 4 wt% surfactant sorbitan laurate (Span 20) (Kermel Chemical Reagent, China, CAS: 1338-39-2) was used as the continuous phase. The addition of the surfactant reduced the contact angle between the continuous phase and microchannel wall so that stable water-in-oil droplets can be formed. The density ρ and viscosity η of the continuous phase were 872.5 kg·m^{-3} and 26 mPa·s, respectively. The contact angle of the continuous phase on the plat microchannel wall was 33.2°. All of the experiments were conducted at T_k = 298.15 K and atmospheric pressure.

Polyethylene oxide (PEO)-glycerol solutions with various PEO molecular weights and 50 wt% glycerol solution were used as the dispersed phase. The molecular weights M_w and mass concentrations c of PEO (Micxy Chemical Reagent, China, CAS: 68441-17-8) are 1×10^5 g·mol^{-1}, 3×10^5 g·mol^{-1}, 1×10^6 g·mol^{-1} and 0.3 wt%, 0.1 wt%, 0.05 wt%, which are noted by 100 K, 300 K and 1000 K, respectively. The composition and the physical properties of the dispersed phase are listed in Table 3-1.

Table 3-1 Compositions and physical properties of the dispersed phase.

M_w (g·mol^{-1})	c (wt %)		ρ_d (kg·m^{-3})	η_d (mPa·s)	γ (mN·m^{-1})	λ_{eff} (s)	El
	PEO	Glycerol					
/	/	50	1125.8	5.10	2.96	/	/
1×10^5	0.3	40.7	1102.3	5.26	3.43	4.4×10^{-6}	5.2×10^{-4}
3×10^5	0.1	41.9	1108.9	5.28	2.40	2.1×10^{-5}	2.5×10^{-3}
1×10^6	0.05	40	1100.7	5.24	1.89	1.6×10^{-4}	1.9×10^{-2}

PEO-glycerol solution is a typical Boger fluid with elasticity and shear rate-independent viscosity. A rotational rheometer was employed to measure the rheological property of Boger fluid. The viscosities of the Boger fluids were approximated to 5 mPa·s, as shown in Fig. 3-3. At 298.15 K, the Newtonian fluid of 50 wt% glycerol with the same shear viscosity was used as the reference solution, so

that the effect of the elasticity could be investigated under a constant viscosity. The elasticity of Boger fluid is normalized by the elasticity number *El* [240]:

$$El = \frac{\eta_d \lambda_{eff}}{\rho_d w_c^{\ 2}} \tag{3-1}$$

where w_c is the width of microchannel and ρ_d, η_d, λ_{eff} are the density, viscosity and effective relaxation time of PEO-glycerol solution.

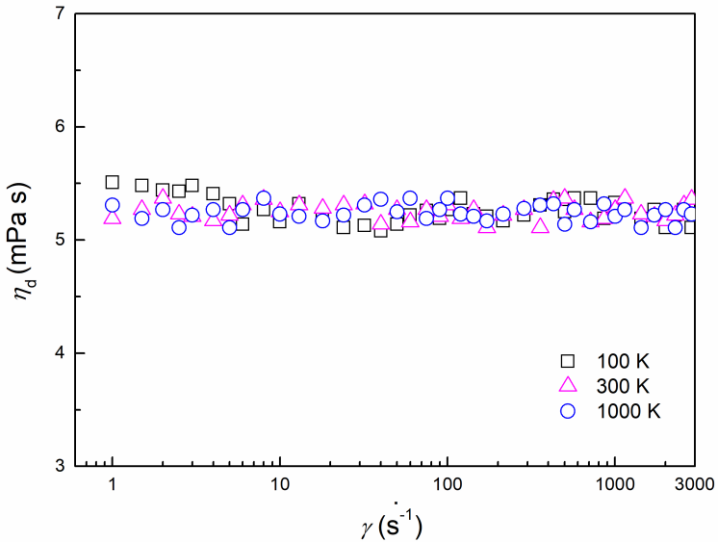


Fig. 3-3 Rheological properties of PEO-glycerol solutions.

For dilute PEO solution $(0.01 \le c/c^* \le 1)$, the expression of the effective relaxation time λ_{eff} is:

$$\lambda_{eff} = 0.463 \frac{[\eta]\eta_s M_w}{N_A k_B T_K} \left(\frac{c}{c^*} \right)^{0.65} \tag{3-2}$$

where η_s is the solvent viscosity, N_A is the Avogadro's number, k_B is the Boltzmann constant, T_K is the Kelvin temperature of the experimental environment. $[\eta] = 0.072 M_w^{\ 0.65}$ and $c^* = 1/[\eta]$ are the intrinsic viscosity and critical overlap concentration of PEO solution [237], respectively. The interfacial tensions between the four pairs of liquids were measured by a tensiometer with the pendant drop method, as shown in Table 3-1, the variation of which is much smaller than the magnitude of the elasticity number $El \in [5.2\times10^{-4}, 1.9\times10^{-2}]$.

3.2.2 Liquid properties for the droplet formation in the flow-focusing device

Silicone oil was used as the dispersed phase and elastic polyethylene oxide (PEO) aqueous solutions were used as the continuous phase. The molecular weight of PEO is 1×10^5 g·mol^{-1} and the concentration is 0.1 wt%, 0.3 wt% and 0.6 wt%, respectively. The surfactant of 0.3 wt% sodium dodecyl sulfate (SDS) was added to reduce the contact angle between the continuous phase and the microchannel wall. The wettability was enhanced to form stable oil in water droplets. The physical properties of the experimental liquids are gathered in Table 3-2.

Table 3-2 Physical properties of experimental liquids.

Liquids	ρ (kg·m^{-3})	γ (mN·m^{-1})	η (mPa·s)	θ (°)	
				Liquid-solid [a]	Liquid-liquid-solid [b]
Silicone oil	917.8	/	5.30	/	/
0.1 wt% PEO	998.9	10.94	/	46.3	25.3
0.3 wt% PEO	999.3	14.35	/	53.4	29.7
0.6 wt% PEO	999.8	15.25	/	61.5	33.2

Notes: (a) The contact angle of the PEO solution on the microchannel surface.

(b) The contact angle of a silicone oil droplet in the presence of PEO solutions wetting the microchannel surface.

The rheological properties of the shear-thinning PEO aqueous solutions were determined by the rheometer. In the range of the shear rate from 1 to 1000 s^{-1}, the viscosities of the PEO solutions were measured, as shown in Fig. 3-4. The Carreau model was employed to describe the rheological properties of PEO solutions [241, 242]:

$$\frac{\eta-\eta_\infty}{\eta_0-\eta_\infty}=[1+(\lambda\dot{\gamma})^2]^{(n-1)/2} \tag{3-3}$$

where η_0 and η_∞ represent the zero-shear viscosity and infinite shear viscosity, respectively. The zero-shear viscosity was considered as the approximate viscosity corresponding to an extremely small shear rate of 1 s^{-1} in this work. The viscosity of the solvent was used as the infinite shear viscosity. Here the solvent was deionized water with 0.3 wt% SDS. The viscosity of 1.01 mPa·s was measured by the

Ubbelohde capillary viscometer (iVisc, LAUDA, Germany). The relaxation time λ and power index n were fitted from the rheological data. The rheological properties of the PEO solutions were gathered in Table 3-3. All of the experiments were conducted at 298.15 K and atmospheric pressure.

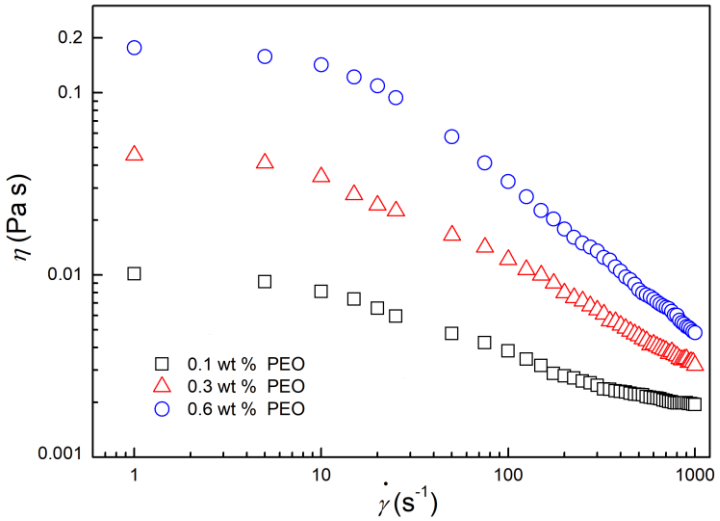


Fig. 3-4 Rheological properties of the PEO solutions.

Table 3-3 Rheological properties of the PEO solutions.

Liquids	η_0 (mPa·s)	η_∞ (mPa·s)	λ (s)	n
0.1 wt% PEO	10.13	1.01	0.130	0.52
0.3 wt% PEO	45.37	1.01	0.134	0.42
0.6 wt% PEO	176.78	1.01	0.137	0.24

3.3 Results and discussion

3.3.1 Formation of elastic droplets in a microfluidic T-junction

3.3.1.1 Two-phase flow patterns

In the experiments, the ranges of the volumetric flow rates of the dispersed phase and the continuous phase were $50 < Q_d < 600$ μL·h^{-1} and $25 < Q_c < 6000$ μL·h^{-1},

respectively. Both the two-phase flow rates and the elasticity of the dispersed phase display a noticeable effect on the flow regime. Taking the 300 K PEO solution (El = 2.5×10^{-3}) as an example, four flow regimes were observed under various two-phase flow rates when the elasticity of the dispersed phase was fixed: slug, dripping, beads-on-string and stratified flows, as illustrated in Fig. 3-5(a-d). Slug flow [Fig. 3-5(a)]: when the flow rate of the continuous phase is relatively low, the shear force exerted on the dispersed phase is smaller so that the slug droplet is formed with a bullet-shaped head. The droplet length l_d is larger than the channel width. Dripping flow [Fig. 3-5(b)]: as the flow rate of the continuous phase increases, the dripping flow is formed. The length and width of the droplets are smaller than the channel width. Beads-on-string flow [Fig. 3-5(c)]: when the flow rate of the continuous phase further increases, the dispersed thread is elongated to the downstream channel in the axial direction. A string of droplets is connected to each other by long and thin threads. In comparison with the flow regime observed in a Newtonian fluid in the microfluidic T-junction [243], the elasticity leads to the emergence of beads-on-string flow. Stratified flow [Fig. 3-5(d)]: when the flow rate of the dispersed phase increases to a critical value, the shear force from the continuous phase is insufficient to pinch the dispersed phase off to form droplets. The two-phase fluids are layered at two sides of the microchannel, and stratified flow with a stable interface is observed.

The effect of fluid elasticity on the flow regime was studied at fixed two-phase flow rates, as shown in [Fig. 3-5(e-h)]. For the three types of elastic fluids employed in the experiment, the neck of the dispersed phase is elongated into the downstream microchannel to form long and thin threads. The stronger the fluid elasticity is, the longer is the thread length at the breakup moment. For instance, when Q_d = 100 μL·h^{-1} and Q_c = 400 μL·h^{-1}, a single dispersed thread connected to the downstream droplet is formed in 100 K [Fig. 3-5(f)] and 300 K PEO solutions [Fig. 3-5(g)], while several threads connected with droplets are observed in 1000 K PEO solution [Fig. 3-5(h)]. When a Newtonian fluid is employed, the dispersed neck is elongated without thread formation in the droplet formation process [Fig. 3-5(e)]. The flow patterns map plotted as a function of two-phase flow rates for a fixed elasticity of the dispersed phase is shown in Fig. 3-5(i). When Q_d < 400 μL·h^{-1}, the slug, dripping and beads-on-string flows can be observed in turn with the increase of Q_c. When Q_d > 400 μL·h^{-1}, only stratified flow can be observed, regardless of the value of Q_c.

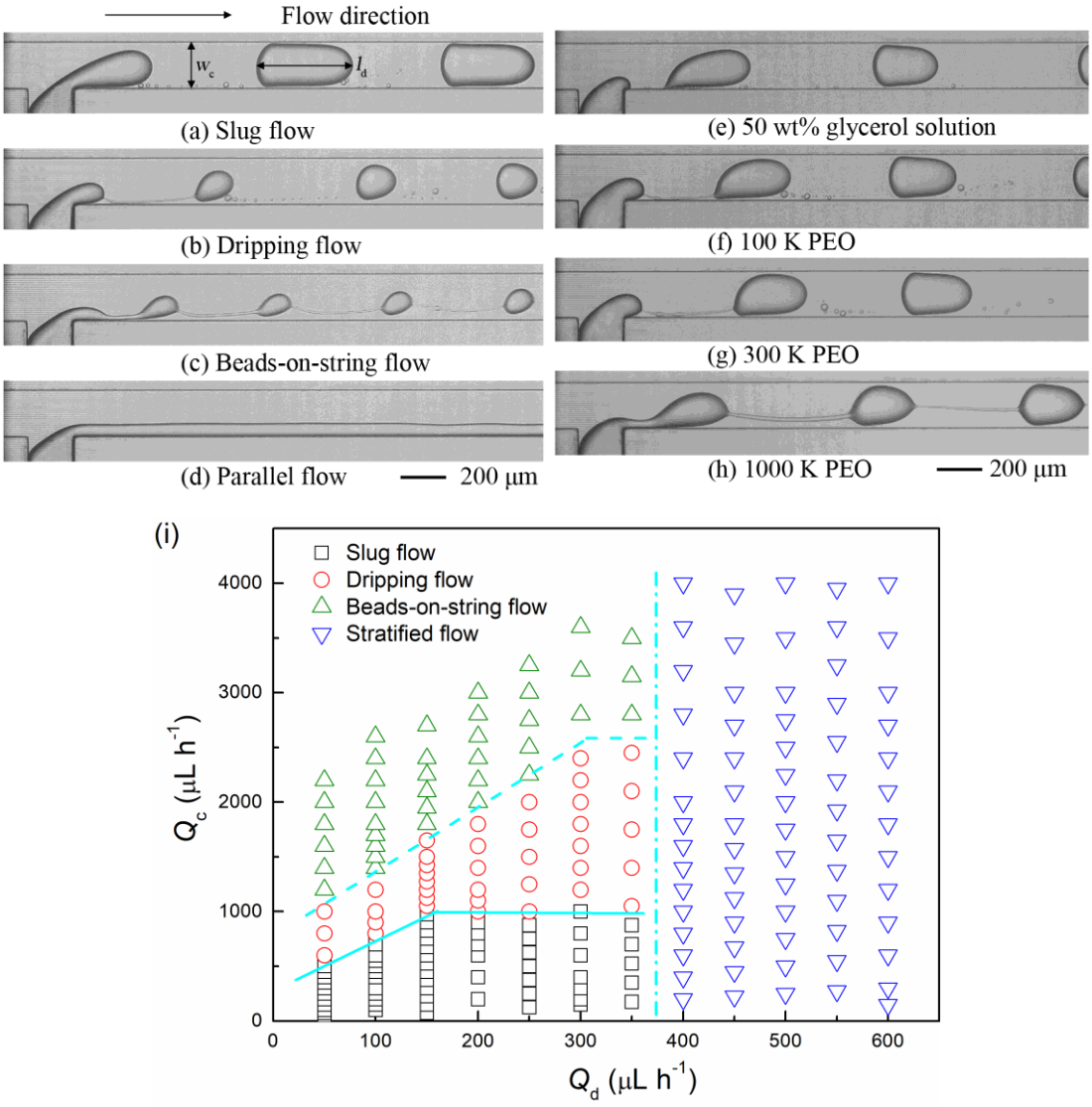


Fig. 3-5 (a-d) Flow patterns with the two-phase flow rates, 300 K PEO solution, El = 2.5×10^{-3}, (a) Slug flow: Q_d = 100 μL·h^{-1}, Q_c = 200 μL·h^{-1}. (b) Dripping flow: Q_d = 100 μL·h^{-1}, Q_c = 800 μL·h^{-1}. (c) Beads-on-string flow: Q_d = 100 μL·h^{-1}, Q_c = 2400 μL·h^{-1}. (d) Stratified flow: Q_d = 400 μL·h^{-1}, Q_c = 800 μL·h^{-1}. (e-h) Flow patterns with the elasticity of the dispersed phase, Q_d = 100 μL·h^{-1}, Q_c = 400 μL·h^{-1}, (e) 50 wt% glycerol solution, El = 0. (f) 100 K PEO solution, El = 5.2×10^{-4}. (g) 300 K PEO solution, El = 2.5×10^{-3}. (h) 1000 K PEO solution, El = 1.9×10^{-2}. (i) Flow patterns map of the two-phase flow in the microfluidic T-junction, 300 K PEO solution, El = 2.5×10^{-3}, Solid line: transition between slug and dripping flow; dashed line: transition between dripping and beads-on-string flow; dashed dotted line: transition between stratified flow and the other flow regimes.

3.3.1.2 Dynamics of droplet formation

As the dispersed thread is stretched to its maximum length, the upstream end would break up at first, and then the thread breaks up from the upstream to the downstream channel progressively. A new droplet is formed when the downstream end of the thread fully detaches from the droplet. The time zero $t = 0$ is set as the moment when the dispersed thread is fully separated from the droplet. The droplet formation dynamics in 100 K PEO solution in a temporary cycle T is studied as illustrated in Fig. 3-6. The whole process could be divided into three stages: expansion, squeezing and stretching stages. After the upstream end of the dispersed thread is detached from the neck [Fig. 3-6(a)], droplet formation comes to the expansion stage [Fig. 3-6(b-c)]. The minimum width of the dispersed thread w_m increases with the droplet head moving downstream. Successively, it turns to the squeezing stage when the width of the dispersed thread reaches the maximum value [Fig. 3-6(c)]. In this stage, the squeezing force exerted by the continuous phase on the dispersed thread progressively becomes predominated. The neck of the dispersed thread converts from convex outward to concave inward under the shearing effect by the crossing-flow, and the width of the dispersed thread becomes progressively thinned [Fig. 3-6(d-g)]. The neck of the dispersed thread experiences a stretching stage after the squeezing stage [Fig. 3-6(h-i)]. The elasticity of the dispersed phase begins to take action. The neck of the dispersed thread is elongated in the axial direction by the downstream droplet and progressively evolves into a long and thin thread. The minimum width of the dispersed thread remains constant while the length increases. The dispersed thread ruptures at the upstream end when it is stretched to its maximum length [Fig. 3-6(i)], and a droplet generation cycle is ended. Differently, the droplet formation process in the Newtonian fluid is divided into three stages: expansion, squeezing and pinch-off stages, and the dispersed thread breaks up immediately in the pinch-off stage without being stretched.

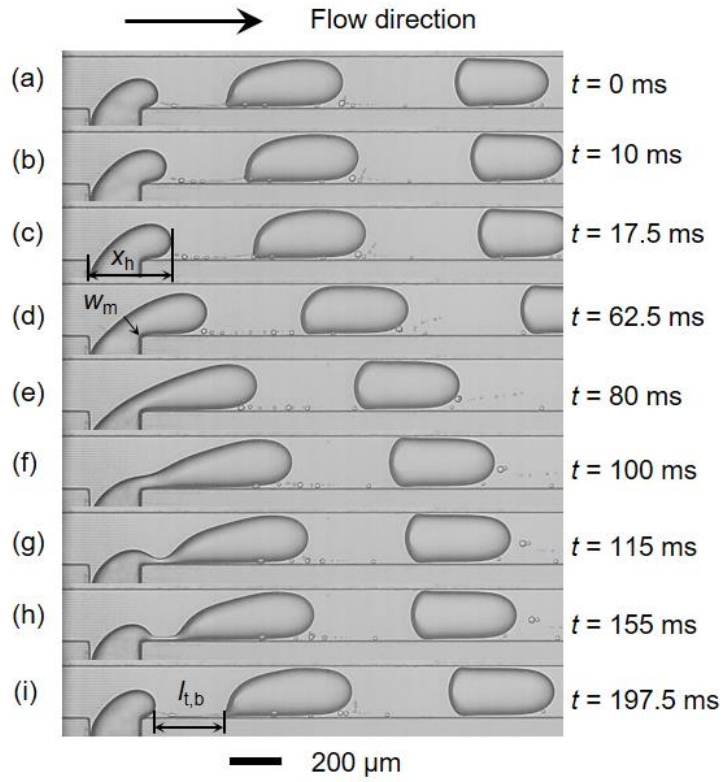


Fig. 3-6 Break-up process of the dispersed thread for droplet formation in the slug regime at the T-junction. 100 K PEO, $El = 5.2\times10^{-4}$, $Q_d = 100$ μL·h^{-1}, $Q_c = 400$ μL·h^{-1}. x_h: the position of the droplet head, w_m: the minimum width of the dispersed thread, $l_{t,b}$: the thread length at the breakup.

The effect of the elasticity of the dispersed phase on the velocity of the droplet head u_h is illustrated in Fig. 3-7, where x_h refers to the distance from the droplet head to the upstream side of the inlet channel of the dispersed phase and $u_h = dx_h/dt$. The velocity of the droplet head u_h rises with time t in the droplet formation process. Compared with the two-phase superficial velocity u ($u = u_d + u_c$), the velocity of the droplet head turns from $u_h < u$ to $u_h > u$. The elasticity of the dispersed phase has a comparatively limited effect on the velocity of the droplet head at given two-phase flow rates. van Steijn et al. [244] studied the droplet velocity at different cross sections perpendicular to the axial direction and found that the droplet velocity increased with the decrease of the size of the gap between the droplet and the microchannel wall. Similar phenomena were also found in the present experiments: with the expansion of the droplet head, the gap size reduces until the droplet width equals to the channel width. The increase of the droplet blocking effect on the upstream fluid reduces the leakage flow, thus the droplet velocity increases owing to the larger driving force.

Cubaud and Mason [245] found in a flow-focusing microchannel that the velocity of droplet head was less than the two-phase superficial velocity in the early stage and then progressively increases until exceeding the later one. However, Fu et al. [42] also used the microfluidic flow-focusing and found that the velocity of the droplet head was less than the two-phase superficial velocity in the whole cycle. This phenomenon was caused by the leakage of the continuous phase in the gap between the droplet head and the microchannel wall.

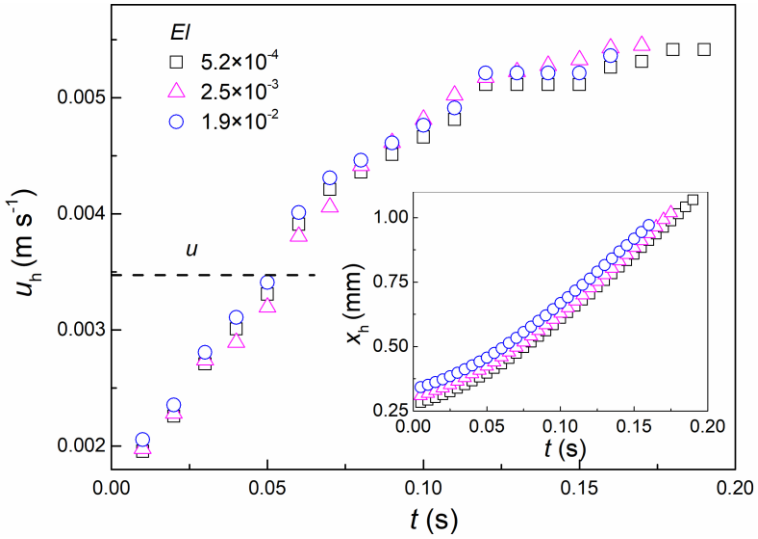


Fig. 3-7 Effects of the elasticity on the velocity of the droplet head u_h. Q_d = 100 μL·h^{-1}, Q_c = 400 μL·h^{-1}. The horizontal dash line represents the two-phase superficial velocity, u = 0.00347 m·s^{-1}. The insets: the temporal evolution of the position of the droplet head x_h.

The evolutions of the dimensionless minimum width of the dispersed thread w_m/w_c in a droplet formation cycle are compared in Fig. 3-8 for the PEO-glycerol solution and the Newtonian fluid. In contrast to the Newtonian fluid, the expansion stage is shorter for PEO-glycerol solution. The droplet formation process would enter the squeezing stage once the dimensionless minimum width of the dispersed thread reaches its maximum value. Due to the presence of the dispersed thread for PEO-glycerol solution, the pinch-off process of the thread is slowed down and leads to a longer squeezing stage. After the squeezing stage, the dispersed thread would switch to the stretching stage rather than the breakup stage that happens in the Newtonian fluid. The PEO molecular turns from the coiled to the elongated state

under the stretching effect. In this stage, the minimum width of the dispersed thread remains unchanged and the length increases with time until breakup.

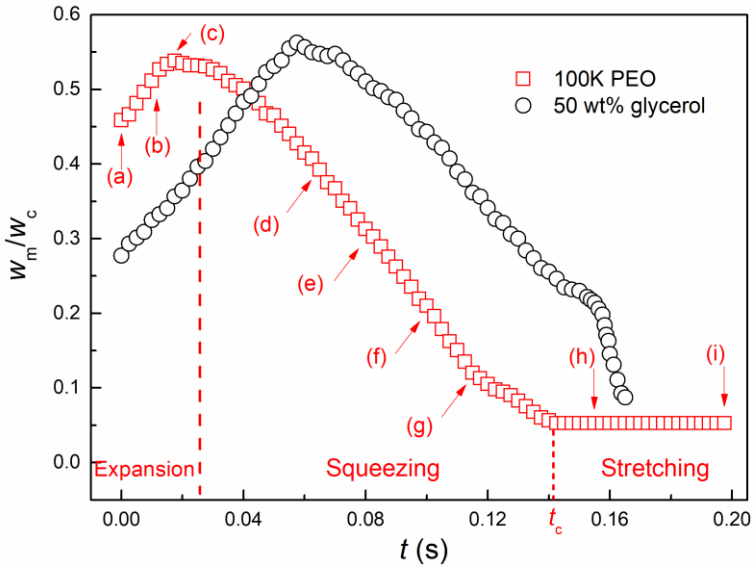


Fig. 3-8 Evolutions of the dimensionless minimum width of the dispersed thread w_m/w_c in a droplet formation cycle in 100K PEO solution and a Newtonian fluid of 50 wt% glycerol. Q_d = 100 μL·h^{-1}, Q_c = 400 μL·h^{-1}. Dots named (a)-(i) correspond to the images in Fig. 3-4. Dashed line: the transition from expansion to squeezing stage. Short dashed line: the transition from squeezing to stretching stage. t_c: the change time from the squeezing stage to the stretching stage.

In the squeezing stage, the minimum width of the dispersed thread decreases linearly with time. At the same time, the changing rate of the thread width accelerates with the increase of the flow rate of the continuous phase. When the shear force plays a dominant role in the dispersed thread, the changing rate of the thread width is supposed to increase equal-proportionally with the increase of the flow rate of the continuous phase [36]. However, in the present experiments, the changing rates of the thread width are 7×10^{-4}, 8×10^{-4} and 1.1×10^{-3} m·s^{-1}, respectively, which are not equal-proportional with the change of the flow rate of the continuous phase (Q_c = 400, 600 and 800 μL·h^{-1}). It suggested that the thinning of the dispersed thread is controlled not only by the squeezing force but also by other forces such as the elastic force.

In the stretching stage, the dispersed neck evolves into a thin thread with a constant minimum width and becomes longer under the stretching of the downstream

droplet. The dimensionless length of the dispersed thread l_t/w_c increases linearly with the dimensionless relative time $(t-t_c)/\tau$, as shown in Fig. 3-9, where t_c is defined as the change time from the squeezing stage to the stretching stage and $\tau = \eta_d w / \sigma$ represents the viscocapillary time of the dispersed phase [52]. Under the same two-phase flow rate, the dispersed phase with stronger elasticity would lead to a longer thread, in this case, the dispersed thread needs higher time from the beginning of generation to the final rupture and tends to be sluggish for the breakup.

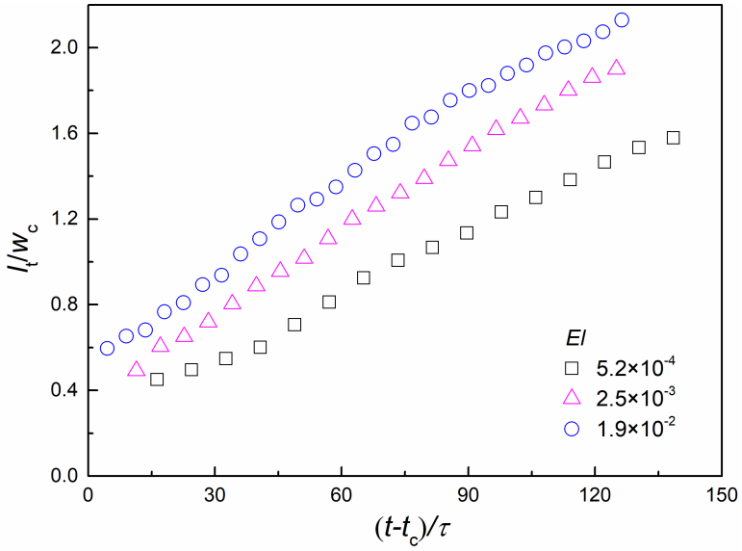


Fig. 3-9 Effect of the elasticity on the dimensionless length of the dispersed thread l_t/w_c with the dimensionless remaining time $(t-t_c)/\tau$ in the stretching stage. $Q_d = 100$ μL·h^{-1}, $Q_c = 400$ μL·h^{-1}.

The breakup of the dispersed thread takes firstly place at the upstream end with the increase of its length that is noted $l_{t,b}$ for the breakup moment. Fig. 3-10 shows the variation of the thread length at breakup moment with two-phase flow rates and the elasticity of the dispersed phase. When the flow rate of the dispersed phase is fixed, $l_{t,b}$ increases firstly before decreasing with the flow rate of the continuous phase. A maximum of $l_{t,b}$ is observed and can be correlated to the flow rate of the dispersed phase. The higher the maximum is, the lower is the corresponding flow rate of the continuous phase. For a constant elasticity of the dispersed phase, the same trend is also found when increasing the flow rate of the continuous phase. The maximum is straightforwardly correlated to the elasticity of the dispersed phase but inversely related to the flow rate of the continuous phase.

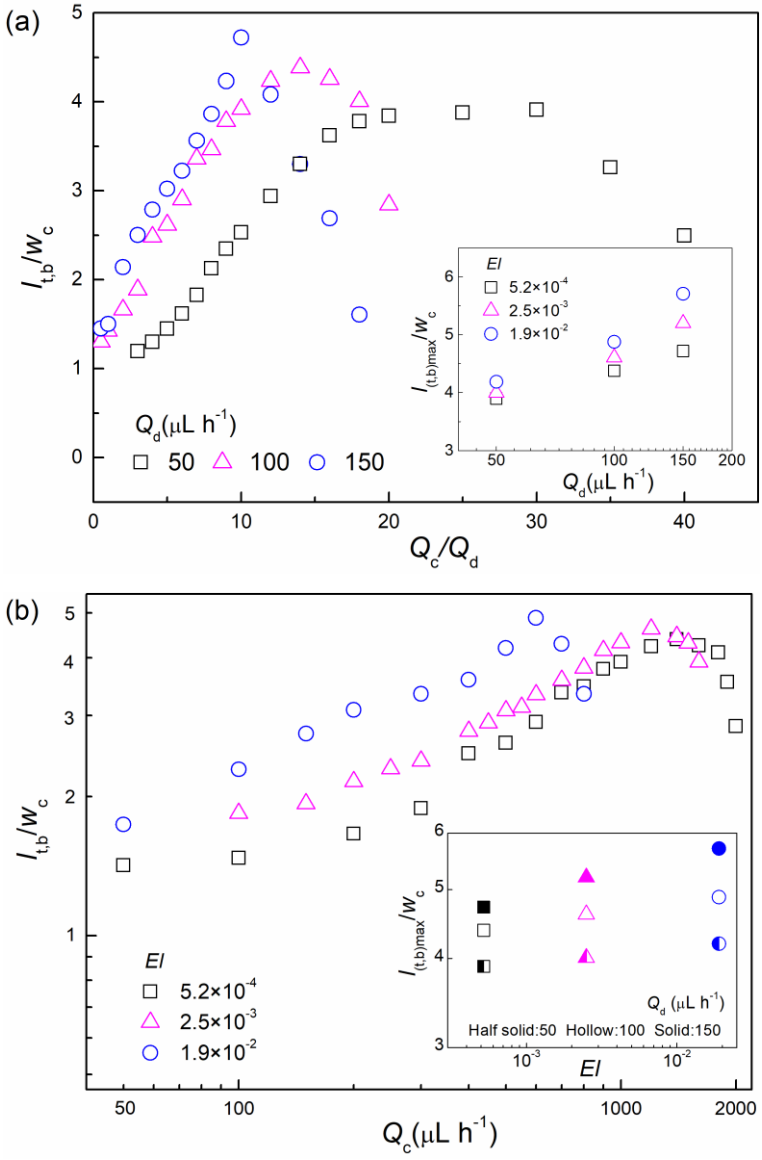


Fig. 3-10 Effects on the dimensionless thread length at breakup $l_{t,b}/w_c$. (a) The two-phase flow rates: 100 K PEO solution, $El = 5.2\times10^{-4}$. Inset: maximum of the dimensionless thread length at breakup $l_{(t,b)max}/w_c$ with the flow rates of the dispersed phase. (b) The elasticity of the dispersed phase: $Q_d = 100$ μL·h^{-1}, inset: maximum of the dimensionless thread length at breakup $l_{(t,b)max}/w_c$ with elasticity.

Lee at al. [53] studied the variation of the thread length with the capillary number in viscoelastic fluid in a flow-focusing device. For the dispersed phase of PEO with $M_w = 3\times10^5$ g·mol^{-1}, the thread length at breakup displayed a maximum with increasing the capillary number *Ca*, this is consistent with the phenomenon observed in our experiments. They attributed the occurrence of this phenomenon to the change

of the controlling mechanism on the thread formation when the capillary number increases. Therefore, the force balance analysis on the dispersed thread in the stretching process is necessary for facilitating the understanding of the thread rupture process. The drag force and inertia on the downstream droplet and the elastic force of the dispersed phase co-exist in the axial direction in the stretching process. When the drag force and inertia dominate, the thread would be elongated. Similar to a spring, the stretching process of the dispersed thread follows a kind of Hooke law and the elongation of the dispersed thread is proportional to the drag force. The $l_{t,b}$ reaches then a maximum once the drag force and inertia are balanced by the elastic force. After that, the elastic force becomes dominated and the $l_{t,b}$ declines progressively. The larger the elasticity and the flow rate of the dispersed phase are, the faster can the elastic force overcome the drag force and inertia. Of course, this scenario should be moderated as the role of dynamical interfacial force remains still an open question in the literature.

There always exists a maximum for the thread length at breakup moment under different flow conditions. Here it is called as the maximum of the thread length at breakup $l_{(t,b)max}$, as shown in the sub-figures of Fig. 3-10. For a given flow rate of the dispersed phase, the increase in elasticity prevents the thread from being stretched to breakup, thus $l_{(t,b)max}$ increases. The $l_{(t,b)max}$ also increases with the flow rate of the dispersed phase under the same elasticity of the dispersed phase.

3.3.1.3 Size prediction of droplets

In this work, the droplet length is normalized by the channel width. The influence of the flow rate of the dispersed phase Q_d, the flow rate of the continuous phase Q_c, the capillary number Ca_c and the elasticity number El on the dimensionless droplet size l_d/w_c was illustrated in Fig. 3-11. Under a fixed flow rate of the dispersed phase, the squeezing force exerted by the continuous phase on the dispersed phase increase with the flow rate of the continuous phase and the two-phase flow rate ratio. Consequently, the dispersed phase is pinched off more easily to form smaller droplets. Under a constant flow rate of the continuous phase, the continuous phase needs a longer time for accumulating more energy to pinch the dispersed phase off when the flow rate of the dispersed phase increases. As a result, the bigger droplets are formed. The dimensionless droplet length could be scaled with the two-phase flow rate ratio as

a power law with an exponent of $\alpha = -0.58$. For the same dispersed phase, the droplet size decreases with the capillary number of the continuous phase. Under a fixed capillary number of the continuous phase, the droplet size increases with the elasticity number of the dispersed phase.

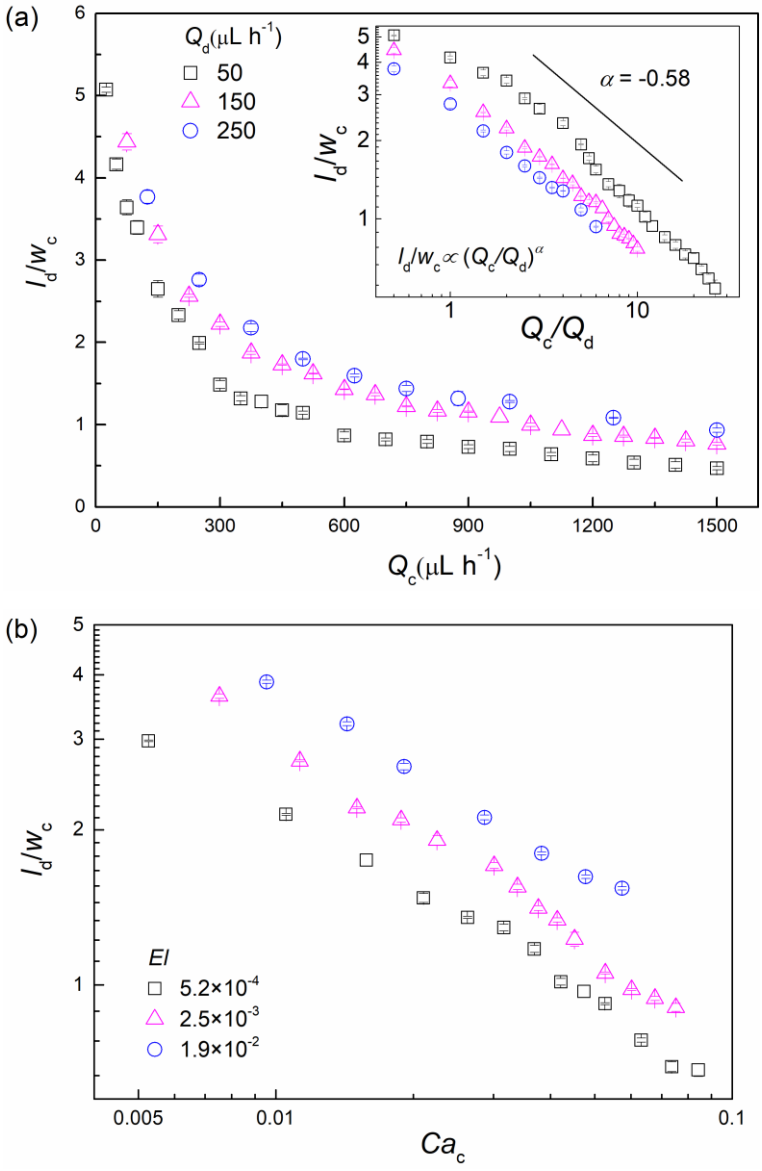


Fig. 3-11 Effect of various factors on the dimensionless size of droplets. (a) The two-phase flow rates, inset: effects of the two-phase flow rate ratio, 100 K PEO solution, $El = 5.2\times10^{-4}$. (b) The capillary number of the continuous phase, $Q_d = 100$ μL·h^{-1}.

Husny and Cooper-White [51] indicated that the elasticity had a negligible effect on the droplet size. To the best of our knowledge, the previous studies on the droplet

size were mainly devoted to the Newtonian fluids, very few concerning elastic liquids. The correlations on the size of the droplet/bubble formed in the microfluidic T-junction in the literature are gathered in Table 3-4. All of the liquids used in the literature are Newtonian fluids, but in our experiments, the dispersed phase is the elastic PEO-glycerol solution. Obviously, the prediction models in the literature cannot precisely predict the size of the elastic droplet. A modified scaling law of droplet size was accordingly proposed by taking into account the two-phase flow rate ratio Q_c/Q_d, capillary number Ca_c and elasticity number El:

$$l_d/w_c = 0.92(Q_c/Q_d)^{-0.22} Ca_c^{-0.36} El^{0.08} \quad (3\text{-}4)$$

Table 3-4 Correlations on the size of the droplet/bubble formed in the microfluidic T-junction in the literature.

Authors	Device material	Size of the cross section (μm)	Operating conditions	Size Correlations
Garstecki et al. [36]	PDMS	w_c: 100 h_c: 33	Liquid-liquid Gas-liquid $Ca_c < 0.01$	$l_d/w_c = 1+aQ_d/Q_c$
Fu et al. [41]	Glass	w_c: 120 h_c: 40	Gas-liquid $0.0058 < Ca_c < 0.013$	$(l_d w_d)^{0.5}/w_c=0.26(Q_c/Q_d)^{-0.18}Ca_c^{-0.25}$
Christopher et al. [231]	PDMS	w_c: 150 h_c: 50	Liquid-liquid $0.01 < Ca_c < 0.1$	$V/(w_c^2 h_c) \propto (Q_d/Q_c)Ca_c^{-1/3}$
Xu et al. [232]	PMMA	w_c: 200 h_c: 150	Liquid-liquid $0.002 < Ca_c < 0.01$	$l_d/w_c = 0.75(Q_c/Q_d)^{-1/3}Ca_c^{-0.2}$
Su et al. [233]	PMMA	w_c: 500 h_c: 500	Liquid-liquid $0.005\ m\cdot s^{-1} < u_d < 0.035\ m\cdot s^{-1}$	$l_d/w_c = 0.768\ (Q_c/Q_d)^{-0.194}(Ca^*)^{-0.24}$

The ranges of the three parameters are $Q_c/Q_d \in [0.5, 35]$, $Ca_c \in [0.0013, 0.1655]$ and $El \in [5.2\times10^{-4}, 1.9\times10^{-2}]$, respectively. Compared to the other two variables, the elasticity number corresponding to three kinds of elastic liquids has different orders of magnitude: 10^{-4}, 10^{-3} and 10^{-2}, respectively. The magnitude of the droplet size affected by the elasticity is much smaller than the elasticity itself. The effect of elasticity of the dispersed phase on the droplet size is not significant, but far from being negligible. The comparison between the predicted values by Eq. 3-4 and the experimental data is shown in Fig. 3-12, with a mean relative deviation of 9.41% and a maximum relative deviation of 26.23%. The relative deviation and the mean relative deviation could be calculated by $\left|l_{cal} - l_{exp}\right| / l_{exp}$ and $\left(\sum_{i=1}^{n} \left|l_{cal} - l_{exp}\right| / l_{exp}\right) / n$, respectively. These results indicate that the scaling law could be applied to predict the droplet size for elastic fluids in microfluidic T-junctions with acceptable accuracy.

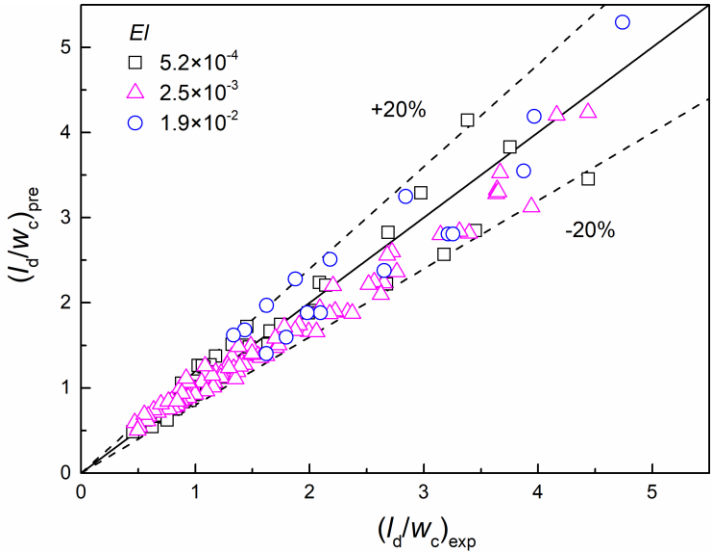


Fig. 3-12 Comparison between the predicted values and experimental data of the droplet sizes.

3.3.2 Droplet formation in elastic fluid at a flow-focusing microchannel

3.3.2.1 Two-phase flow patterns

In the experiment, the ranges for the two-phase fluids were $0.2 < Q_d < 70$ mL·h^{-1} and $0.8 < Q_c < 600$ mL·h^{-1}, respectively. At fixed flow rates of the dispersed phase, three flow patterns of the slug flow, dripping flow and jetting flow were observed by increasing the flow rate of the continuous phase, as shown in Fig. 3-13.

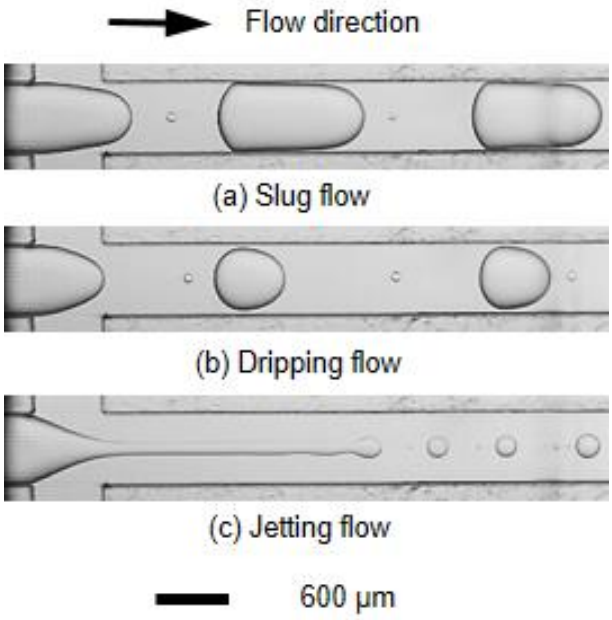


Fig. 3-13 Flow patterns of silicone oil-PEO solution in the flow-focusing microchannel. Q_d = 50 mL·h^{-1}. (a) Q_c = 60 mL·h^{-1}. (b) Q_c = 190 mL·h^{-1}. (c) Q_c = 210 mL·h^{-1}.

(a) Slug flow: the slug flow forms when the flow rate of the continuous phase is relatively small (0.2 mL·h^{-1} ≤ Q_d ≤ 30 mL·h^{-1} ∩ 0.8 mL·h^{-1} ≤ Q_c ≤ 174 $Q_d^{0.12}$ mL·h^{-1}) ∪ (30 mL·h^{-1} ≤ Q_d ≤ 70 mL·h^{-1} ∩ 40 mL·h^{-1} ≤ Q_c ≤ 2909 $Q_d^{-0.71}$ mL·h^{-1}). The length of the slug droplet is larger than the channel width. (b) Dripping flow: the dripping flow forms with the increasing of the flow rate of the continuous phase (0.2 mL·h^{-1} ≤ Q_d ≤ 20 mL·h^{-1} ∩ 174 $Q_d^{0.12}$ mL·h^{-1} ≤ Q_c ≤ 359 $Q_d^{0.018}$ mL·h^{-1}) ∪ (20 mL·h^{-1} ≤ Q_d ≤ 30 mL·h^{-1} ∩ 174 $Q_d^{0.12}$ mL·h^{-1} ≤ Q_c ≤ 2912 $Q_d^{-0.68}$ mL·h^{-1}) ∪ (30 mL·h^{-1} ≤ Q_d ≤ 70 mL·h^{-1} ∩ 2909 $Q_d^{-0.71}$ mL·h^{-1} ≤ Q_c ≤ 2912 $Q_d^{-0.68}$ mL·h^{-1}). The diameter of the spherical-shaped droplet is smaller than the channel width. The distance between every two successive droplets is larger compared with that in the slug flow. (c) Jetting flow: the jetting flow forms when the flow rate of the continuous phase is much larger than that of the dispersed phase (0.2 mL·h^{-1} ≤ Q_d ≤ 20 mL·h^{-1} ∩ 359 $Q_d^{0.018}$ mL·h^{-1} ≤ Q_c ≤ 600 mL·h^{-1}) ∪ (20 mL·h^{-1} ≤ Q_d ≤70 mL·h^{-1} ∩ 2912 $Q_d^{-0.68}$ mL·h^{-1} ≤ Q_c ≤ 600 mL·h^{-1}). The filament of the dispersed phase is elongated in the axial direction and breaks up at the downstream of the junction. The parallel flow was not observed at even larger flow rates of the continuous phase. Cubaud et al. [245] studied the two-phase flow pattern in a flow-focusing microchannel. The glycerol and silicone oil were used as the dispersed and continuous phase, respectively. It was found that when

the flow rate of the dispersed phase is relatively large, the parallel flow could be observed by increasing the flow rate of the continuous phase. Since the parallel flow is more likely to occur at higher viscosity of the dispersed phase. The viscosity of the dispersed phase is 5.3 mPa·s in this work, which is much smaller than the viscosity of the dispersed phase 1214 mPa·s used by Cubaud et al. [245]. Thus the parallel flow was not observed in this work.

The capillary number *Ca* and the Weber number *We* are regarded as the major parameters to distinguish various flow patterns. Fu et al. [42] and Ren et al. [246] investigated the flow patterns and their transition in the Newtonian and non-Newtonian fluids, respectively. The capillary number Ca_c representing the ratio of the viscosity of the continuous phase to the interfacial tension and the Weber number We_d representing the ratio of the inertia of the dispersed phase to the interfacial tension were utilized to plot the flow patterns map.

$$Ca_c = \frac{\eta_{c,0} u_c}{\gamma} \tag{3-5}$$

$$We_d = \frac{\rho_d w_c u_d^2}{\gamma} \tag{3-6}$$

where $\eta_{c,0}$ indicates the zero-shear viscosity of the continuous phase. u_d and u_c represent the velocity of the dispersed phase and the continuous phase, respectively. γ represents the interfacial tension between the two-phase fluids. ρ_d refers to the density of the dispersed phase and w_c is the width of the microchannel.

The map of flow patterns drawn with Ca_c and We_d is displayed in Fig. 3-14. When Ca_c and We_d are relatively small, the interfacial tension plays a dominant role in the droplet formation and results in the slug flow. For the same value of We_d, the viscous force gradually overcomes the effect of interfacial tension with the increasing of Ca_c. The transition from the slug flow to the dripping flow occurs before the jetting flow forms, where the viscous force of the continuous phase dominates. The transition between the slug and dripping flow could be expressed as ($We_d > 10^{-2} \cap We_d = 1\times10^{-4} Ca_c^{-3.2}$) $\cup$ ($We_d < 10^{-2} \cap We_d = 7\times10^{7} Ca_c^{13.2}$), and the transition between the dripping and jetting flow is ($We_d > 10^{-2} \cap We_d = 4\times10^{-4} Ca_c^{-2.8}$) $\cup$ ($We_d < 10^{-2} \cap We_d = 2\times10^{34} Ca_c^{64.9}$). Fu et al. [42] focused on the transition from the dripping to the jetting flow and found the transition line could be determined as $We_d = 7\times10^{-6} Ca_c^{-1.9}$ when

$Ca_c \geq 10^{-2} \cap We_d \geq 10^{-2}$. Comparing with the transition line in this experiment, it was found that it's more difficult to form the jetting flow when the shear-thinning non-Newtonian fluid serves as the continuous phase.

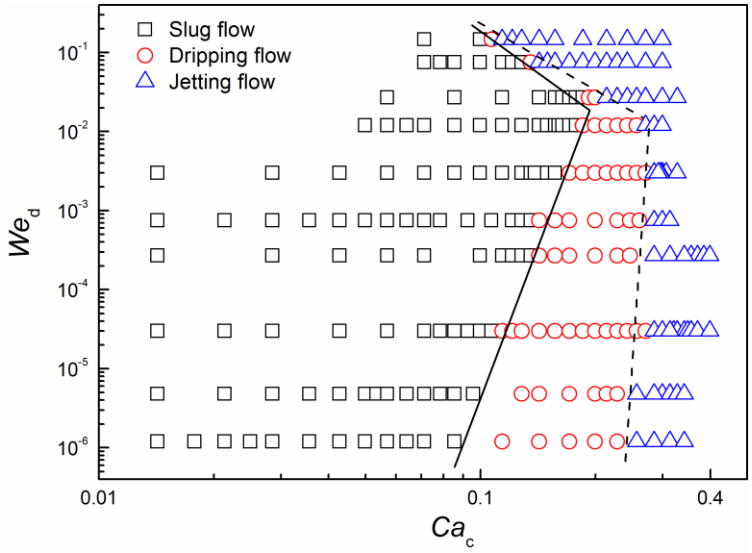


Fig. 3-14 Flow patterns map and transition lines in the flow-focusing microchannel. The dispersed phase: silicone oil. $0.2 < Q_d < 70$ mL·h^{-1}. The continuous phase: 0.1 wt% PEO solution. $0.8 < Q_c < 600$ mL·h^{-1}. Solid lines: transition lines from the slug to dripping flow. Dashed lines: transition lines from the dripping to jetting flow.

The slug flow occupies the largest area among the observed flow patterns in the covered operating range and is considered as the most common flow pattern in the microfluidic devices. Meanwhile, the elastic droplets are widely used in the emulsification and crystallization et al. [247, 248]. Therefore, this work focused on the slug droplet and investigated both the formation dynamics and the size correlation.

3.3.2.2 Dynamics of droplet formation

The formation dynamics of a slug droplet in an entire cycle includes the waiting, expansion, squeezing and pinch-off stages. The width of the dispersed neck w_m indicates the maximum width in the expansion stage and the minimum width in the collapse and pinch-off stages. The moment when the dispersed thread is ruptured is defined as the time zero. It comes to the waiting stage [Fig. 3-15(a)-(b)] as soon as the breakup of the dispersed thread occurs. The dispersed phase undergoes a short

retraction stage in the axial direction under the effect of the interfacial tension. The width of the dispersed neck equals to the channel width in this stage. In the expansion stage [Fig. 3-15(c)], the filament of the dispersed phase is elongated in the axial direction and expands in the radial direction. The continuous phase continuously accumulates energy at the same time. The width of the dispersed neck becomes larger than the channel width until the maximum neck width. In the squeezing stage [Fig. 3-15(d)-(e)], the expansion of the dispersed phase is obstructed by the channel walls. The dispersed phase gradually stretches in the axial direction and squeezed by the continuous phase in the radial direction. The width of the dispersed neck gradually decreases. Then it comes to the pinch-off stage [Fig. 3-15(f)-(g)] until the final rupture [Fig. 3-15(h)]. The temporal evolution for the width of the dispersed thread in a whole cycle of droplet formation is displayed in Fig. 3-15(i).

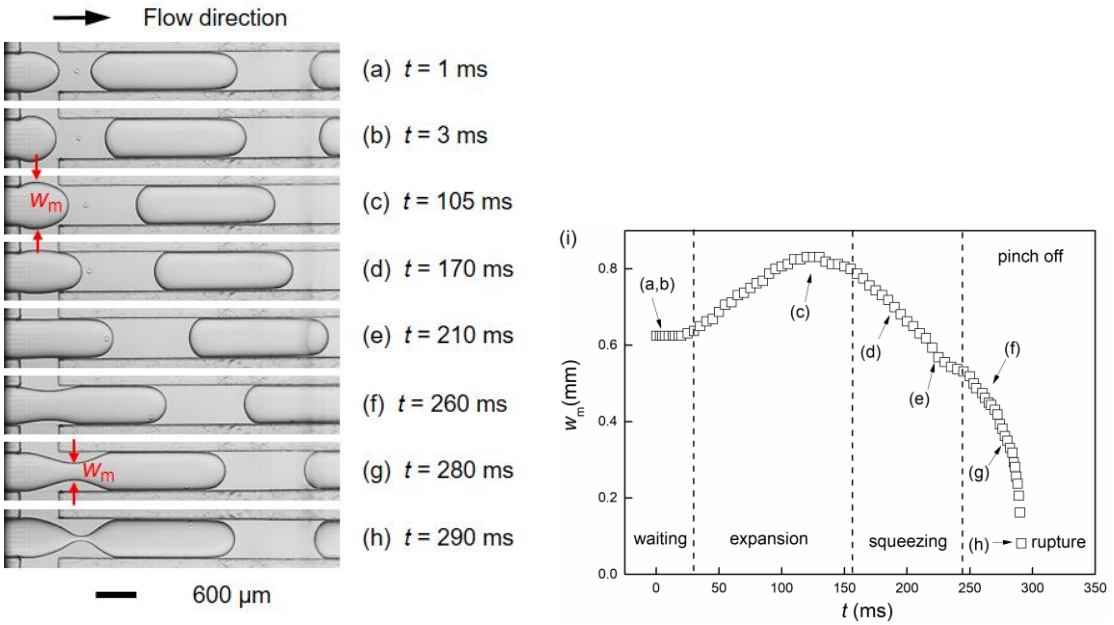


Fig. 3-15 Dynamics of the slug droplet formation in a flow-focusing microchannel. 0.1 wt% PEO solution, Q_d = 10 mL·h^{-1}, Q_c = 20 mL·h^{-1}. (a)-(h) Sequences of the slug droplet formation. (i) Temporal evolution for the width of the dispersed thread w_m in a whole cycle.

The dynamics of droplet formation with PEO solutions is similar to that of the slender bubble in a flow-focusing device [39, 40]. Both procedures consist of four stages and the evolution of the neck width in the pinch-off stage attracts more attention. Dollet et al. [21] considered that the neck thinning was driven by the inertia instead of

the interfacial tension. The scaling law for the width of the dispersed thread in function of the remaining time (T-t) was established as $w_m \propto (T-t)^{1/3}$ in the pinch-off stage. The variations of the thread width with the remaining time in the pinch-off stage of slug droplet formation are displayed in Fig. 3-16. The exponents of 1/3 at various flow rates of the continuous phase and PEO concentrations are consistent with the results from Dollet et al. [21], indicating that the pinch-off mechanism of droplet formation in viscoelastic liquids is the same as that of the bubble formation, which is also dominated by the inertial force.

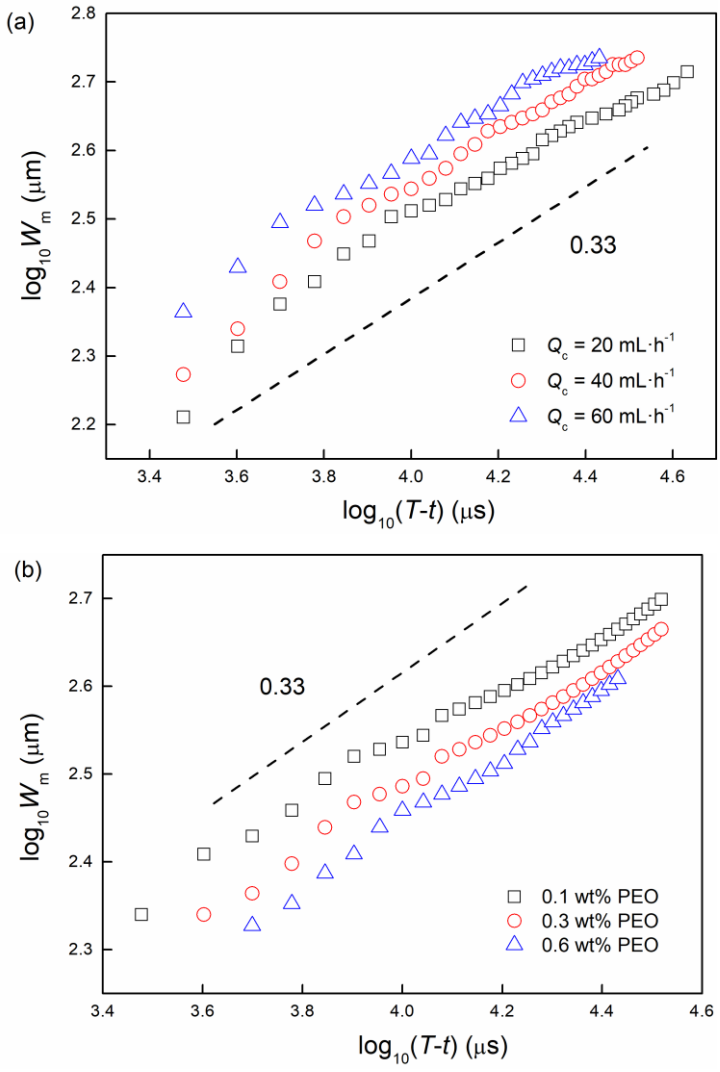


Fig. 3-16 Variation of the thread width w_m in function of the remaining time (T-t) in the pinch-off stage. (a) Flow rate of the continuous phase, 0.1 wt% PEO, Q_d = 10 mL·h^{-1}. (b) PEO concentration, Q_d = 3 mL·h^{-1}, Q_c = 20 mL·h^{-1}.

3.3.2.3 Size prediction of droplets

The effects of various factors on the size of the slug droplet are shown in Fig. 3-17. At fixed flow rates of the dispersed phase, the squeezing force exerted on the continuous phase at the flow-focusing junction increases with the flow rate of the continuous phase. The dispersed phase is more likely to pinch off and form droplets with smaller lengths. At constant flow rates of the continuous phase, the continuous phase needs to accumulate more energy to rupture the dispersed phase at increasing flow rates of the dispersed phase. Thus the droplet length increases accordingly, as shown in Fig. 3-17(a). At the same capillary number of the continuous phase and the elastic number *El*, the droplet size increases with the oil-water flow rate ratio, as shown in Fig. 3-17(b)-(c).

The viscosity of the continuous phase would decrease with the shear rate due to its shear thinning property. Therefore, the viscosity corresponding to different flow rates of the continuous phase used in the capillary number needs to be recalculated. According to the Carreau model [241], the formula to calculate the viscosities corresponding to various flow rates of the continuous phase is as follows.

$$\eta=\eta_{\infty}+(\eta_0-\eta_{\infty})[1+(\lambda\dot{\gamma})^2]^{(n-1)/2} \tag{3-7}$$

where the shear rate of the continuous phase $\dot{\gamma}$ was correlated to the ratio between the apparent flow velocity and the channel width. The rheological parameters of PEO solutions with various concentrations are shown in Table 3-3. By substituting the shear rate and the fitted rheological parameters into Eq. 3-7, the viscosity of the PEO solution corresponding to various flow rates could be obtained.

The apparent flow velocity increases so that the viscosity decreases with the flow rate of the continuous phase. Due to the increasing rate of the apparent flow velocity is far greater than the decreasing rate of the viscosity, the capillary number of the continuous phase increases with the flow rate. At a fixed two-phase flow rate ratio, both the capillary number of the continuous phase and the shearing force acting on the interface increase as a result. The pinch-off of the dispersed phase is accelerated and the size of the slug droplet decreases.

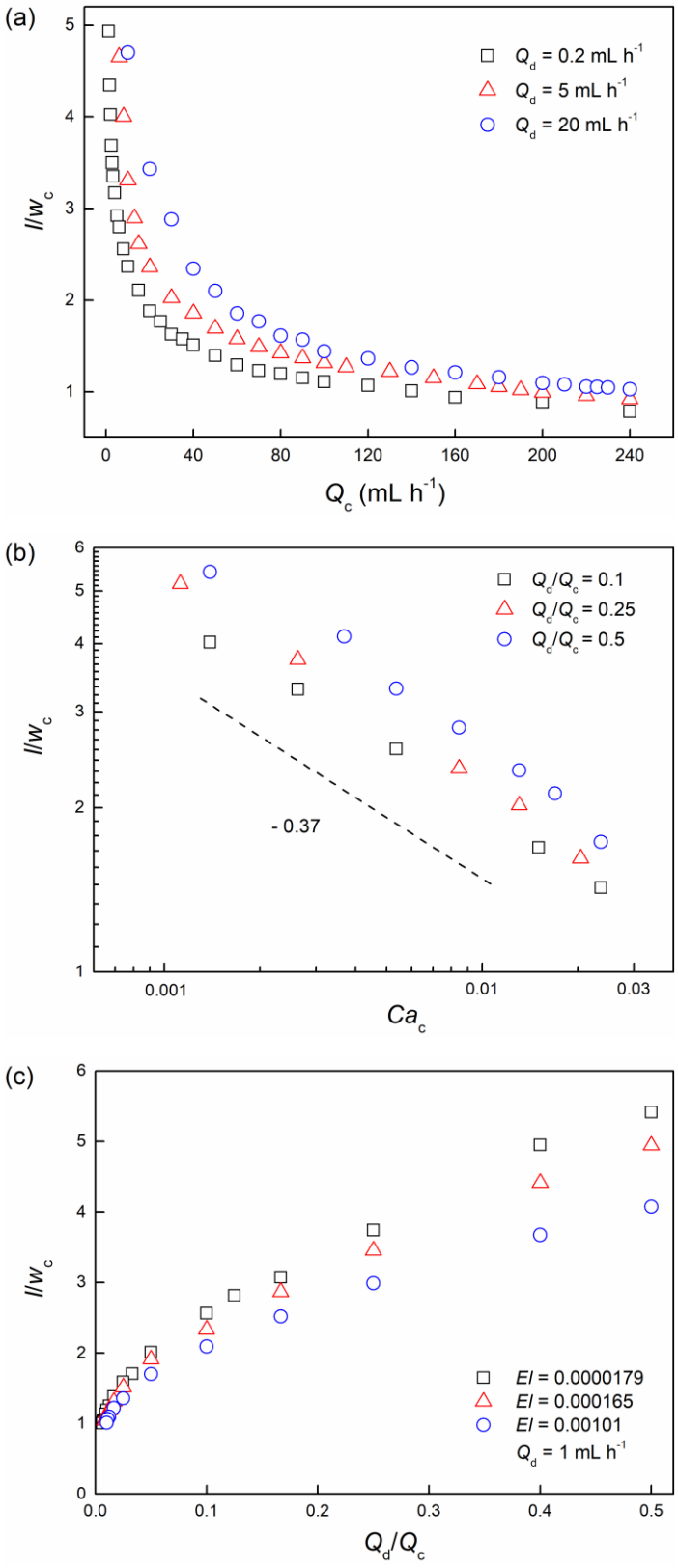


Fig. 3-17 Effect of various factors on the dimensionless size of slug droplet. (a) Two-phase flow rates. (b) The capillary number of the continuous phase. (c) Elasticity number of the continuous phase.

To quantify the elasticity of the PEO solution, the dimensionless elastic number *El* reflecting the relative magnitude of the elastic force to the inertial force was introduced. The relationship between the effective relaxation time λ_{eff} and the longest relaxation time λ_{Z} for dilute PEO solutions $\lambda_{\mathrm{eff}} = \lambda_{\mathrm{Z}} \left(c / c^* \right)^{0.65}$ was proposed by Tirtaatmadja et al. [237]. The effect of the PEO concentration on the droplet elasticity can be included in the elastic number by replacing the longest relaxation time with the effective relaxation time. The elastic number is displayed in the following Eq. 3-8.

$$El = \frac{\lambda_{\mathrm{eff}} \eta_{\mathrm{c},0}}{\rho_{\mathrm{c}} w_{\mathrm{c}}^{\ 2}} \tag{3-8}$$

As shown in Fig. 3-17(c), the size of the slug droplet decreases with the elastic number. The elastic number is about two orders of magnitude larger by increasing the PEO concentration from 0.1 wt% to 0.6 wt% in our experiment. The resulted variation in the droplet size is much smaller than that of the elastic number. Compared with the influences of the two-phase flow rate ratio and the capillary number on the size of the slug droplets, the effect of the elasticity could be neglected.

It's generally considered that the mechanism governing the droplet formation in the microfluidic devices mainly includes the shearing and squeezing mechanism. Thorsen et al. [229] firstly proposed the shearing mechanism. They held the opinion that the viscous force dominated the droplet formation and the droplet size was affected by the capillary number of the continuous phase. The squeezing mechanism proposed by Garstecki et al. [36] considered that the squeezing force from the continuous phase dominated and the droplet size was closely related to the two-phase flow rate ratio. For droplets that are longer than the channel width, it is considered that the formation is dominated by the squeezing mechanism, while the formation of smaller droplets is dominated by the shearing mechanism.

Based on the above-mentioned mechanisms, Cubaud et al. [245] focused on the droplet size when the dispersed phase is highly viscous. The correlation of droplet size in a flow-focusing device was proposed within two ranges divided by $l / w_{\mathrm{c}} = 2.5$.

$$l / w_{\mathrm{c}} = \begin{cases} 0.0022 \left(\dfrac{Q_{\mathrm{c}}}{Q_{\mathrm{d}} + Q_{\mathrm{c}}} Ca_{\mathrm{c}} \right)^{-1} & \text{for } l / w_{\mathrm{c}} > 2.5 \\ 0.5 \left(\dfrac{Q_{\mathrm{c}}}{Q_{\mathrm{d}} + Q_{\mathrm{c}}} Ca_{\mathrm{c}} \right)^{-0.17} & \text{for } l / w_{\mathrm{c}} < 2.5 \end{cases} \tag{3-9}$$

Then the predicting model of droplet size in two ranges divided by $l / w_c = 2.35$ was proposed by Fu et al. [42] as follows.

$$l / w_c = \begin{cases} 0.30(Q_d / Q_c)^{0.23} Ca_c^{-0.42} & \text{for } l / w_c > 2.35 \\ 0.72(Q_d / Q_c)^{0.14} Ca_c^{-0.19} & \text{for } l / w_c \le 2.35 \end{cases} \quad (3\text{-}10)$$

The experimental results were compared with the two predicting correlations above. The mean relative deviations were 36.66% and 29.22% and the maximum relative deviations were 89.11% and 53.71%, respectively. Since the models were proposed on the basis of the typical Newtonian fluids, the deviation is relatively large compared with the elastic liquids. Therefore, the correlations established in the literature are unable to predict the accurate droplet size in this work and needs to be modified.

Fu et al. [49] studied the bubble formation in elastic fluids in a flow-focusing device. The force analysis showed that the bubble formation was jointly controlled by the interfacial tension, viscous force, inertial force and the pressure from the dispersed phase. It was found that the rheological properties of the elastic liquid had significant influences on the dynamics and size of the bubble. The predicting model for the bubble size was established with the two-phase flow rate ratio, the capillary number and the Reynolds number *Re* of the continuous phase. At a fixed two-phase flow rate ratio, the size of the droplet size depends on the absolute value of the two-phase flow rates as well. Thus the influence of the absolute two-phase flow rates and the flow rate ratio need to be included in the model. The absolute value of the flow rate can be reflected by introducing the Reynolds number in the model.

The correlations for predicting the size of the slug droplet were proposed in two ranges of the droplet size by taking the two-phase flow rate ratio, the capillary number and the Reynolds number of the continuous phase into account.

$$l / w_c = \begin{cases} 1.31(Q_d / Q_c)^{0.16} Re_c^{-0.08} Ca_c^{-0.20} & \text{for } l / w_c > 2.5 \\ 0.86(Q_d / Q_c)^{0.06} Re_c^{-0.11} Ca_c^{-0.23} & \text{for } 1 < l / w_c \le 2.5 \end{cases} \quad (3\text{-}11)$$

Figure 3-18 shows the comparison between the calculated slug droplet size according to Eq. 3-11 and the experimental data. In the two ranges of the droplet size, the mean relative deviation was 5.05% and 2.85% and the maximum relative deviation was 16.37% and 18.66%, respectively. The results indicate that the model

could be applied to predict the droplet size for elastic fluids in a flow-focusing device with acceptable accuracy.

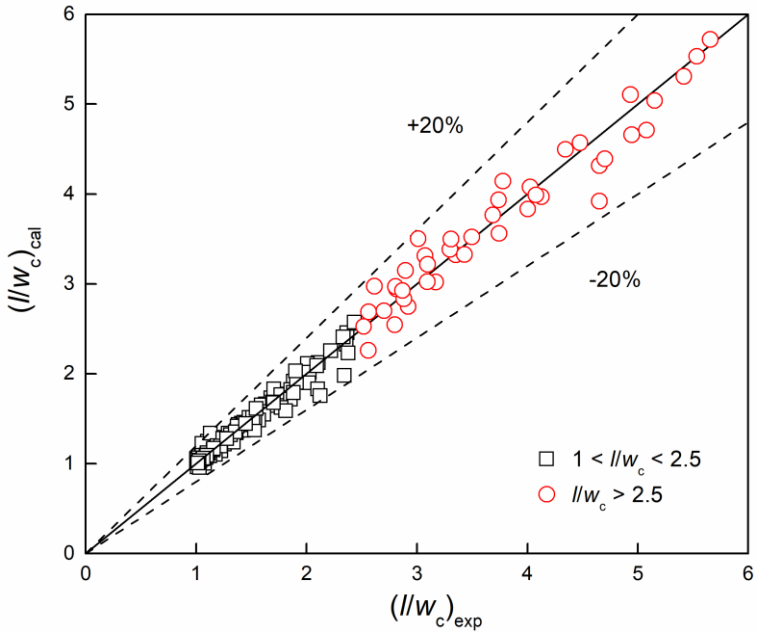


Fig. 3-18 Comparison between calculated values and experimental data for the dimensionless sizes of the slug droplets.

3.3.2.4 Velocity fields during the droplet formation

To provide deep insights into the inner flow field during the droplet formation, the high-speed micro-PIV technique was applied in this work. Previous studies mainly focused on the flow fields in the continuous phase in the liquid-liquid two-phase flows at microscale [42, 57, 249]. Herein, the velocity fields in the dispersed phase during the droplet formation corresponding to three flow regimes were experimentally measured.

In the slug flow as shown in Fig. 3-19, two situations were categorized according to whether the reverse flow was observed in the upstream dispersed phase at the breakup moment. (a) With a reverse flow: The time zero t = 0 ms also indicated the breakup moment of the dispersed neck. At lower flow rates of the dispersed phase, the velocity vectors in the upstream dispersed fluid were in the opposite direction with the downstream slug droplet, which was the so-called reverse flow due to the interfacial energy release accompanying the breakup. Then the dispersed thread retracted from

the breakup points and formed satellite droplets due to interface tension. Meanwhile, both the dispersed thread in the upstream and the mother droplet in the downstream evolved into much smoother profiles at t = 2 ms. Followed by a latent stage, it transformed into the expanding stage where the dispersed head gradually expanded in the axial direction towards the downstream. The appearance of the vertical vectors around the dispersed neck at t = 25 ms represented the beginning of the squeezing stage. The neck width decreased as a result of the squeezing effect from the feeding of the continuous phase. A dispersed filament connecting the upstream dispersed phase and the downstream slug droplet formed before the final pinch-off at t = 62.5 ms, it worth mentioning that the latex particles in the dispersed filament were drained into the side parts. (b) Without a reverse flow: In contrast to the first case, the intrinsic difference in this situation was that no reverse flow was observed at the breakup moment. At higher the flow rates of the dispersed phase, the inertial force prohibited the instability of the dispersed thread at the final pinch-off. Hence both the dispersed thread and the newly formed slug droplet moved towards the downstream channel without the appearance of any reverse flow.

In the dripping flow as displayed in Fig. 3-20, the reverse flow and satellite droplets also emerged as soon as the breakup of the dispersed neck. The evolution of the velocity fields was generally like that in the slug flow except for the absence of the confinement from the channel walls due to the smaller droplet diameter. Thus, the velocity fields evolved towards all directions along the liquid-liquid interface, rather than the vectors only located in the axial direction around the obstructed slug droplet.

In the jetting flow where the flow rate of the continuous phase was much larger than the high flow rate of the dispersed phase, the thread of the dispersed phase in the middle of the microchannel was elongated in the axial direction towards the downstream. According to the velocity fields shown in Fig. 3-21, only parallel horizontal vectors in the same direction as the dispersed flow were observed among the focused area at the flow-focusing junction. It was revealed that no squeezing effect by the continuous phase from the side channels was exerted on the long filament at both the junction and the upstream in this jetting regime. The velocity fields in the jetting flow presented by Lan et al. [250] proved the existence of the vectors perpendicular to the liquid-liquid interface in the downstream channel at the jet tip where a string of droplets formed.

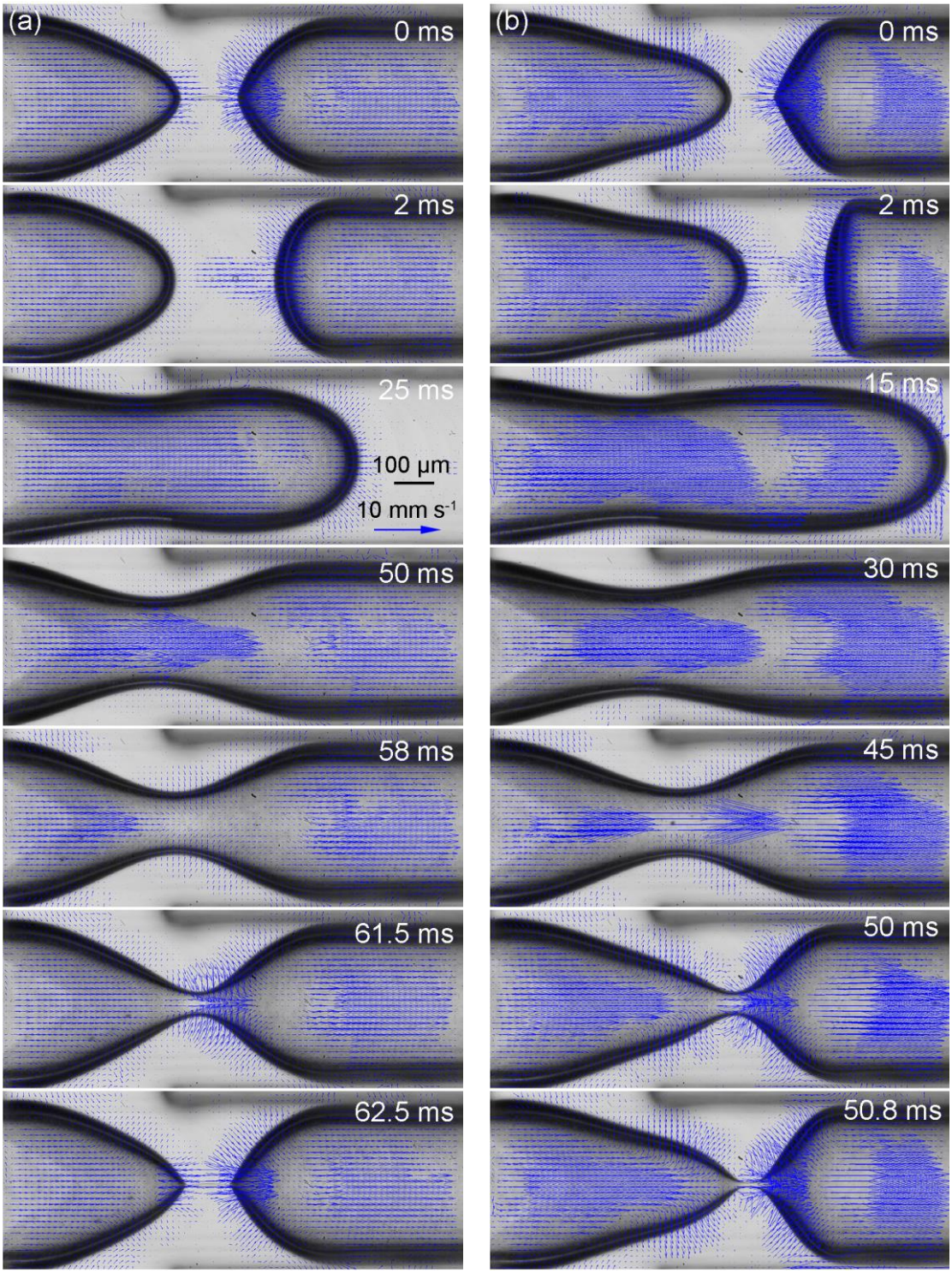


Fig. 3-19 Velocity fields in the slug flow at the flow-focusing junction. (a) With a reverse flow: Q_d = 6 mL·h^{-1}, Q_c = 4 mL·h^{-1}. (b) Without a reverse flow: Q_d = 12 mL·h^{-1}, Q_c = 4 mL·h^{-1}. All images share the same scale bars of 100 μm and 10 mm·s^{-1} for the length and velocity, respectively.

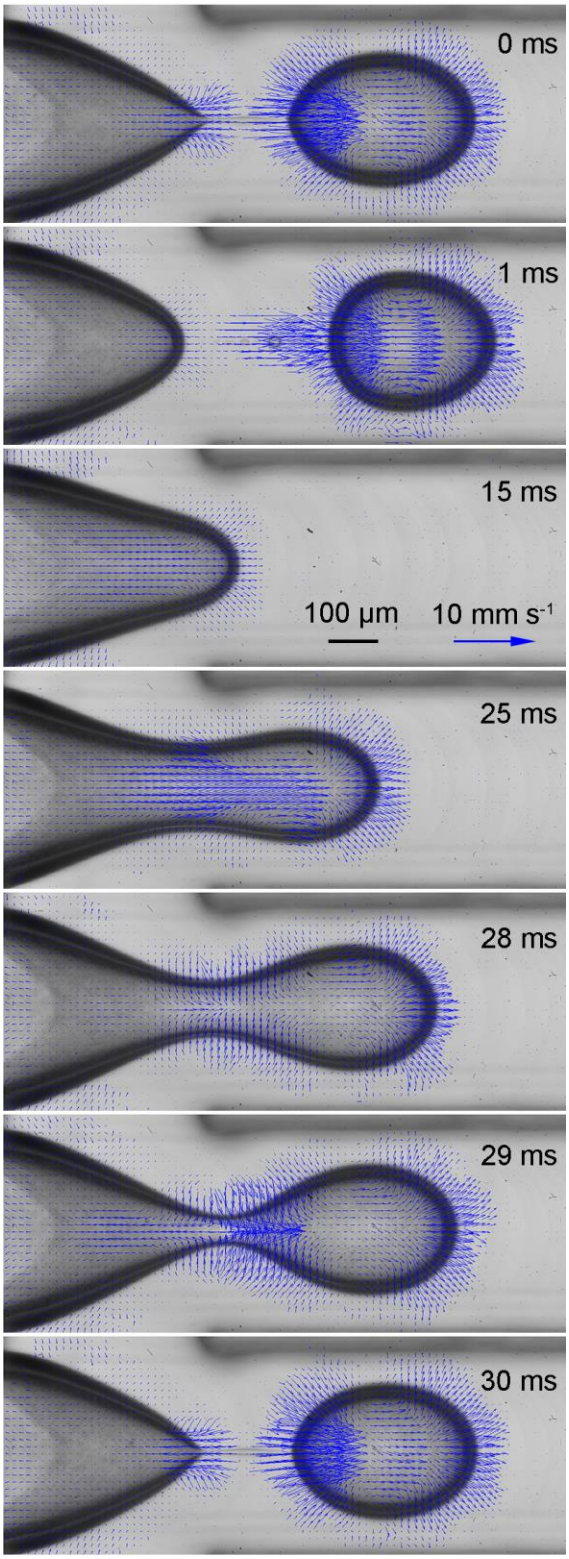


Fig. 3-20 Velocity fields in the dripping flow at the flow-focusing junction. Q_d = 1.5 mL·h^{-1}, Q_c = 15 mL·h^{-1}. The scale bars for length and velocity represent 100 μm and 10 mm·s^{-1}, respectively.

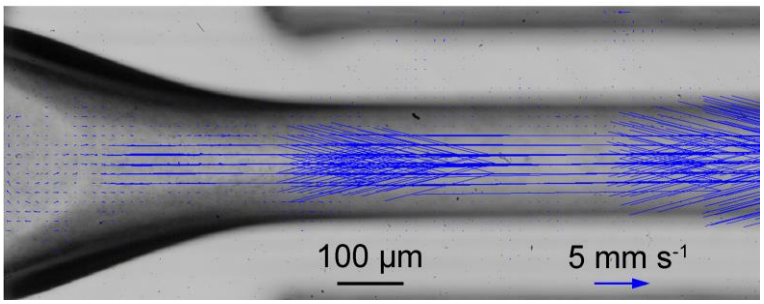


Fig. 3-21 Velocity fields in the jetting flow at the flow-focusing junction. Q_d = 24 mL·h^{-1}, Q_c = 30 mL·h^{-1}. The scale bars for length and velocity represent 100 μm and 5 mm·s^{-1}, respectively.

3.4 Summary

To summarize, the liquid-liquid two-phase flow pattern and the droplet formation in both T-junction and flow-focusing devices were investigated in this chapter.

For the formation of elastic droplets in a microfluidic T-junction, four flow regimes including the slug, dripping, beads-on-string and stratified flows were observed. The decrease rate of the minimum width of the dispersed thread is not equally proportional to the change of the flow rate of the continuous phase in the squeezing stage. The maximum of the thread length at breakup is positively related to the flow rate and elasticity of the dispersed phase. A modified scaling law of droplet size is proposed based on an elasticity number.

For the droplet formation in the elastic fluids in a flow-focusing junction, the slug flow, dripping flow and jetting flow were observed by adjusting the two-phase flow rates. The flow pattern map and the predicting correlations for the transition lines were given in function of the capillary number and the Weber number. In the pinch-off stage, the width of the dispersed thread in function of the remaining time could be fitted with a power law with an exponent of 1/3. The predicting correlation for the size of the slug droplet was proposed by taking the two-phase flow rate ratio, the capillary number and the Reynolds number of the continuous phase into account.

Apart from the droplet formation, the deformation and stretching of elastic droplet also deserves further study and will be discussed in the following chapter.

Chapter 4 Stretching and breakup of elastic droplets in consecutive flow-focusing device

In this chapter, the stretching and breakup of elastic droplets in a microfluidic flow-focusing device were investigated experimentally by a high-speed camera. By employing various PEO solutions corresponding to a wide range of elasticities, the effects of the elasticity on the flow regime and the dynamics of each regime were systematically investigated.

4.1 Introduction

Based on the liquid-liquid two-phase flow at the microscale, the research of the droplet-based microfluidic technology involves the droplet formation, motion, breakup, distribution/filtration and coalescence [27, 251, 252]. Precise and effective control on the droplet size could be realized by the microfluidic devices and shows promising prospects in the fields of chemical analysis, drug encapsulation, biology and material synthesis [218, 253, 254], etc. The droplet breakup could simultaneously form daughter droplets of unequal sizes in the same microfluidic device and achieve the size control on the sub-droplets, which improves the efficiency and flexibility of the microfluidic devices and have been widely used in chemical reactions and fluid mixing [255, 256].

Droplet breakup could be categorized into both passive and active methods [166]: The former realizes the droplet breakup on the confined space in the microfluidic devices and does not rely on the introduction of any external force, while the latter depends on the additional forces or the inherent properties of the fluids. Previous studies focused on the passive droplet breakup of the Newtonian fluids and viscoelastic fluids and the active breakup of droplets and bubbles in the Newtonian fluids. T-junction is one of the most commonly used configurations for the passive droplet breakup in the microfluidic devices. Previous studies proposed the critical conditions of the droplet breakup in the Newtonian fluids: At relatively large capillary numbers, the critical condition could be expressed as $Ca_{cr} = \alpha\varepsilon_0(1/\varepsilon_0^{2/3} - 1)^2$. Here,

the prefactor α is related to both the viscosity ratio of the two-phase fluids and the geometry of the microfluidic device, the initial extension of the droplet ε_0 is defined as the ratio of the droplet length to its circumference [72]. The critical condition $l_0/w_c = 1.3Ca^{-0.21}$ is suitable for a wide range of the capillary number [73].

The droplet breakup at a symmetric T-junction was investigated by the three-dimensional numerical simulation [251]. It was found that the droplet breakup could be divided into two stages including the two-dimensional breakup and the three-dimensional rapid pinch-off. The minimum neck width obeys the power-law relationship with the remaining time in the second stage. The passive breakup of the viscoelastic droplet was studied [257]. It was claimed that the viscoelastic droplets were more unstable than the Newtonian fluid droplets during the breakup procedure. The elastic filaments formed during the stretching process. The variation of the filament volume could be indicated by the Hencky strain of ε_l and ε_d, which were calculated based on the length and radius of the filament. Furthermore, the relaxation time of the viscoelastic fluid could also be estimated on the basis of the theoretical model and the experimental results.

Compared with the above-mentioned passive methods, the active methods could realize the flexible control on the droplet breakup. One of the common manners is to introduce an external fluid into the flow-focusing junction of the microfluidic devices. At present, relatively little attention has been paid to the droplet or bubble breakup by active methods. Cubaud [79] focused on the active breakup of highly viscous droplets at a symmetric microfluidic flow-focusing junction. Three regimes of relaxing, convective breakup and absolute breakup. In the regime of relaxed deformation, the deformed droplets are symmetrical and related to the capillary number. The asymmetrical droplets would exhibit various spoon-liked shapes. Furthermore, the predicting models of the maximum stretching length and the final length of the mother droplet were also proposed. Wang et al. [258] concentrated on the bubble breakup in the microfluidic flow-focusing junction and also observed the deformation and breakup regimes. The effects of the initial bubble length, viscosity and superficial velocity of the liquid on the transition between different regimes were investigated. The critical condition of the bubble breaking was proposed based on the deformation time and breakup time of bubbles.

To the best of our knowledge, no research has focused on the elastic stretching and active breakup of the elastic droplets in the microfluidic flow-focusing junction. In the present section, the process of elastic stretching and the controlled breakup of elastic droplets in a microfluidic flow-focusing junction was systematically investigated. The effects of fluid elasticity and two-phase flow rates on the flow pattern, the droplet breakup dynamics and the size of the daughter droplets were studied.

4.2 Experimental section

The schematic diagram of the experimental apparatus is shown in Fig. 4-1(a). The microfluidic chip was horizontally placed on the platform of the microscope (Nikon, ECLIPSE Ti-CU, Japan). The working fluids were injected into the microchannels by the syringe pumps (Harvard Apparatus, PHD 2000, USA). The high-speed images were recorded by the high-speed camera (Photron, SA 1.1, USA) equipped with the microscope. The magnification of the microscope was 20 or 40 times. The capturing rate of the high-speed camera was 2000 fps or 6000 fps. The images should be collected when the regimes of droplet breakup are stabilized after adjusting the flow rates of the working fluids.

The microfluidic device employed in the experiments is composed of two PMMA plates with a size of 100 mm (length) × 60 mm (width) × 8 mm (height). The microchannels with a cross-section of 400 μm (depth) × 400 μm (width) were fabricated on the chip plate. Another plate with the same size was used to seal the microfluidic device. The three-dimensional structure of the microfluidic device is shown in Fig. 4-1(b). The dispersed phase L1 was injected into the main channel at the flow rate of Q_1 and the continuous phase L2 was injected into the side channels at the total flow rate Q_2. The immiscible two-phase fluids contacted at the first flow-focusing junction to continuously generate new droplets. The droplets were in contact with the continuous phase L3 with a flow rate of Q_3 when they moved downstream to the second flow-focusing junction. The elastic stretching or active breakup behaviors of the droplets at this second junction were observed. The flow rates of the above-mentioned fluids are $0.3 < Q_1 < 1.5$ mL·h^{-1}, $0.3 < Q_2 < 1.5$ mL·h^{-1} and $0.3 < Q_3 < 22.5$ mL·h^{-1}, respectively.

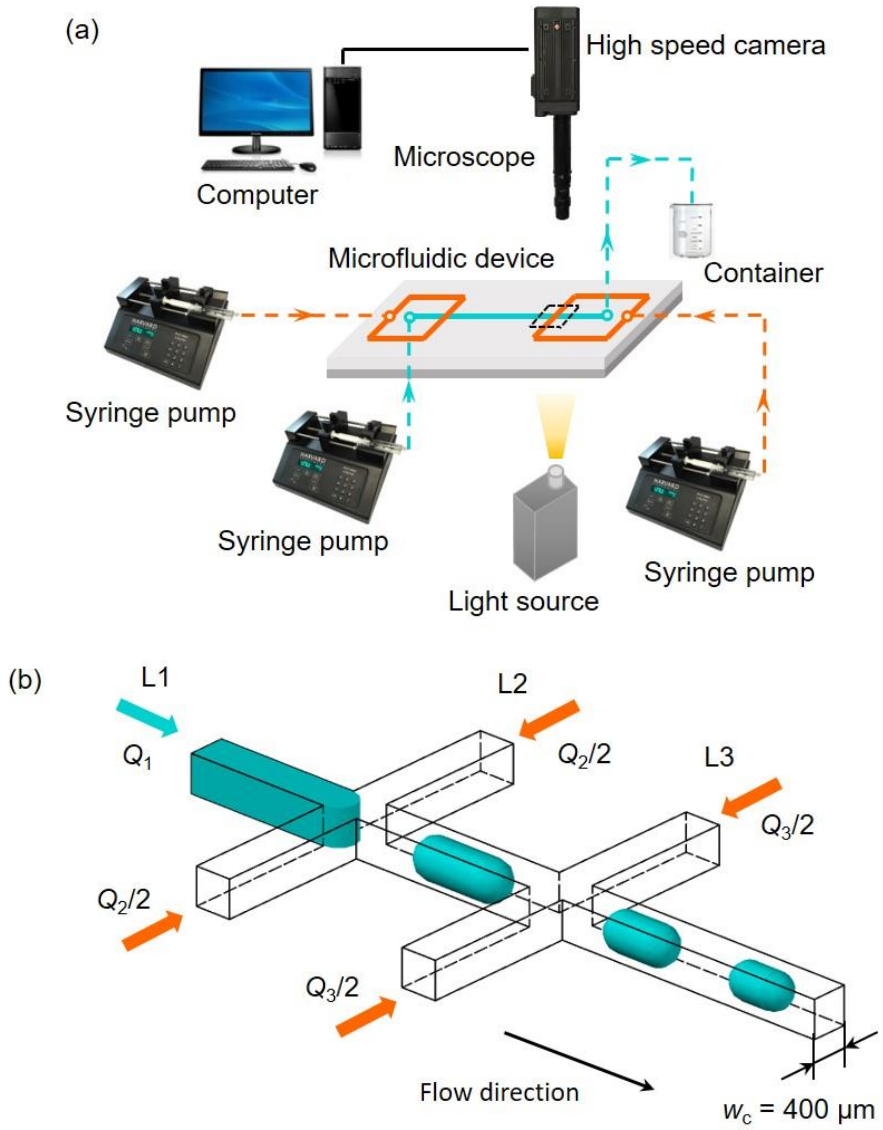


Fig. 4-1 (a) Schematic diagram of the experimental apparatus. The focus was given to the droplet behaviors at the second flow-focusing junction; (b) Three-dimensional structure of the microfluidic device: all the cross-sections of the channels are 400 μm (width) × 400 μm (height).

PEO-glycerol aqueous solutions with various PEO molecular weights and 50 wt% glycerol aqueous solution were employed as the dispersed phase L1. The molecular weights M_w of PEO are 1×10^5 g·mol^{-1}, 3×10^5 g·mol^{-1}, 1×10^6 g·mol^{-1} and 5×10^6 g·mol^{-1}. In the range of the dilute PEO solution with the dimensionless concentration of $0.01 \leqslant c/c^* \leqslant 1$, the employed dimensionless concentrations in the experiments are 0.3, 0.5 and 0.7, respectively. $c^*=1/[\eta]$ is the critical overlap concentration of PEO solution. $[\eta]=0.072M_w^{0.65}$ refers to the intrinsic viscosity of PEO solution [237]. The critical overlap concentrations c^* of the four kinds of PEO solutions are 0.781

wt%, 0.382 wt%, 0.175 wt% and 0.061 wt%, respectively. The compositions and physical properties of the dispersed phase fluids are shown in Table 4-1. The mineral oil containing 4 wt% (four times of the critical micelle concentration [54]) surfactant Span 20 served as the continuous phase fluids (L2, L3). The density and viscosity are $\rho_{2,3}$ = 872.5 kg·m^{-3} and $\eta_{2,3}$ = 26 mPa·s, respectively.

Table 4-1 Compositions and properties of the dispersed phase fluids (298.15 K).

PEO			$c_{glycerol}$ (wt %)	η_1 (mPa·s)	ρ_1 (kg·m^{-3})	γ (mN·m^{-1})	*Ec*
M_w (g·mol^{-1})	*c* (wt %)	*c*/*c**					
/	/	/	50	5.31	1127.1	4.04	/
	0.234	0.3	41.985	5.85	1106.9	4.10	6.51×10^{-3}
1×10^5	0.391	0.5	38.928	5.83	1106.2	4.30	9.55×10^{-3}
	0.547	0.7	35.871	5.31	1090.3	4.40	1.34×10^{-2}
	0.115	0.3	41.010	5.62	1106.0	4.64	4.70×10^{-2}
3×10^5	0.191	0.5	36.387	5.74	1091.9	4.21	5.82×10^{-2}
	0.268	0.7	31.765	5.39	1078.6	4.51	8.26×10^{-2}
	0.052	0.3	39.632	5.41	1101.9	4.57	0.35
1×10^6	0.087	0.5	34.386	5.67	1084.5	4.47	0.46
	0.122	0.7	29.141	5.34	1073.3	4.74	0.64
5×10^6	0.031	0.5	40.310	5.84	1102.5	4.88	6.88

The PEO-glycerol aqueous solutions are regarded as a typical elastic fluid and the addition of the glycerol makes its viscosity independent of the shear rate. The viscosity was measured by the rotational rheometer within the shear rate range of 1 to 100 s^{-1}. The results indicated that the viscosities of various PEO-glycerol aqueous solutions were nearly unaffected by the shear rate. The elasto-capillary number *Ec* was chosen to describe the elasticity of the PEO-glycerol aqueous solution [52]:

$$Ec = \frac{\lambda_{\text{eff}}\gamma}{\eta_1 w_{\text{c}}} \tag{4-1}$$

where γ, η_1, w_c are the interfacial tension, the viscosity of the PEO-glycerol aqueous solution and the width of the microchannel. $\lambda_{\text{eff}} = 0.463\frac{[\eta]\eta_s M_w}{N_A k_B T_K}\left(\frac{c}{c^*}\right)^{0.65}$ is the

effective relaxation time of the dilute PEO solutions, where η_s is the viscosity of the solvent, N_A is the Avogadro constant, k_B is the Boltzmann constant. T_K = 298.15 K is the Kelvin temperature of the experimental environment.

4.3 Results and discussion

4.3.1 Breakup regimes of the droplets in the flow-focusing junction

Three typical regimes were observed at the second flow-focusing junction by adjusting the operating condition and the elasticity of the dispersed phase: Stretch-rebound without tail (regime I), stretch-rebound with tails (regime II) and stretch-breakup (regime III), as displayed in Fig. 4-2. For the dispersed phase fluids with low elasticity ($E_c \leq 0.083$), only the droplet stretching was observed when the flow rate of the continuous phase L3 was relatively small, and no tail emerged in the rebound stage [Fig. 4-2(a)]. By increasing the flow rate of the continuous phase L3, three kite-shaped tails were observed during the rebound process [Fig. 4-2(b)]. At comparatively large flow rates of the continuous phase L3, the droplet breakup occurred following the stretching stage and a long tail at the middle of the droplet rear was noticed at the same time [Fig. 4-2(c)].

In order to elucidate the effect of the fluid elasticity and operating condition on the flow pattern, the elasto-capillary number of the dispersed phase fluid and a combining factor $\varphi_3 Ca_3$ for the continuous phase L3 were employed to draw the phase diagram of the elastic stretching and breakup of elastic droplets, as shown in Fig. 4-3. Here, $\varphi_3 = Q_3/(Q_1+Q_2+Q_3)$ and $Ca_3 = u_3\eta_3/\gamma$ refer to the volume fraction and capillary number of the continuous phase L3. For the dispersed phase fluids with low elasticity ($E_c \leq 0.083$), three regimes appeared in sequence with the flow rate of the continuous phase L3. When the elasto-capillary number was in the range of $0.35 \leq E_c \leq 0.64$, the increase of the flow rate of the continuous phase L3 only resulted in the emergence of “regime I” and “regime II” without the droplet breakup. For the disperse phase fluid with extremely strong elasticity ($Ec \geq 6.88$), only “regime I” was observed within the operating conditions. The phenomenon of droplet breakup and the tails at the rear of the droplets were not found. The stretching and breakup of droplets

were less likely to occur as the elasticity of the dispersed phase fluid increased, indicating the resistance of droplet elasticity in response to the external forces.

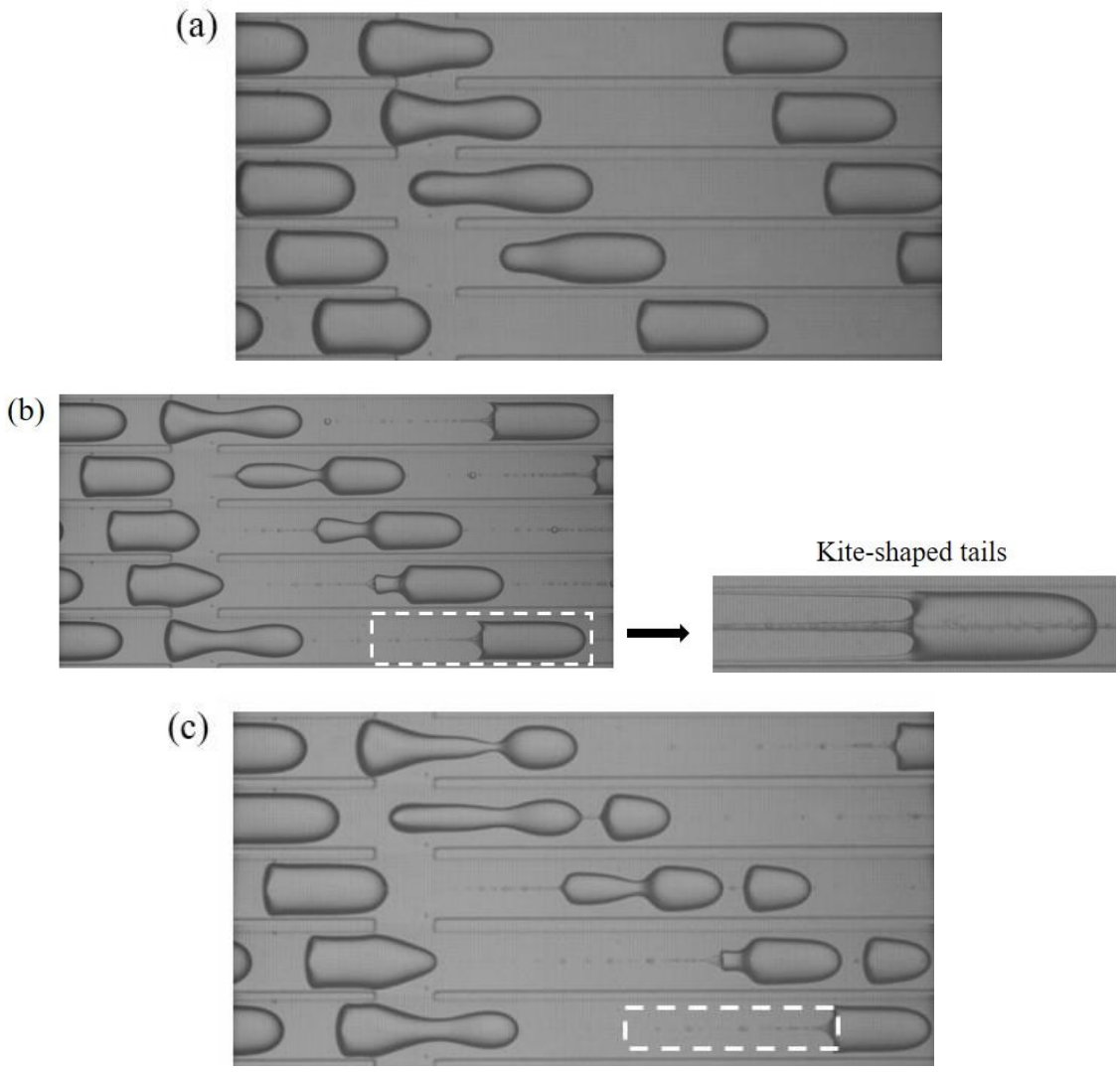


Fig. 4-2 Evolution of elastic stretching and active breakup for elastic droplets in a microfluidic flow-focusing junction. (a) Stretch-rebound without tail (regime I): M_w = 1×10^6 g·mol^{-1}, c/c^* = 0.5, Ec = 0.46, Q_1 = 0.5 mL·h^{-1}, Q_2 = 0.5 mL·h^{-1}, Q_3 = 1 mL·h^{-1}; (b) Stretch-rebound with tails (regime II): M_w = 3×10^5 g·mol^{-1}, c/c^* = 0.5, Ec = 0.058, Q_1 = 1 mL·h^{-1}, Q_2 = 1 mL·h^{-1}, Q_3 = 2 mL·h^{-1}; (c) Stretch-breakup (regime III): M_w = 3×10^5 g·mol^{-1}, c/c^* = 0.5, Ec = 0.058, Q_1 = 1 mL·h^{-1}, Q_2 = 1 mL·h^{-1}, Q_3 = 3 mL·h^{-1}.

In the regime II and regime III, a single tail and the multiple kite-shaped tails at the rear of the droplets emerged in the axial direction of the microchannel. Similar tails at the rear of the droplets were also observed in the studies by Wu et al. [259].

When the droplets moved towards the downstream of the main channel, the interface at the rear of the droplet was concave and the shearing force exerted on the droplet interfaces between the channel walls became stronger. Thus the droplet was elongated where it contacted the channel walls to form the long filaments at the rear of the droplet, which was the so-called phenomenon of “tail stream”.

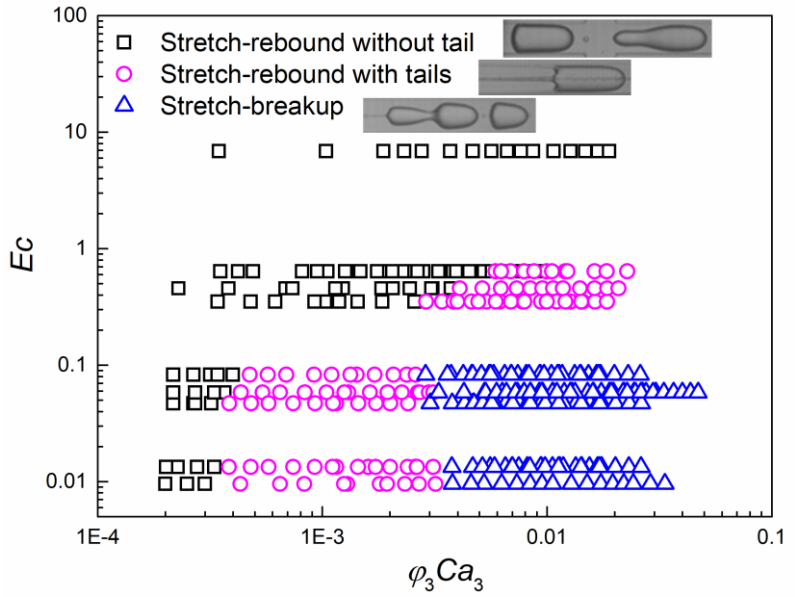


Fig. 4-3 Phase diagram of the elastic stretching and breakup of elastic droplets between *Ec* and $\varphi_3 Ca_3$.

4.3.2 Dynamics of the droplet stretch-rebound

For the two regimes of the droplet stretch-rebound, the dynamics of the interfacial evolution in both the axial and radial directions of the main channel was investigated. The time zero $t = 0$ is defined when the tip of the droplet moves to the upstream wall where the continuous phase L3 is injected into the second flow-focusing junction. The sequences of the droplet stretch-rebound in regime I and regime II are displayed in Fig. 4-4(a) and Fig. 4-4(b), respectively.

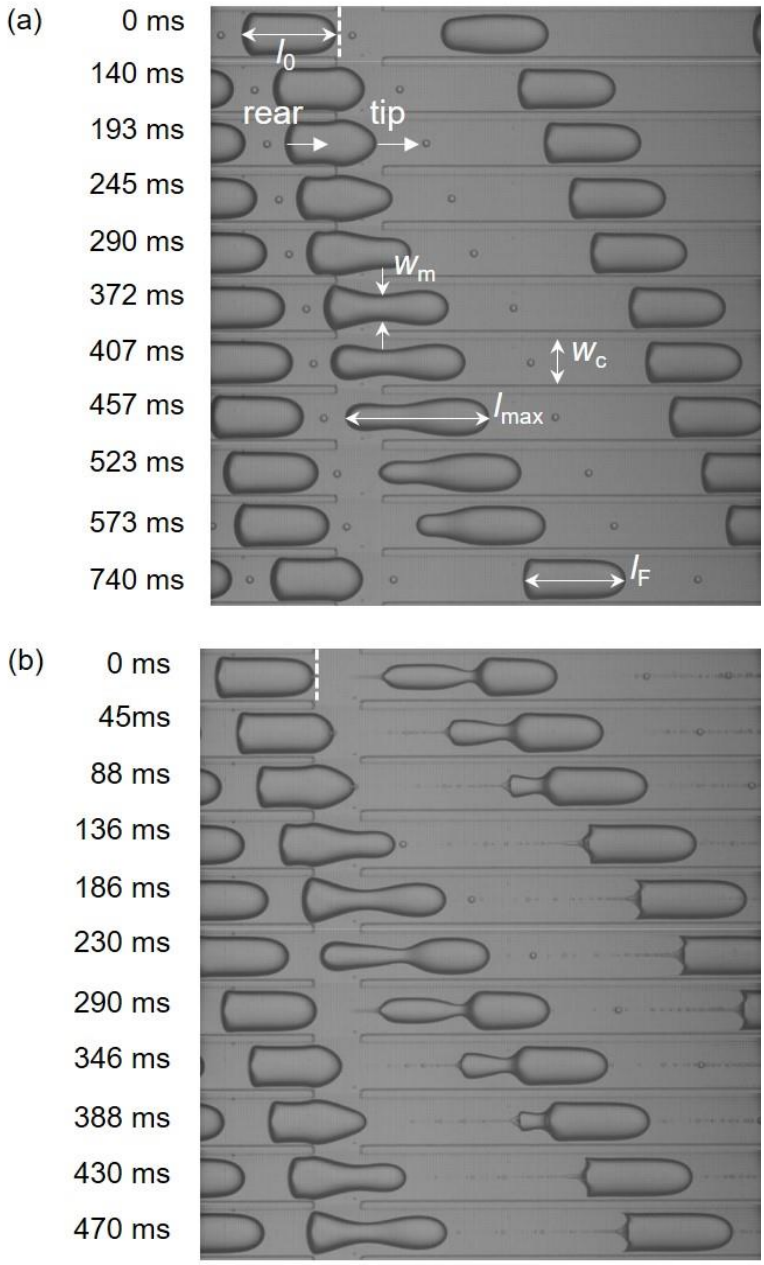


Fig. 4-4 Sequence for the two regimes of the droplet stretch-rebound in a whole cycle. (a) Stretch-rebound without tail (regime I): M_w = 1×10^6 g·mol^{-1}, c/c^* = 0.5, Ec = 0.46, Q_1 = 0.5 mL·h^{-1}, Q_2 = 0.5 mL·h^{-1}, Q_3 = 1 mL·h^{-1}; (b) Stretch-rebound with tails (regime II): M_w = 3×10^5 g·mol^{-1}, c/c^* = 0.5, Ec = 0.058, Q_1 = 1 mL·h^{-1}, Q_2 = 1 mL·h^{-1}, Q_3 = 2 mL·h^{-1}. t = 0 is defined as the moment when the tip of droplet moves to the upstream wall where L3 flows into the flow-focusing junction. l_0, l_{max} and l_F represent the initial length, maximum length and final length of droplet, respectively. w_m and w_c represents the minimum width of the droplet neck and the width of the channel, respectively.

The interfacial evolution during the droplet stretch-rebound could be divided into three stages of moving, stretching and rebound. When the tip of the droplet entered the flow-focusing junction, the continuous phase L3 squeezed the droplet to deform through the conversion of kinetic energy (inertia) to orthogonal pressure. The droplet continued to move towards the downstream. Then the droplet deformed and became stretched when the continuous phase L3 accumulated enough energy to squeeze the droplet. It came to the stretching stage with increasing droplet length and decreasing width of the droplet neck. It moved on to the rebound stage after the droplet was stretched to its maximum length. The droplet length decreased and the neck width increased until the deformation of the droplet was completely restored and recovered to the original shape.

The evolutions of the velocities for the droplet tip and rear as well as the droplet length in a stretch-rebound cycle were investigated, as shown in Fig. 4-5. The initial velocities of the droplet tip and rear u_0 equaled to the apparent velocity of the droplet J_0 when the droplet tip just reached the second flow-focusing junction. The velocity of the droplet tip increased rapidly when it entered the flow-focusing junction and squeezed by the continuous phase L3. While the rear of the droplet was still in the upstream of the flow-focusing junction and its velocity remained the same. The droplet was stretched at this stage and the droplet length gradually increased. As soon as the droplet rear arrived at the flow-focusing junction, the velocity of the droplet rear increased sharply under the squeezing effect of the continuous phase L3. The droplet length reached its maximum when the velocity of the droplet rear equaled to that of the droplet tip. The droplet began to rebound as the velocity of the droplet rear continued to increase and became faster than that of the droplet tip. The droplet length gradually decreased and reached the plateau until the velocities of both the droplet tip and rear equaled to the final value of u_F.

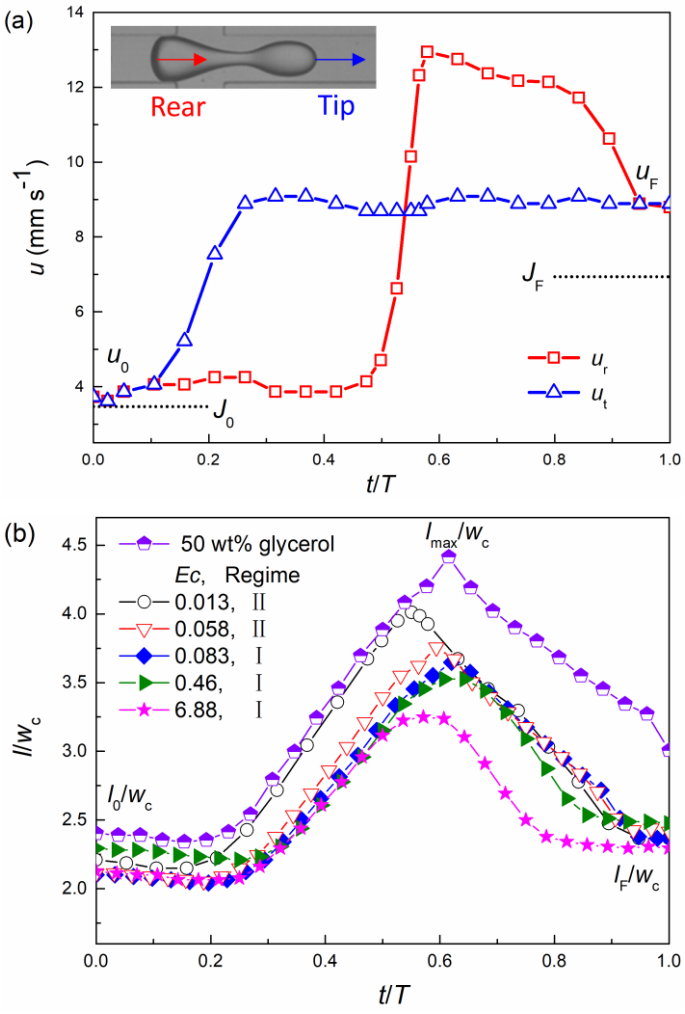


Fig. 4-5 (a) Evolution of the velocities for the tip and rear of the droplet in a droplet stretch-rebound cycle; (b) Evolution of the dimensionless droplet length in a cycle, M_w = 3×10^5 g·mol^{-1}, c/c^* = 0.5, Ec = 0.058, Q_1 = 1 mL·h^{-1}, Q_2 = 1 mL·h^{-1}, Q_3 = 3 mL·h^{-1}.

For the dispersed phase with various elasticities, the variation of the dimensionless maximum length of droplet l_{max}/l_0 with χCa_3 in regime I and regime II is shown in Fig. 4-6. Here, χ represents the ratio between the terminal velocity to the initial velocity. Since the viscous force tends to deform the droplets while the interfacial tension could resist the droplet stretching, the capillary number of the second continuous phase Ca_3 should also be considered as an affecting factor on l_{max}/l_0. For the low-elasticity fluids ($Ec \leq 0.083$), the peak value of the maximum droplet length could reach 2.2 times of the initial droplet length l_0. It transformed into the stretch-breakup regime when l_{max}/l_0 was larger than 2.2. For the fluids of high elasticities ($0.35 \leq Ec \leq 6.88$), the droplet would continue to stretch instead of breakup

after being stretched to $2.2l_0$. It could reach $l_{max}/l_0 = 9$ within the experimental conditions in our works. The power-law relationship between l_{max}/l_0 and χCa_3 could be expressed as Eq. 4-2:

$$\begin{cases} l_{max}/l_0 = 7.63(\chi Ca_3)^{0.30} & Ec \le 0.083 \\ l_{max}/l_0 = 33.94(\chi Ca_3)^{0.68} & 0.35 \le Ec \le 6.88 \end{cases} \quad (4\text{-}2)$$

Previous works by Cubaud [79] focused on the stretching and breakup of highly-viscous droplets in the microfluidic flow-focusing junction. The linear predicting correlation on the dimensionless maximum length of the droplet was established as $l_{max}/l_0 = 1+17.7\chi Ca_3$. The comparison between the correlations in the present work and the literature is shown in Fig. 4-6. It was found that little difference between the dimensionless maximum lengths of droplets corresponding to the two correlations was observed when the flow rate of the continuous phase L3 was small. As the flow rate of the continuous phase L3 increased, the deviations between the two predicting correlations gradually increased, indicating stronger elasticity of the dispersed fluid.

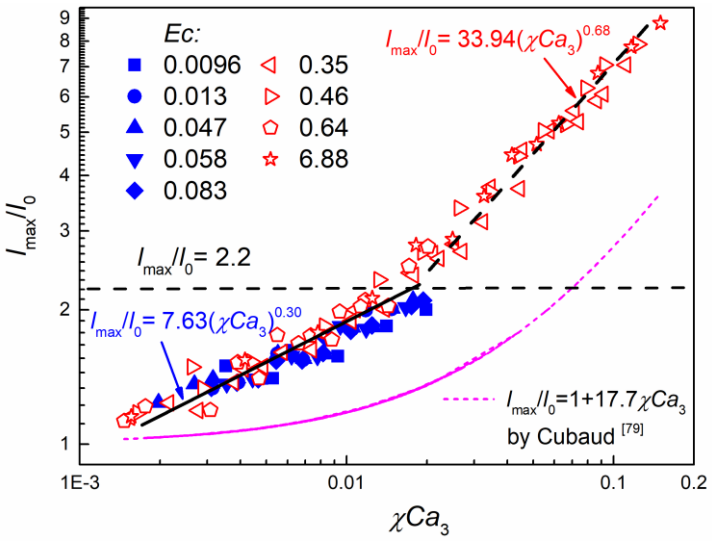


Fig. 4-6 Variation of the dimensionless maximum length of the droplet in regime I and II. Dotted curve: the predicting correlation $l_{max}/l_0 = 1+17.7\chi Ca_3$ proposed by Cubaud [79].

The droplet deformation in the radial direction of the microchannel was reflected in the minimum width of the droplet neck. The minimum width of the droplet neck in a cycle with or without the emergence of the tails at the droplet rear was investigated,

as shown in Fig. 4-7. It was found that the trends were similar between the two regimes in the moving and stretching stages. The difference is reflected in the rebound stage: (1) In regime I without a tail, the droplet appeared as a bowling ball with a smooth interface at the droplet rear. The minimum width of the droplet neck gradually increased until the droplet returned to its original shape. (2) In regime II with tails, the interface at the rear of the droplet shrank under the drag of the tail. The minimum width of the droplet neck kept almost unchanged and the droplet length decreased in the rebound stage.

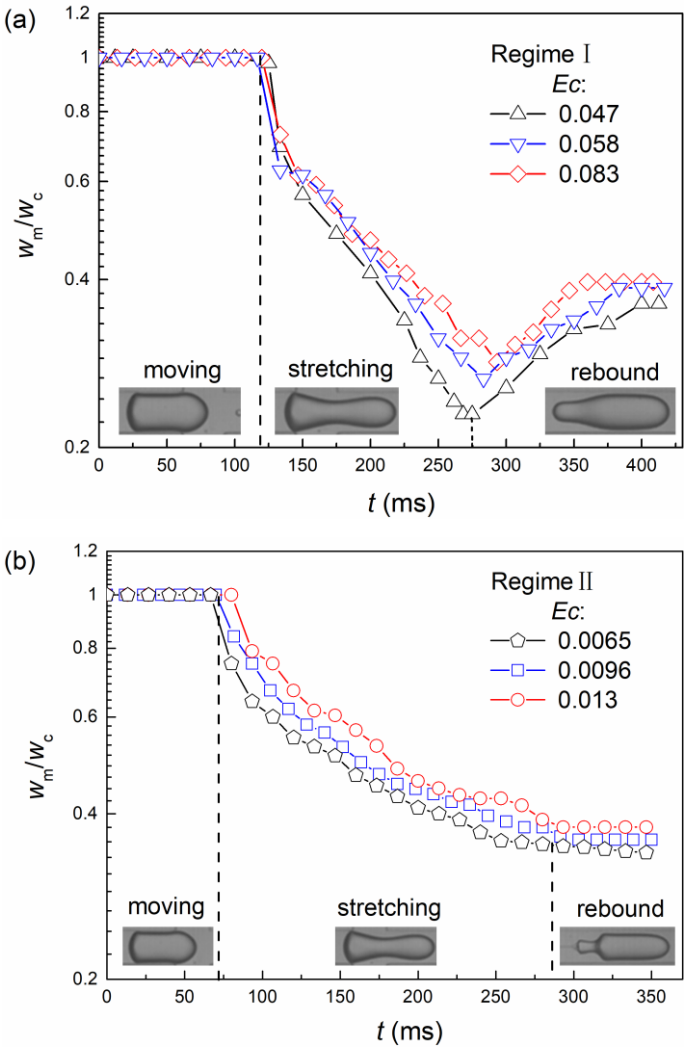


Fig. 4-7 Evolution of the dimensionless minimum width of the droplet neck in the two regimes of droplet stretch-rebound. Q_1 = 1 mL·h^{-1}, Q_2 = 1 mL·h^{-1}, Q_3 = 2 mL·h^{-1}. (a) Stretch-rebound without tail (regime I): (b) Stretch-rebound with tails (regime II).

4.3.3 Dynamics of the droplet stretch-breakup

Taking the droplet breakup into two daughter droplets as an example, the shape and size evolutions of the droplet stretch-breakup in regime III were investigated. The daughter droplet in the downstream was defined as the "daughter droplet 1" while the other in the upstream was named as the "daughter droplet 2", as shown in Fig. 4-8. Compared with the stretch-rebound regime, the interfacial evolution in the stretch-breakup regime was almost the same in the first two stages of moving and stretching. Here, the continuous phase L3 could accumulate more pressure stemming from the kinetic energy to squeeze and stretch the droplets due to its high flow rates in this regime. In the late stretching stage, a thin thread formed, connecting the bullet-shaped "daughter droplet 1" and the spoon-liked "daughter droplet 2". Then the thread was ruptured under the elastic flow instabilities [260]. The daughter droplets formed as soon as the mother droplet ruptured, this moment was defined as the breakup time of the droplet t_b. The "daughter droplet 1" moved towards the downstream and maintained a steady shape like a bullet. While the "daughter droplet 2" went through the final rebound stage and deformed in both the axial and radial directions towards eventually stable shapes. The rebound was reflected in the decreasing droplet length and the expanding width of the droplet neck.

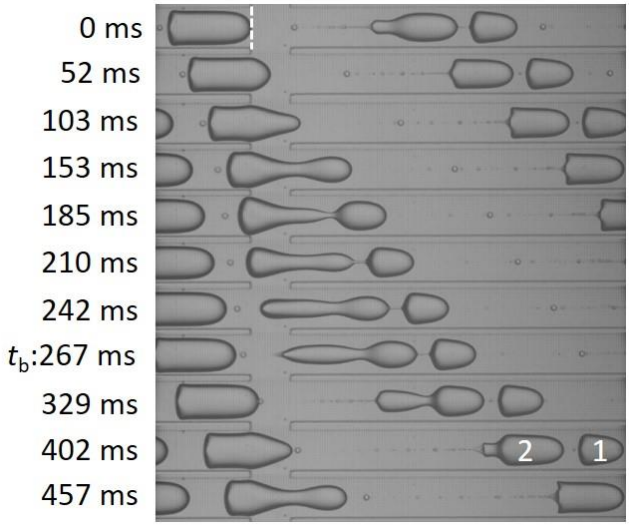


Fig. 4-8 Evolution of droplet stretch-breakup (regime III) for elastic droplets in a flow-focusing junction. M_w = 3×10^5 g·mol^{-1}, c/c^* = 0.5, Ec = 0.058, Q_1 = 1 mL·h^{-1}, Q_2 = 1 mL·h^{-1}, Q_3 = 3 mL·h^{-1}. t_b represents the breakup time of the droplet.

The variation of the dimensionless length for the mother droplet and two daughter droplets in a droplet breakup cycle was plotted in Fig. 4-9(a). The results showed that the size of the mother droplet was less affected by the fluid elasticity. The size ratio between the two daughter droplets $\kappa = l_2 / l_1$ from the breakup time of the droplet t_b was illustrated in Fig. 4-9(b). Obviously, the size ratio decreased with time until the "daughter droplet 2" reached a steady shape at the end of a cycle. For the droplets of various elasticities, the size ratio was smaller with larger elasto-capillary numbers. This was consistent with the results shown in Fig. 4-5(b), where the droplet elasticity showed a negative effect on the maximum droplet length and proved the inhibition on the stretching.

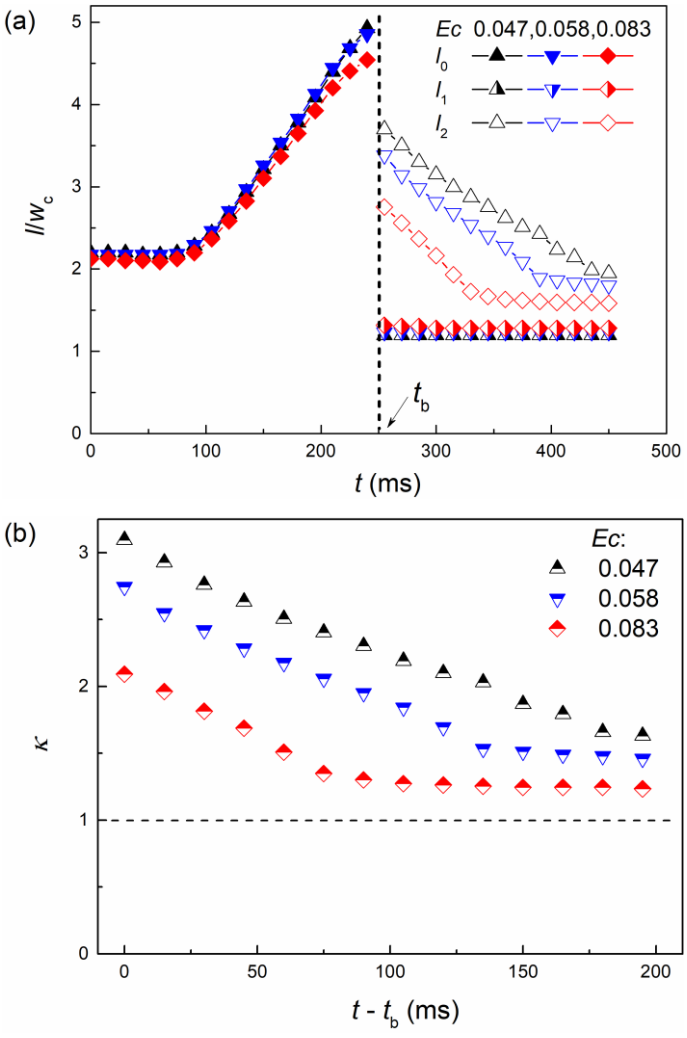


Fig. 4-9 Evolution of the droplet length in a cycle in the stretch-breakup regime. M_w = 3×10^5 g·mol^{-1}, c/c^* = 0.5, Ec = 0.058, Q_1 = 1 mL·h^{-1}, Q_2 = 1 mL·h^{-1}, Q_3 = 3 mL·h^{-1}. (a) Variation of the dimensionless droplet length. (b) Variation of the size ratio between two daughter droplets.

4.4 Summary

The stretching and breakup of elastic droplets in a microfluidic device with two consecutive flow-focusing junctions were studied in this chapter. Three typical regimes involving the stretch-rebound without tail, the stretch-rebound with tails and the stretch-breakup were observed. The phase diagram was plotted based on the drop elasticity and the operating conditions. The predicting correlations for the maximum droplet length in the two stretch-rebound regimes were proposed. The stretch-rebound regime underwent the stretch-breakup regime when the maximum length of the droplet was larger than 2.2 times of its initial length. Also, the size ratio between two daughter droplets in the stretch-breakup regime decreased with the drop elasticity.

In Chapter 3 and Chapter 4, the liquid-liquid flow and droplet behavior were investigated in microfluidic devices with the cross sections of hundreds of micrometers. The droplet formation dynamics, deformation, and breakup were significantly affected by the space confinement in the microchannel. The complex triple line contact between liquid, liquid and channel's wall remains an open problem. In the following chapters, the length scale of drops is voluntarily extended and varies from several hundreds of micrometers to millimeters. The emphasis will be given on the unconfined drop slow impact followed by coalescence on a flat liquid or spreading on a solid surface. Even drops of millimeters are employed, the characteristic length of drop coalescence or spreading will be drastically reduced to several micrometers along with the typical time scale of microsecond as ultrafast phenomena are involved.

Chapter 5 Initial coalescence of an aqueous drop at a planar liquid surface

In the present chapter, an ultra-high-speed DC electrical device with an acquisition interval of 0.8 μs along with a high-speed camera and a high-speed micro-PIV with a frequency of 3000 velocity fields per second were utilized for the first time to have a deeper understanding of the dynamics for the initial coalescence of a pendant drop at a planar liquid surface. Unlike the individual drops for drop impact, it is worth emphasizing the choice of a pendant drop in the present study, which is motivated by either the DC electrical device or a better monitoring of the initial coalescence stage. The working liquids are extended from the Newtonian liquids to the highly viscous non-Newtonian liquids with the zero-shear viscosities varying by nearly five orders of magnitude.

5.1 Introduction

Drop/bubble coalescence is of both academic and industrial interest and plays a major role in numerous applications including foams, emulsions, oil recovery and falling raindrops in a pool [136, 261]. From the physical point of view, a drop may bounce, coalesce or splash at liquid interface according to its initial impact velocity [96, 97, 102] when impinging with a bath of the same liquid. The coalescence of a drop into a pool of liquid can be either instant or delayed [118], complete or partial [112, 120] and affected by various factors including the fluid density [113], surface tension gradient [117], surfactant [115], thermal effect [118] and air pressure [98].

The short dynamics for the drop coalescence in the first few microseconds has never been fully understood. In recent decades, many researchers have focused on this scientific issue. Drop coalescence could be observed at a planar liquid-liquid [111-113, 115] or air-liquid interface [98, 102, 117, 118, 140]. In addition, the coalescence of two separate drops was also extensively investigated, either between spreading drops on a substrate [122, 125, 126] or two drops of identical liquid or different miscible liquids [116, 123]: the meniscus bridge between two drops evolves as a self-similar shape, where the

width for the meniscus bridge increases much faster than its height and could be scaled as a power-law with an exponent of 1/2 [136, 137]. It's generally acknowledged that the drop coalescence has two typical regimes referred to as the viscous [136] and the inertial regime [136, 137], where the coalescing width W and time t are rescaled as $\Phi = W / D_{\max}$ and $\tau = t / t_{\mathrm{i}}$ by the maximum drop width $D_{\max}$ and the inertial time t_{i} ($t_{\mathrm{i}} = \sqrt{\rho D_{\max}^3 / \gamma}$, where ρ is the liquid density and γ the surface tension) and follow $\Phi \sim \tau \ln \tau$ and $\Phi \sim \tau^{1/2}$, respectively. Then an inertially limited viscous (ILV) regime $\Phi \sim \tau$ was identified for the coalescence of two drops, based on the scaling consideration between the inertia and viscous forces [123, 138, 139].

Previous studies on drop coalescence were mainly conducted experimentally by a visualized high-speed camera (from the side view or both side and bottom view) with a minimum interval of about 0.01 ms, which is far from sufficient to study the fast dynamics of very initial contact within a typical length of 100 μm. To overcome the limitations of both the capturing rate and spatial resolution, innovative approaches including the AC electrical measurement system [132-134] and ultrafast X-ray phase-contrast imaging technique [135] were introduced to probe the coalescence between two liquid drops of equal size. Besides, numerical simulation [120, 125, 140, 141] was also conducted to gain insight into the initial coalescence which cannot be accessible by experiments. Recently, molecular dynamics simulations were performed and revealed the coalescence of nanodroplets could expand to less than 10 nm within 56 ps in a so-called thermal regime close to the molecular scale [141].

5.2 Experimental section

A schematic diagram of the experimental setup is displayed in Fig. 5-1. A transparent polymethyl methacrylate (PMMA) tank of square section (40 mm × 40 mm) was placed under a stainless steel nozzle (inner and outside diameter of 0.6 mm and 0.97 mm, respectively). A pendant drop of the identical liquid in the tank was generated at the nozzle through a syringe pump (PHD 2000, Harvard Apparatus, USA) at the flow rate ranging from 0.02 to 0.1 mL·min^{-1}, corresponding to an approaching velocity of 0.06 mm·s^{-1} to 0.29 mm·s^{-1} towards the planar liquid surface. For all experimental liquids, the vertical distance between the nozzle and liquid surface is kept constant as 3.81 ± 0.14 mm to ensure the contact of the drop with the planar

liquid surface takes place before significant neck thinning until breakup. To push both the spatial and temporary limits further, a DC electrical circuit was developed in this work based on an improved Howland current source [215]. The main feature of the DC circuit is shown in the inset of Fig. 5-1: one electrode is connected to the metallic nozzle and the other immersed in the liquid at the tank bottom, so that a coalescing liquid drop serves as a load resistance R in the circuit. The DC electrical voltage $U(t)$ of drop-liquid interface connection was acquired at a frequency of 1.25×10^6 Hz by a self-developed acquisition system. By carefully calibrating the voltage to a wide range of standard resistance from 0 to 800 kΩ, the very initial stage of a coalescing drop with the planar liquid surface was monitored through the drop resistance reflecting the coalescing area $R(t)$. To have a superimposed transition with the above electrical system and beyond, coalescence sequences were recorded by a high-speed camera Phantom V711 (Vision Research, USA) equipped with a macro lens (EF 100mm f/2.8, Canon, Japan) from the side view. 84054 frames per second (fps) at an image resolution of 240 × 240 pixels is a compromise between the spatial and temporary resolutions. All the voltage data and images obtained were analyzed through self-programmed MATLAB algorithms.

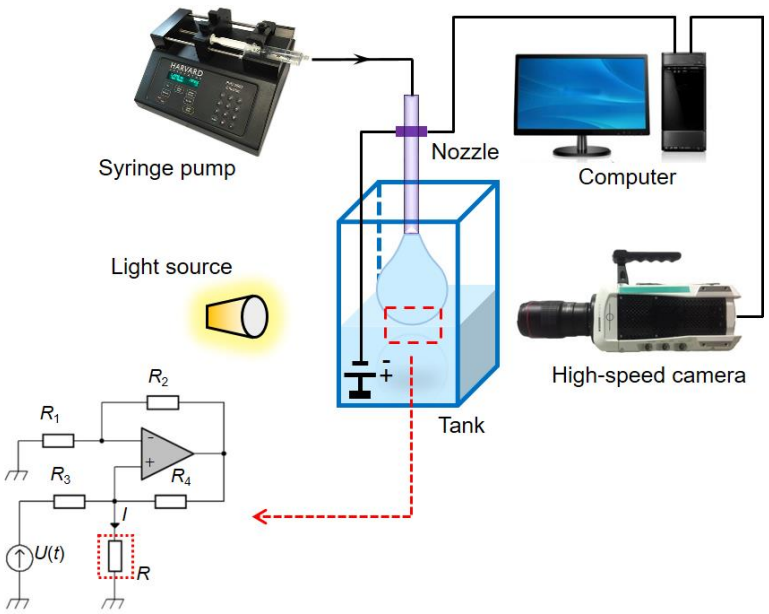


Fig. 5-1 Schematic diagram of the experimental setup. The inset shows the main feature of the DC Howland current source for the ultra-high-speed electrical resistance measurements. The coalescing liquid drop serves as a load resistance R in the circuit.

A high-speed micro-PIV technique was employed to follow the flow field during the initial coalescence both in the drop and the liquid surface. A small amount of silver coated hollow glass spheres (S-HGS-10, Dantec Dynamics, Denmark) with an average diameter of 10 μm or fluorescence particles (MF-RhB-Partikel-G020, Dantec Dynamics, Denmark) with a diameter of 1-20 μm were added in aqueous Newtonian and non-Newtonian fluids. Two lasers (LaserMax Inc., USA) of 1 mW were placed in the opposite direction to excite seeding particles in the laser sheet located inside the pendant drop and liquid pool. The images were captured by the high-speed camera Phantom V711 coupled with a zoom lens (MP-E 65mm f/2.8, Canon, Japan) up to 3000 fps. The flow fields were computed by the software DynamicStudio (Dantec Dynamics, Denmark).

Seven different liquids were employed in the experiments, including distilled water, 2 wt% carboxymethyl cellulose sodium (high viscosity CMC of molecular weight 7×10^4 $g\cdot mol^{-1}$) solution, 1 wt% polyethylene oxide (medium and high molecular weights of 1×10^6 and 5×10^6 $g\cdot mol^{-1}$, represented by MM and HM PEO, respectively) solutions and 0.5 wt%, 2.0 wt% polyacrylamide (PAAm of molecular weight 1.3×10^7 $g\cdot mol^{-1}$) solutions. The electrical conductivity of polymer solutions was too weak to ensure sensible measurements, e.g. 1.125 $mS\cdot cm^{-1}$ only for 0.5 wt% PAAm solution. 5 wt% or 10 wt% NaCl was added to strengthen the electrical conductivity of these liquids and to improve the sensibility of electrical signals. The addition of salt decreases often the viscosity of aqueous polymer solutions due to ionic forces toward a critical salt concentration of about 5 wt%, above which the viscosity of salt-added polymer solution no longer decreases significantly. The rheological properties of all the non-Newtonian fluids were characterized by a rheometer (AR-G2, TA Instruments, USA). In order to display the effect of salt addition on the liquid viscosity, the rheological curves of the non-Newtonian fluids with and without salt addition were gathered in Fig. 5-2(a) to demonstrate the effect of the salt addition. The rheological properties presented in Fig. 5-2(b) correspond to the salt-added polymer solutions effectively employed in our experiments. Viscous Newtonian fluids of 20 wt% Emkarox solution and 47.5 wt% glycerol solution were also tested, the results did not reveal a noticeable difference compared with the non-Newtonian fluids. The initial contact followed by the coalescence takes place as soon the drop touches the liquid surface and ends in several milliseconds, the

zero-shear viscosity at small shear rate was used in the present work for the non-Newtonian fluids used. The properties of the liquids used are gathered in Table 5-1. Our dynamic tensiometer Tracker (IT Concept, France) based on the bubble pressure method cannot yet allow the measurements of the dynamic surface tension at the time scale of the initial coalescence within 0.2 ms.

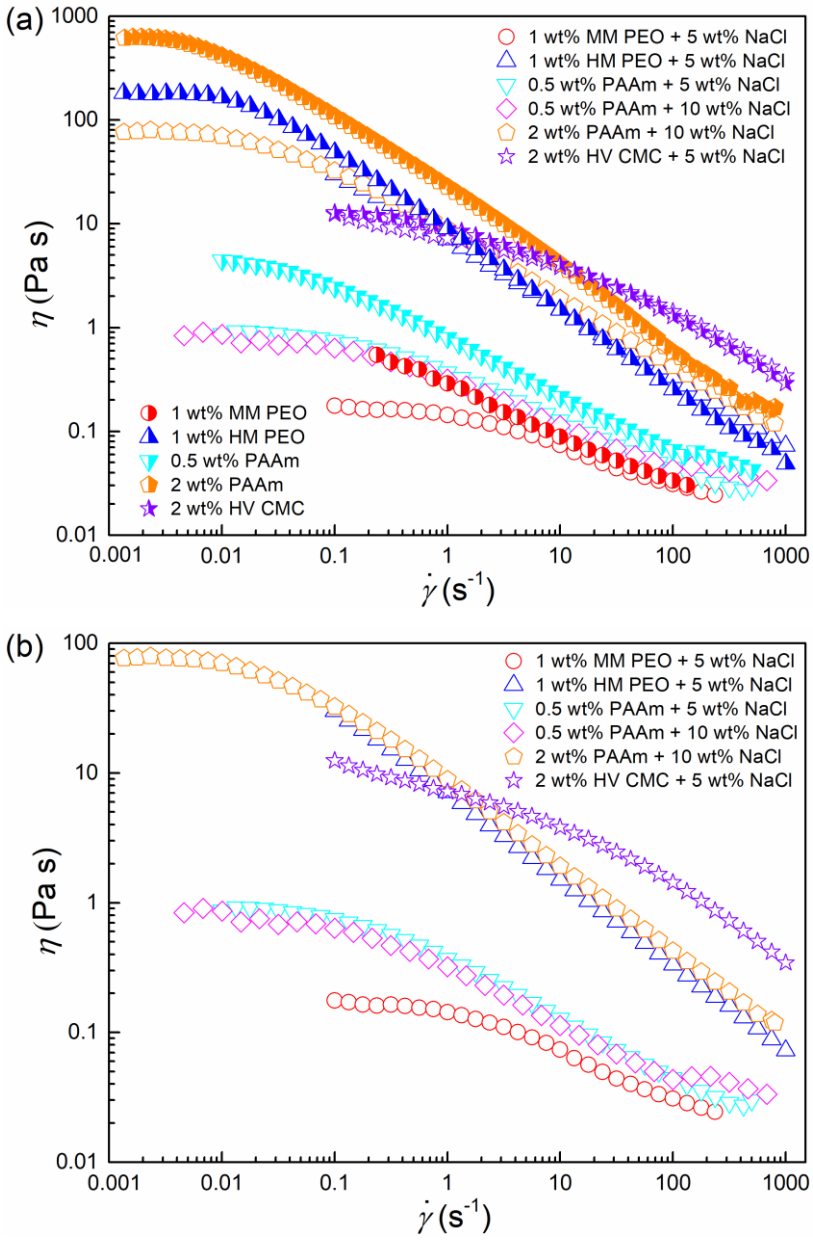


Fig. 5-2 (a) Comparison of the rheological properties between the non-Newtonian fluids with and without salt addition. (b) Rheological properties of the salt-added non-Newtonian fluids effectively employed in our experiments.

Table 5-1 Properties of the liquids used.

Liquids	ρ (kg·m^{-3})	γ (mN·m^{-1})	η_0 (Pa·s)	σ (mS·cm^{-1})
Water + 5 wt% NaCl	1034	72.00	0.001	95.8
1 wt% MM PEO + 5 wt% NaCl	1064	61.00	0.177	63.9
1 wt% HM PEO + 5 wt% NaCl	1064	60.00	29.96	76.3
0.5 wt% PAAm + 5 wt% NaCl	1058	69.30	0.870	82.2
0.5 wt% PAAm + 10 wt% NaCl	1117	69.30	0.837	153.4
2 wt% PAAm + 10 wt% NaCl	1136	66.20	77.44	144.7
2 wt% HV CMC + 5 wt% NaCl	1075	66.00	12.43	101.3

5.3 Results and discussion

Sequences for the initial coalescence of pendant drops at liquid surface are illustrated in Fig. 5-3. The electrical device and high-speed camera are synchronized and time zero t = 0 ms is defined when the first decreasing point of electrical resistance is detected. Taking 0.5 wt% PAAm solution with 10 wt% NaCl as an example [Fig. 5-3(a)], the drop coalesces and spreads spontaneously as soon it touched the liquid surface. In a very short interval, the gas film between the drop and liquid surface is evacuated to induce the coalescence. According to the images at t = 0.25 ms and t = 0.50 ms, the coalescing width W at the liquid interface increases from 0.84 mm to 1.18 mm in 0.25 ms while the upper part of the drop displays very few deformation. Successively, the bottom part of the drop evolves quickly with an increasing coalescing section. Within 1.00 ms, the contour of the drop shape resembles a vase where the width in the middle part exhibits much larger than those at both the nozzle outlet and the coalescing section. Here “the middle part” refers to the section where the vertical distance below the nozzle outlet equals to half the distance between the nozzle outlet and the liquid surface, which is 1.97 ± 0.07 mm below the nozzle outlet. The electrical resistance is mainly located in the narrowest coalescing zone. As the drop continues to coalesce with the bulk liquid, the coalescing section becomes much wider than the middle of drop (t = 7.50 ms) and evolves as a cylinder until the final breakup (t = 110.00 ms). As shown for water with 5 wt% NaCl [Fig.

5-3(f)], there is no noticeable difference compared with 0.5 wt% PAAm solution during the initial coalescence. Certainly, the pinch-off until breakup depends significantly on the liquid nature: the water neck would rupture immediately at t = 18.98 ms instead of a longer elongation of three orders of magnitude in 2 wt% PAAm solution due to the high viscoelasticity.

The flow field in the drop and liquid surface during the initial coalescence is quite similar regardless of the liquids used in this work. A sequence is illustrated in Fig. 5-4 for 2 wt% PAAm. As soon as the pendant drop coalesces with the planar liquid surface, the release of surface energy stems from the Laplace disjunction pressure due to the local curvature evolution to accelerate both the axial and radial velocities as revealed by the PIV technique shown in Fig. 5-4(a). The progressive decrease of the velocity magnitude with time in Fig. 5-4(b) and 4-4(c) reveals that the transformation of surface energy to kinetic energy is more pronounced at the beginning of the coalescence. When the coalescing section broadens, radial velocity develops at the base of the drop and the axial velocity inflects to form a vortex in the corner as the drop gradually shrinks, as shown in Fig. 5-4(b). The flow field in Fig. 5-4(c) describes an axial velocity in the drop driven both by the pinch-off and liquid feed and a radial velocity at the coalescing zone. The main difference in much less viscous water resides in certain damping after the coalescence due to low drag. However, the magnitude of these apparent velocities was too close to the accuracy of the PIV technique to be determined. The inevitable sedimentation of seeding particles makes also experimental measurements more delicate in water.

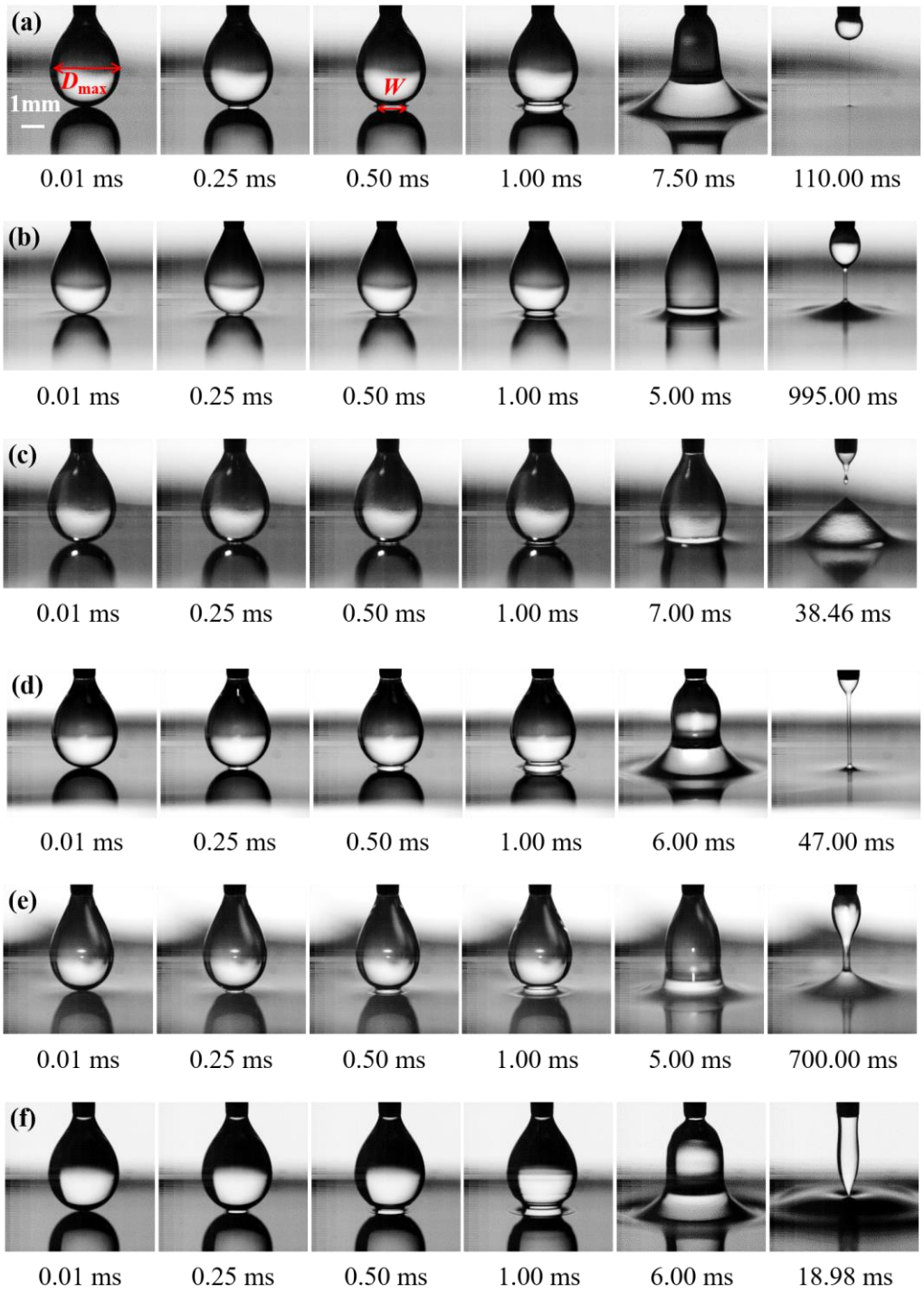


Fig. 5-3 Sequence for initial coalescence of a pendant drop at planar liquid surface. v_0 = 0.29 mm·s^{-1}. (a) 0.5 wt% PAAm with 10 wt% NaCl. (b) 2 wt% PAAm with 10 wt% NaCl. (c) 2 wt% HV CMC with 5 wt% NaCl. (d) 1 wt% MM PEO with 5 wt% NaCl. (e) 1 wt% HM PEO with 5 wt% NaCl. (f) Water with 5 wt% NaCl. D_{max} and W represent the maximum drop width at initial coalescence and the coalescing width, respectively. The scale bar indicates 1 mm.

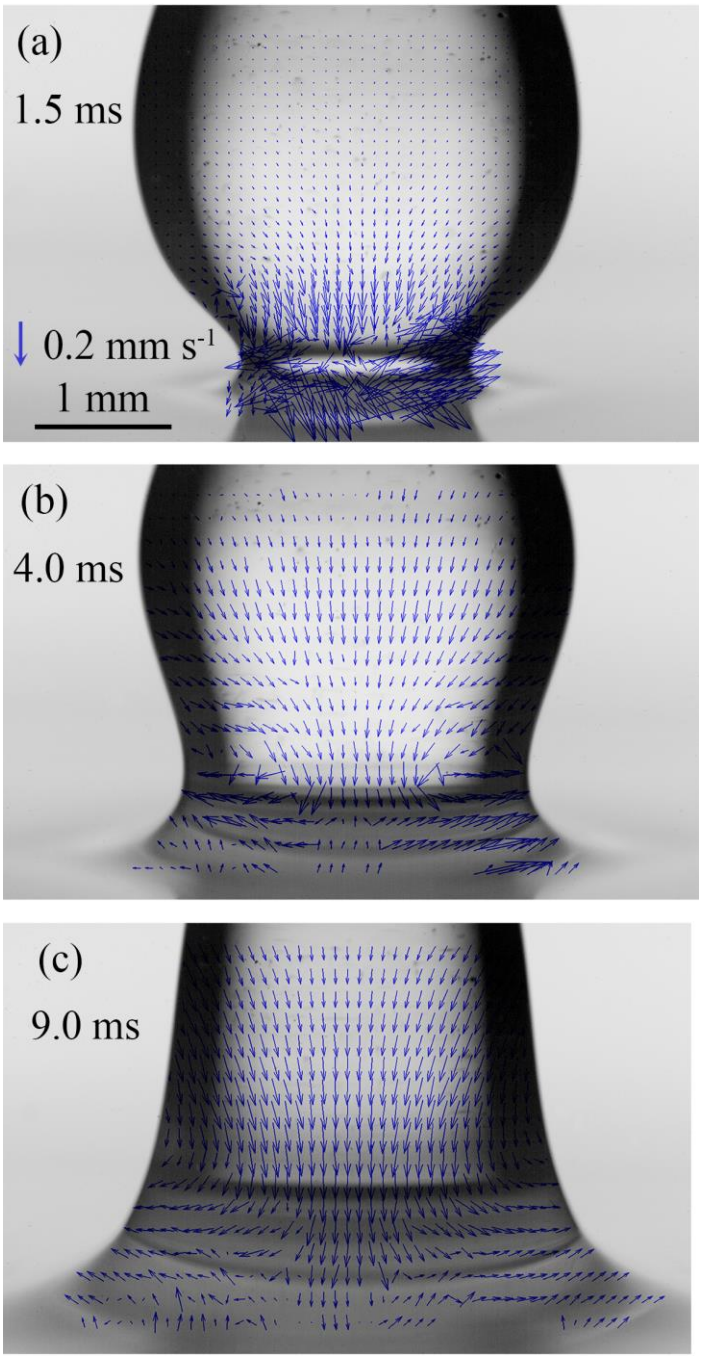


Fig. 5-4 Velocity fields in the drop and liquid surface during the initial coalescence. 2 wt% PAAm solution with 10 wt% NaCl. v_0 = 0.29 mm·s^{-1}. The scale bars for length and velocity indicate 1 mm and 0.2 mm·s^{-1}, respectively.

The variation of the electrical resistance R with time during the initial coalescence is shown in Fig. 5-5(a). This resistance decreases drastically in relation to the contact area between the drop and the bulk liquid. In only 0.1 ms, the resistance reduces by nearly two orders of magnitude from 578173 Ω to a minimum value of

about 8930 Ω, 13764 Ω and 11880 Ω respectively for water, PEO and PAAm solutions, as shown in Fig. 5-5(b). Then with the thinning of the neck, the resistance increases slowly until the maximum which corresponds to the breakup of the drop. Due to the elasticity of PEO and PAAm solutions, the drop neck would be elongated thus the whole period is much longer than water and CMC solution. Furthermore, we found that the coalescence of drops is much faster than the final pinch-off, which aroused our interest in taking a deep insight into the dynamics of initial coalescence.

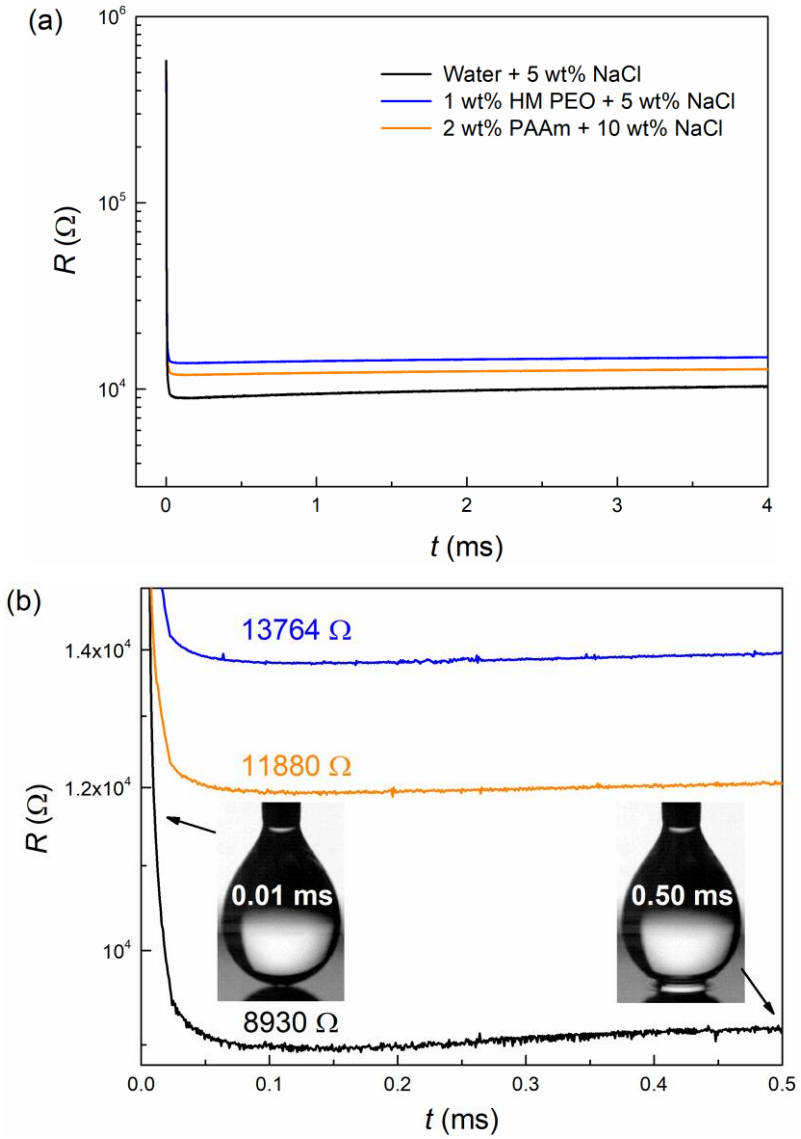


Fig. 5-5 (a)Variation of the electrical resistance during the initial coalescence of a drop at planar liquid surface within 4 ms. v_0 = 0.29 mm·s^{-1}. (b) Scale up of the minimum drop resistance within 0.5 ms.

The close up of the dynamics of initial coalescence from both electrical signals and visualized images are illustrated in Fig. 5-6(a). The drop conductance *G* is nothing but the reverse of the resistance: $G = 1/R = \sigma \iint_S \boldsymbol{E} \cdot d\boldsymbol{S} \,/\, \int_A^B \boldsymbol{E} \cdot d\boldsymbol{l}$ that depends mainly on the minimum section along the falling drop where the motion of ions is largely obstructed, either at the drop coalescing section *S* in contact with the planar surface or neck. For a fixed height *l* between the nozzle *A* and the planar liquid surface *B*, an integration by the electrostatic software GetDP reveals that the dominant conductance *G* is located in the coalescing section *S* when the latter is less than 2.5% of the minimum liquid section at the outlet of the nozzle in a linear way: $S \sim G$. This leads to the following relationship for the coalescing width: $W \sim G^{1/2}$ when $W \leq 95$ μm that is experimentally corroborated by the high-speed camera. Due to both the enlarging section *S* and the drop shape evolution, the above-mentioned relationship is no longer valid after 7.2 μs as shown by the experimental *G* curve. The drop spreads with time and the neck between the nozzle and the coalescing surface gradually begins to take effect. Then the drop coalescing section increased to larger than the drop neck and the neck width became more and more dominant in the conductance. The neck gradually pinches-off and the conductance started to decrease until the breakup of the drop not shown here.

In our experiments, the electrical conductance related to the drop evolution follows a power-law of with time during the initial coalescence, as illustrated in Fig. 5-6(a). The exponent of different solutions displays a similar trend with $\alpha = 1.98 \pm 0.19$ within 7.2 μs, regardless of the liquid viscosity and drop's approaching velocity. This indicates that the initial coalescence results from the spreading of the aqueous solvent instead of macromolecules, thus the drop conductances are nearly the same despite the zero-shear viscosities vary by nearly five orders of magnitude for all working liquids. This large exponent indicates that once the drop and liquid surface contact, the drop coalescence takes place in a very short time with the coalescing section expanding extremely fast. Then the drop spreads much slower after 7.2 μs. Similarly, the coalescing width also follows a power law of $W \sim t^{\beta}$ with $\beta = 0.58 \pm 0.02$, which is consistent with the exponent 1/2 reported for the coalescence between two drops [138]. It is worth noting the slight difference

between these two coalescence scenarios: curved surface to plate surface in our case and curved surface to curved surface in the case of two drops.

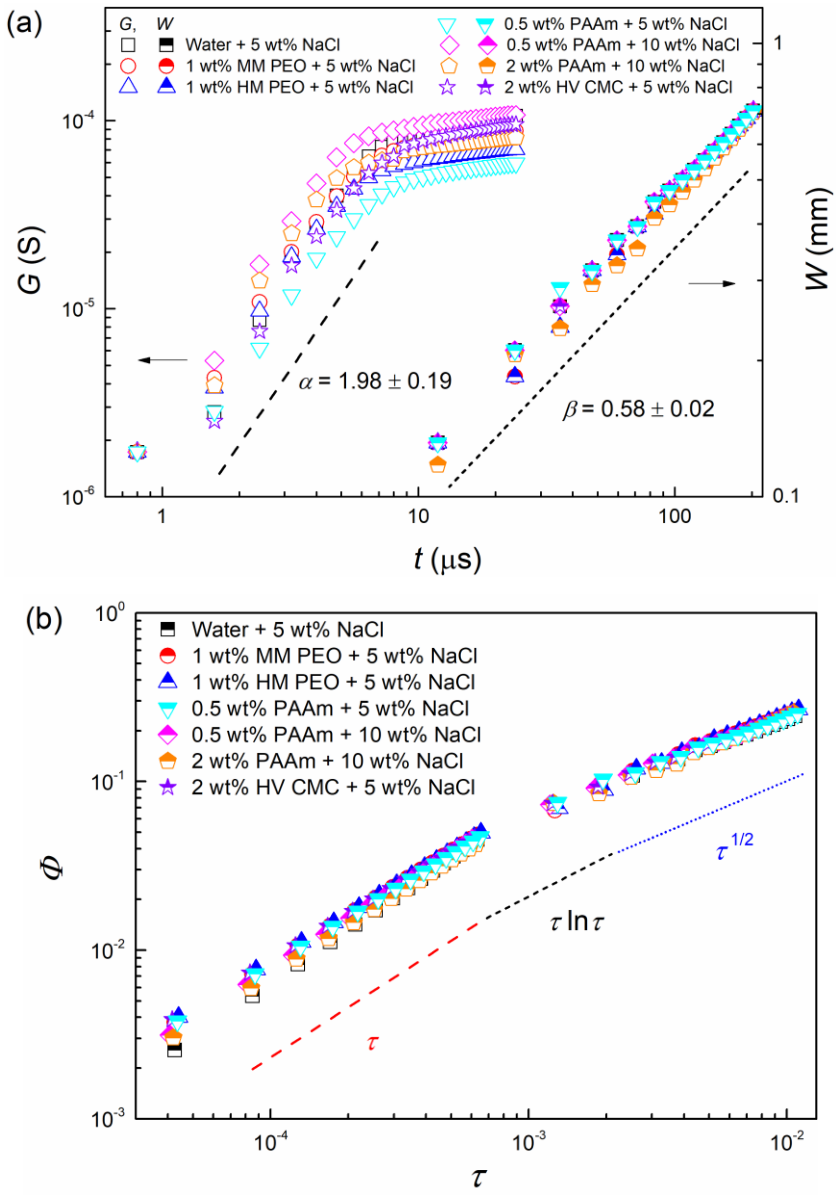


Fig. 5-6 Dynamics of initial coalescence at a planar liquid surface. v_0 = 0.29 mm·s^{-1}. (a) Variation of the drop conductance G (hollow symbols, left Y-axis) and the coalescing width W (half solid symbols, right Y-axis) within 200 μs. (b) Variation of the rescaled coalescing width Φ with the normalized time τ.

To better fitting all curves, we tried to rescale the relationship between the coalescing width and time. For instance, the dimensionless Ohnesorge number

$Oh = \eta_0 / \sqrt{\rho\gamma W}$ representing the ratio of viscous forces to inertial and surface tension forces was introduced to rescale the coalescing width. As shown in Fig. 5-7, the variation of the Ohnesorge numbers for all liquids used are given with time t and the dimensionless viscous time τ_v ($\tau_v = t / t_v$ and $t_v = D_{max}\eta_0 / \gamma$ is the viscous time), respectively. However, the Ohnesorge number of all liquids used within 200 μs failed in gathering all data suitably, as shown in Table 5-2. It is worth noting that after numerous trials, the rescaled coalescing width and the normalized time $\tau = t / t_i$ based on the inertial time could scale all data reasonably.

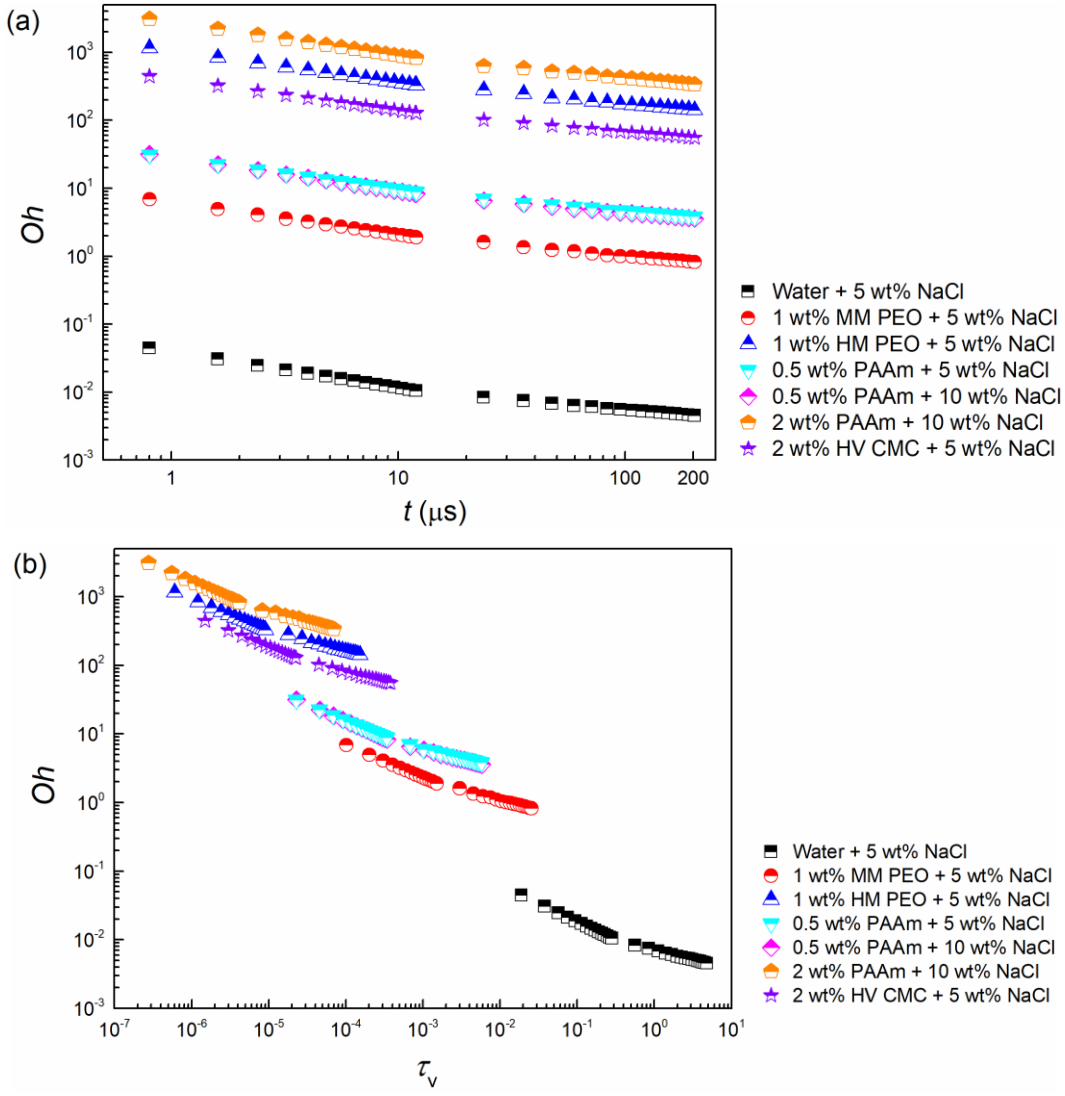


Fig. 5-7 (a) Variation of the Ohnesorge number with time. (b) Variation of the Ohnesorge number with the dimensionless viscous time.

Table 5-2 Ohnesorge numbers of all liquids used within 200 μs.

Liquids	*Oh*	
	t = 0.8 μs	t = 200 μs
Water + 5 wt% NaCl	4.43×10^{-2}	4.54×10^{-3}
1 wt% MM PEO + 5 wt% NaCl	6.86	8.23×10^{-1}
1 wt% HM PEO + 5 wt% NaCl	1.15×10^{3}	1.41×10^{2}
0.5 wt% PAAm + 5 wt% NaCl	3.11×10^{1}	3.81
0.5 wt% PAAm + 10 wt% NaCl	3.16×10^{1}	3.57
2 wt% PAAm + 10 wt% NaCl	3.09×10^{3}	3.36×10^{2}
2 wt% HV CMC + 5 wt% NaCl	4.45×10^{2}	5.54×10^{1}

The temporary evolution of the rescaled coalescing width Φ is gathered in Fig. 5-6(b) for both the electrical approach and high-speed camera visualization with an overlay area ranging from $4.23\times10^{-5} < \tau < 6.30\times10^{-4}$. A quasi-linear relationship $\Phi \sim \tau^{0.99\pm0.09}$ confirms unambiguously the previously reported ILV regime [123, 138, 139]. In this regime, the inertia and viscous force should display a competing role in the coalescence dynamics. The dominant inertia stemming from the surface energy located at a small neck as illustrated by our micro-PIV measurements prevents the coalescence at this stage from being in the viscous Stokes regime, even the latter shows only a delayed flow field due to the limitation of the acquisition rate up to 3000 fps. At 0.8 μs, the coalescing width varies between 7.4 - 11.0 μm for all experimental liquids, reducing an order of magnitude from the minimum optical width through the high-speed camera. It is worth noting that for the PAAm solutions having the highest molecular weight among the liquids used, the radius of gyration measured by the multi-angle light scattering (MALS, Wyatt Technology, USA) is R_g = 101.70 nm under highly diluted conditions, then well below the monitored scale by the electrical device and the high-speed camera. This could explain the absence of the viscous effect induced by macromolecules on the initial coalescence at the scale investigated in this work. In this ILV regime, the logarithmic correction $\Phi \sim \tau \ln \tau$ issued from a full theory [136] is negligible as observed elsewhere [138]. After $\tau = 1.89\times10^{-3}$ the inertial regime arises as $\Phi \sim \tau^{1/2}$, where the viscous force is negligible. Between the ILV and inertial regimes, a transition seems to be emerging as the viscous regime with the above logarithmic correction which is drawn in Fig. 5-6(b) to guide the eye.

However, there are limited data to deepen the role of viscous effect as covered only by the high-speed camera in this zone.

5.4 Summary

In summary, the initial coalescence of a drop with its own bulk liquid surface was jointly investigated by means of three different techniques for a wide range of fluid properties extended to highly viscous non-Newtonian fluids. With a time resolution of 0.8 μs, the ultra-high-speed DC electrical device allowed to monitoring the evolution of the coalescing width down to 7.4 μm within a duration of 10 μs. Afterwards, the high-speed camera took the relay to extend the investigation. The relationship between the rescaled coalescing width Φ by the drop's maximum diameter and the normalized time τ by the inertial time confirms the distinct regimes previously reported for drop-drop configuration: linear in the ILV regime $\Phi \sim \tau$ ($4.23\times10^{-5} < \tau < 6.30\times10^{-4}$); square root in the inertial regime $\Phi \sim \tau^{1/2}$ ($\tau > 1.89\times10^{-3}$); possibly a transient viscous regime in between with a logarithmic correction $\Phi \sim \tau \ln \tau$. The flow fields measured by the micro-PIV reveal the transformation of surface energy to kinetic energy during the fast coalescence, so that the inertia located at the coalescing area of small width, down to 7.4 μm in this work, could be dominant with respect to the viscous force in both the ILV and inertial regimes.

In addition to the initial coalescence of an aqueous drop at a planar surface of the identical liquid in this chapter, the contact and spreading of a drop at a solid surface also deserve deep investigation in the next chapter. Further new effects such as the wetting and triple line contact phenomena could be investigated as additionally interfacial phenomena with respect to the drop coalescence with a bulk liquid.

Chapter 6 Drop impact, spreading and breakup on a solid surface

The initial contact and spreading of both the Newtonian and non-Newtonian pendant drops on a solid surface as well as the filament thinning of the liquid neck were also jointly investigated by the same techniques described in the preceding Chapter. It is worth emphasizing that the velocity fields in the drop during the initial contact and spreading were measured and computed by the high-speed micro-PIV at a frequency up to 5000 velocity fields per second. In the initial spreading stage within 10 μs after contact, the power-law relationship between the spreading radius and time was monitored by the ultrahigh-speed DC electrical device.

6.1 Introduction

The wetting and spreading of liquids on a solid surface is a ubiquitous process in our daily life, such as the raindrop on the windshield, inkjet printing, spray coating, cream application on the skin, pesticide spraying, etc [262-267]. The behavior of drop spreading is closely relevant to the triple line contact dynamics between liquid, air and solid. When a liquid drop deposited on a solid surface, a microscopic precursor film propagates ahead of the drop and then the interfacial force drives drop spreading until it reaches the final equilibrium contact angle [159]. For a completely wetting surface, the initial spreading is mainly dominated by the inertia, while the later spreading is dominated by the viscous force [148, 149]. The initial spreading is faster than the later spreading process [147, 268]. While for partially wetting surfaces such as hydrophobic surfaces for aqueous drops, spreading is usually an integral part of the impact process with some restoring forces [269].

Much effort has been devoted to investigating the effects of liquid properties (density, viscosity and surface tension) and substrate state (material, roughness, wettability and pattern) on the initial contact [163, 270-276]. For low-viscosity liquids, it is well known that the drop spreading radius r grows exponential with time t as $r \sim t^{1/2}$ in the inertial regime [148, 149]; while for high-viscosity drops, the spreading process is dominated by viscous force with an exponent varies from 0.8 at initial contact to 0.1

at final equilibrium during the spreading process [150]. Recently the research emphasis turned to the very initial dynamics of drop spreading on a solid surface. Bird et al. [149] studied the early stage of drop wetting on a solid surface and revealed that the spreading radius followed a power law whose exponent is only dependent on the equilibrium contact angle of the liquids on the surface, i.e. the surface wettability. Chen et al. [273, 277] studied spontaneous spreading of drops on soft, viscoelastic rubber films and further confirmed that the early stage of spreading is also dominated by the inertia and the wetting dynamics mainly depends on the wettability, but not on softness. They derived a similar scaling law with an exponent ranging from 1/5 to 1/2. Recently Mitra et al. [154] studied the drop spreading on a substrate either submitted in water and exposed in the air. They revealed that the drop spreading always began from an initial viscous regime with $r \sim t$, followed by an intermediate inertial regime with $r \sim t^{1/2}$ and a final Tanner's regime with $r \sim t^{1/10}$.

Previous studies were conducted experimentally by the high-speed camera from the side view or both the side and bottom views [150, 154] and simulation approaches [163, 275, 278], but the visualized methods with an interval about 0.01 ms are far from enough to study the fast dynamics of very initial contact at even smaller time scale. Here, we pay particular attention to the initial contact and spreading of both Newtonian and non-Newtonian pendant drops on a solid surface through an ultra-high-speed DC electrical device, a high-speed camera and a high-speed micro-PIV.

6.2 Experimental section

Figure 6-1(a) shows the schematic diagram of the experimental apparatus. The stainless steel nozzle (inner and outer diameter of 0.6 mm and 0.97 mm, respectively) was used to generate pendant drops in ambient air through a syringe pump (PHD 2000, Harvard Apparatus, USA). The flow rates of 0.02 $mL \cdot min^{-1}$ and 0.1 $mL \cdot min^{-1}$ correspond to an approaching velocity of 0.06 $mm \cdot s^{-1}$ and 0.29 $mm \cdot s^{-1}$ towards the plate. A round plate of stainless steel was horizontally placed under the nozzle. For all liquids in our experiments, the vertical distance between the nozzle and metallic surface is relatively small, hence the contact of pendant drops with the metallic surface goes before the occurrence of neck thinning and the neck width keeps constant during the very initial contact process, which is called "contact before necking". The

metallic disk with a diameter of 4 cm and a thickness of 0.4 cm was deeply polished before use.

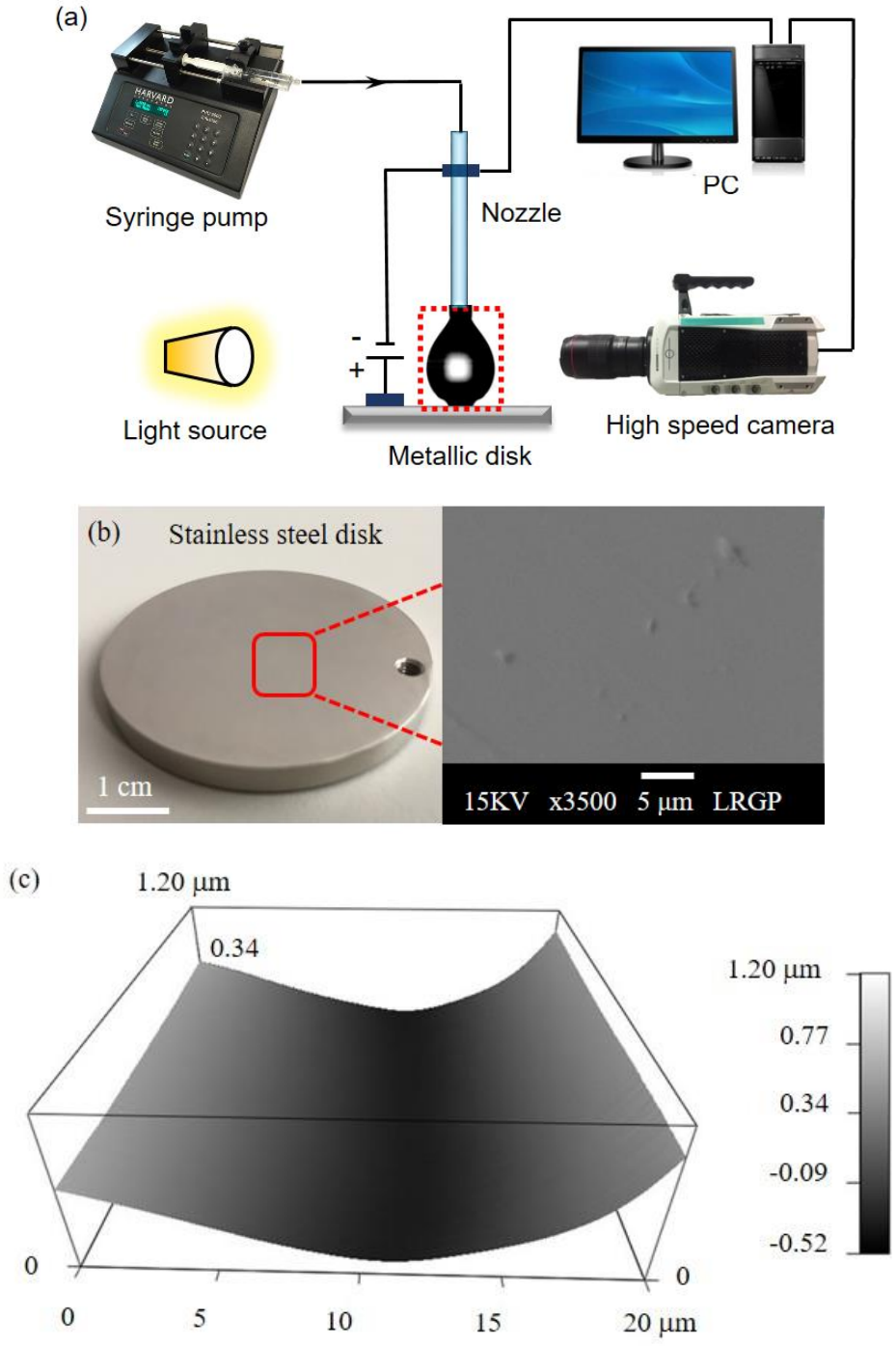


Fig. 6-1 (a) Schematic diagram of the experimental apparatus. (b) SEM image for the surface of the stainless steel plate. (c) AFM result for the surface of the stainless steel plate.

The scanning electron microscope (SEM, JSM-6490LV, JEOL, Japan) and atomic force microscopy (AFM, MFP-3D, Oxford Instruments, UK) for the surface of the stainless steel disk gave a detailed structure of the surface roughness, as shown in Fig. 6-1(b) and Fig. 6-1(c). The maximum height of the surface roughness is within 1 μm. The DC electrical voltage $U(t)$ of drop-solid surface connection was recorded using an ultra-high-speed DC electrical device at a frequency of 1.25×10^6 Hz by a self-developed acquisition system, as employed and detailed described in the previous Chapter. One electrode was connected to the nozzle and the other to the disk, so that the liquid serves as a conducting bridge in the circuit. To visualize the initial contact and spreading process, spreading images from the side view were captured with a high-speed camera Phantom V711 (Vision Research, USA) coupled with a macro lens (EF 100mm f/2.8, Canon, Japan). The chosen image capturing speed is up to 84054 frames per second (fps) according to the fluid type and image resolution. All the voltage data and images obtained were analyzed through self-programmed algorithms in MATLAB (R2012a, MathWorks, USA).

A high-speed micro-PIV technique was developed to follow the flow field in the drop during the initial contact in the drop. A small amount of silver coated hollow glass spheres (S-HGS-10, Dantec Dynamics, Denmark) with an average diameter of 10 μm were uniformly dispersed in the aqueous Newtonian and non-Newtonian fluids. Two lasers (LaserMax Inc., USA) of 1 mW were placed in the opposite direction to excite seeding particles in the laser sheets located inside the pendant drop, as shown in Fig. 6-2. The images were captured by the high-speed camera Phantom V711 equipped with a zoom lens (MP-E 65mm f/2.8, Canon, Japan) at up to 5000 fps. The flow fields were processed using the adaptive PIV method by the software DynamicStudio (Dantec Dynamics, Denmark).

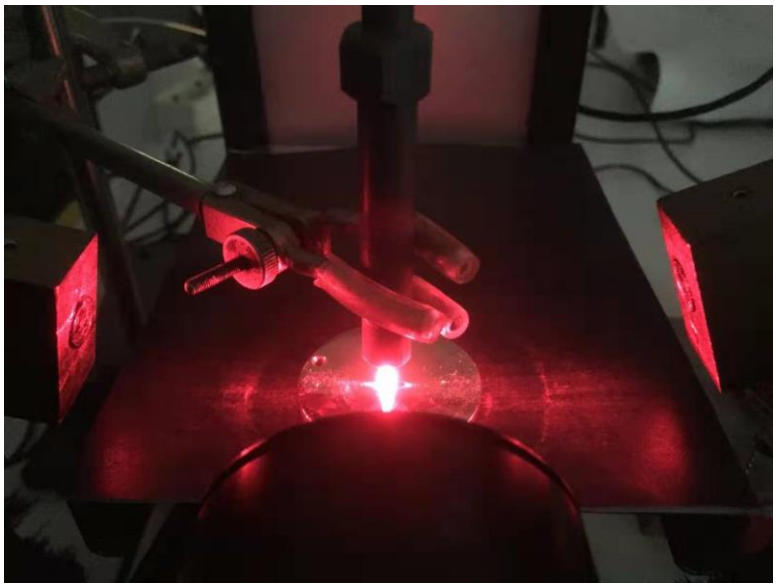


Fig. 6-2 Photograph of the micro-PIV devices.

The fluids in our experiments consisted of both the Newtonian and non-Newtonian fluids: distilled water, 1 wt% polyethylene oxide (low molecular weights of 3×10^5 g/mol and referred as LM PEO) solution, 2 wt% carboxymethyl cellulose sodium (low and medium viscosity of molecular weight 7×10^4 g·mol^{-1}, represented by LV and MV CMC, respectively) solutions and 2.0 wt% polyacrylamide (PAAm of molecular weight 1.3×10^7 g·mol^{-1}) solution. In order to enhance the electrical conductivity for the liquids, 10 wt% NaCl was added into the PAAm solution and 5 wt% NaCl into others. Fig. 6-3 shows the rheological properties of all the working liquids measured by a rheometer (AR-G2, TA Instruments, USA). The range of the shear rate was determined according to the liquid viscosity. The addition of seeding particles would result in a slight increase in the liquid viscosity. The initial contact takes place as soon the drop enters in contact with the plate surface of the disk in a very short time, the zero shear viscosity η_0 of the non-Newtonian fluids was used in this work. The properties of all the working liquids are gathered in Table 6-1.

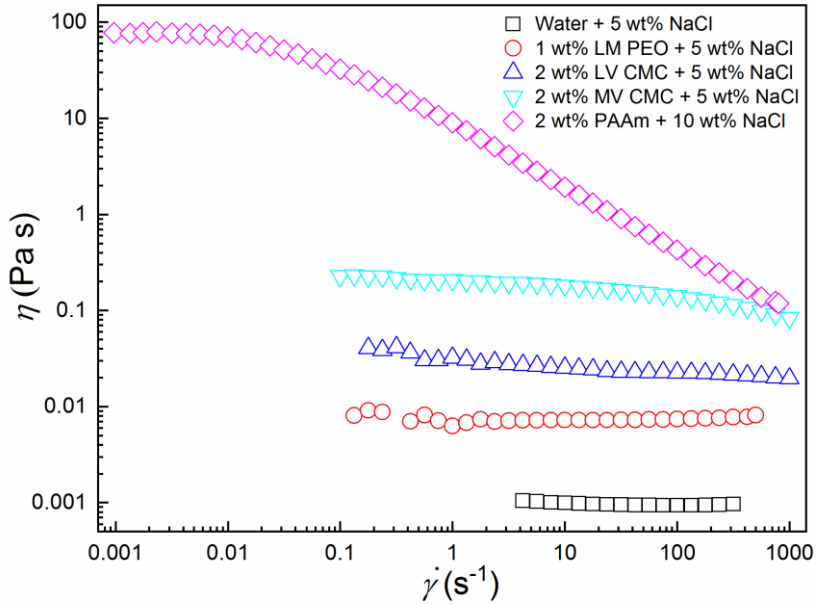


Fig. 6-3 Rheological properties of all the working liquids.

Table 6-1 Properties of all the liquids used.

Liquids	ρ (kg·m^{-3})	γ (mN·m^{-1})	η_0 (Pa·s)	σ (mS·cm^{-1})
Water + 5 wt% NaCl	1034	72.00	0.001	95.8
1 wt% LM PEO + 5 wt% NaCl	1064	63.00	0.008	59.8
2 wt% LV CMC + 5 wt% NaCl	1075	71.00	0.041	94.5
2 wt% MV CMC + 5 wt% NaCl	1075	69.00	0.227	98.2
2 wt% PAAm + 10 wt% NaCl	1136	66.20	77.44	144.7

6.3 Results and discussion

6.3.1 Initial contact and spreading of a pendant drop at solid surface

The electrical circuit and high-speed camera are synchronized and time zero t = 0 ms is defined when the first decreasing point of electrical resistance is detected. Sequences for the initial contact and spreading of various liquid drops at the solid surface are illustrated in Fig. 6-4. Taking 1 wt% LM PEO solution with 5 wt% NaCl as an example [Fig. 6-4(a)], the drop spread spontaneously as soon it touched the solid substrate. As the drop touched the surface, in a very short time, the air cushion

between the drop and the metallic surface was rejected. A capillary wave was generated along the surface of the drop. From the images of t = 0.25 ms to t = 0.50 ms, the spreading radius increased while the drop body kept a smooth shape. The voltage decreased gently compared to the very initial contact. With the increasing spreading radius, the bottom part of the drop began to be trapezoid and the upper part was no longer smooth. At t = 1.00 ms, the drop was much like a vase and the largest width laid in the middle part instead of the nozzle outlet and the spreading section. Due to the continuous feeding of the liquid under a constant flowrate, the upper part of the pendant drop shrank while the bottom part continued to expand. At t = 10 ms, the drop evolved quite like a pear and the voltage decreased into a local extremum. Thereafter, the upper part of the pendant drop gradually evolved into a liquid neck. The neck thinned to be a liquid column and then detached from the nozzle end. The voltage increased continuously until the final pinch-off at t = 198.13 ms. Due to the viscoelasticity of PEO and PAAm solutions, the drop neck would be elongated thus the whole period was much longer than those for the water and CMC drops. For water with 5 wt% NaCl and 2 wt% CMC solutions with 5 wt% NaCl [Fig. 6-4(b-d)], the drop evolved in the same manner as PEO and PAAm before a thin neck formed, then the water neck would break up immediately instead of a long elongation process. The whole cycle of the drop spreading corresponding to water with 5 wt% NaCl, 2 wt% LV CMC solution with 5 wt% NaCl and 2 wt% MV CMC solution with 5 wt% NaCl are 14.85 ms, 17.37 ms and 26.74 ms, respectively.

The flow fields in the drop during the initial contact and spreading were obtained for the first time by the micro-PIV up to 5000 velocity fields per second. Sequences corresponding to water, 2 wt% PAAm, 2 wt% LV CMC and 2 wt% MV CMC solutions were illustrated from Fig. 6-5 to Fig. 6-12. As soon as the drop touched the solid substrate, the surface energy released suddenly in the form of the kinetic energy due to the fast evolution of the local curvature at the triple contact line. The velocity acceleration in both the axial and radial directions could be observed. An interesting phenomenon of damping in the axial direction attracted our attention. Put the flow fields all together, it could be found that the damping phenomenon was more evident at higher approaching velocities and smaller liquid viscosities. In comparison with the flow fields in the drop coalescence, the velocity rebound in the axial direction was enhanced while the radial velocity slowed down during the drop contact and

spreading on a solid substrate. Obviously, the viscous dissipation is higher in the case of liquid-solid contact than for liquid-liquid coalescence.

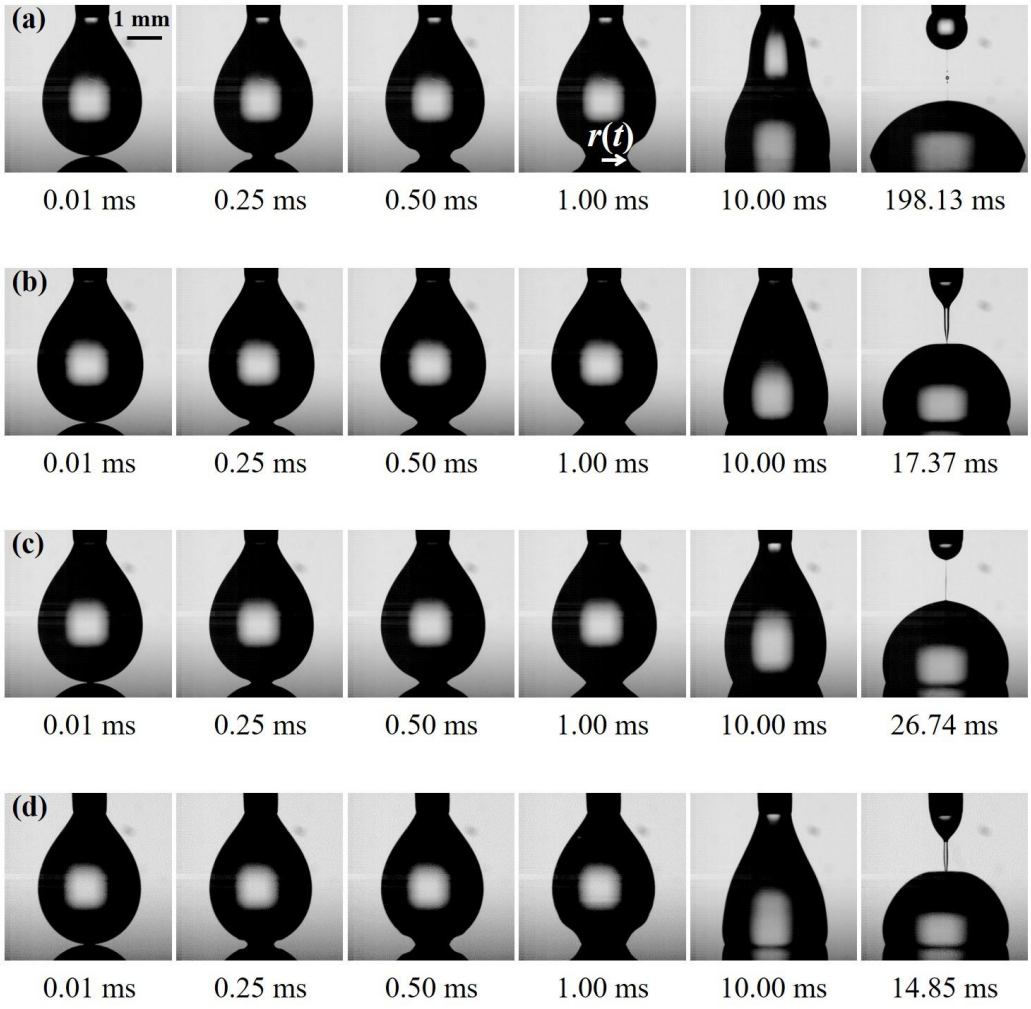


Fig. 6-4 Sequence for initial contact and spreading of a pendant drop on a stainless steel surface. v_0 = 0.29 mm·s^{-1}. (a) 1 wt% LM PEO solution with 5 wt% NaCl. (b) 2 wt% LV CMC solution with 5 wt% NaCl. (c) 2 wt% MV CMC solution with 5 wt% NaCl. (d) Water with 5 wt% NaCl. $r(t)$ is the time-dependent spreading radius. All images share the same scale bar of 1 mm.

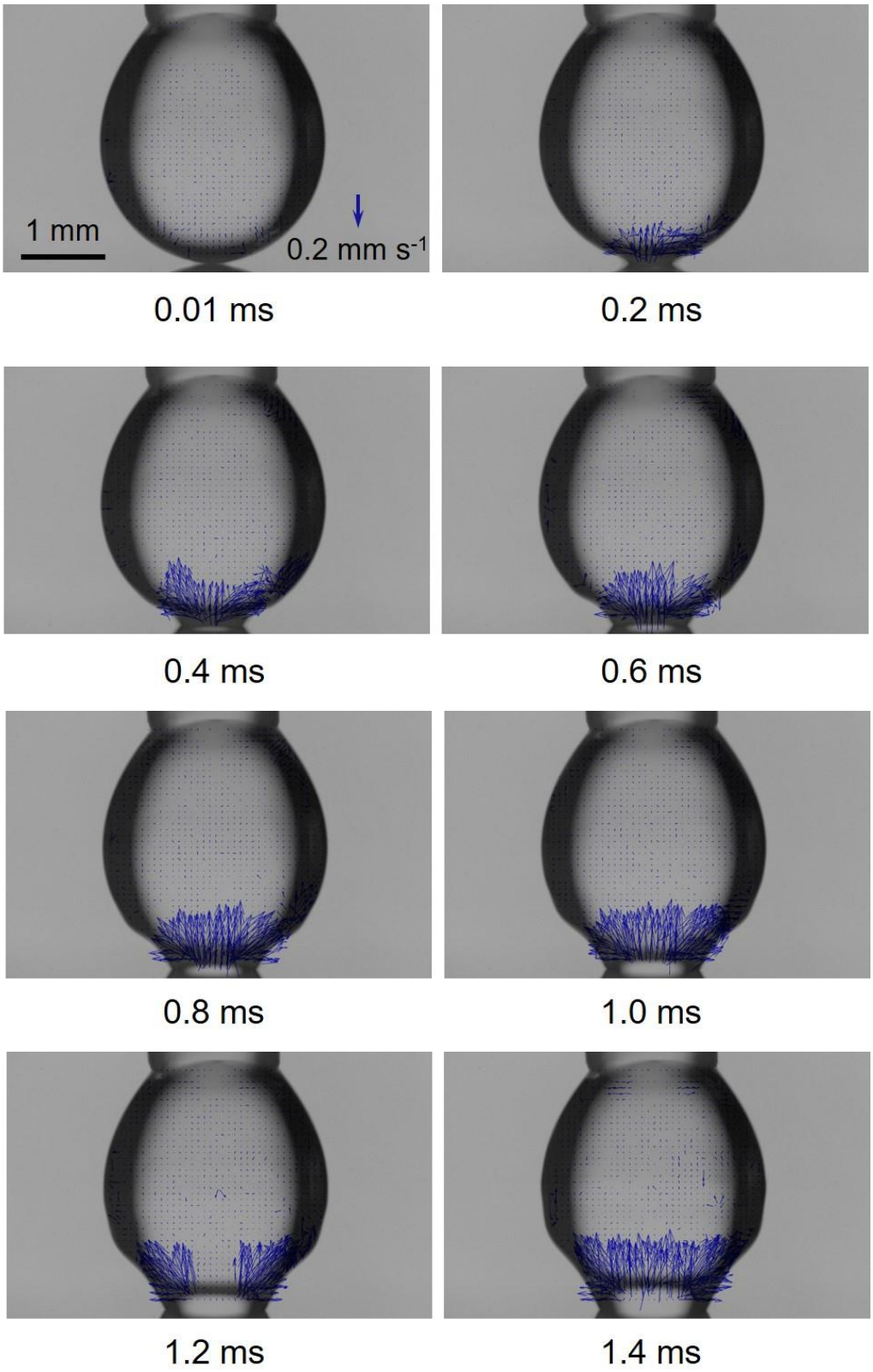


Fig. 6-5 Velocity fields in the drop during the initial contact and spreading. Water with 5 wt% NaCl. v_0 = 0.06 mm·s^{-1}. 5000 velocity fields per second. The scale bars for length and velocity indicate 1 mm and 0.2 mm·s^{-1}, respectively.

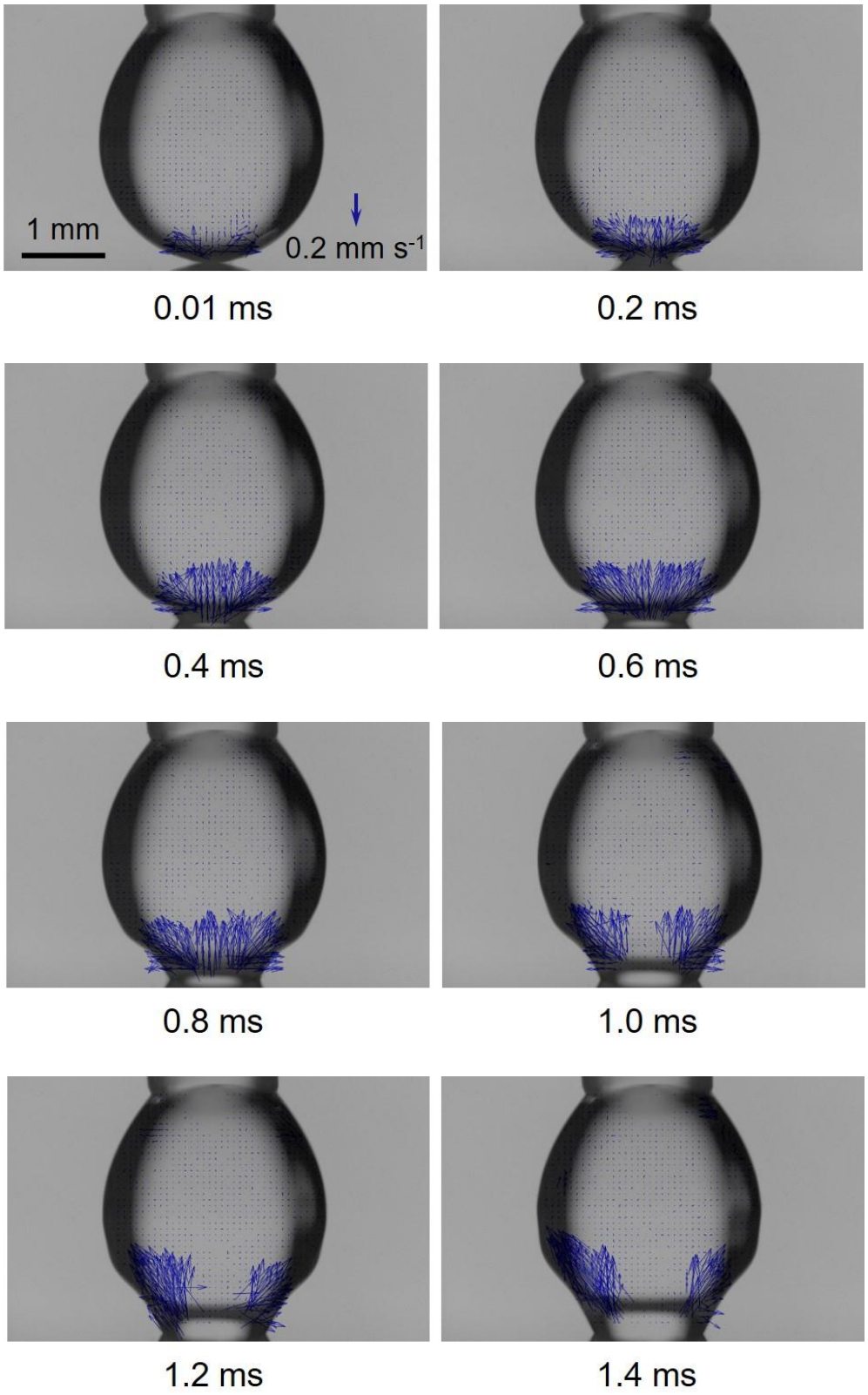


Fig. 6-6 Velocity fields in the drop during the initial contact and spreading. Water with 5 wt% NaCl. v_0 = 0.29 mm·s^{-1}. 5000 velocity fields per second. The scale bars for length and velocity indicate 1 mm and 0.2 mm·s^{-1}, respectively.

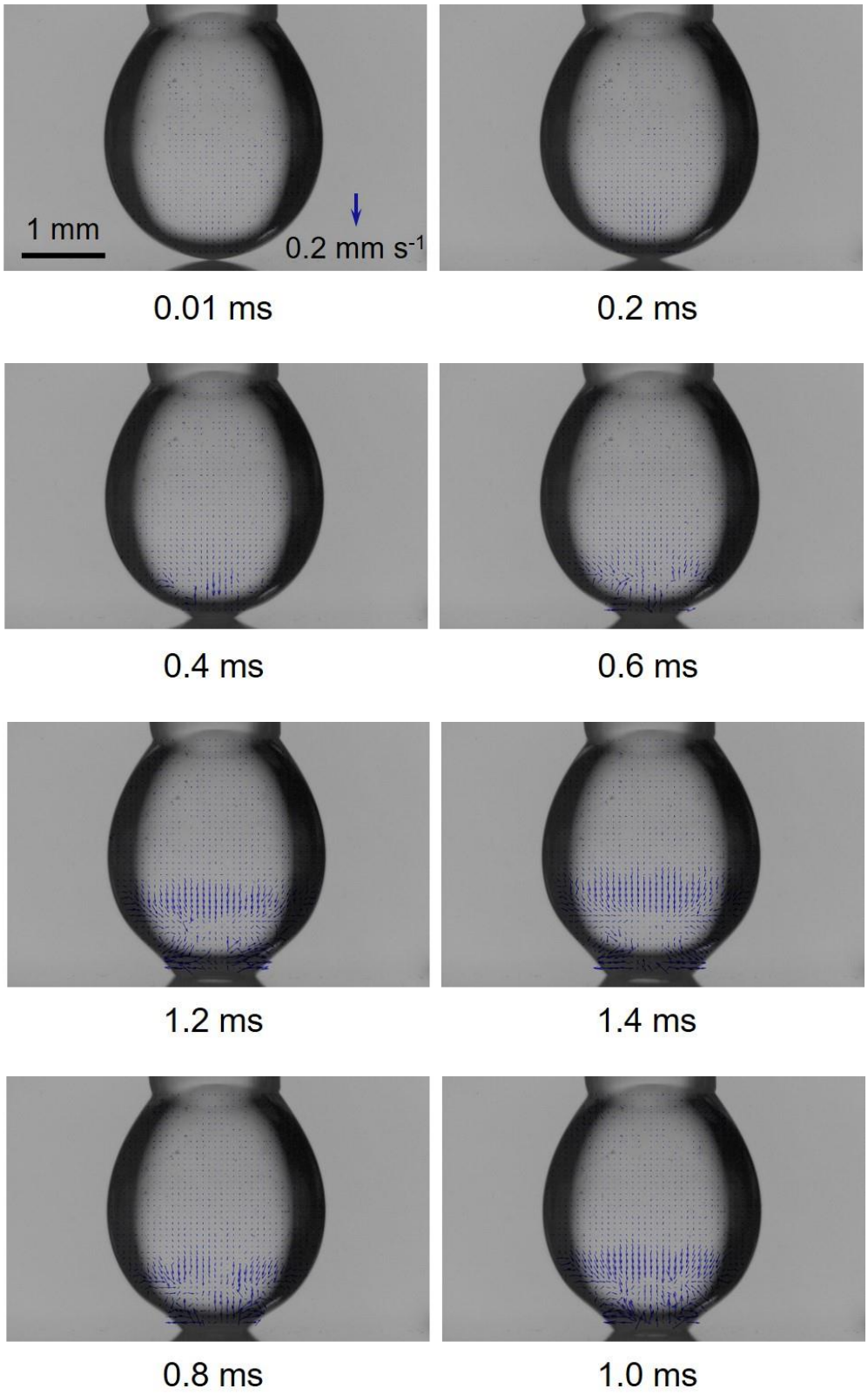


Fig. 6-7 Velocity fields in the drop during the initial contact and spreading. 2 wt% PAAm solution with 10 wt% NaCl. v_0 = 0.06 mm·s^{-1}. 5000 velocity fields per second. The scale bars for length and velocity indicate 1 mm and 0.2 mm·s^{-1}, respectively.

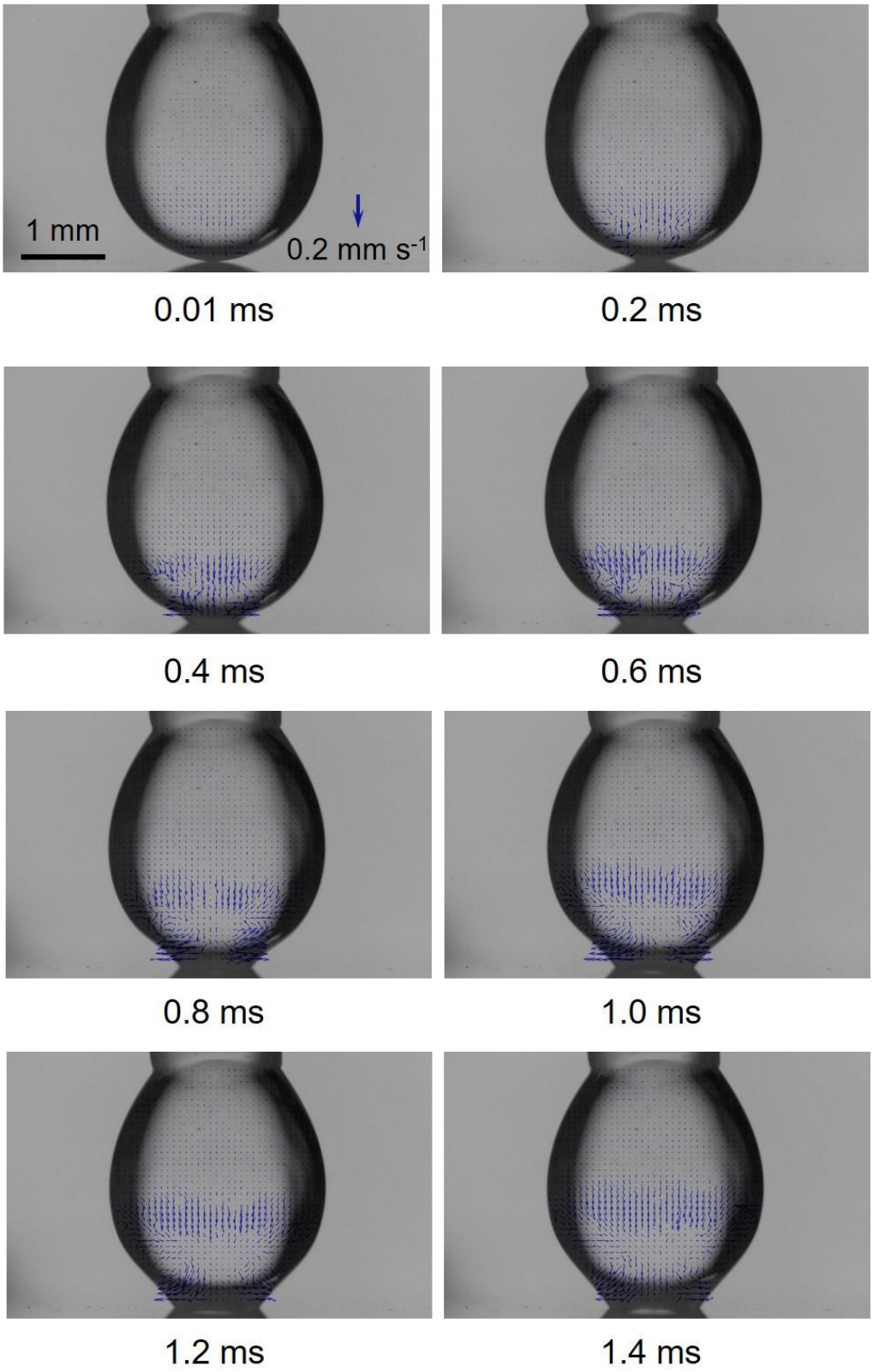


Fig. 6-8 Velocity fields in the drop during the initial contact and spreading. 2 wt% PAAm solution with 10 wt% NaCl. v_0 = 0.29 mm·s^{-1}. 5000 velocity fields per second. The scale bars for length and velocity indicate 1 mm and 0.2 mm·s^{-1}, respectively.

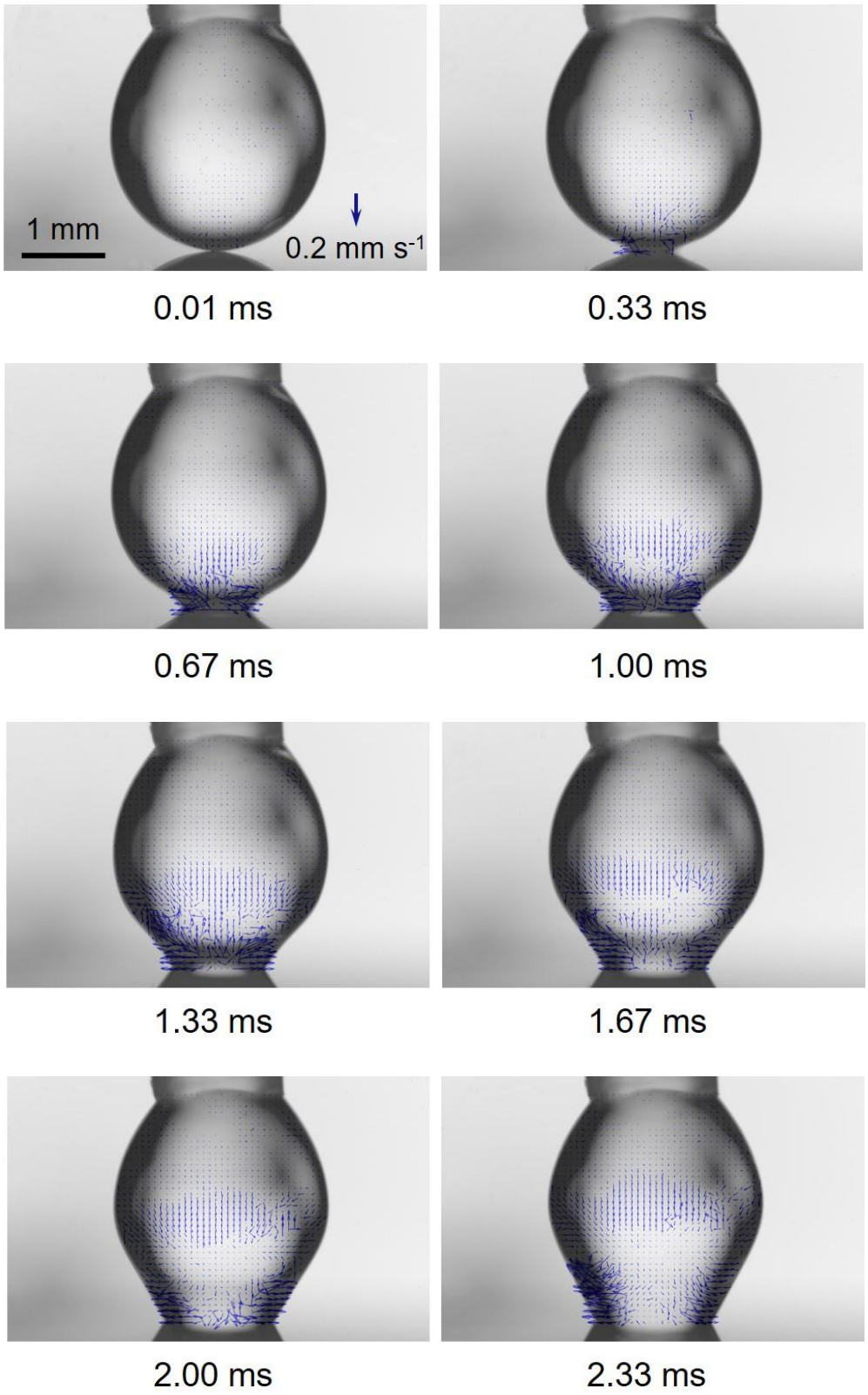


Fig. 6-9 Velocity fields in the drop during the initial contact and spreading. 2 wt% LV CMC solution with 5 wt% NaCl. v_0 = 0.06 mm·s^{-1}. 3000 velocity fields per second. The scale bars for length and velocity indicate 1 mm and 0.2 mm·s^{-1}, respectively.

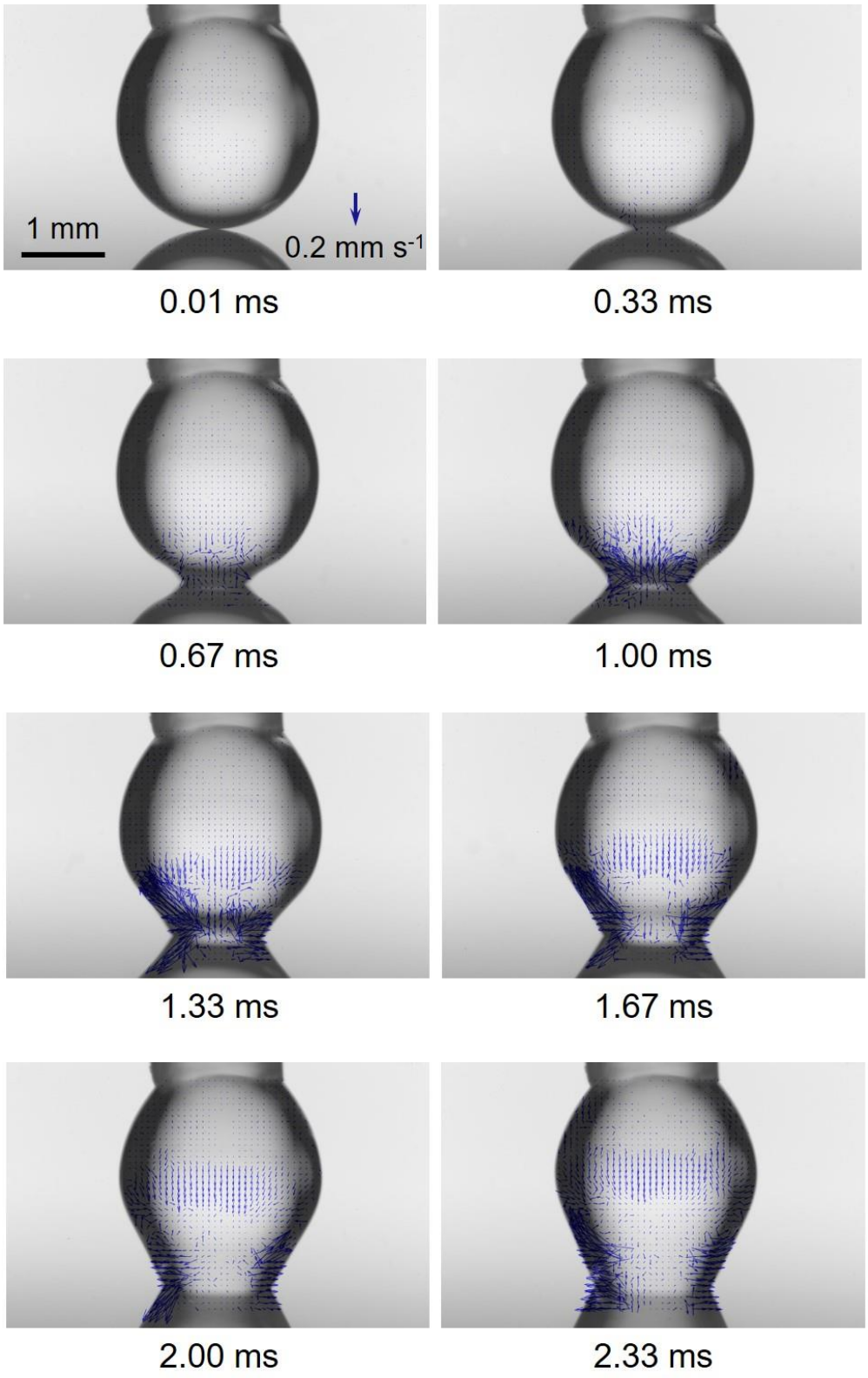


Fig. 6-10 Velocity fields in the drop during the initial contact and spreading. 2 wt% LV CMC solution with 5 wt% NaCl. v_0 = 0.29 mm·s^{-1}. 3000 velocity fields per second. The scale bars for length and velocity indicate 1 mm and 0.2 mm·s^{-1}, respectively.

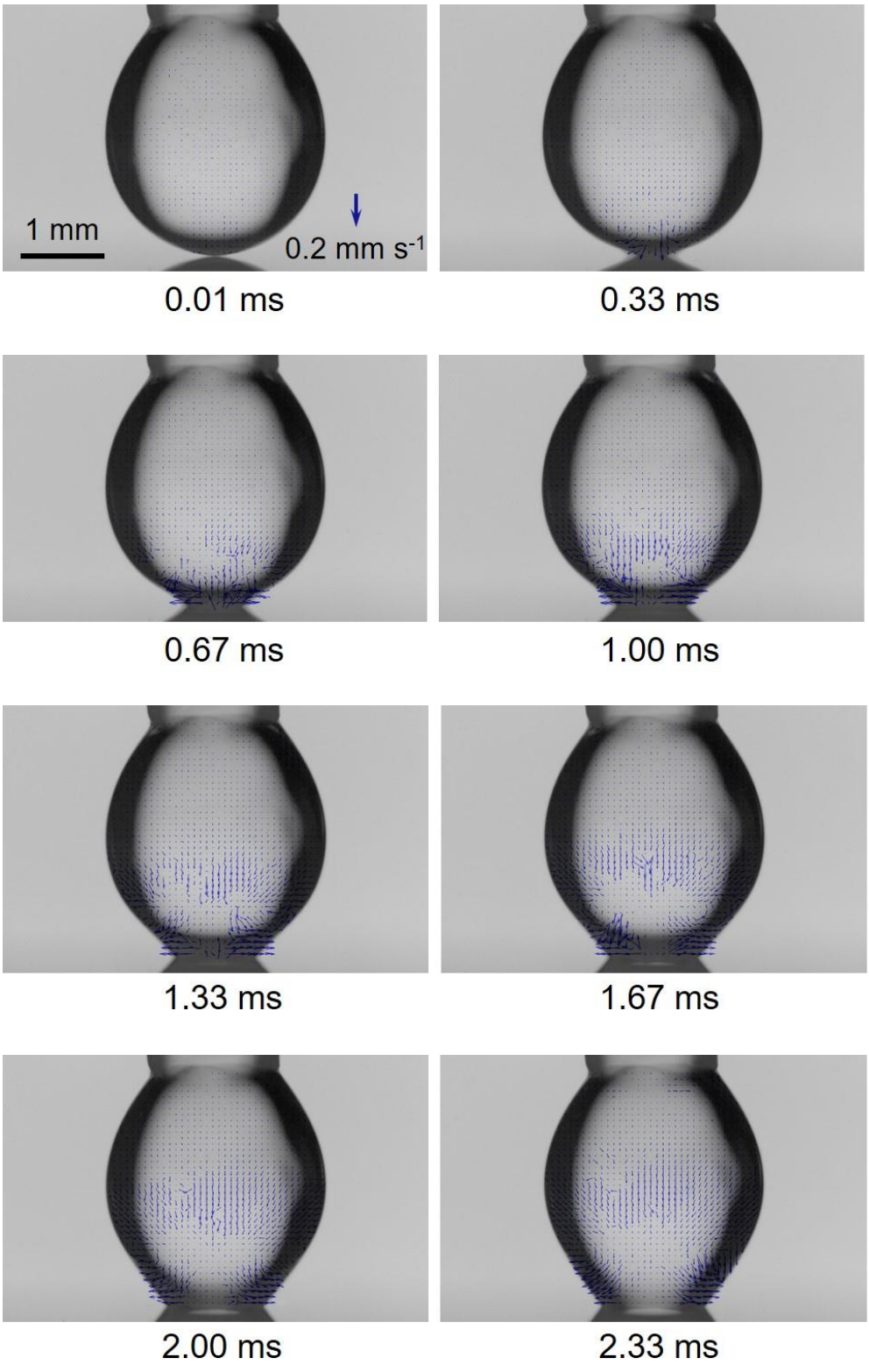


Fig. 6-11 Velocity fields in the drop during the initial contact and spreading. 2 wt% MV CMC solution with 5 wt% NaCl. v_0 = 0.06 mm·s^{-1}. 3000 velocity fields per second. The scale bars for length and velocity indicate 1 mm and 0.2 mm·s^{-1}, respectively.

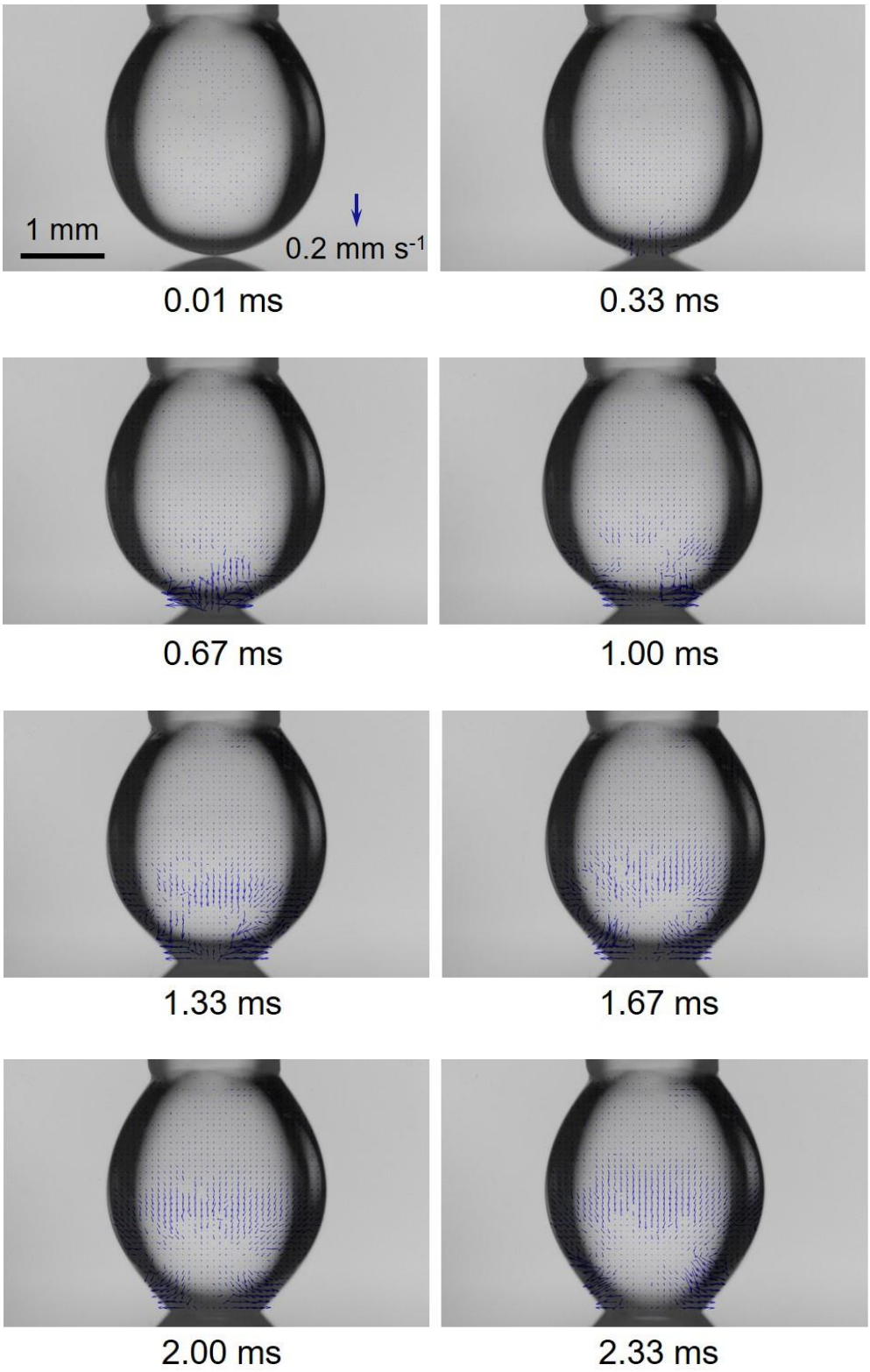


Fig. 6-12 Velocity fields in the drop during the initial contact and spreading. 2 wt% MV CMC solution with 5 wt% NaCl. v_0 = 0.29 mm·s^{-1}. 3000 velocity fields per second. The scale bars for length and velocity indicate 1 mm and 0.2 mm·s^{-1}, respectively.

The variation of the electrical resistance R with time during the initial contact and spreading is displayed in Fig. 6-13(a). The circuit formed as soon the falling drop contacted the solid surface, and the voltage decreased rapidly due to the connection of the circuit. At around t = 0.5 ms, the electrical resistance reached a minimum value of 8627 Ω, 9770 Ω and 10632 Ω for water, PEO and PAAm solutions, as displayed in Fig. 6-13(b). The electrical resistance increased slowly with the thinning of the liquid neck and reached the maximum value until the final breakup. The initial contact and spreading within the first 0.5 ms was much faster than the final pinch-off and attracted our attention for further investigation.

The close-ups of the electrical signals during the initial contact and spreading are plotted in Fig. 6-14(a). As mentioned in the previous Chapter, the drop conductance G indicates the reverse of the drop resistance and depends on the minimum section along the liquid column. The motion of electrons is mainly obstructed at the minimum sections, either at the initial spreading area at the solid surface or the liquid neck during the pinch-off. The smaller the liquid width, the larger the drop resistance. At very early stage of the initial contact, the spreading radius of several micrometers, even at the molecular level, is much shorter than that of the drop neck. The electrical signal was then dominated by the spreading radius, which contributes 98.4% to the drop resistance. It was revealed by the electrostatic software GETDP that the dominant conductance G followed the linear relationship with the spreading section S. Consequently, the relationship between the spreading radius r and the drop conductance G was obtained as $r \sim G^{1/2}$, which was applicable to the initial times when the spreading radius was less than 47 μm. As shown in Fig. 6-14(a), this relationship is no longer valid after 6.4 μs due to the shape evolution of the liquid column and the expanding spreading section. As time goes by, the drop continues to spread and the neck gradually began to intervene in the drop conductance. The drop base and neck contributed equally to the conductance when the spreading section became adequate with the cross section of the neck. The drop conductance reaches its maximum at this moment. Then the spreading section increased to larger than the neck and the minimum section along the liquid column turned to located at the neck. Hereafter, the section of the neck became more and more dominant in the drop conductance. The neck gradually thinned and the conductance started to decrease until the final pinch-off, where the contribution of the spreading section on the drop

conductance was less than 0.01%. In the initial spreading stage where the spreading section was smaller than the drop neck, the dominating role of the spreading section in the conductance was inversely proportional to its radius, this point is nothing but the justification of the electrical signals in investigating the very early stage of the drop spreading.

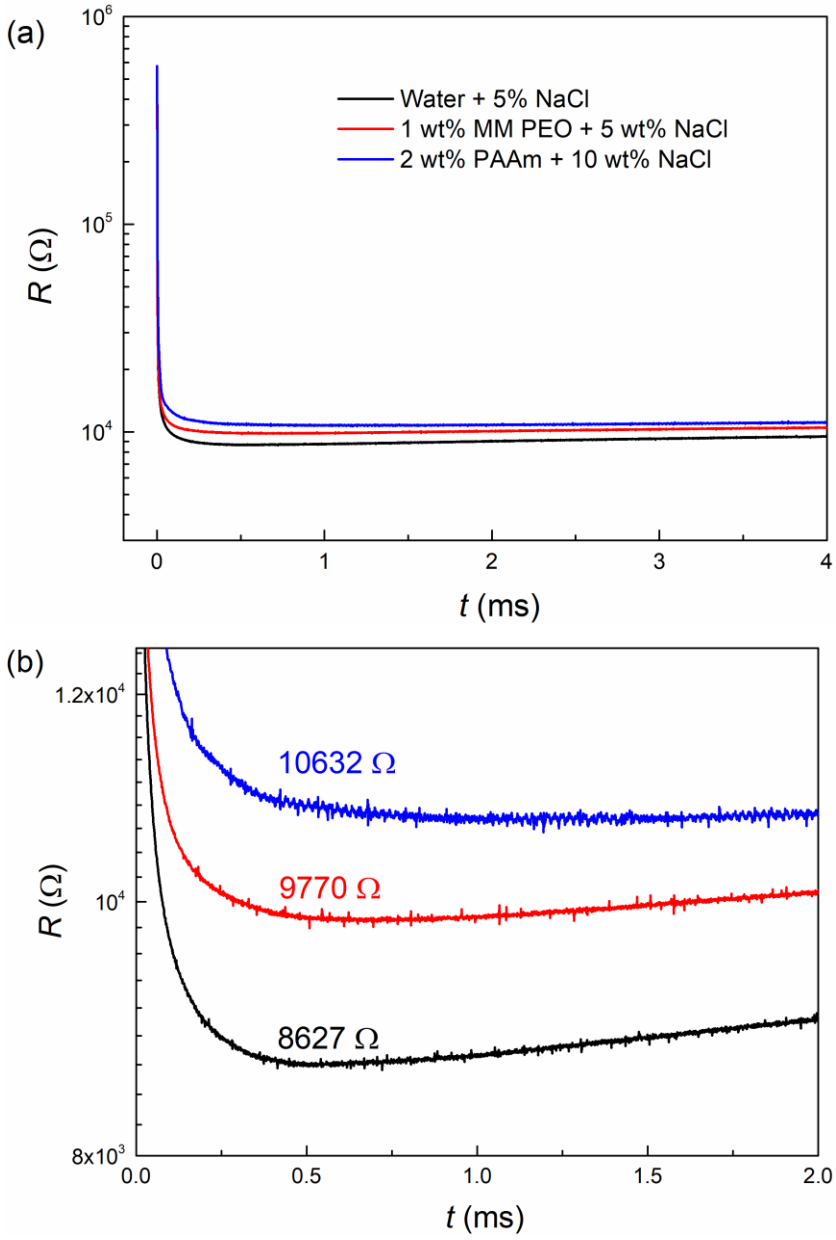


Fig. 6-13 (a) Variation of the electrical resistance with time during the initial drops contact for water, 1 wt% MM PEO and 2 wt% PAAm solutions on a stainless steel plate. v_0 = 0.29 mm·s^{-1}. (b) Scale-down of the minimum drop resistance within 2 ms.

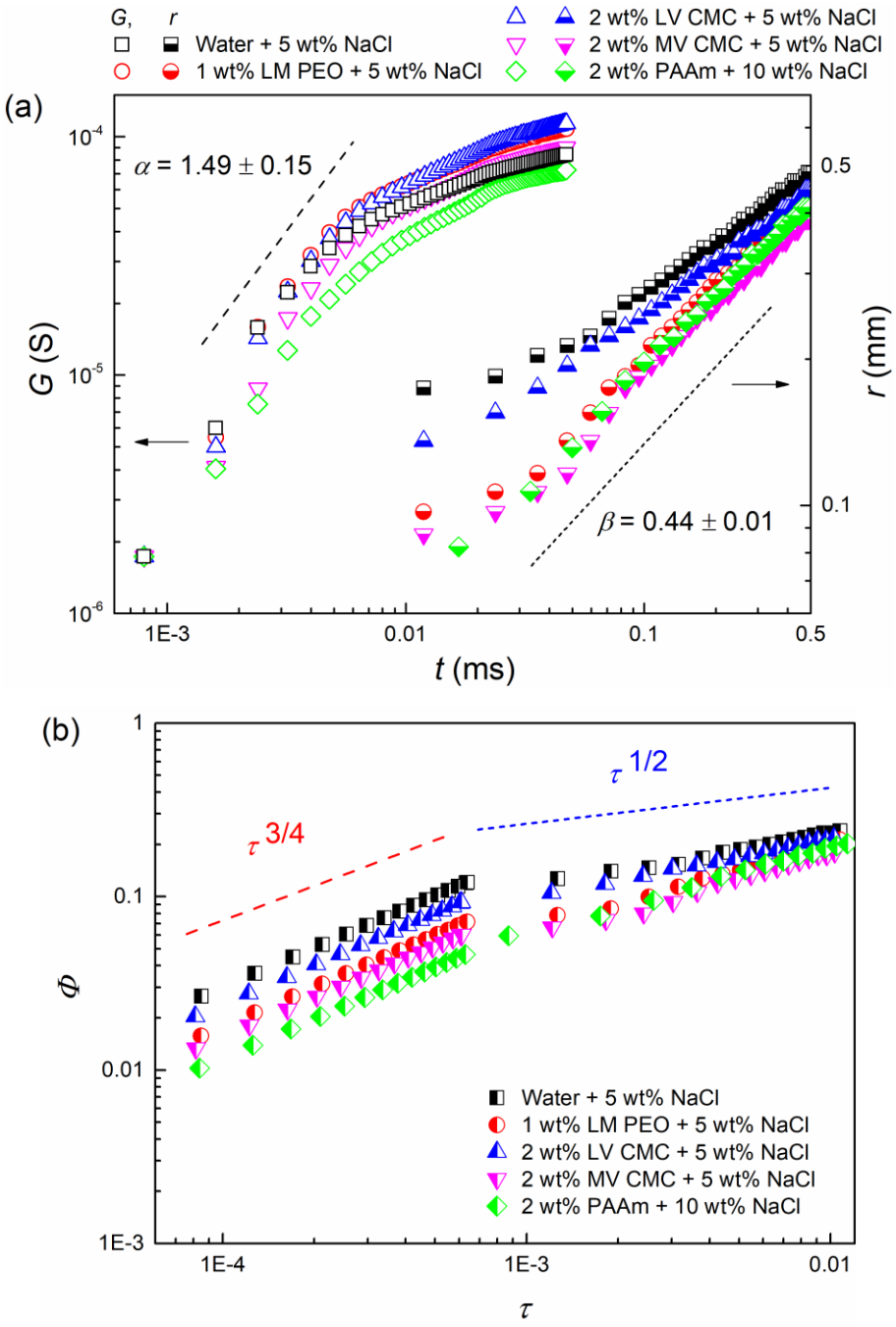


Fig. 6-14 Dynamics of initial contact and spreading on a stainless steel plate. v_0 = 0.29 mm·s^{-1}. (a) Variation of the drop conductance G (hollow symbols, left Y axis) and the spreading radius r (half solid symbols, right Y axis) within 0.5 ms. (b) Variation of the rescaled spreading radius Φ with the normalized time τ.

In this work, we focused on the initial contact and spreading of the drop before the maximum of conductance G. The drop conductance follows a power-law of $G \sim t^{\alpha}$ with time during the initial contact and spreading, as shown in Fig. 6-14(a).

The exponents for various solutions at a large approaching velocity showed similar values as $\alpha = 1.49 \pm 0.15$ within 6.4 μs and independent of the liquid viscosities. For the pendant drops with a small approaching velocity, the slightly decreased exponents of 1.34 ± 0.13 were observed within 6.4 μs. The viscosity-independent exponents indicated that the initial spreading resulted from the spreading of the aqueous solvent instead of the macromolecules, even if the zero-shear viscosities for all working liquids varied by nearly five orders of magnitude. The large exponents showed that once the drop contacted the solid surface, the drop spreading took place in a very short time with an extremely rapid expanding speed. In comparison with the exponents of 1.98 ± 0.19 corresponding to the drop coalescence at a liquid surface, the exponents for the drop spreading at various approaching velocities were smaller. The decline could be attributed to the viscous drag stemming from the rigid solid surface on the initial drop spreading. The rebound velocities shown in the flow fields during the drop spreading also provided credible evidence to the decline in the exponent with respect to the coalescence. Based on the high-speed images, the spreading radius also followed a power-law relationship of $r \sim t^{\beta}$ with the exponent of $\beta = 0.44 \pm 0.01$. The exponents showed that both the drop spreading on a solid substrate and the drop coalescence at a liquid surface exhibited a relatively similar trend with the exponents approximately equal to 1/2. It is worth noting that the value of the exponent is again slightly smaller in the case of the drop spreading, certainly due to the liquid-solid friction. The spreading radius r and time t are rescaled as $\Phi = r / r_{\max}$ and $\tau = t / t_{\mathrm{i}}$ by the maximum drop radius at initial contact $r_{\max}$ and the inertial time t_{i} ($t_{\mathrm{i}} = \sqrt{\rho r_{\max}^3 / \gamma}$. Thus all data could be scaled and gathered together by the rescaled parameters.

The temporary evolution of the rescaled coalescing width Φ is plotted in Fig. 6-14(b) by both the electrical device and high-speed camera visualization. In the early spreading stages, it followed the power law of $\Phi \sim \tau^{3/4}$ at a large approaching velocity and $\Phi \sim \tau^{2/3}$ at a small approaching velocity. This difference of the exponent could arise from an inertial effect as the approaching velocities differ from a factor of 4.83. The rebound velocities in the drop measured by the micro-PIV after the initial contact provide tangible proof of this assumption. Here, we gave rise to a new regime in the early spreading times, which has never been reported in the literature. In this regime, the inertia and viscous force should display a competing role in the drop

spreading. The inertial effect stemming from the release of the surface energy at the liquid neck was illustrated in the flow fields by the micro-PIV measurements and prevented the spreading from being in the later viscous regime. At 0.8 μs, the spreading radius varied between 8.4 - 23.0 μm for all working liquids, reducing an order of magnitude from the minimum width through the optical method by the high-speed camera.

It underwent the inertial regime after $\tau = 6.37\times10^{-4}$, where the rescaled coalescing width followed the power law with an exponent of 1/2. Due to there are a few data in the overlay area between the two regimes, further investigation is required to gain deep insight into the viscous effect.

6.3.2 Filament thinning of the liquid neck

During the drop contact and spreading process, the liquid neck became limiting on the drop resistance when its cross section was smaller than the spreading section. From this moment on, the liquid neck would go through the filament thinning process until the final pinch-off. Then further analysis was performed on the variation of the electrical signals in the pinch-off stages.

The variations of the electrical resistance for the Newtonian liquids and the non-Newtonian liquids without the polymer groups of high molecular weight were shown in Fig. 6-15. The initial spreading and the pinch-off stages were divided by the minimum resistance that emerged at around 0.5 ms. The pinch-off stage was much longer than the initial spreading. According to the electrical results, the whole period for water and 2 wt% MV CMC solution was 15.08 ms and 30.03 ms, respectively.

Then the electrical signals for the PEO and PAAm solutions were also analyzed, as shown in Fig. 6-16 to Fig. 6-18. Surprisingly, regular peak signals were observed in the evolution of the electrical resistance. For LM PEO solution with 5 wt% NaCl, there are 6 peaks in total during the increase of the drop resistance. For the PAAm solutions of various concentrations, regular peaks not only existed in the evolution where the resistance gradually increased, but also in the saturation stage of the electric circuit after the resistance returned to the maximum of 578173 Ω. The number of peak signals increased with both the molecular weight and concentration of the polymer, with the molecular weight of 3×10^5 g/mol for LM PEO and 1.3×10^7 g·mol^{-1} for PAAm.

Furthermore, it can be found that the time interval between every two successive peaks was almost the same 20 ms, both in the main evolutive curve and the saturation plateau. This interesting phenomenon stimulated us to analogize the liquid filament as a switch which regularly adjusted the transportation of the charged polymer groups and controlled the local conductivity of the filament. In addition, the whole period for PAAm and PEO solutions acquired from the electrical signals was a little shorter than that from the high-speed images, which might result from the disappearance of the electrical signals when the liquid neck thinned to smaller than 200 μm.

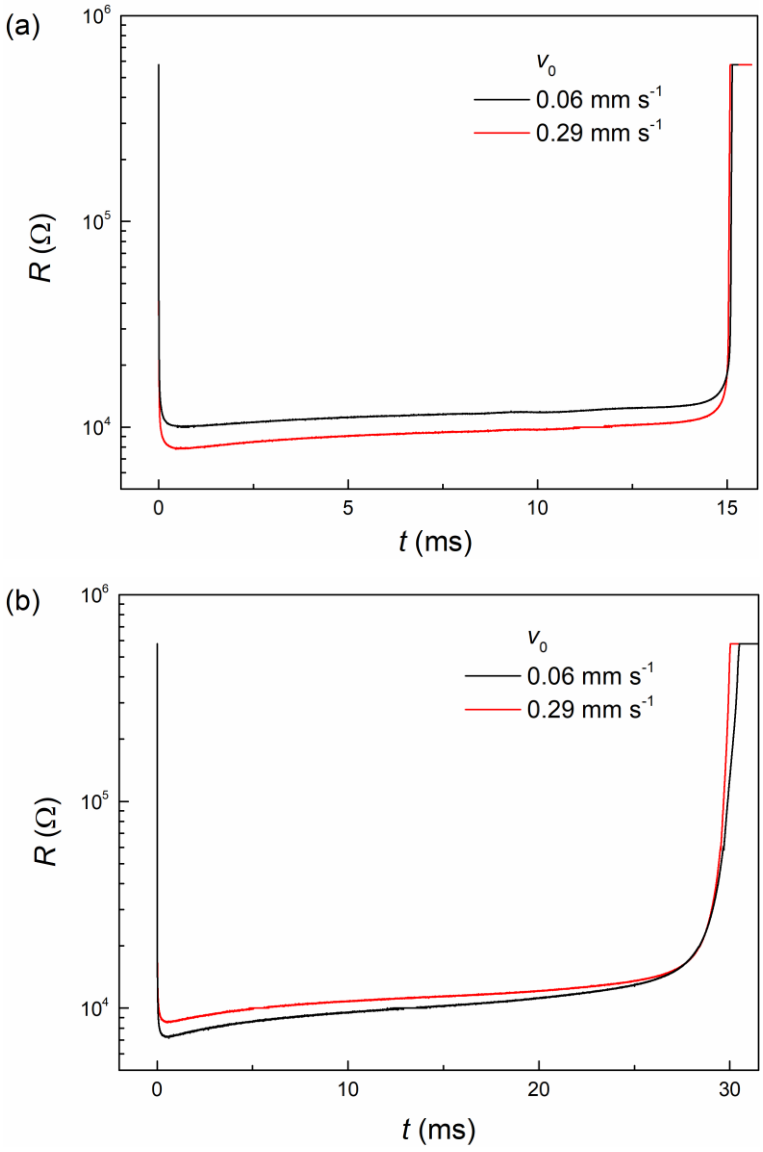


Fig. 6-15 Variation of the electrical resistance during the filament pinch-off. (a) Water with 5 wt% NaCl. (b) 2 wt% MV CMC solution with 5 wt% NaCl.

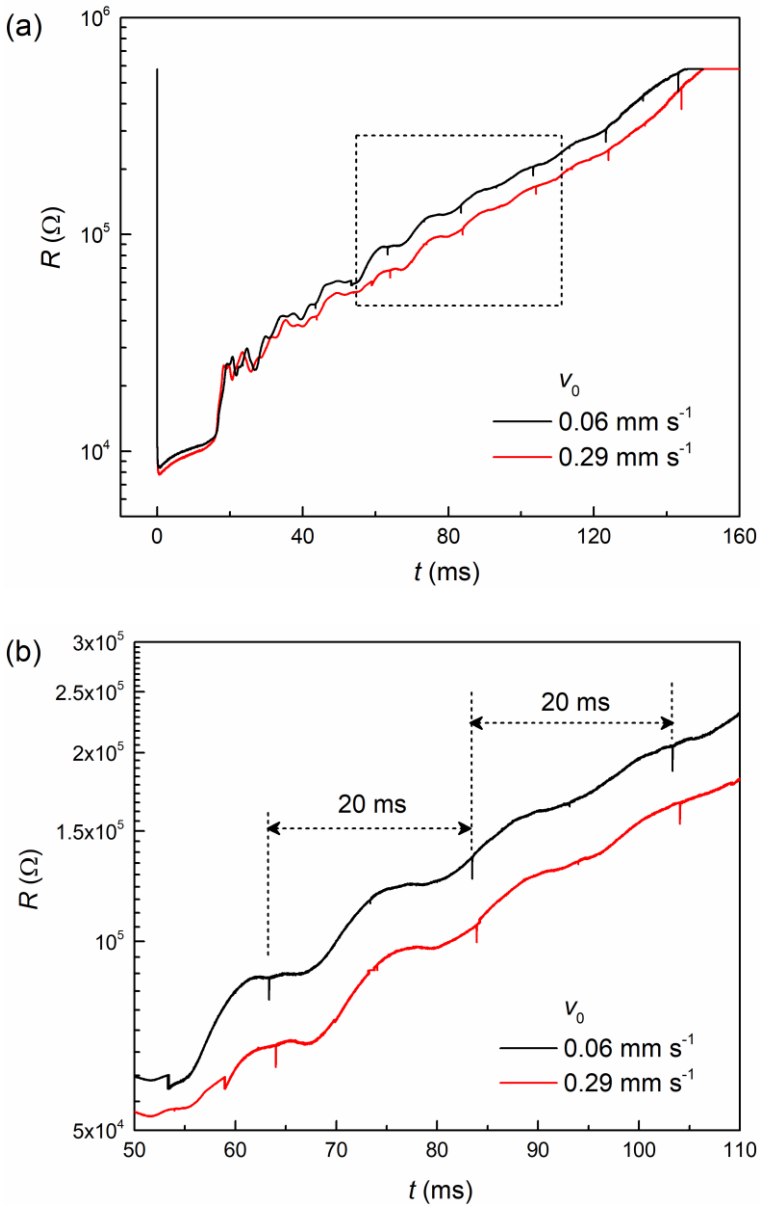


Fig. 6-16 Variation of the electrical resistance during the filament pinch-off of 1% LM PEO solution with 5 wt% NaCl. (a) In a whole cycle. (b) Scale-up of from 50 ms to 110 ms, as indicated in the dotted rectangular in the figure above.

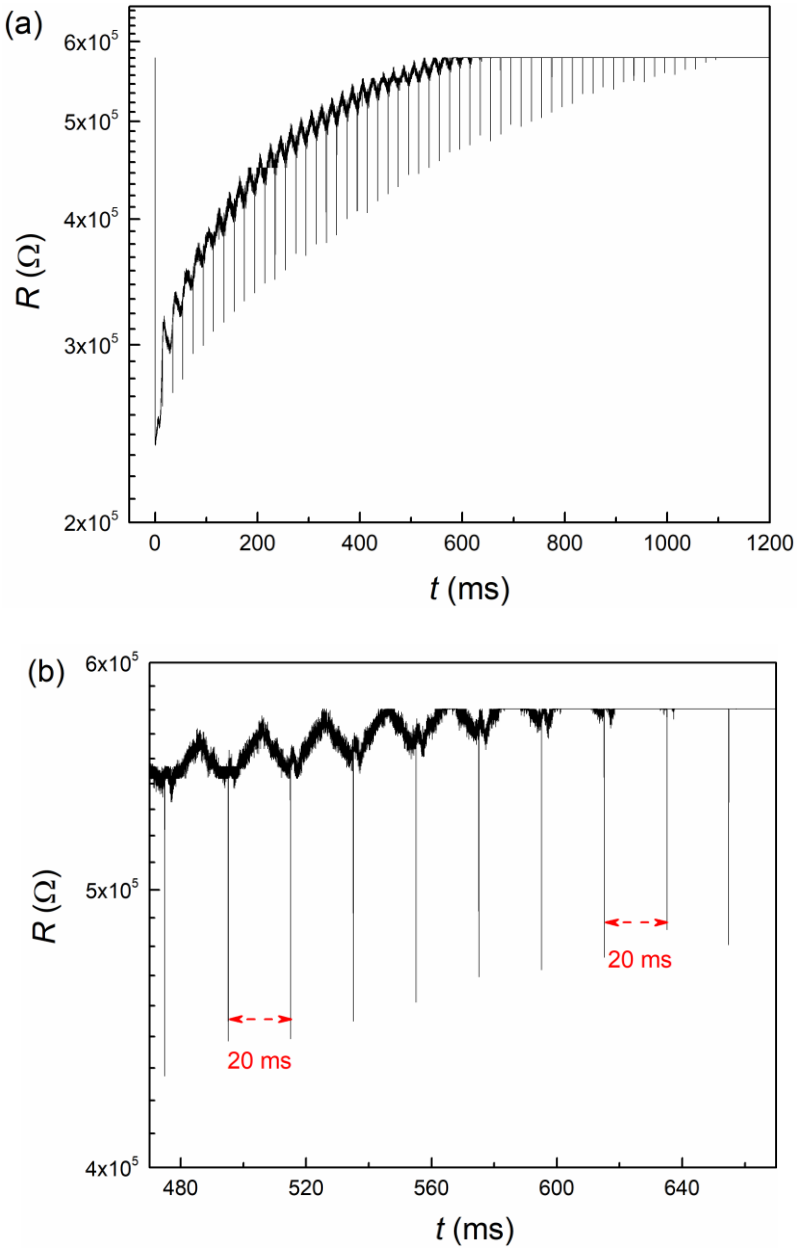


Fig. 6-17 Variation of the electrical resistance during the filament pinch-off of 1 wt% PAAm solution. v_0 = 0.29 mm·s^{-1}. (a) In a whole cycle. (b) Scale-up of from 470 ms to 670 ms.

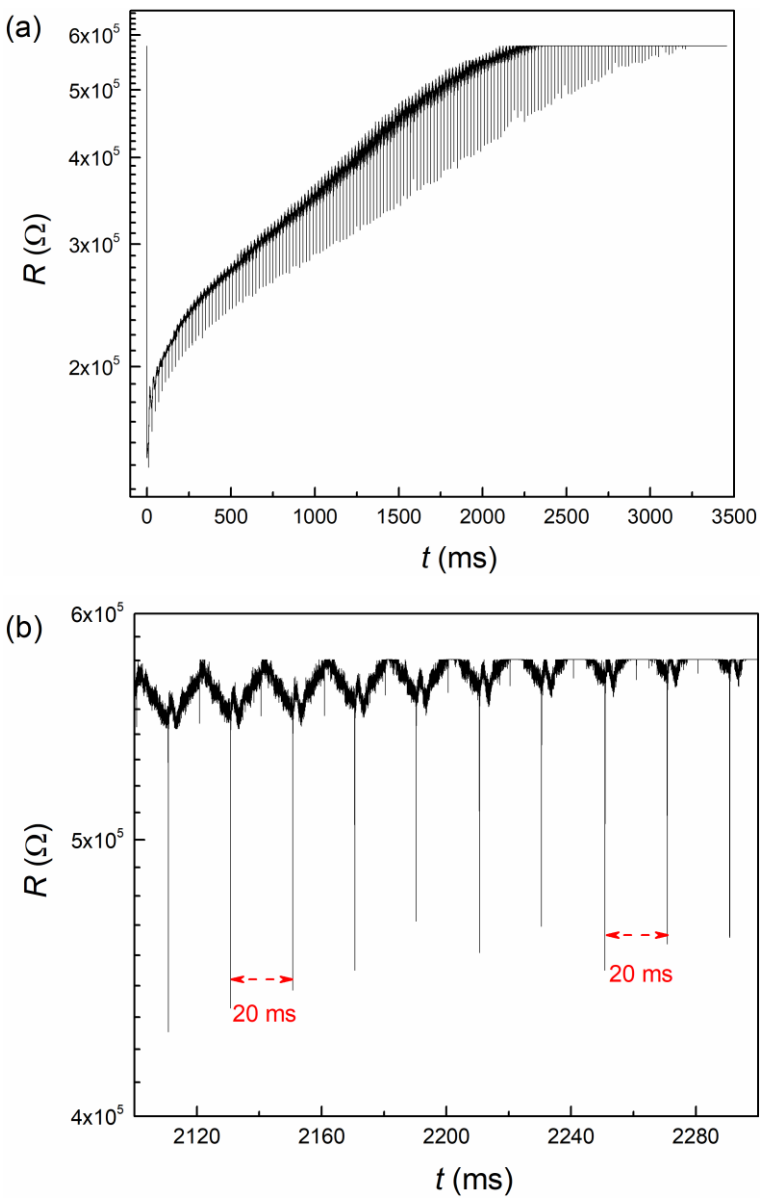


Fig. 6-18 Variation of the electrical resistance during the filament pinch-off of 2 wt% PAAm solution. v_0 = 0.29 mm·s^{-1}. (a) In a whole cycle. (b) Scale-up of from 2100 ms to 2300 ms.

To figure out whether the peaks were resulted from the alternating current with a frequency of 50 Hz used for the computer, the acquisition system connected to the DC circuit, the reference liquids with water and PAAm solutions were also employed with both electrodes immersed in the liquid, as shown in Fig. 6-19. No peak was observed in the partial magnification of the electrical signals within 100 ms, indicating that the effect of the alternating current on the regular signals could be excluded.

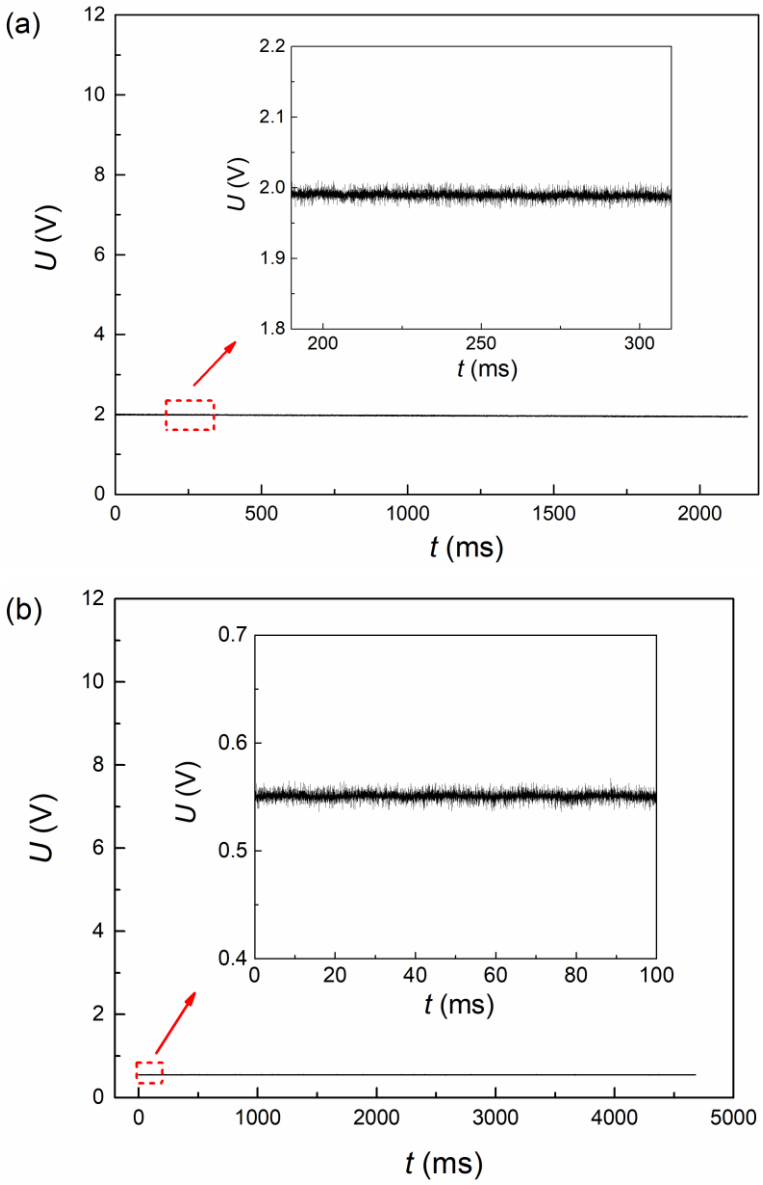


Fig. 6-19 Reference data with both electrodes immersed in the liquid. (a) Water with 5 wt% NaCl. (b) 2 wt% PAAm solution with 10 wt% NaCl.

To verify the stability and accuracy of the self-developed DC electrical device, an electronic oscilloscope with an acquisition frequency up to 20 MHz was also employed to track the variation of the electrical signals during the pinch-off of polymer filaments. Taking 2 wt% PAAm solution with 10 wt% NaCl as an example, regular peaks with an interval of 20 ms were also observed, as shown in Fig. 6-20. Again, the existence of such regularly spaced peaks, confirmed by the oscilloscope at an acquisition frequency of a faster decade at least than the DC circuit, was not an artifact. Due to the complicated relationship between the electric signals and the

visualized high-speed images, it still requires further investigations especially on the feature of the peak signal.

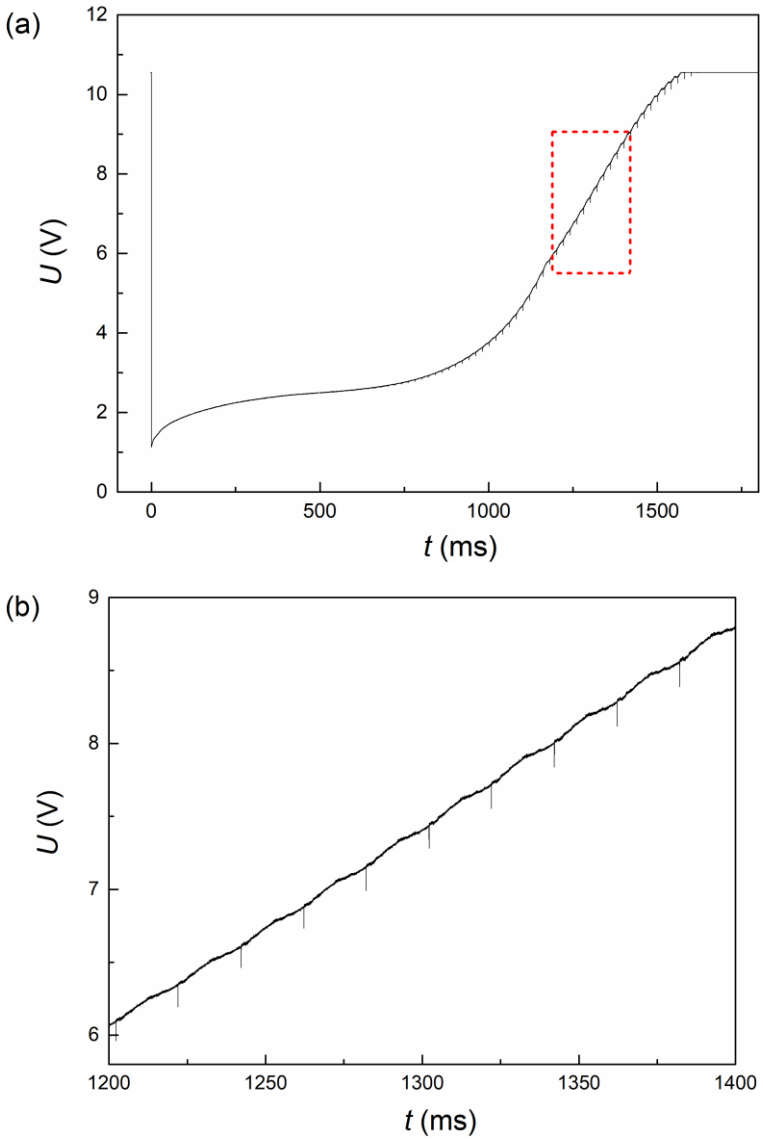


Fig. 6-20 Variation of the electrical voltage during the pinch-off measured by the electronic oscilloscope. 2 wt% PAAm solution with 10 wt% NaCl. (a) The whole pinch off process. (b) Partial scale-up from 1200 ms to 1400 ms.

6.4 Summary

The initial contact and spreading of a pendant drop on a solid surface were also jointly investigated through three techniques. The evolution of the electrical signal was firstly detected by the ultra-high-speed DC electrical device with a resolution of 0.8 μs at the time scale within 10 μs after the contact. The power-law relationship between the rescaled spreading radius Φ and the normalized time τ confirms the distinct regimes for the drop spreading dynamics. In the initial spreading stage ($4.06\times10^{-5} < \tau < 6.38\times10^{-4}$), the exponent was 3/4 at a large drop approaching velocity and 2/3 at a small drop approaching velocity, regardless of the viscosities of the various non-Newtonian liquids. This fast-spreading regime was reported for the first time based on the electrical signals. Then the high-speed camera took the relay on the inertial regime with an exponent of 1/2 ($\tau > 8.74\times10^{-4}$). In the flow fields measured by the micro-PIV, velocity rebound in the axial direction gave evidence to the decline of the power-law exponents in the initial stage in comparison with the linear relationship of the drop coalescence. During the filament thinning process of the polymer solutions, the electrical peaks with an interval of 20 ms were observed in the curve of the electrical resistance. Both the molecular weight and polymer concentration showed positive effects on the number and magnitude of the electrical peaks. However, the origin of these peaks remains still mysterious.

In the previous chapters, all the multiphase flows and drop behaviors are emphasized by the passive methods. As introduced in Chapter 1, the active methods are also widely used on the manipulation of the multiphase flows and interfacial phenomena. The active control of the coalescence-breakup of a ferrofluid drop at its bulk surface will be investigated under an external magnetic field in the following Chapter.

Chapter 7 Magnetic manipulation on the coalescence of a ferrofluid drop at its bulk surface

In this part, the active control on ferrofluid drops was realized by an external magnetic field. In the situations with and without a magnetic field, the initial coalescence of a pendant ferrofluid drop at a planar ferrofluid surface was investigated by a high-speed camera. A high-speed micro-PIV technique was employed with a transparent model fluid to reveal the flow fields during the initial coalescence. The scaling laws on the coalescing width were focused to quest the differences in comparison with those in the homogenous Newtonian liquids and the non-Newtonian aqueous liquids.

7.1 Introduction

As stated above in Chapter 4, the coalescence is a widely encountered physical phenomenon at various length scales, from the cell-cell coalescence in micro-biological systems to the solar eruption and magnetic reconnection in the Universe. The initial dynamics of the drop coalescence would significantly affect the coalescing performance, thus a deeper understanding of the drop coalescence dynamics is essential for understanding the complex interfacial phenomena such as emulsion stability. Over the recent decades, numerous studies have been dedicated to the drop coalescence by theoretical, experimental and computational approaches [130, 279, 280]. It was commonly considered that the drop coalescing width expands in a power-law with an exponent of 1/2 in the inertial regime [131, 136-138], where the inertia dominates and the viscous force could be considered negligible. Then the ultrahigh-speed AC and DC electrical devices were developed to push both the spatial and temporary limit further, where the coalescing width extended to highly viscous non-Newtonian liquids of electrolyte polymer solutions was found to expand linearly with time in the inertially limited viscous regime [123, 281].

The above-mentioned studies on drop coalescence were mainly performed using typical Newtonian or non-Newtonian aqueous liquids, which is known as the passive

method without any external force. Furthermore, drop coalescence could also be manipulated through active methods, for example, by applying an additional magnetic field [282], an electric field [189, 283], a focused powerful laser [284] or an acoustic surface wave [193] to cause the instability of interfaces. The magnetic field is unintrusive for fluid, meanwhile, the magnetic control is insensitive to temperature, pH and ion concentration [285], which shows obvious advantages over other active approaches and provides a new contactless alternative for the drop coalescence. Applying a magnetic field is one of the commonly used methods to realize the active control on the ferrofluid drop coalescence.

Placed in an external magnetic field, the ferrofluid would deform into a spiked cone and then divide into many ferrofluid peaks as the magnet gradually approaches the ferrofluid [201]. The shape evolution and pinch-off mechanism for ferrofluid drops generated at a nozzle have attracted attention. The volume and shape of ferrofluid drops could be actively controlled by applying an upward or a downward magnetic field [236]. However, the self-similar pinch-off behavior of ferrofluid drops remains unaffected by the direction of the magnetic field. Under an external axial magnetic field, two drops of the same ferrofluid would exhibit a cycle of coalescence and breakup under the competing effect between the magnetic force, surface tension, inertia and gravity, which is the coalescence-breakup cycle. This periodic phenomenon is also pervasive in the universe, which causes the energy release via a positive feedback mechanism between coronal filament ejection and magnetic reconnection in the solar eruptions [105]. As far as we are concerned, none of the above-mentioned studies reports the periodic coalescence-breakup process of ferrofluid drops in the literature. Moreover, similar phenomena were mainly found on the cosmic scale. Whether the initial coalescing width of ferrofluid drop displays a similar trend as in the Newtonian and non-Newtonian liquids still remains unknown and requires further investigation. The present study aims at performing experimentally the coalescence-breakup cycles of ferrofluid drops under a magnetic field for the first time. The coalescence behavior was also privileged to investigate in particular possible coalescence scaling law for a pendant ferrofluid drop at its bulk surface with and without a magnetic field.

7.2 Experimental section

Ferrofluid is a stable colloid-liquid dispersion where ferromagnetic nanoparticles with a nominal diameter of 10 nm are homogenously suspended in a carrier liquid owing to the presence of surfactants [216]. The oil-based ferrofluid (EMG 900, Ferrotec, Germany) was employed in this work. At 25°C, the measured density and viscosity of the ferrofluid are 1693 kg m^{-3} and 46.43 mPa·s, respectively. The surface tension of the ferrofluid in ambient air is 25.5 mN m^{-1}. The magnetic particle concentration is 16.8 vol%. Fig. 7-1 shows the schematic diagram of the experimental setup. The ferrofluid was driven by a syringe pump (PHD 2000, Harvard Apparatus, USA) to form ferrofluid drops through the stainless steel nozzle. The inner and outer diameters of the nozzle are 0.6 and 0.97 mm, respectively. Three different flowrates of 1.5, 5 and 10 μL·min^{-1} were applied to adjust the approaching velocity of the upper ferrofluid drop, which are referred to hereinafter as $v_{0,s}$, $v_{0,m}$ and $v_{0,l}$, respectively. The approaching velocities of the upper ferrofluid drop before coalescence corresponding to various operating conditions are gathered in Table 7-1. A circular neodymium iron boron (NdFeB) magnet (Supermagnete, France) was placed on a fine-tuning platform to form an external axial magnetic field. A ferrofluid container was deposed between the nozzle and the magnet. The magnetic flux density *B* at the tip of the ferrofluid peak was measured using a Gaussmeter (GM07, Hirst, UK).

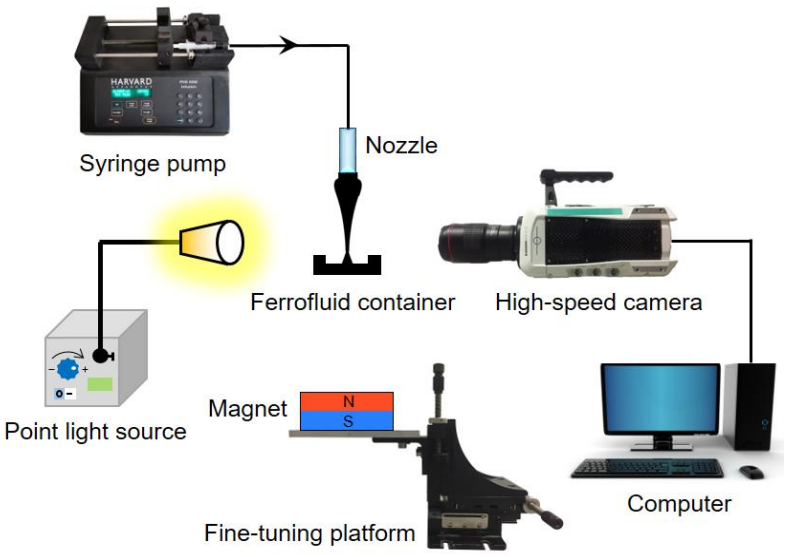


Fig. 7-1 Schematic diagram of the experimental setup.

Table 7-1 Approaching velocities of the upper ferrofluid drop before coalescence.

Magnetic field	$v_{0,s}$ (mm·s^{-1})	$v_{0,m}$ (mm·s^{-1})	$v_{0,l}$ (mm·s^{-1})
/	13.19	16.50	19.80
B = 73.10 mT	8.97	13.46	15.70
B = 85.54 mT	62.82	71.79	76.28
B = 95.25 mT	83.58	89.74	94.23

By adjusting the fine-tuning platform, the vertical distance z starting from the top surface of the magnet varied between 4 mm and 110 mm. The magnetic fields B corresponding to various vertical distances z were measured using a Gaussmeter (GM07, Hirst, UK), as plotted in Fig. 7-2.

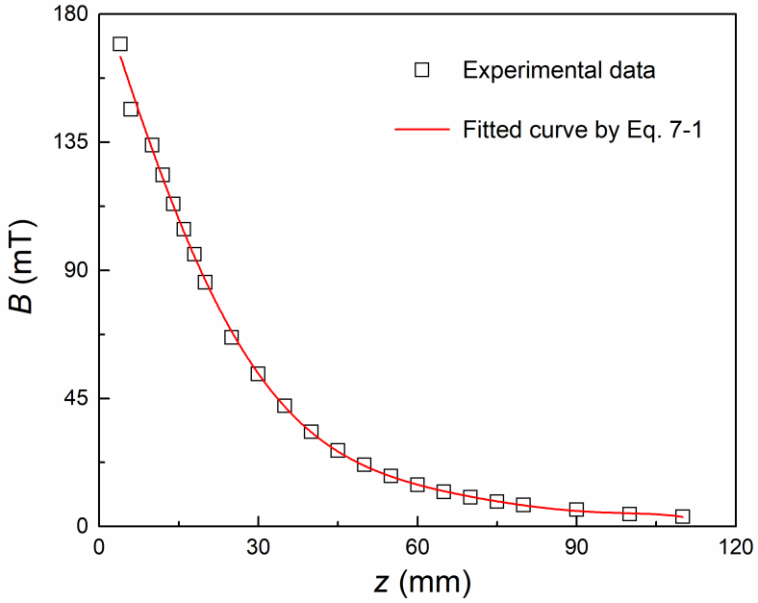


Fig. 7-2 Variation of the magnetic field B with the vertical distance z from the top surface of the magnet.

The relationship between B and z was fitted by a sixth-order polynomial:

$$B(z) = -1.1\times10^{-9}z^6 + 3.87\times10^{-7}z^5 - 5.30\times10^{-5}z^4 + 2.97\times10^{-3}z^3 - 1.11\times10^{-2}z^2 - 5.66z + 187.77 \quad (7\text{-}1)$$

where B and z are in mT and mm, respectively. When performing the coalescence-breakup of ferrofluid drops, the vertical distances between the initial coalescing point and the top surface of the magnet were measured. Thus, the

corresponding magnetic fields at the initial coalescing point could be calculated according to Eq. 7-1. All the magnetic fields *B* mentioned below indicate the values at the initial coalescing point.

By adjusting the fine-tuning platform, the magnetic flux density exerted on the ferrofluid becomes stronger when the magnet moves vertically upwards toward the nozzle. The ferrofluid would be divided into more ferrofluid peaks, thus the volume of each peak decreases and the height becomes lower. As shown in Fig. 7-3, there are 20, 22 and 28 ferrofluid peaks at the edge of the container, corresponding to the magnetic flux density of 73.10 mT, 85.54 mT and 95.25 mT, respectively. In the experiments, one of the ferrofluid peaks at the edge of the container was focused to observe the coalescence with the pendant ferrofluid drop generated at the nozzle. As there are tens of ferrofluid peaks in total in the container, the volume increasing in the container resulted from the continuous feeding of the pendant ferrofluid drop has a negligible influence on a single ferrofluid peak. Thus, the shape of the ferrofluid peak is regarded as stable in the experiments.

The whole process for ferrofluid drop coalescence was recorded by a high-speed camera Phantom V711 (Vision Research, USA) coupled with a zoom lens (MP-E 65mm f/2.8, Canon, Japan). The images were captured at up to 35015 frames per second (fps). The image resolution was 400 × 360 pixels without a magnetic field and 192 × 600 pixels under various magnetic fields. The coalescing width in the obtained images was analyzed one by one through a self-programmed MATLAB algorithm. Due to the limitation of the high-speed camera that can only provide the temporary variation of the coalescing width from the visualized images, a high-speed micro-PIV was developed to gain insight into the flow field evolution during the initial coalescence. To capture the trajectory of the seeding particles in the laser sheet by the high-speed camera, a transparent Newtonian fluid of glycerol solution of similar viscosity as the ferrofluid was employed as a model fluid for the black-brown ferrofluid. The fluorescence particles (MF-RhB-Partikel-G020, Dantec Dynamics, Denmark) with a diameter of 1-20 μm was added. The seeding particles in the laser sheet were excited by two oppositely placed lasers of 1 mW (LaserMax Inc., USA). The high-speed images recording the temporary position of the seeding particles were captured at 3000 fps and then processed by the software DynamicStudio (Dantec Dynamics, Denmark). By tracking the particle moving distance between every two

successive images with a fixed time interval of 0.33 ms, the velocity fields were computed by the adaptive PIV algorithm with a grid step size of 16 × 16.

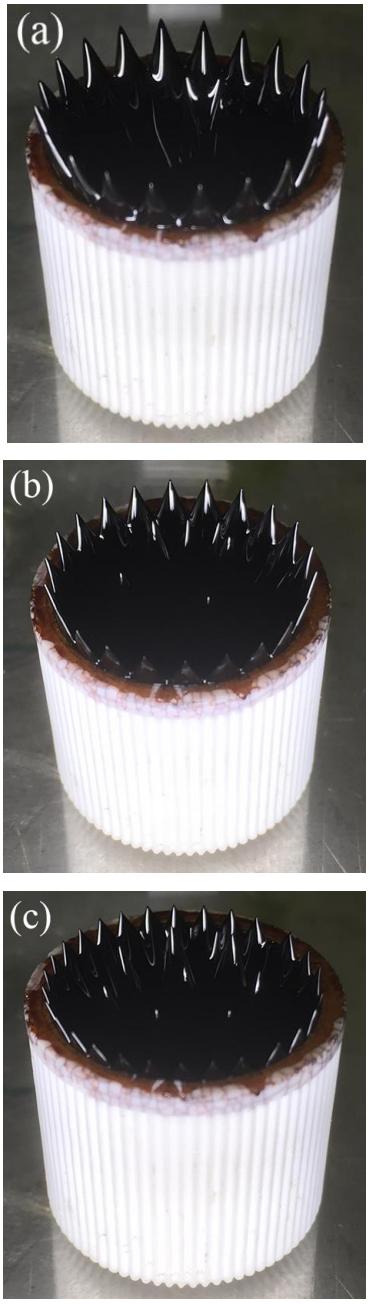


Fig. 7-3 Ferrofluid peaks in the container under various magnetic fields. (a) B = 73.10 mT: 20 ferrofluid peaks in total at the edge of the container. (b) B = 85.54 mT: 22 ferrofluid peaks in total at the edge of the container. (c) B = 95.25 mT: 28 ferrofluid peaks in total at the edge of the container. The circular magnet is placed on a fine-tuning platform below the ferrofluid container and not shown in the image.

7.3 Results and discussion

7.3.1 Initial coalescence of a ferrofluid drop without a magnetic field

The initial coalescence of a pendant ferrofluid drop at the surface of the same ferrofluid was firstly investigated in the absence of an external magnetic field. The time zero t = 0 ms is defined when the first contact of the pendant ferrofluid drop and the bulk ferrofluid surface is observed from the high-speed images. At 1 ms before the coalescence (t = -1.00 ms), the shapes of the liquid surface and its pendant drop corresponding to the ferrofluid and the Newtonian fluid are displayed in Fig. 7-4(a) and Fig. 7-4(b), respectively. The upper pendant ferrofluid drop becomes elongated towards the bulk ferrofluid and evolves as an ellipsoid, while the ferrofluid surface exhibits a conical shape towards the ferrofluid drop. The obvious differences were observed in comparison with the round-shaped pendant drop and the planar liquid surface of the Newtonian fluid [Fig. 7-4(b)] as well the non-Newtonian polymer solutions. Sequences for the initial coalescence of a ferrofluid drop at various approaching velocities of the upper ferrofluid drop are illustrated in Fig. 7-4(c)-(e). As soon the upper ferrofluid drop touched the ferrofluid surface, the coalescing section would form a ferrofluid bridge. Then the meniscus bridge continued to expand and the profile of the coalescing section gradually evolved into a curved interface. The coalescing width kept increasing until the maximum and then entered the thinning process until the final pinch-off followed by the final breakup. According to the high-speed images, no obvious difference in the coalescing width was observed by the naked eye.

The ferromagnetic nanoparticles dispersing in the carrier fluid could be regarded as numerous individual magnets. The north pole or the south pole of the magnetic particles in the upper pendant ferrofluid drop would attract their opposite ones in the bulk ferrofluid. The pendant ferrofluid drop and its bulk surface would move towards each other under the magnetic attraction between dispersed ferromagnetic particles. Due to the relatively small vertical distance between the ferrofluid drop tip and its bulk surface and the high concentration of the ferromagnetic particles, noticeable deformation in Fig. 7-4(a) could be observed as an interaction consequence between ferromagnetic particles.

The conical angle of the ferrofluid surface θ is 158° at the first contact. Among the covered range of the approaching velocities in this work, the cone angle is independent of the ferrofluid drop approaching velocity. A similar Taylor cone was also observed in the electrically driven coalescence between two oppositely charged drops, and the drop coalescence would always occur when the cone angle is below a critical value of 118.4°. Otherwise, they rebound without coalescence [183].

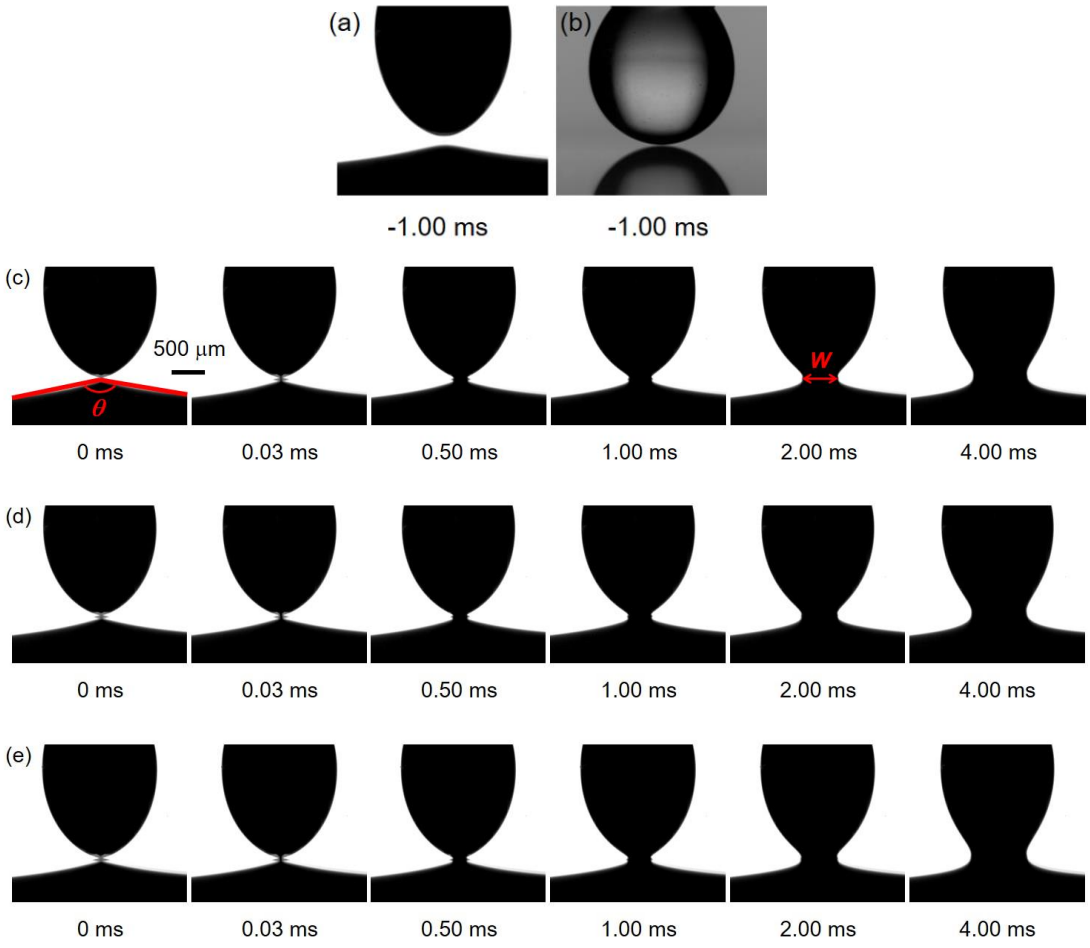


Fig. 7-4 (a) Shape of the ferrofluid surface and the pendant ferrofluid drop at 1 ms before the coalescence (t = -1.00 ms). (b) Shape of the Newtonian fluid surface and its pendant drop at t = -1.00 ms. (c) Sequence for the initial coalescence of a ferrofluid drop without a magnetic field. $v_{0,\,s}$ = 13.19 mm·s^{-1}. The conical angle θ of the ferrofluid surface is 158° at t = 0 ms. W indicates the coalescing width which is nothing but the ferrofluid cylinder diameter. (d) Sequence for the initial coalescence of a ferrofluid drop. $v_{0,\,m}$ = 16.50 mm·s^{-1}. (e) Sequence for the initial coalescence of a ferrofluid drop. $v_{0,\,l}$ = 19.80 mm·s^{-1}. The same scale bar of 500 μm applies for all images.

The temporary variation of the coalescing width W of the ferrofluid drop at its bulk surface in the absence of an external magnetic field is displayed in Fig. 7-5. Without a magnetic field, the coalescing section follows a power law with time. The exponent $\alpha = 0.64 \pm 0.01$ is regardless of the approaching velocity of the upper ferrofluid drop, as shown in Fig. 7-4(c)-(e). The coalescing width corresponding to the Newtonian liquid of water + 5 wt% NaCl with an exponent of $\alpha' = 0.58$ was also plotted for comparison. Both the exponents for the ferrofluid drop without a magnetic field and the Newtonian liquid are in coincidence with our previous works on the non-Newtonian liquids, where the coalescing width varies as the square root of time. The above-mentioned variations of the coalescing width lie in the inertial regime, where the inertia dominates and the viscous force is negligible. As the coalescing section continues to expand, it reaches a maximum width W_{max} of 1.37 mm at about 10 ms after the coalescence.

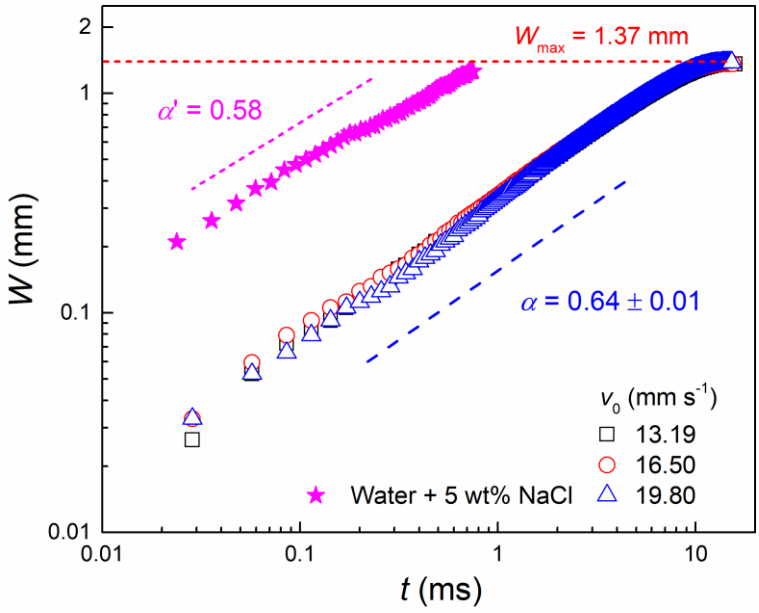


Fig. 7-5 Temporary variation of the coalescing width W for the ferrofluid drop at its bulk surface in the absence of a magnetic field. W_{max} indicates the maximum coalescing width. Solid star symbols represent the coalescing width corresponding to the Newtonian liquid of water + 5 wt% NaCl with an exponent of $\alpha' = 0.58$.

7.3.2 Initial coalescence of a ferrofluid drop under a magnetic field

7.3.2.1 Dynamics of the initial coalescence of a ferrofluid drop

Then the axial magnetic field was applied to investigate its effect on the initial coalescence of a ferrofluid drop at the bulk ferrofluid surface. When the magnetic field is applied, the ferrofluid in the reservoir would immediately exhibit peaks. Then, the ferrofluid is fed through the nozzle to form a ferrofluid drop. Once the pendant ferrofluid drop reaches a critical size, it deforms into a conic shape and the magnetic force attracts the upward and the downward ferrofluid together. In addition, high-speed images demonstrate that the ferrofluid drops deform into more spiked cones as getting closer to the coalescing point. As soon as the ferrofluid drops get in touch, a small amount of ferrofluid pierces the surface of the tips between the two leading edges of the approaching cones. Then, a thin ferrofluid bridge forms with a visible gap in the order of tens of micrometers between the leading edges. For water drops in ambient air, the bridge forms only when the gap between salt drops is 280^{+370}_{-160} nm and then the van der Waals forces play the leading roles [110]. This implies that the van der Waals force is not the driving force to form the ferrofluid bridge in our experiments. The ferrofluid bridge makes plain that the convex curvature around the thin bridge is much larger than the concave curvature across the neck at the initial coalescence. Thus, the capillary pressure in the neck is larger than the center of the drop. This causes then the collapse of the neck.

Sequences for the initial coalescence of a ferrofluid drop at its bulk surface under various magnetic fields are displayed in Fig. 7-6. The pendant ferrofluid drop deforms into sharp conical shapes before coalescence. The conical angle ψ of the pendant ferrofluid drop at the first contact is 18°, 16° and 13° under low, medium and high magnetic flux density, respectively. The conical angle δ of the ferrofluid peak in the bulk container at the first contact increases with the applied magnetic flux density, which is 32°, 42° and 50°, respectively. During the very initial stage of the coalescence, the upper and lower ferrofluid peaks would form a ferrofluid bridge. Then a sudden transition to a smooth interface profile occurred in the coalescing section, as illustrated in the last three sub-figures in Fig. 7-6(a) and Fig. 7-6(b). Such a sudden transition was not observed at the high magnetic flux density of B = 95.25 mT.

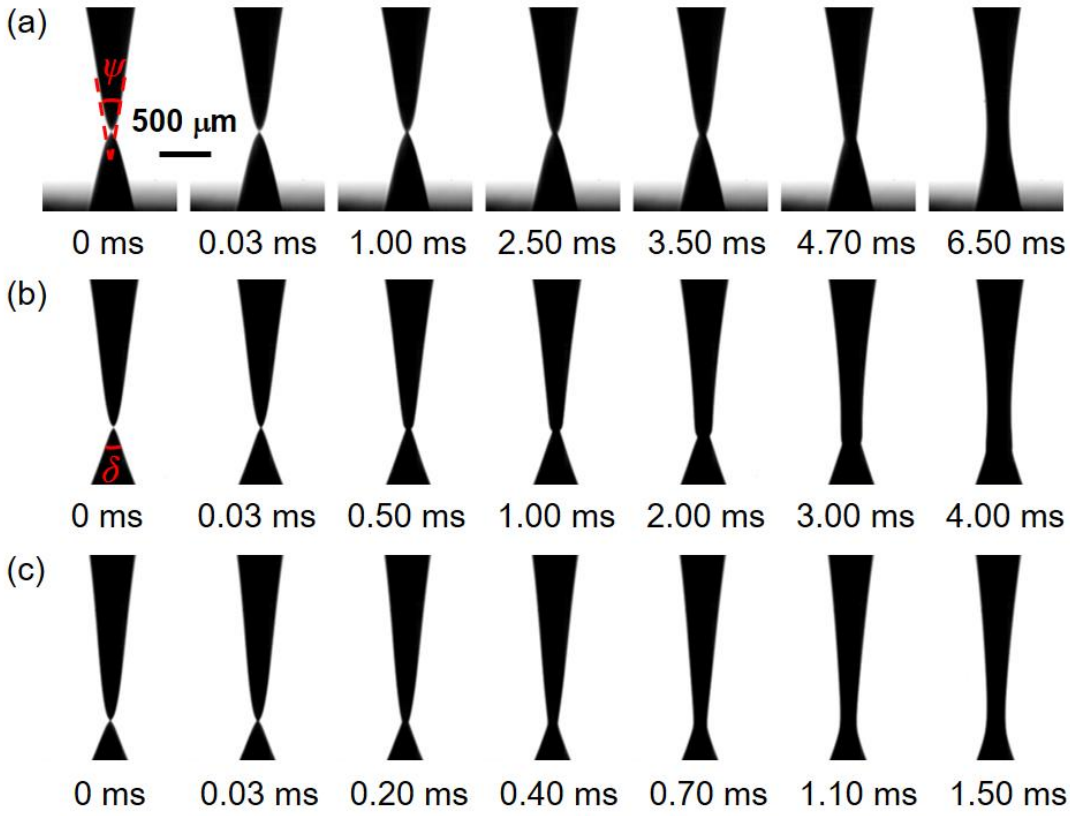


Fig. 7-6 Sequences for the initial coalescence of a ferrofluid drop at its bulk surface under various magnetic fields. (a) B = 73.10 mT, $v_{0,s}$ = 8.97 mm·s^{-1}, ψ = 18°, δ = 32°. (b) B = 85.54 mT, $v_{0,s}$ = 62.82 mm·s^{-1}, ψ = 16°, δ = 42°. (c) B = 95.25 mT, $v_{0,s}$ = 83.58 mm·s^{-1}, ψ = 13°, δ = 50°. All images share the same scale bar of 500 μm.

To discover the mechanism governing the initial coalescence dynamics, a high-speed micro-PIV technique was applied to a transparent Newtonian model liquid of glycerol-water solution. It displays similar properties compared to the ferrofluid, in particular the viscosity, and allows then the velocity field quantification in both the drop and bulk liquid. The sequence of the high-speed images and velocity fields at t = 0.33 ms, t = 0.67 ms and t = 1.00 ms are illustrated in Fig. 7-7, respectively. Owing to the sudden release of surface energy and its conversion to kinetic energy, both the radial and axial velocities accelerated during the initial coalescence. In the radial direction, the coalescing section expanded as the radial velocity developed. As soon as the drop contacted the liquid surface, an interesting phenomenon of damping in the axial direction drew our attention. According to our previous study on the highly viscous non-Newtonian liquid, the reflection of velocity was cushioned due to the

high liquid viscosity. Compared with highly viscous liquids, the axial velocities oscillate between the nozzle and the coalescing zone and they are mainly caused by the low drag exerted on the pendant drop in this much less viscous liquid.

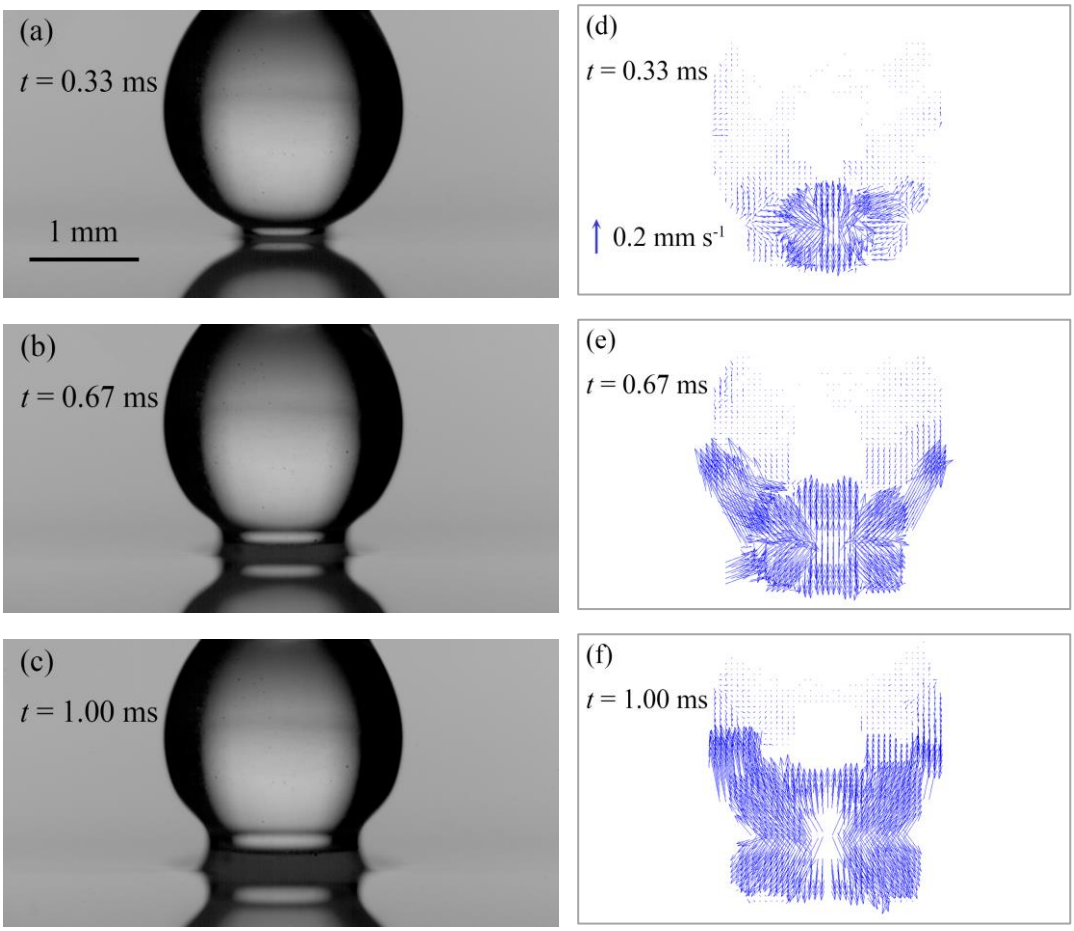


Fig. 7-7 Experiments by the micro-PIV to follow the velocity fields in the drop and bulk liquid during the initial coalescence in a transparent Newtonian model liquid. (a-c) High-speed images of the initial coalescence at t = 0.33 ms, t = 0.67 ms and t = 1.00 ms. (d-f) Velocity fields of the initial coalescence at t = 0.33 ms, t = 0.67 ms and t = 1.00 ms. Newtonian fluid of glycerol solution with similar viscosity to the ferrofluid. $v_{0,}$ = 0.06 mm·s^{-1}. The scale bars for length and velocity indicate 1 mm and 0.2 mm·s^{-1}, respectively.

Under various external magnetic fields, the corresponding coalescing widths are plotted in Fig. 7-8. At low magnetic flux density of B = 73.10 mT, the coalescing section grows to 0.1 mm within 4 ms as a power law with an exponent of $\beta_1 = 0.59 \pm 0.01$. The damping phenomenon resisted the breakup of the liquid film

and thus led to a delay of the ferrofluid drop coalescence. The inertia and magnetic attraction in the axial direction towards the coalescing section gradually dominated as the reflecting velocities, similar to the previously reported rebound on the solid surface to some extent, became weakened. Then the coalescence is accelerated with an exponent of $\beta_2 = 3.02^{+0.22}_{-0.18}$. The sudden transition of the interface profile shown in Fig. 7-6(a) gives reliable evidence to the acceleration of the coalescing width, which also arises at about 4 ms after the first contact.

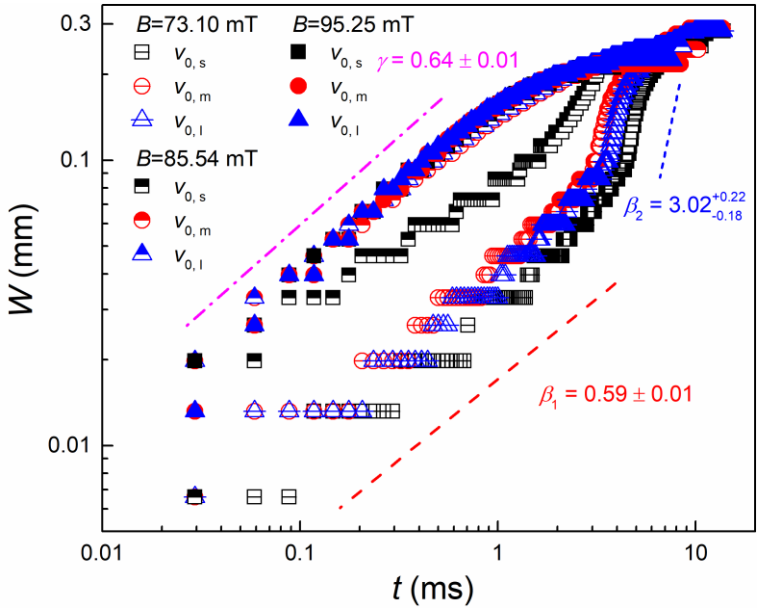


Fig. 7-8 Temporary variation of the coalescing width *W* for the ferrofluid drop at its bulk surface in the presence of various magnetic fields. The applied magnetic flux densities *B* were 73.10 mT, 85.54 mT and 95.25 mT.

At high magnetic flux density of *B* = 95.25 mT, the coalescing section expands with the same exponent of $\gamma = 0.64 \pm 0.01$ within 1 ms as that without a magnetic field, then it slowed down towards a maximum coalescing width of 0.22 mm.

At medium magnetic flux density of *B* = 85.54 mT, a transition trend between the lower and higher magnetic flux densities attracted our attention. The coalescing width at low approaching velocity showed a similar trend with those under low magnetic flux density of *B* = 73.10 mT. While the width at the other two approaching velocities developed the same as that under high magnetic flux density of *B* = 95.25 mT. It is worth noting that the only transient trend at low approaching velocity under a medium magnetic field was observed. The mechanism behind this peculiar

phenomenon requires further investigation to better understand a possible competing mechanism between the magnetic flux density and the approaching velocity of the drop.

The maximum coalescing widths W_{max} for all cases are also collected, as illustrated in Fig. 7-9. The maximum coalescing widths regardless of the approaching velocity are 1.37 mm without a magnetic field and 0.28 mm, 0.25 mm and 0.22 mm under low, medium and high magnetic flux density. The maximum coalescing width decreases with the magnetic flux density, indicating an opposite effect on the ferrofluid drop coalescence by the magnetic field. The maximum coalescing widths under various magnetic flux densities could be fitted as an exponential function, as expressed in Eq. (7-2). The predicting model enabled one to estimate the maximum coalescing width corresponding to the magnetic flux densities beyond the covered range of our works. This result is consistent with the following analysis based on the force balance between the inertia, surface tension, magnetic force and gravity (cf. below). As the oscillating frequency exponentially increases with the magnetic flux density, the maximum coalescing width would exponentially decrease with the magnetic flux density: a faster oscillation does not allow a sufficient expansion of the maximum coalescing width.

$$W_{max} = 1.37\exp(-0.02B) \tag{7-2}$$

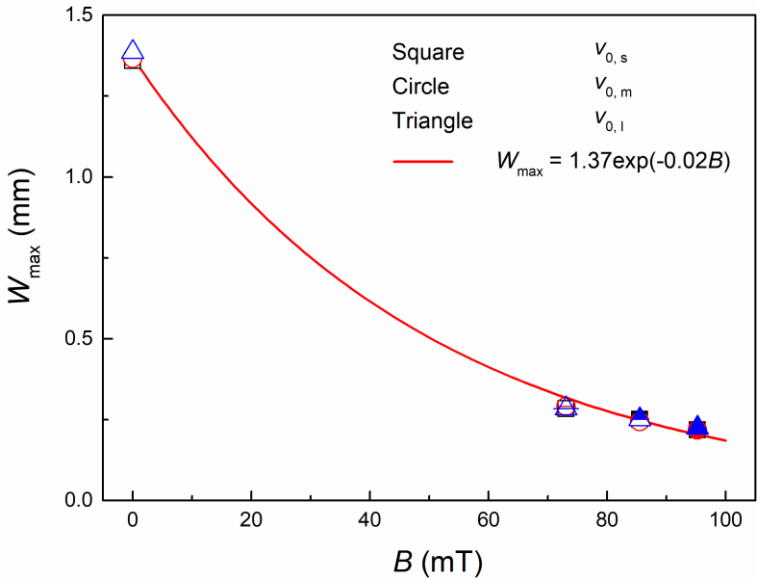


Fig. 7-9 Variation of the maximum coalescing width with and without a magnetic field.

7.3.2.2 Self-sustained coalescence-breakup cycles of ferrofluid drops

The ferrofluid column exhibits various behaviors after reaching its maximum coalescing width: under a relatively small magnetic field, the column would maintain its maximum coalescing width with the continuous feeding of ferrofluid by the syringe pump; under a higher magnetic field, the column would then gradually collapse until the final breakup. A critical magnetic field around B = 35 mT was observed in our experiments, above which the ferrofluid column will enter the periodic oscillation of breakup and coalescence. For moderate magnetic fields, the ferrofluid column evolves into a filament before collapsing at the lower end prior to the upper end. After the final breakup, the filament recoils to the upper ferrofluid drop without a satellite droplet. At higher magnetic fields, the ferrofluid column gradually emerges as a sharp cone before the breakup. The transition of the pinch-off and breakup pattern is caused by the difference between the pinch-off rates.

After the breakup, the upper ferrofluid drop recoils towards the nozzle and the lower remaining ferrofluid peak evolves into a self-organized and reshape stage. With the continuous feeding of the ferrofluid by the syringe pump to increase the upper pendant ferrofluid drop, a new cycle of coalescence-breakup would start again and the periodic phenomenon repeats in a self-sustained way. Unlike a cylindrical liquid column undergoing capillary instability, a rigorous analysis is still beyond reach for the above-mentioned coalescence-breakup cycle of ferrofluid drops, which is never reported in the literature. It is worth noting that the magnetic field B is a function of the vertical distance z and the shape of both the upper ferrofluid drop and bottom ferrofluid peak varies drastically with z and time t. The singularity corresponding to the coalescence and breakup poses also a particular problem. Nevertheless, a simplified force balance could gain some insight into the physical mechanism of this periodic phenomenon. A certain ferrofluid volume V showed in the inserted circle of Fig. 7-10(a) including both the upper drop and bottom peak in touch (either coalescence or breakup) is considered through a local curvature r based on the surface shape divergence $\nabla.\vec{n}$ in terms of the two principal radii of the upper ferrofluid drop R_1 ($\approx d_c/2$) and the bottom ferropeak R_2: $\nabla.\vec{n} = 1/R_1 + 1/R_2 \approx 2/W_n = 1/r$, where W_n is the previously defined neck width. The balance applies for the inertia $\vec{F}_i$, surface tension $\vec{F}_\sigma$, magnetic $\vec{F}_m$ and gravity $\vec{F}_g$ forces acting in this representative volume V: $\vec{F}_i + \vec{F}_\sigma + \vec{F}_m + \vec{F}_g = \vec{0}$.

According to the cylindrical coordinate system displayed in Fig. 7-10(b), this force balance can be further simplified in the horizontal radial *r* direction

$$\frac{d^2r}{dt^2} + \omega_0^2 r = 0 \tag{7-3}$$

where a proper pulsation $\omega_0 = \sqrt{\sigma / \rho V}$ can be deduced for this oscillator and related to a frequency $\omega_0 = 2\pi f$.

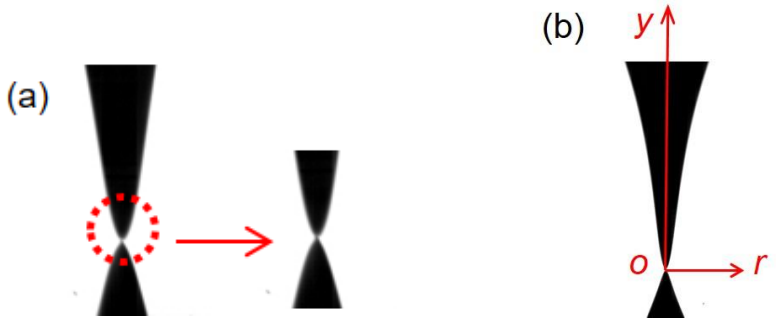


Fig. 7-10 (a) Partial magnification of the liquid bridge at initial coalescence. (b) Definition of the origin point and the cylindrical coordinate system.

In this work, the periodic frequency *f* ($f = \omega_0 / 2\pi$) of the coalescence-breakup cycles was experimentally found to increases with the magnetic field, as shown in Fig. 7-11. The frequency could be fitted as an exponential function with the magnetic field

$$f = 0.58 - 0.61\exp(-0.004B) \tag{7-4}$$

Under a higher magnetic field, the magnetic force exerted on the upper ferrofluid drop is larger, in combination with the gravity, thus the cyclic frequency increases consecutively. At *B*=169 mT, the frequency of the whole coalescence-breakup cycle increases by nearly an order of magnitude compared with that under a critical magnetic field around 35 mT. In the above force balance leading to a harmonic oscillator, the relationship between the magnetic field *B* and the frequency *f* is apparently not straightforward. However, a close look at the representative volume *V* shown in Fig. 7-10(a) used in the establishment of the above-mentioned force balance reveals that *V* depends inversely on the magnetic field *B*. Obviously, under a low magnetic field, the shape of both the upper and bottom ferrofluid drops is much more rounded than that under a higher magnetic field and this leads to a bigger volume *V*. The following relationship could then be inferred: $V \propto 1/B$. As $f \propto \omega_0 \propto 1/V^{1/2}$

(Eq. 7-3), one can deduct that the oscillation frequency increases with the magnetic field. This confirms the experimental measurements (Eq. 7-4). Certainly, a rigorous modeling of a spatial distributed magnetic field $B(r,\mathrm{y})$ in the volume V instead of a constant value B at a given position would be required through a detailed numerical approach. A real relationship between f and B should be of complex and non-linear nature. To the best of our knowledge, it is never reported in the literature for this periodic phenomenon stemming from a dynamical competition between mainly the inertia, surface tension, magnetic force and gravity.

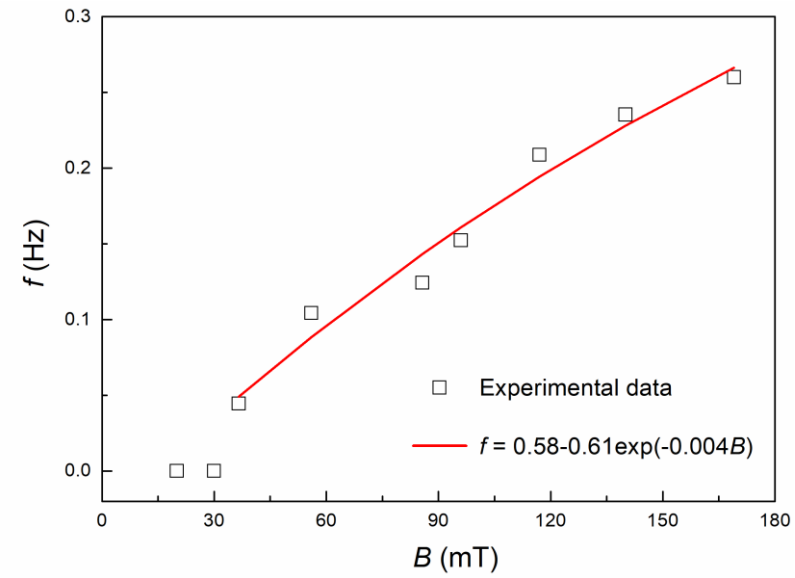


Fig. 7-11 Frequency variation for the whole coalescence-breakup cycle as a function of the magnetic fields.

7.4 Summary

In summary, the active manipulation on the coalescence and breakup of a ferrofluid drop was realized by applying an external magnetic field. In the absence of a magnetic field, the ferrofluid drop becomes elongated in the axial direction towards the conical ferrofluid surface. The cone angle of the ferrofluid surface was 158° and independent of the approaching velocity of the upper ferrofluid drop. The width of the coalescing section followed the power-law with time with an exponent of 0.64.

When applying a magnetic field, both the pendant ferrofluid drop and ferrofluid surface in the bulk deform into sharp conical peaks before coalescence. The upper conical angle decreases from 18° to 13° and the lower conical angle increase from 32° to 50° in the covered magnetic flux density range. The power-law exponent of the coalescing width was 0.64 under the medium and high magnetic fields. A similar exponential trend was observed within 4 ms under the low magnetic field, followed by a sudden acceleration to an exponent of 3.02. The damping phenomenon shown in the flow fields through the use of the transparent model fluid at the initial coalescing gave evidence to the dramatic increase in the coalescing speed. The mechanism behind the only transient trend at low approaching velocity under the medium magnetic field requires further investigation.

The ferrofluid column turned to the pinch-off and breakup stage after reaching its maximum coalescing width. A critical magnetic field around 35 mT was observed, above which the ferrofluid column will collapse and the coalescence-breakup cycle repeats periodically. A simplified force balance between the inertia, surface tension, magnetic force and gravity revealed the periodic character of a driven harmonic oscillator, and confirmed the experimentally observed dependence of the oscillation frequency f with the magnetic field B: $f = 0.58 - 0.61\exp(-0.004B)$. The discovery of the self-sustained coalescence-breakup pattern could lay a foundation for further applications such as the magnetic valves. In addition, a drivable colloidal suspension like ferrofluid could gain new insight into the complex coalescence phenomena with respect to a homogenous liquid.

Chapter 8 Conclusions, innovations and perspectives

8.1 General conclusions

The multiphase flows and interfacial phenomena, in particular the drop coalescence and spreading, at different scales have been systematically and comprehensively investigated in the present work. A high-speed camera, an ultra-high-speed DC electrical device, and a high-speed micro-PIV were utilized to have a deep insight into the flow behaviors. The general conclusions can be summarized as follows:

(1) For the elastic droplet formation in a microfluidic T-junction, the peculiar beads-on-string flow was observed due to the droplet elasticity. In the stretching stage of droplet formation, the maximum value of the thread length at the breakup point is positively correlated to the droplet elasticity. The droplet elasticity plays a significant role in the droplet formation process, while its positive effect on the final droplet size is relatively limited. A new scaling law of the droplet size was proposed by introducing the elasticity number. For the formation of silicone oil droplets in elastic solutions at a flow-focusing junction, three flow regimes were divided by the dimensionless parameters of *We* and *Ca* in the map of various flow patterns. The width of the dispersed thread followed the power law with an exponent of 1/3 before the final pinch-off. The flow fields in the dispersed phase gave a deep insight into the dynamics of droplet formation. A modified model for predicting the droplet size was proposed as well.

(2) The stretching and breakup of elastic droplets were also performed in a flow-focusing device. The regime diagram was plotted based on the drop elasticity and the operating condition to distinguish three regimes. In the stretch-rebound regimes with and without a tail, the predicting models for the maximum droplet length were proposed within two ranges divided *Ec*. The droplet transformed from elongation into breakup when its maximum length was larger than 2.2 times of the initial length. In the stretch-breakup regime, the negative effect of the drop elasticity on the size ratio between two daughter droplets was also investigated.

(3) The initial drop coalescence at a planar liquid surface was jointly investigated by three techniques. With a resolution of 0.8 μs, the ultra-high-speed DC electrical device allowed to monitoring the evolution of the coalescing width down to 7.4 μm within a duration of 10 μs. The relationship between the rescaled coalescing width by the drop's maximum diameter and the normalized time by the inertial time confirms the distinct regimes previously reported for drop-drop configuration: linear in the ILV regime, square root in the inertial regime and possibly a transient viscous regime in between. The flow fields with a frequency of 3000 velocity fields per second were measured by the micro-PIV and revealed the transformation of surface energy to kinetic energy during the fast coalescence.

(4) The initial contact and spreading of a drop at a polished solid surface were also investigated experimentally by three techniques. In the initial spreading, the rescaled spreading radius followed the power-law relationship with the normalized time, where the exponent is 3/4 at large approaching velocity and 2/3 at a small approaching velocity. It worth noting that the measurements of the flow fields were extended to 5000 velocity fields per second, a frequency never reported in the literature. The significant rebound of the axial velocity was observed in the flow fields during the initial drop spreading, which could explain the observed deviation between various exponents of the drop coalescence with a liquid and the drop spreading on a solid. Also, the electrical peaks with an interval of 20 ms were observed during the filament pinch-off of the polymer solutions with high molecular weights. The polymer filament served as a switch which regularly adjusted the transportation of the electrically charged macromolecule.

(5) The active manipulation on the coalescence and breakup of a ferrofluid drop was realized by applying an external magnetic field. Evident elongation of the ferrofluid drop in the axial direction could be observed even in the absence of a magnetic field due to the internal organization of magnetic colloids. When applying a magnetic field, both the pendant ferrofluid drop and the bulk ferrofluid surface deformed into sharp conical peaks before coalescence. The upper conical angle decreased from 18° to 13° and the lower conical angle increased from 32° to 50° in the covered magnetic flux density range. The coalescing width followed a power law with an exponent of 0.64 for the situation without a magnetic field and with medium and high magnetic fields. A similar exponential trend was observed within 4 ms under

the low magnetic field, followed by a sudden acceleration to an exponent of 3.02. The damping phenomenon shown in the flow fields at the initial coalescing stage gives evidence to the dramatic increase in the coalescing speed. The self-sustained coalescence-breakup cycles of ferrofluid drops were observed for the first time above a critical magnetic field around 35 mT. A simplified force balance allowed to capturing the periodic mechanism involved in this driven harmonic oscillator. The periodic frequency of the coalescence-breakup cycles was found to increase exponentially with the applied magnetic field as $f = 0.58 - 0.61\exp(-0.004B)$.

8.2 Innovations

The innovations and highlights of the research are featured as follows:

(1) The elastic PEO solutions were employed to study the dynamics of droplet formation, stretching and breakup. To quantify the effects of the liquid elasticity on the droplet behaviors, the strength of the elasticity was characterized by the elasticity number and the elasto-capillary number. The predicting models for the droplet size in the microfluidic devices were established in consideration of the dimensionless parameters.

(2) To have a deep insight into the flow fields and push both the spatial and temporary limit further, the high-speed micro-PIV up to 5000 velocity fields per second and the ultra-high-speed DC electrical device with a sampling speed of 1.25×10^6 Hz were firstly developed and employed on the initial drop coalescence, initial drop spreading and the thinning of the polymer thread. The initial regimes of drop coalescence and spreading were revealed by analyzing the electrical signals and high-speed images. The evolutions of the velocity fields revealed the energy transformation and provided evidence for the initial dynamics of drop coalescence and spreading.

(3) The active manipulation of ferrofluid drops was realized by introducing an external magnetic field. In the absence and presence of a magnetic field, the shape evolution and the coalescing width during the coalescence of a ferrofluid drop at the bulk surface were investigated experimentally. The coalescence-breakup cycle of a ferrofluid drop at its bulk liquid surface was reported for the first time. The

exponential model was proposed to predict the increasing periodic frequency with the applied magnetic field.

8.3 Perspectives

The present work aimed at studying the multiphase flows and interfacial phenomena at multiscale, which could lay a solid foundation on the design and optimization of the multiphase flow devices and promoted the development of the theoretical models. However, there are still numerous research fields of interest that require further investigation.

(1) In our work on the initial coalescence between an aqueous drop and the flat liquid surface, few data were acquired for the transient viscous regime due to the overlay between the DC approach and high-speed camera. Further investigation is required to verify a possible viscous effect in the initial drop coalescence. Such as the numerical simulation by the molecular dynamics and lattice Boltzmann approaches, which could put the temporal resolution further than the experimental methods.

(2) The thinning and pinch-off of the polymer solution's thread requires further investigation. Advance experimental devices such as the X-ray scattering would supply solid explanations on the regular electrical peaks during the thinning of the polymer filament.

(3) The drop coalescence at a bulk liquid surface with a layer of superhydrophobic particles was initiated and some preliminary results are shown in Fig. 8-1. The velocity fields during the initial coalescence deserve further explorations in-depth.



Fig. 8-1 Sequence for the initial coalescence of a pendant drop at planar liquid surface covered with superhydrophobic particles.

(4) The aqueous drop impact on a superhydrophobic solid surface is shown in Fig. 8-2. The bouncing phenomenon might emerge due to the existence of the superhydrophobic properties. The velocity fields in the drop during the contact and bouncing require further studies.

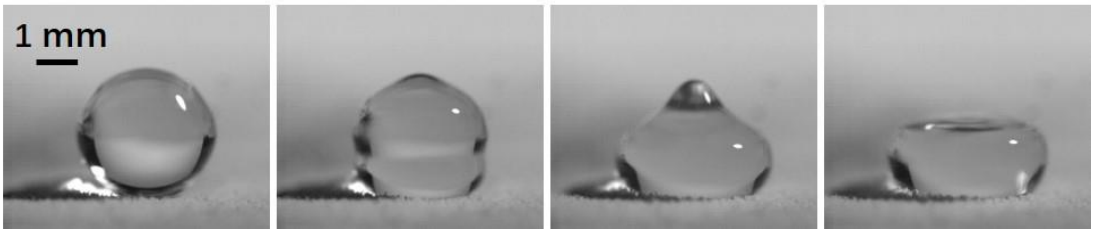


Fig. 8-2 Sequence for initial contact and spreading of a drop on a superhydrophobic solid surface.

(5) The interface disturbance could be conducted by a rotating rod, a rising bubble, and superhydrophobic particles. The dynamical behavior of liquid-liquid and liquid-superhydrophobic solid interfaces under a controlled solicitation through the passage of the rising gas bubble of the desired size deserves further exploration. The rising bubble at the liquid interface of 20 wt% Emkarox solution before and after the bursting is shown in Fig. 8-3. For liquid-liquid (L-L) systems, both the Newtonian and non-Newtonian aqueous solutions (such as PAAm or PEO solutions) could be employed as the heavy phase. Silicone oil of various viscosity could serve as the light phase.

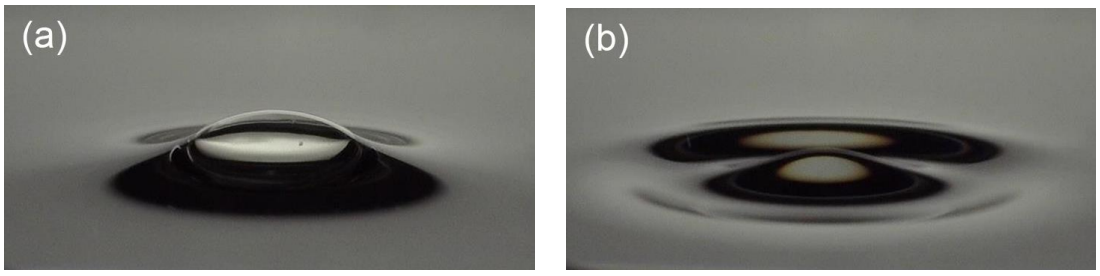


Fig. 8-3 Bubble life at the liquid interface. (a) Rising bubble at the liquid interface before bursting. (b) Rising bubble at the liquid interface at the bursting moment. Liquid: 20 wt% Emkarox.

At a liquid-superhydrophobic solid interface, the rising bubble would drain the superhydrophobic particles before the bursting, as displayed in Fig. 8-4. The instantaneous velocity fields around the rising bubble could be measured using a PIV

system. Besides the potential industrial applications, the bubble life at liquid-liquid and liquid-solid under various operating conditions can also provide the interfacial modeling and numerical simulation with adequate experimental validation for the boundary conditions at an interface.

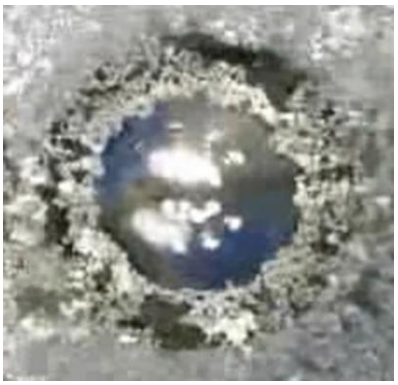


Fig. 8-4 Bubble life at the water-superhydrophobic solid interface. Top view of the bubble draining superhydrophobic particles before bursting.

(6) Both the viscoelastic fluids and the active manipulation method by an external magnetic field were employed in the present thesis, they could be combined and applied in our further works. Motivated by the negative wake behind either a sedimenting solid sphere or a rising gas bubble in viscoelastic fluids such as PAAm solutions, the velocity fields around the horizontally moving “microswimmer” in the viscoelastic fluids could be investigated experimentally. In the horizontal direction regardless of gravity, the iron balls of various diameters could act as microswimmers due to the manipulation by a well-controlled moving magnetic field. The velocity fields around the microswimmer in the viscoelastic fluids could be tracked and computed by our previously developed high-speed micro-PIV technique. A negative wake in the opposite direction with the moving microswimmer, the main signature of the viscoelastic properties, could be observed as shown in Fig. 8-5. The results need to be compared with the negative wake behind either a sedimenting sphere or a rising bubble in the viscoelastic fluids at different scales.

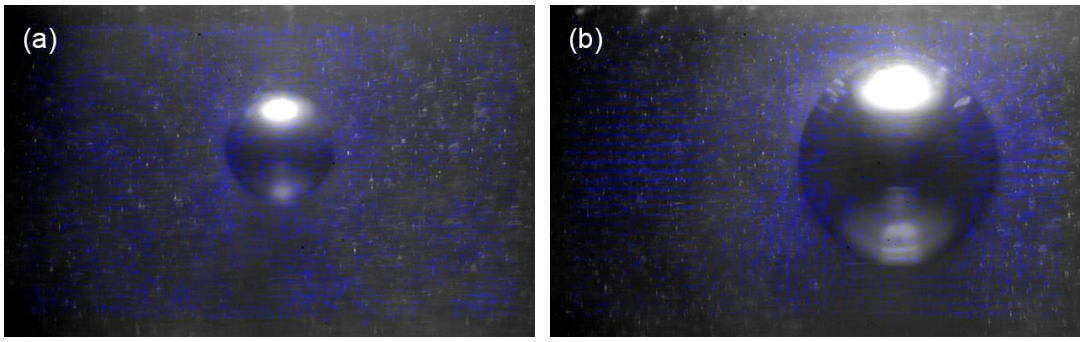


Fig. 8-5 Negative wake behind the microswimmer. Liquid: 1 wt% PAAm solution. Seeding particles: silver coated hollow glass spheres with an average diameter of 10 μm. (a) A microswimmer with a diameter of 1 mm. (b) A microswimmer with a diameter of 2 mm.

References

[1] Gunther A, Khan S A, Thalmann M, et al. Transport and reaction in microscale segmented gas-liquid flow [J]. Lab on a Chip, 2004, 4 (4): 278-286.

[2] Wu Z, Cao Z, Sundén B. Liquid-liquid flow patterns and slug hydrodynamics in square microchannels of cross-shaped junctions [J]. Chemical Engineering Science, 2017, 174: 56-66.

[3] Tang C, Liu M, Xu Y. 3-D numerical simulations on flow and mixing behaviors in gas-liquid-solid microchannels [J]. AlChE Journal, 2013, 59 (6): 1934-1951.

[4] Schrimpf M, Esteban J, Rösler T, et al. Intensified reactors for gas-liquid-liquid multiphase catalysis: From chemistry to engineering [J]. Chemical Engineering Journal, 2019, 372: 917-939.

[5] Wörner M. Numerical modeling of multiphase flows in microfluidics and micro process engineering: A review of methods and applications [J]. Microfluidics and Nanofluidics, 2012, 12 (6): 841-886.

[6] Charpentier J-C. Among the trends for a modern chemical engineering, the third paradigm: The time and length multiscale approach as an efficient tool for process intensification and product design and engineering [J]. Chemical Engineering Research and Design, 2010, 88 (3): 248-254.

[7] Frank X, Charpentier J-C, Ma Y, et al. A multiscale approach for modeling bubbles rising in non-Newtonian fluids [J]. Industrial & Engineering Chemistry Research, 2011, 51 (4): 2084-2093.

[8] Günther A, Jhunjhunwala M, Thalmann M, et al. Micromixing of miscible liquids in segmented gas-liquid flow [J]. Langmuir, 2005, 21 (4): 1547-1555.

[9] Baraldi P T, Hessel V. Micro reactor and flow chemistry for industrial applications in drug discovery and development [J]. Green Processing and Synthesis, 2012, 1 (2): 149-167.

[10] Bandara T, Nguyen N-T, Rosengarten G. Slug flow heat transfer without phase change in microchannels: A review [J]. Chemical Engineering Science, 2015, 126: 283-295.

[11] Dittrich P S, Tachikawa K, Manz A. Micro total analysis systems. Latest advancements and trends [J]. Analytical Chemistry, 2006, 78 (12): 3887-3908.

[12] Xu J H, Li S W, Tan J, et al. Controllable preparation of monodisperse O/W and W/O emulsions in the same microfluidic device [J]. Langmuir, 2006, 22 (19): 7943-7946.

[13] Leng J, Salmon J B. Microfluidic crystallization [J]. Lab on a Chip, 2009, 9 (1): 24-34.

[14] Hartman R L, Jensen K F. Microchemical systems for continuous-flow synthesis [J]. Lab on a Chip, 2009, 9 (17): 2495-2507.

[15] Haliburton J R, Kim S C, Clark I C, et al. Efficient extraction of oil from droplet microfluidic emulsions [J]. Biomicrofluidics, 2017, 11 (3): 034111.

[16] Qu W, Mudawar I. Analysis of three-dimensional heat transfer in micro-channel heat sinks [J]. International Journal of Heat and Mass Transfer, 2002, 45 (19): 3973-3985.

[17] Hetsroni G, Mosyak A, Pogrebnyak E, et al. Heat transfer in micro-channels: Comparison of experiments with theory and numerical results [J]. International Journal of Heat and Mass Transfer, 2005, 48 (25): 5580-5601.

[18] Plouffe P, Roberge D M, Macchi A. Liquid-liquid flow regimes and mass transfer in various micro-reactors [J]. Chemical Engineering Journal, 2016, 300: 9-19.

[19] Watts P, Wiles C. Micro reactors: A new tool for the synthetic chemist [J]. Organic & Biomolecular Chemistry, 2007, 5 (5): 727-732.

[20] Wiles C, Watts P. Recent advances in micro reaction technology [J]. Chemical Communications, 2011, 47 (23): 6512-6535.

[21] Dollet B, van Hoeve W, Raven J-P, et al. Role of the channel geometry on the bubble pinch-off in flow-focusing devices [J]. Physical Review Letters, 2008, 100 (3): 034504.

[22] Ushikubo F Y, Birribilli F S, Oliveira D R B, et al. Y- and T-junction microfluidic devices: Effect of fluids and interface properties and operating conditions [J]. Microfluidics and Nanofluidics, 2014, 17 (4): 711-720.

[23] Fu T, Ma Y. Bubble formation and breakup dynamics in microfluidic devices: A review [J]. Chemical Engineering Science, 2015, 135: 343-372.

[24] Lan W, Jing S, Guo X, et al. Study on “interface - shrinkage - driven” breakup of droplets in co-flowing microfluidic devices [J]. Chemical Engineering Science, 2017, 158: 58-63.

[25] van Dijke K, Veldhuis G, Schroen K, et al. Parallelized edge-based droplet generation (EDGE) devices [J]. Lab on a Chip, 2009, 9 (19): 2824-2830.

[26] Christopher G F, Bergstein J, End N B, et al. Coalescence and splitting of confined droplets at microfluidic junctions [J]. Lab on a Chip, 2009, 9 (8): 1102-1109.

[27] Jose B M, Cubaud T. Droplet arrangement and coalescence in diverging/converging microchannels [J]. Microfluidics and Nanofluidics, 2011, 12 (5): 687-696.

[28] Li X-B, Li F-C, Yang J-C, et al. Study on the mechanism of droplet formation in T-junction microchannel [J]. Chemical Engineering Science, 2012, 69 (1): 340-351.

[29] Schwartz J A, Vykoukal J V, Gascoyne P R. Droplet-based chemistry on a programmable micro-chip [J]. Lab on a Chip, 2004, 4 (1): 11-17.

[30] Moghimi S M, Hunter A C, Murray J C. Nanomedicine: Current status and future prospects [J]. FASEB Journal, 2005, 19 (3): 311-330.

[31] Lignos I, Protesescu L, Stavrakis S, et al. Facile droplet-based microfluidic synthesis of monodisperse IV-VI semiconductor nanocrystals with coupled in-line NIR fluorescence detection [J]. Chemistry of Materials, 2014, 26 (9): 2975-2982.

[32] Kang D K, Gong X, Cho S, et al. 3D droplet microfluidic systems for high-throughput biological experimentation [J]. Analytical Chemistry, 2015, 87 (21): 10770-10778.

[33] Gañán-Calvo A M, Gordillo J M. Perfectly monodisperse microbubbling by capillary flow focusing [J]. Physical Review Letters, 2001, 87 (27): 274501.

[34] Nisisako T, Torii T, Higuchi T. Droplet formation in a microchannel network [J]. Lab on a Chip, 2002, 2 (1): 24-26.

[35] Garstecki P, Stone H, Whitesides G. Mechanism for flow-rate controlled breakup in confined geometries: A route to monodisperse emulsions [J]. Physical Review Letters, 2005, 94 (16): 164501.

[36] Garstecki P, Fuerstman M J, Stone H A, et al. Formation of droplets and bubbles in a microfluidic T-junction—scaling and mechanism of break-up [J]. Lab on a Chip, 2006, 6 (3): 437-446.

[37] Dietrich N, Poncin S, Midoux N, et al. Bubble formation dynamics in various flow-focusing microdevices [J]. Langmuir, 2008, 24 (24): 13904-13911.

[38] van Hoeve W, Dollet B, Versluis M, et al. Microbubble formation and pinch-off scaling exponent in flow-focusing devices [J]. Physics of Fluids, 2011, 23 (9): 092001.

[39] Fu T, Ma Y, Funfschilling D, et al. Bubble formation and breakup mechanism in a microfluidic flow-focusing device [J]. Chemical Engineering Science, 2009, 64 (10): 2392-2400.

[40] Fu T, Funfschilling D, Ma Y, et al. Scaling the formation of slug bubbles in microfluidic flow-focusing devices [J]. Microfluidics and Nanofluidics, 2010, 8 (4): 467-475.

[41] Fu T, Ma Y, Funfschilling D, et al. Squeezing-to-dripping transition for bubble formation in a microfluidic T-junction [J]. Chemical Engineering Science, 2010, 65 (12): 3739-3748.

[42] Fu T, Wu Y, Ma Y, et al. Droplet formation and breakup dynamics in microfluidic flow-focusing devices: From dripping to jetting [J]. Chemical Engineering Science, 2012, 84: 207-217.

[43] Du W, Fu T, Zhu C, et al. Breakup dynamics for high-viscosity droplet formation in a flow-focusing device: Symmetrical and asymmetrical ruptures [J]. AIChE Journal, 2016, 62 (1): 325-337.

[44] Chiarello E, Derzsi L, Pierno M, et al. Generation of oil droplets in a non-Newtonian liquid using a microfluidic T-junction [J]. Micromachines, 2015, 6 (12): 1825-1835.

[45] Rostami B, Morini G L. Generation of Newtonian and non-Newtonian droplets in silicone oil flow by means of a micro cross-junction [J]. International Journal of Multiphase Flow, 2018, 105: 202-216.

[46] Rostami B, Morini G L. Experimental characterization of a micro cross-junction as generator of Newtonian and non-Newtonian droplets in silicone oil flow at low capillary numbers [J]. Experimental Thermal and Fluid Science, 2019, 103: 191-200.

[47] Fu T, Ma Y, Funfschilling D, et al. Gas-liquid flow stability and bubble formation in non-Newtonian fluids in microfluidic flow-focusing devices [J]. Microfluidics and Nanofluidics, 2011, 10 (5): 1135-1140.

[48] Fu T, Ma Y, Funfschilling D, et al. Bubble formation in non-Newtonian fluids in a microfluidic T-junction [J]. Chemical Engineering and Processing, 2011, 50 (4): 438-442.

[49] Fu T, Ma Y, Funfschilling D, et al. Breakup dynamics of slender bubbles in non-Newtonian fluids in microfluidic flow-focusing devices [J]. AlChE Journal, 2012, 58 (11): 3560-3567.

[50] Carrier O, Dervin E, Funfschilling D, et al. Formation of satellite droplets in flow-focusing junctions: Volume and neck rupture [J]. Microsystem Technologies, 2015, 21 (3): 499-507.

[51] Husny J, Cooper-White J J. The effect of elasticity on drop creation in T-shaped microchannels [J]. Journal of Non-Newtonian Fluid Mechanics, 2006, 137 (1-3): 121-136.

[52] Steinhaus B, Shen A Q, Sureshkumar R. Dynamics of viscoelastic fluid filaments in microfluidic devices [J]. Physics of Fluids, 2007, 19 (7): 073103.

[53] Lee W, Walker L M, Anna S L. Competition between viscoelasticity and surfactant dynamics in flow focusing microfluidics [J]. Macromolecular Materials and Engineering, 2011, 296 (3-4): 203-213.

[54] Du W, Fu T, Zhang Q, et al. Breakup dynamics for droplet formation in a flow-focusing device: Rupture position of viscoelastic thread from matrix [J]. Chemical Engineering Science, 2016, 153: 255-269.

[55] Du W, Fu T, Zhang Q, et al. Self-similar breakup of viscoelastic thread for droplet formation in flow-focusing devices [J]. AlChE Journal, 2017, 63 (11): 5196-5206.

[56] Adrian R J. Particle-imaging techniques for experimental fluid mechanics [J]. Annual Review of Fluid Mechanics, 1991, 23 (1): 261-304.

[57] Xiong R, Bai M, Chung J N. Formation of bubbles in a simple co-flowing micro-channel [J]. Journal of Micromechanics and Microengineering, 2007, 17 (5): 1002-1011.

[58] Kinoshita H, Kaneda S, Fujii T, et al. Three-dimensional measurement and visualization of internal flow of a moving droplet using confocal micro-PIV [J]. Lab on a Chip, 2007, 7 (3): 338-346.

[59] Chinaud M, Roumpea E-P, Angeli P. Studies of plug formation in microchannel liquid-liquid flows using advanced particle image velocimetry techniques [J]. Experimental Thermal and Fluid Science, 2015, 69: 99-110.

[60] Roumpea E, Chinaud M, Angeli P. Experimental investigations of non-Newtonian/Newtonian liquid-liquid flows in microchannels [J]. AlChE Journal, 2017, 63 (8): 3599-3609.

[61] Tsaoulidis D, Angeli P. Effect of channel size on liquid-liquid plug flow in small channels [J]. AlChE Journal, 2016, 62 (1): 315-324.

[62] Sang L, Hong Y, Wang F. Investigation of viscosity effect on droplet formation in T-shaped microchannels by numerical and analytical methods [J]. Microfluidics and Nanofluidics, 2009, 6 (5): 621-635.

[63] Qiu D, Silva L, Tonkovich A L, et al. Micro-droplet formation in non-Newtonian fluid in a microchannel [J]. Microfluidics and Nanofluidics, 2009, 8 (4): 531-548.

[64] Shi Y, Tang G H. Lattice Boltzmann simulation of droplet formation in non-Newtonian fluids [J]. Communications in Computational Physics, 2015, 17 (4): 1056-1072.

[65] Bhatnagar P L, Gross E P, Krook M. A model for collision processes in gases. I. Small amplitude processes in charged and neutral one-component systems [J]. Physical Review, 1954, 94 (3): 511-525.

[66] Qian Y H, D'Humières D, Lallemand P. Lattice BGK models for Navier-Stokes equation [J]. Europhysics Letters, 1992, 17 (6): 479-484.

[67] Sontti S G, Atta A. CFD analysis of microfluidic droplet formation in non-Newtonian liquid [J]. Chemical Engineering Journal, 2017, 330: 245-261.

[68] Taassob A, Manshadi M K D, Bordbar A, et al. Monodisperse non-Newtonian micro-droplet generation in a co-flow device [J]. Journal of the Brazilian Society of Mechanical Sciences and Engineering, 2017, 39 (6): 2013-2021.

[69] Nooranidoost M, Izbassarov D, Muradoglu M. Droplet formation in a flow focusing configuration: Effects of viscoelasticity [J]. Physics of Fluids, 2016, 28 (12): 123102.

[70] Gupta A, Sbragaglia M. A lattice Boltzmann study of the effects of viscoelasticity on droplet formation in microfluidic cross-junctions [J]. European Physical Journal E, 2016, 39 (1): 2.

[71] Ren Y, Seng Koh K, Kai Chin J, et al. Droplet formation and fission in shear-thinning/Newtonian multiphase system using bilayer bifurcating microchannel [J]. Journal of Heat Transfer, 2018, 140 (1): 012405.

[72] Link D, Anna S, Weitz D, et al. Geometrically mediated breakup of drops in microfluidic devices [J]. Physical Review Letters, 2004, 92 (5): 054503.

[73] Leshansky A M, Pismen L M. Breakup of drops in a microfluidic T junction [J]. Physics of Fluids, 2009, 21 (2): 023303.

[74] Jullien M C, Tsang Mui Ching M J, Cohen C, et al. Droplet breakup in microfluidic T-junctions at small capillary numbers [J]. Physics of Fluids, 2009, 21 (7): 072001.

[75] Samie M, Salari A, Shafii M B. Breakup of microdroplets in asymmetric T junctions [J]. Physical Review E, 2013, 87 (5): 053003.

[76] Sun X, Zhu C, Fu T, et al. Dynamics of droplet breakup and formation of satellite droplets in a microfluidic T-junction [J]. Chemical Engineering Science, 2018, 188: 158-169.

[77] Che Z, Nguyen N-T, Wong T N. Hydrodynamically mediated breakup of droplets in microchannels [J]. Applied Physics Letters, 2011, 98 (5): 054102.

[78] Wang B, Zhang S, Chen X. Deformation dynamics and breakup criteria of confined fluid threads in motion [J]. Physics of Fluids, 2019, 31 (12): 121702.

[79] Cubaud T. Deformation and breakup of high-viscosity droplets with symmetric microfluidic cross flows [J]. Physical Review E, 2009, 80 (2): 026307.

[80] Cubaud T, Jose B M, Darvishi S, et al. Droplet breakup and viscosity-stratified flows in microchannels [J]. International Journal of Multiphase Flow, 2012, 39: 29-36.

[81] Wu Y, Fu T, Ma Y, et al. Active control of ferrofluid droplet breakup dynamics in a microfluidic T-junction [J]. Microfluidics and Nanofluidics, 2015, 18 (1): 19-27.

[82] Ma R, Fu T, Zhang Q, et al. Breakup dynamics of ferrofluid droplet in a microfluidic T-junction [J]. Journal of Industrial and Engineering Chemistry, 2017, 54: 408-420.

[83] Li H, Wu Y, Wang X, et al. Magnetofluidic control of the breakup of ferrofluid droplets in a microfluidic Y-junction [J]. RSC Advances, 2016, 6 (1): 778-785.

[84] Wang X, Zhu C, Fu T, et al. Critical lengths for the transition of bubble breakup in microfluidic T-junctions [J]. Chemical Engineering Science, 2014, 111: 244-254.

[85] Wang X, Zhu C, Fu T, et al. Bubble breakup with permanent obstruction in an asymmetric microfluidic T-junction [J]. AlChE Journal, 2015, 61 (3): 1081-1091.

[86] Wang X, Zhu C, Wu Y, et al. Dynamics of bubble breakup with partly obstruction in a microfluidic T-junction [J]. Chemical Engineering Science, 2015, 132: 128-138.

[87] Fu T, Ma Y, Funfschilling D, et al. Dynamics of bubble breakup in a microfluidic T-junction divergence [J]. Chemical Engineering Science, 2011, 66 (18): 4184-4195.

[88] Lu Y, Fu T, Zhu C, et al. Dynamics of bubble breakup at a T junction [J]. Physical Review E, 2016, 93 (2): 022802.

[89] Fu T, Ma Y, Li H Z. Hydrodynamic feedback on bubble breakup at a T-junction within an asymmetric loop [J]. AlChE Journal, 2014, 60 (5): 1920-1929.

[90] Bedram A, Darabi A E, Moosavi A, et al. Numerical investigation of an efficient method (T-junction with valve) for producing unequal-sized droplets in micro- and nano-fluidic systems [J]. Journal of Fluids Engineering, 2014, 137 (3): 031202.

[91] Liu H, Ju Y, Wang N, et al. Lattice Boltzmann modeling of contact angle and its hysteresis in two-phase flow with large viscosity difference [J]. Physical Review E, 2015, 92 (3): 033306.

[92] Fu Y, Bai L, Jin Y, et al. Theoretical analysis and simulation of obstructed breakup of micro-droplet in T-junction under an asymmetric pressure difference [J]. Physics of Fluids, 2017, 29 (3): 032003.

[93] Aboutalebi M, Bijarchi M A, Shafii M B, et al. Numerical investigation on splitting of ferrofluid microdroplets in T-junctions using an asymmetric magnetic field with proposed correlation [J]. Journal of Magnetism and Magnetic Materials, 2018, 447: 139-149.

[94] Calderon A J, Eshpuniyani B, Fowlkes J B, et al. A boundary element model of the transport of a semi-infinite bubble through a microvessel bifurcation [J]. Physics of Fluids, 2010, 22 (6): 061902.

[95] Chen X, Zielinski R, Ghadiali S N. Computational analysis of microbubble flows in bifurcating airways: Role of gravity, inertia, and surface tension [J]. Journal of Biomechanical Engineering, 2014, 136 (10): 101007.

[96] Rein M. Phenomena of liquid drop impact on solid and liquid surfaces [J]. Fluid Dynamics Research, 1993, 12 (2): 61-93.

[97] Rein M. The transitional regime between coalescing and splashing drops [J]. Journal of Fluid Mechanics, 1996, 306: 145-165.

[98] Marcotte F, Michon G J, Séon T, et al. Ejecta, corolla, and splashes from drop impacts on viscous fluids [J]. Physical Review Letters, 2019, 122 (1): 014501.

[99] Yarin A L. Drop impact dynamics: Splashing, spreading, receding, bouncing… [J]. Annual Review of Fluid Mechanics, 2006, 38 (1): 159-192.

[100] Deegan R D, Brunet P, Eggers J. Complexities of splashing [J]. Nonlinearity, 2008, 21 (1): C1-C11.

[101] Leng L J. Splash formation by spherical drops [J]. Journal of Fluid Mechanics, 2001, 427: 73-105.

[102] Fedorchenko A I, Wang A-B. On some common features of drop impact on liquid surfaces [J]. Physics of Fluids, 2004, 16 (5): 1349-1365.

[103] Chen S, Bertola V. Morphology of viscoplastic drop impact on viscoplastic surfaces [J]. Soft Matter, 2017, 13: 711-719.

[104] Zweibel E G, Yamada M. Magnetic reconnection in astrophysical and laboratory plasmas [J]. Annual Review of Astronomy and Astrophysics, 2009, 47 (1): 291-332.

[105] Wyper P F, Antiochos S K, DeVore C R. A universal model for solar eruptions [J]. Nature, 2017, 544 (7651): 452-455.

[106] Sarojini Kg K, Dhar P, Varughese S, et al. Coalescence dynamics of PEDOT: PSS droplets impacting at offset on substrates for inkjet printing [J]. Langmuir, 2016, 32 (23): 5838-5851.

[107] Rosen M J, Wang H, Shen P, et al. Ultralow interfacial tension for enhanced oil recovery at very low surfactant concentrations [J]. Langmuir, 2005, 21 (9): 3749-3756.

[108] Melle S, Lask M, Fuller G G. Pickering emulsions with controllable stability [J]. Langmuir, 2005, 21 (6): 2158-2162.

[109] Cuvelier D, Derenyi I, Bassereau P, et al. Coalescence of membrane tethers: Experiments, theory, and applications [J]. Biophysical Journal, 2005, 88 (4): 2714-2726.

[110] Paulsen J D. Approach and coalescence of liquid drops in air [J]. Physical Review E, 2013, 88 (6): 063010.

[111] Mohamed-Kassim Z, Longmire E K. Drop coalescence through a liquid/liquid interface [J]. Physics of Fluids, 2004, 16 (7): 2170-2181.

[112] Aryafar H, Kavehpour H P. Drop coalescence through planar surfaces [J]. Physics of Fluids, 2006, 18 (7): 072105.

[113] Yokota M, Okumura K. Dimensional crossover in the coalescence dynamics of viscous drops confined in between two plates [J]. Proceedings of the National Academy of Sciences of the United States of America, 2011, 108 (16): 6395-6398.

[114] Dong T, Weheliye W H, Angeli P. Laser induced fluorescence studies on the distribution of surfactants during drop/interface coalescence [J]. Physics of Fluids, 2019, 31 (1): 012106.

[115] Weheliye W H, Dong T, Angeli P. On the effect of surfactants on drop coalescence at liquid/liquid interfaces [J]. Chemical Engineering Science, 2017, 161: 215-227.

[116] Thoroddsen S T, Qian B, Etoh T G, et al. The initial coalescence of miscible drops [J]. Physics of Fluids, 2007, 19 (7): 072110.

[117] Blanchette F, Messio L, Bush J W M. The influence of surface tension gradients on drop coalescence [J]. Physics of Fluids, 2009, 21 (7): 072107.

[118] Geri M, Keshavarz B, McKinley G H, et al. Thermal delay of drop coalescence [J]. Journal of Fluid Mechanics, 2017, 833: R3.

[119] Thoroddsen S T, Takehara K. The coalescence cascade of a drop [J]. Physics of Fluids, 2000, 12 (6): 1265-1267.

[120] Blanchette F, Bigioni T P. Partial coalescence of drops at liquid interfaces [J]. Nature Physics, 2006, 2 (4): 254-257.

[121] Aarts D G A L, Lekkerkerker H N W. Droplet coalescence: Drainage, film rupture and neck growth in ultralow interfacial tension systems [J]. Journal of Fluid Mechanics, 2008, 606: 275-294.

[122] Ristenpart W D, McCalla P M, Roy R V, et al. Coalescence of spreading droplets on a wettable substrate [J]. Physical Review Letters, 2006, 97 (6): 064501.

[123] Paulsen J D, Burton J C, Nagel S R, et al. The inexorable resistance of inertia determines the initial regime of drop coalescence [J]. Proceedings of the National Academy of Sciences of the United States of America, 2012, 109 (18): 6857-6861.

[124] Narhe R D, Beysens D A, Pomeau Y. Dynamic drying in the early-stage coalescence of droplets sitting on a plate [J]. Europhysics Letters, 2008, 81 (4): 46002.

[125] Lee M W, Kang D K, Yoon S S, et al. Coalescence of two drops on partially wettable substrates [J]. Langmuir, 2012, 28 (8): 3791-3798.

[126] Hernandez-Sanchez J F, Lubbers L A, Eddi A, et al. Symmetric and asymmetric coalescence of drops on a substrate [J]. Physical Review Letters, 2012, 109 (18): 184502.

[127] Liu F, Ghigliotti G, Feng J J, et al. Numerical simulations of self-propelled jumping upon drop coalescence on non-wetting surfaces [J]. Journal of Fluid Mechanics, 2014, 752: 39-65.

[128] Verdier C. The influence of the viscosity ratio on polymer droplet collision in quiescent blends [J]. Polymer, 2001, 42 (16): 6999-7007.

[129] Zhang F H, Li E Q, Thoroddsen S T. Satellite formation during coalescence of unequal size drops [J]. Physical Review Letters, 2009, 102 (10): 104502.

[130] Deka H, Biswas G, Chakraborty S, et al. Coalescence dynamics of unequal sized drops [J]. Physics of Fluids, 2019, 31 (1): 012105.

[131] Wu M, Cubaud T, Ho C-M. Scaling law in liquid drop coalescence driven by surface tension [J]. Physics of Fluids, 2004, 16 (7): L51-L54.

[132] Case S C, Nagel S R. Coalescence in low-viscosity liquids [J]. Physical Review Letters, 2008, 100 (8): 084503.

[133] Case S C. Coalescence of low-viscosity fluids in air [J]. Physical Review E, 2009, 79 (2): 026307.

[134] Paulsen J D, Burton J C, Nagel S R. Viscous to inertial crossover in liquid drop coalescence [J]. Physical Review Letters, 2011, 106 (11): 114501.

[135] Fezzaa K, Wang Y. Ultrafast X-Ray phase-contrast imaging of the initial coalescence phase of two water droplets [J]. Physical Review Letters, 2008, 100 (10): 104501.

[136] Eggers J, Lister J R, Stone H A. Coalescence of liquid drops [J]. Journal of Fluid Mechanics, 1999, 401: 293-310.

[137] Duchemin L, Eggers J, Josserand C. Inviscid coalescence of drops [J]. Journal of Fluid Mechanics, 2003, 487: 167-178.

[138] Aarts D G, Lekkerkerker H N, Guo H, et al. Hydrodynamics of droplet coalescence [J]. Physical Review Letters, 2005, 95 (16): 164503.

[139] Paulsen J D, Carmigniani R, Kannan A, et al. Coalescence of bubbles and drops in an outer fluid [J]. Nature Communications, 2014, 5: 3182.

[140] Blanchette F, Bigioni T P. Dynamics of drop coalescence at fluid interfaces [J]. Journal of Fluid Mechanics, 2009, 620: 333-352.

[141] Perumanath S, Borg M K, Chubynsky M V, et al. Droplet coalescence is initiated by thermal motion [J]. Physical Review Letters, 2019, 122 (10): 104501.

[142] Anthony C R, Harris M T, Basaran O A. Initial regime of drop coalescence [J]. Physical Review Fluids, 2020, 5 (3): 033608.

[143] Josserand C, Thoroddsen S T. Drop impact on a solid surface [J]. Annual Review of Fluid Mechanics, 2016, 48 (1): 365-391.

[144] Simpkins P G, Kuck V J. On air entrainment in coatings [J]. Journal of Colloid and Interface Science, 2003, 263 (2): 562-571.

[145] de Gans B J, Duineveld P C, Schubert U S. Inkjet printing of polymers: State of the art and future developments [J]. Advanced materials, 2004, 16 (3): 203-213.

[146] Sundaram A, Sundaram K, Leung J. Droplet spreading and penetration of non-aqueous pesticide formulations and spray diluents in kromekoter cards [J]. Transactions of the ASAE, 1991, 34: 1941-1951.

[147] Tanner L H. The spreading of silicone oil drops on horizontal surfaces [J]. Journal of Physics D: Applied Physics, 1979, 12 (9): 1473-1484.

[148] Biance A-L, Clanet C, Quéré D. First steps in the spreading of a liquid droplet [J]. Physical Review E, 2004, 69 (1): 016301.

[149] Bird J C, Mandre S, Stone H A. Short-time dynamics of partial wetting [J]. Physical Review Letters, 2008, 100 (23): 234501.

[150] Eddi A, Winkels K G, Snoeijer J H. Short time dynamics of viscous drop spreading [J]. Physics of Fluids, 2013, 25 (1): 013102.

[151] Rioboo R, Marengo M, Tropea C. Time evolution of liquid drop impact onto solid, dry surfaces [J]. Experiments in Fluids, 2002, 33 (1): 112-124.

[152] Courbin L, Bird J C, Reyssat M, et al. Dynamics of wetting: From inertial spreading to viscous imbibition [J]. Journal of Physics: Condensed Matter, 2009, 21 (46): 464127.

[153] Jung S, Hutchings I M. The impact and spreading of a small liquid drop on a non-porous substrate over an extended time scale [J]. Soft Matter, 2012, 8 (9): 2686-2696.

[154] Mitra S, Mitra S K. Understanding the early regime of drop spreading [J]. Langmuir, 2016, 32 (35): 8843-8848.

[155] Aboud D G, Kietzig A M. Splashing threshold of oblique droplet impacts on surfaces of various wettability [J]. Langmuir, 2015, 31 (36): 10100-10111.

[156] Yokoi K. Numerical studies of droplet splashing on a dry surface: Triggering a splash with the dynamic contact angle [J]. Soft Matter, 2011, 7 (11): 5120-5123.

[157] Quetzeri-Santiago M A, Yokoi K, Castrejón-Pita A A, et al. Role of the dynamic contact angle on splashing [J]. Physical Review Letters, 2019, 122 (22): 228001.

[158] Rafaï S, Sarker D, Bergeron V, et al. Superspreading: Aqueous surfactant drops spreading on hydrophobic surfaces [J]. Langmuir, 2002, 18 (26): 10486-10488.

[159] Wang X, Chen L, Bonaccurso E. Comparison of spontaneous wetting and drop impact dynamics of aqueous surfactant solutions on hydrophobic polypropylene surfaces: Scaling of the contact radius [J]. Colloid and Polymer Science, 2015, 293 (1): 257-265.

[160] Brunet P, Lapierre F, Zoueshtiagh F, et al. To grate a liquid into tiny droplets by its impact on a hydrophobic microgrid [J]. Applied Physics Letters, 2009, 95 (25): 254102.

[161] Sahu R P, Sett S, Yarin A L, et al. Impact of aqueous suspension drops onto non-wettable porous membranes: Hydrodynamic focusing and penetration of nanoparticles [J]. Colloids and Surfaces A: Physicochemical and Engineering Aspects, 2015, 467: 31-45.

[162] Lunkad S F, Maiti R N, Buwa V V, et al. Numerical study of drop spreading over saturated pores [J]. Canadian Journal of Chemical Engineering, 2010, 88 (4): 661-670.

[163] Frank X, Perre P, Li H Z. Lattice Boltzmann investigation of droplet inertial spreading on various porous surfaces [J]. Physical Review E, 2015, 91 (5): 052405.

[164] Khanna R, Nigam K D P. Partial wetting in porous catalysts: Wettability and wetting efficiency [J]. Chemical Engineering Science, 2002, 57 (16): 3401-3405.

[165] Chen S, Bertola V. Drop impact on spherical soft surfaces [J]. Physics of Fluids, 2017, 29 (8): 082106.

[166] Zhu P, Wang L. Passive and active droplet generation with microfluidics: A review [J]. Lab on a Chip, 2017, 17 (1): 34-75.

[167] Priest C, Herminghaus S, Seemann R. Generation of monodisperse gel emulsions in a microfluidic device [J]. Applied Physics Letters, 2006, 88 (2): 024106.

[168] Li Z, Leshansky A M, Metais S, et al. Step-emulsification in a microfluidic device [J]. Lab on a Chip, 2015, 15 (4): 1023-1031.

[169] Chung C, Lee M, Char K, et al. Droplet dynamics passing through obstructions in confined microchannel flow [J]. Microfluidics and Nanofluidics, 2010, 9 (6): 1151-1163.

[170] Salkin L, Schmit A, Courbin L, et al. Passive breakups of isolated drops and one-dimensional assemblies of drops in microfluidic geometries: Experiments and models [J]. Lab on a Chip, 2013, 13 (15): 3022-3032.

[171] Li Q, Chai Z, Shi B, et al. Deformation and breakup of a liquid droplet past a solid circular cylinder: A lattice Boltzmann study [J]. Physical Review E, 2014, 90 (4): 043015.

[172] Postek W, Kaminski T S, Garstecki P. A passive microfluidic system based on step emulsification allows the generation of libraries of nanoliter-sized droplets from microliter droplets of varying and known concentrations of a sample [J]. Lab on a Chip, 2017, 17 (7): 1323-1331.

[173] Alam A, Afzal A, Kim K-Y. Mixing performance of a planar micromixer with circular obstructions in a curved microchannel [J]. Chemical Engineering Research and Design, 2014, 92 (3): 423-434.

[174] Yin Y, Zhu C, Fu T, et al. Enhancement effect and mechanism of gas-liquid mass transfer by baffles embedded in the microchannel [J]. Chemical Engineering Science, 2019, 201: 264-273.

[175] Nieves-Remacha M J, Kulkarni A A, Jensen K F. Gas-liquid flow and mass transfer in an advanced-flow reactor [J]. Industrial & Engineering Chemistry Research, 2013, 52 (26): 8996-9010.

[176] Jackson D P, Miranda J A. Confined ferrofluid droplet in crossed magnetic fields [J]. European Physical Journal E, 2007, 23 (4): 389-396.

[177] Tan S-H, Nguyen N-T, Yobas L, et al. Formation and manipulation of ferrofluid droplets at a microfluidic T-junction [J]. Journal of Micromechanics and Microengineering, 2010, 20 (4): 045004.

[178] Zhu G P, Nguyen N T, Ramanujan R V, et al. Nonlinear deformation of a ferrofluid droplet in a uniform magnetic field [J]. Langmuir, 2011, 27 (24): 14834-14841.

[179] Liu J, Tan S-H, Yap Y F, et al. Numerical and experimental investigations of the formation process of ferrofluid droplets [J]. Microfluidics and Nanofluidics, 2011, 11 (2): 177-187.

[180] Jiang X F, Li H Z. Self-similar pinch-off mechanism and scaling of ferrofluid drops [J]. Physical Review E, 2015, 92 (6): 061003.

[181] Ray A, Varma V B, Jayaneel P J, et al. On demand manipulation of ferrofluid droplets by magnetic fields [J]. Sensors and Actuators B: Chemical, 2017, 242: 760-768.

[182] Farhan N M, Tafreshi H V. Using magnetic field to measure detachment force between a nonmagnetic droplet and fibers [J]. Langmuir, 2019, 35 (25): 8490-8499.

[183] Bird J C, Ristenpart W D, Belmonte A, et al. Critical angle for electrically driven coalescence of two conical droplets [J]. Physical Review Letters, 2009, 103 (16): 164502.

[184] Ristenpart W D, Bird J C, Belmonte A, et al. Non-coalescence of oppositely charged drops [J]. Nature, 2009, 461 (7262): 377-380.

[185] Hamlin B S, Creasey J C, Ristenpart W D. Electrically tunable partial coalescence of oppositely charged drops [J]. Physical Review Letters, 2012, 109 (9): 094501.

[186] Liu T, Seiffert S, Thiele J, et al. Non-coalescence of oppositely charged droplets in pH-sensitive emulsions [J]. Proceedings of the National Academy of Sciences of the United States of America, 2012, 109 (2): 384-389.

[187] Yun S, Hong J, Kang K H. Suppressing drop rebound by electrically driven shape distortion [J]. Physical Review E, 2013, 87 (3): 033010.

[188] Huang Y, Wang Y L, Wong T N. AC electric field controlled non-Newtonian filament thinning and droplet formation on the microscale [J]. Lab on a Chip, 2017, 17 (17): 2969-2981.

[189] Liu Z, Fu X, Binks B P, et al. Coalescence of electrically charged liquid marbles [J]. Soft Matter, 2017, 13 (1): 119-124.

[190] Kar S, Joshi S, Chaudhary K, et al. Generation of droplets to serpentine threads on a rotating compact-disk platform [J]. Applied Physics Letters, 2015, 107 (24): 244101.

[191] Schuler F, Schwemmer F, Trotter M, et al. Centrifugal step emulsification applied for absolute quantification of nucleic acids by digital droplet RPA [J]. Lab on a Chip, 2015, 15 (13): 2759-2766.

[192] Lin S C, Mao X, Huang T J. Surface acoustic wave (SAW) acoustophoresis: Now and beyond [J]. Lab on a Chip, 2012, 12 (16): 2766-2770.

[193] Sesen M, Alan T, Neild A. Microfluidic on-demand droplet merging using surface acoustic waves [J]. Lab on a Chip, 2014, 14 (17): 3325-3333.

[194] Baroud C N, Delville J-P, Gallaire F, et al. Thermocapillary valve for droplet production and sorting [J]. Physical Review E, 2007, 75 (4): 046302.

[195] Kwon G, Panchanathan D, Mahmoudi S R, et al. Visible light guided manipulation of liquid wettability on photoresponsive surfaces [J]. Nature Communications, 2017, 8 (1): 14968.

[196] Arayanarakool R, Shui L, van den Berg A, et al. A new method of UV-patternable hydrophobization of micro- and nanofluidic networks [J]. Lab on a Chip, 2011, 11 (24): 4260-4266.

[197] Neuringer J L, Rosensweig R E. Ferrohydrodynamics [J]. Physics of Fluids, 1964, 7 (12): 1927-1937.

[198] Nguyen N-T. Micro-magnetofluidics: Interactions between magnetism and fluid flow on the microscale [J]. Microfluidics and Nanofluidics, 2012, 12 (1): 1-16.

[199] Afkhami S, Tyler A J, Renardy Y, et al. Deformation of a hydrophobic ferrofluid droplet suspended in a viscous medium under uniform magnetic fields [J]. Journal of Fluid Mechanics, 2010, 663: 358-384.

[200] Wu Y, Fu T, Ma Y, et al. Ferrofluid droplet formation and breakup dynamics in a microfluidic flow-focusing device [J]. Soft Matter, 2013, 9 (41): 9792-9798.

[201] Rigoni C, Bertoldo S, Pierno M, et al. Division of ferrofluid drops induced by a magnetic field [J]. Langmuir, 2018, 34 (33): 9762-9767.

[202] Tokarev A, Lee W-K, Sevonkaev I, et al. Sharpening the surface of magnetic paranematic droplets [J]. Soft Matter, 2014, 10 (12): 1917-1923.

[203] Rigoni C, Pierno M, Mistura G, et al. Static magnetowetting of ferrofluid drops [J]. Langmuir, 2016, 32 (30): 7639-7646.

[204] Hu M, Butt H J, Landfester K, et al. Shaping the assembly of superparamagnetic nanoparticles [J]. ACS nano, 2019, 13 (3): 3015-3022.

[205] Kadivar E. Magnetocoalescence of ferrofluid droplets in a flat microfluidic channel [J]. Europhysics Letters, 2014, 106 (2): 24003.

[206] Mahajan M P, Tsige M, Taylor P L, et al. Paramagnetic liquid bridge in a gravity-compensating magnetic field [J]. Physics of Fluids, 1998, 10 (9): 2208-2211.

[207] Malvandi A, Kaffash M H, Ganji D D. Nanoparticles migration effects on magnetohydrodynamic (MHD) laminar mixed convection of alumina/water nanofluid inside microchannels [J]. Journal of the Taiwan Institute of Chemical Engineers, 2015, 52: 40-56.

[208] Moshizi S A, Malvandi A. Magnetic field effects on nanoparticle migration at mixed convection of MHD nanofluids flow in microchannels with temperature-dependent thermophysical properties [J]. Journal of the Taiwan Institute of Chemical Engineers, 2016, 66: 269-282.

[209] Song H, Chen D L, Ismagilov R F. Reactions in droplets in microfluidic channels [J]. Angewandte Chemie, 2006, 45 (44): 7336-7356.

[210] Nguyen N-T, Chai M-F. A stepper micropump for ferrofluid driven microfluidic systems [J]. Micro and Nanosystems, 2009, 1 (1): 17-21.

[211] Gijs M A M, Lacharme F, Lehmann U. Microfluidic applications of magnetic particles for biological analysis and catalysis [J]. Chemical Reviews, 2010, 110 (3): 1518-1563.

[212] Zhang K, Liang Q, Ai X, et al. On-demand microfluidic droplet manipulation using hydrophobic ferrofluid as a continuous-phase [J]. Lab on a Chip, 2011, 11 (7): 1271-1275.

[213] Wu J, Yan Q, Xuan S, et al. Size-selective separation of magnetic nanospheres in a microfluidic channel [J]. Microfluidics and Nanofluidics, 2017, 21 (3): 47.

[214] Tan S H, Nguyen N-T. Generation and manipulation of monodispersed ferrofluid emulsions: The effect of a uniform magnetic field in flow-focusing and T-junction configurations [J]. Physical Review E, 2011, 84 (3): 036317.

[215] Morcelles K F, Sirtoli V G, Bertemes-Filho P, et al. Howland current source for high impedance load applications [J]. Review of Scientific Instruments, 2017, 88 (11): 114705.

[216] Holm C, Weis J. The structure of ferrofluids: A status report [J]. Current Opinion in Colloid & Interface Science, 2005, 10 (3-4): 133-140.

[217] Tabeling P. Recent progress in the physics of microfluidics and related biotechnological applications [J]. Current Opinion in Biotechnology, 2014, 25: 129-134.

[218] Sackmann E K, Fulton A L, Beebe D J. The present and future role of microfluidics in biomedical research [J]. Nature, 2014, 507 (7491): 181-189.

[219] Bhattacharjee N, Urrios A, Kang S, et al. The upcoming 3D-printing revolution in microfluidics [J]. Lab on a Chip, 2016, 16 (10): 1720-1742.

[220] Ruiz-Rus J, Bolaños-Jiménez R, Gutiérrez-Montes C, et al. Controlled formation of bubbles in a planar co-flow configuration [J]. International Journal of Multiphase Flow, 2017, 89: 69-80.

[221] Abate A R, Thiele J, Weitz D A. One-step formation of multiple emulsions in microfluidics [J]. Lab on a Chip, 2011, 11 (2): 253-258.

[222] Elvira K S, Casadevall i Solvas X, Wootton R C, et al. The past, present and potential for microfluidic reactor technology in chemical synthesis [J]. Nature Chemistry, 2013, 5 (11): 905-915.

[223] Zhao F, Lu Y, Wang K, et al. Kinetic study on selective extraction of HCl and H_3PO_4 in a microfluidic device [J]. Chinese Journal of Chemical Engineering, 2016, 24 (2): 221-225.

[224] Pit A, Duits M, Mugele F. Droplet manipulations in two phase flow microfluidics [J]. Micromachines, 2015, 6 (11): 1768-1793.

[225] Nguyen N-T, Wu Z. Micromixers-a review [J]. Journal of Micromechanics and Microengineering, 2005, 15 (2): R1-R16.

[226] De Menech M. Modeling of droplet breakup in a microfluidic T-shaped junction with a phase-field model [J]. Physical Review E, 2006, 73 (3): 031505.

[227] Sivasamy J, Wong T-N, Nguyen N-T, et al. An investigation on the mechanism of droplet formation in a microfluidic T-junction [J]. Microfluidics and Nanofluidics, 2011, 11 (1): 1-10.

[228] Kovalchuk N M, Chowdhury J, Schofield Z, et al. Study of drop coalescence and mixing in microchannel using ghost particle velocimetry [J]. Chemical Engineering Research and Design, 2018, 132: 881-889.

[229] Thorsen T, Roberts R W, Arnold F H, et al. Dynamic pattern formation in a vesicle-generating microfluidic device [J]. Physical Review Letters, 2001, 86 (18): 4163-4166.

[230] van der Graaf S, Nisisako T, Schroën C G P H, et al. Lattice Boltzmann simulations of droplet formation in a T-shaped microchannel [J]. Langmuir, 2006, 22 (9): 4144-4152.

[231] Christopher G F, Noharuddin N N, Taylor J A, et al. Experimental observations of the squeezing-to-dripping transition in T-shaped microfluidic junctions [J]. Physical Review E, 2008, 78 (3): 036317.

[232] Xu J H, Li S W, Tan J, et al. Correlations of droplet formation in T-junction microfluidic devices: From squeezing to dripping [J]. Microfluidics and Nanofluidics, 2008, 5 (6): 711-717.

[233] Su Y, Chen G, Yuan Q. Effect of viscosity on the hydrodynamics of liquid processes in microchannels [J]. Chemical Engineering & Technology, 2014, 37 (3): 427-434.

[234] Dore V, Tsaoulidis D, Angeli P. Mixing patterns in water plugs during water/ionic liquid segmented flow in microchannels [J]. Chemical Engineering Science, 2012, 80: 334-341.

[235] Gupta A, Sbragaglia M. Deformation and breakup of viscoelastic droplets in confined shear flow [J]. Physical Review E, 2014, 90 (2): 023305.

[236] Jiang X F, Wu Y N, Ma Y, et al. Formation and breakup dynamics of ferrofluid drops [J]. Chemical Engineering Research and Design, 2016, 115: 262-269.

[237] Tirtaatmadja V, McKinley G H, Cooper-White J J. Drop formation and breakup of low viscosity elastic fluids: Effects of molecular weight and concentration [J]. Physics of Fluids, 2006, 18 (4): 043101.

[238] James D F. Boger fluids [J]. Annual Review of Fluid Mechanics, 2009, 41 (1): 129-142.

[239] Chiarello E, Gupta A, Mistura G, et al. Droplet breakup driven by shear thinning solutions in a microfluidic T-junction [J]. Physical Review Fluids, 2017, 2 (12): 123602.

[240] Rodd L E, Cooper-White J J, Boger D V, et al. Role of the elasticity number in the entry flow of dilute polymer solutions in micro-fabricated contraction geometries [J]. Journal of Non-Newtonian Fluid Mechanics, 2007, 143 (2-3): 170-191.

[241] Byron Bird R, Carreau P J. A nonlinear viscoelastic model for polymer solutions and melts—I [J]. Chemical Engineering Science, 1968, 23 (5): 427-434.

[242] Del Giudice F, D'Avino G, Greco F, et al. Effect of fluid rheology on particle migration in a square-shaped microchannel [J]. Microfluidics and Nanofluidics, 2015, 19 (1): 95-104.

[243] Xu J H, Luo G S, Li S W, et al. Shear force induced monodisperse droplet formation in a microfluidic device by controlling wetting properties [J]. Lab on a Chip, 2006, 6 (1): 131-136.

[244] van Steijn V, Kreutzer M T, Kleijn C R. μ-PIV study of the formation of segmented flow in microfluidic T-junctions [J]. Chemical Engineering Science, 2007, 62 (24): 7505-7514.

[245] Cubaud T, Mason T G. Capillary threads and viscous droplets in square microchannels [J]. Physics of Fluids, 2008, 20 (5): 053302.

[246] Ren Y, Liu Z, Shum H C. Breakup dynamics and dripping-to-jetting transition in a Newtonian/shear-thinning multiphase microsystem [J]. Lab on a Chip, 2015, 15 (1): 121-134.

[247] Zhao C-X. Multiphase flow microfluidics for the production of single or multiple emulsions for drug delivery [J]. Advanced Drug Delivery Reviews, 2013, 65 (11): 1420-1446.

[248] Huebner A, Sharma S, Srisa-Art M, et al. Microdroplets: A sea of applications? [J]. Lab on a Chip, 2008, 8 (8): 1244-1254.

[249] Cheung Y N, Qiu H. Droplet pinch-off in acoustically actuated flow-focusing devices [J]. Journal of Micromechanics and Microengineering, 2012, 22 (12): 125003.

[250] Lan W, Li S, Luo G. Numerical and experimental investigation of dripping and jetting flow in a coaxial micro-channel [J]. Chemical Engineering Science, 2015, 134: 76-85.

[251] Hoang D A, Portela L M, Kleijn C R, et al. Dynamics of droplet breakup in a T-junction [J]. Journal of Fluid Mechanics, 2013, 717: R4.

[252] Li L, Zhang J, Wang K, et al. Droplet formation of H_2SO_4/alkane system in a T-junction microchannel: Gravity effect [J]. AlChE Journal, 2016, 62 (12): 4564-4573.

[253] Blazek M, Santisteban T S, Zengerle R, et al. Analysis of fast protein phosphorylation kinetics in single cells on a microfluidic chip [J]. Lab on a Chip, 2015, 15 (3): 726-734.

[254] Liu Y, Jiang X. Why microfluidics? Merits and trends in chemical synthesis [J]. Lab on a Chip, 2017, 17 (23): 3960-3978.

[255] Burns M A, Johnson B N, Brahmasandra S N, et al. An integrated nanoliter DNA analysis device [J]. Science, 1998, 282 (5388): 484-487.

[256] Song H, Tice J D, Ismagilov R F. A microfluidic system for controlling reaction networks in time [J]. Angewandte Chemie, 2003, 42 (7): 768-772.

[257] Christopher G F, Anna S L. Passive breakup of viscoelastic droplets and filament self-thinning at a microfluidic T-junction [J]. Journal of Rheology, 2009, 53 (3): 663-683.

[258] Wang X, Zhu C, Fu T, et al. Critical condition for bubble breakup in a microfluidic flow-focusing junction [J]. Chemical Engineering Science, 2017, 164: 178-187.

[259] Wu Y, Fu T, Zhu C, et al. Shear-induced tail breakup of droplets (bubbles) flowing in a straight microfluidic channel [J]. Chemical Engineering Science, 2015, 135: 61-66.

[260] Ballesta P, Alves M A. Purely elastic instabilities in a microfluidic flow focusing device [J]. Physical Review Fluids, 2017, 2 (5): 053301.

[261] Liu J, Zhu C, Wang X, et al. Three-dimensional numerical simulation of coalescence and interactions of multiple horizontal bubbles rising in shear-thinning fluids [J]. AIChE J., 2015, 61 (10): 3528-3546.

[262] de Gennes P G. Wetting: Statics and dynamics [J]. Reviews of Modern Physics, 1985, 57 (3): 827-863.

[263] Bergeron V, Bonn D, Martin J Y, et al. Controlling droplet deposition with polymer additives [J]. Nature, 2000, 405: 772-775.

[264] Weinstein S J, Ruschak K J. Coating flows [J]. Annual Review of Fluid Mechanics, 2004, 36: 29-53.

[265] Singh M, Haverinen H M, Dhagat P, et al. Inkjet printing-process and its applications [J]. Advanced materials, 2010, 22 (6): 673-685.

[266] Sprittles J E, Shikhmurzaev Y D. The dynamics of liquid drops and their interaction with solids of varying wettabilities [J]. Physics of Fluids, 2012, 24 (8): 082001.

[267] Wijshoff H. The dynamics of the piezo inkjet printhead operation [J]. Physics Reports, 2010, 491 (4-5): 77-177.

[268] Saritha S, Zhang X, Neogi P. Wetting kinetics of films containing nonadsorbing polymers [J]. Journal of Chemical Physics, 2005, 122 (24): 244711.

[269] Lv C, Hao P, Zhang X, et al. Drop impact upon superhydrophobic surfaces with regular and hierarchical roughness [J]. Applied Physics Letters, 2016, 108 (14): 141602.

[270] Bonn D, Eggers J, Indekeu J, et al. Wetting and spreading [J]. Reviews of Modern Physics, 2009, 81 (2): 739-805.

[271] Liang Z-P, Wang X-D, Lee D-J, et al. Spreading dynamics of power-law fluid droplets [J]. Journal of Physics: Condensed Matter, 2009, 21 (46): 464117.

[272] Ravi V, Jog M A, Manglik R M. Effects of pseudoplasticity on spread and recoil dynamics of aqueous polymeric solution droplets on solid surfaces [J]. Interfacial Phenomena and Heat Transfer, 2013, 1 (3): 273-287.

[273] Chen L, Bonaccurso E, Shanahan M E R. Inertial to viscoelastic transition in early drop spreading on soft surfaces [J]. Langmuir, 2013, 29 (6): 1893-1898.

[274] Sun R, Bai H, Ju J, et al. Droplet emission induced by ultrafast spreading on a superhydrophilic surface [J]. Soft Matter, 2013, 9 (39): 9285-9289.

[275] Winkels K G, Weijs J H, Eddi A, et al. Initial spreading of low-viscosity drops on partially wetting surfaces [J]. Physical Review E, 2012, 85 (5): 055301.

[276] Carlson A, Kim P, Amberg G, et al. Short and long time drop dynamics on lubricated substrates [J]. Europhysics Letters, 2013, 104 (3): 34008.

[277] Chen L, Auernhammer G K, Bonaccurso E. Short time wetting dynamics on soft surfaces [J]. Soft Matter, 2011, 7 (19): 9084-9089.

[278] Ritos K, Dongari N, Borg M K, et al. Dynamics of nanoscale droplets on moving surfaces [J]. Langmuir, 2013, 29 (23): 6936-6943.

[279] Ghaffari A, Hashemabadi S H, Bazmi M. CFD simulation of equilibrium shape and coalescence of ferrofluid droplets subjected to uniform magnetic field [J]. Colloids and Surfaces A: Physicochemical and Engineering Aspects, 2015, 481: 186-198.

[280] Sprittles J E, Shikhmurzaev Y D. Coalescence of liquid drops: Different models versus experiment [J]. Physics of Fluids, 2012, 24 (12): 122105.

[281] Zhang Q, Jiang X, Brunello D, et al. Initial coalescence of a drop at a planar liquid surface [J]. Physical Review E, 2019, 100 (3): 033112.

[282] García A A, Egatz-Gómez A, Lindsay S A, et al. Magnetic movement of biological fluid droplets [J]. Journal of Magnetism and Magnetic Materials, 2007, 311 (1): 238-243.

[283] Chen X, Liu P, Qi C, et al. Non-coalescence of oppositely charged droplets in viscous oils [J]. Applied Physics Letters, 2019, 115 (2): 023701.

[284] Baroud C N, de Saint Vincent M R, Delville J P. An optical toolbox for total control of droplet microfluidics [J]. Lab on a Chip, 2007, 7 (8): 1029-1033.

[285] Pamme N. Magnetism and microfluidics [J]. Lab on a Chip, 2006, 6 (1): 24-38.

Nomenclature

Symbols

B	Magnetic flux density, T
c	Concentration, %
c^*	Critical overlap concentration, %
D_{max}	Maximum drop width, m
f	Frequency, Hz
G	Electrical conductance, S
h_c	Height of the microchannel, m
k	Thinning rate of the width of the dispersed thread, $m \cdot s^{-1}$
k_B	Boltzmann constant
l_0	Initial length of the droplets, m
l_d	Length of the droplets, m
l_{max}	Maximum length of the droplets, m
l_t	Length of the dispersed thread, m
$l_{t,\,b}$	Length of the dispersed thread at the breakup moment, m
M_w	Molecular weight of polymer, $g \cdot mol^{-1}$
n	Flow index
N_A	Avogadro constant
Q	Volumetric flow rate of liquid, $m^3 \cdot s^{-1}$
r	Radius, m
R	Electrical resistance, Ω
S	Coalescing section, m^2
t	Time, s
t_c	Change time from the squeezing stage to the stretching stage, s
T	Period for droplet generation, s
T_K	Temperature of the experimental environment, K
u	Superficial velocity, $m \cdot s^{-1}$
U	Electrical voltage, V
v	Approaching velocity of a pendant drop, $m \cdot s^{-1}$

V	Droplet volume, m^3
w, W	Width, m
w_b	Width of the droplets/bubbles, m
w_c	Width of the microchannel, m
w_m	Minimum width of the neck of the dispersed thread, m
x_h	The position of the droplet head, m
z	Vertical distance starting from the top surface of the magnet, m

Greek letters

α	Exponent in the power law
β	Exponent in the power law
γ	Surface tension, $N \cdot m^{-1}$
$\dot{\gamma}$	Shear rate, s^{-1}
δ	Cone angle, °
ε	Hencky strain
η	Viscosity, Pa·s
η_0	Zero shear viscosity, Pa·s
η_s	Solvent viscosity, Pa·s
η_∞	Infinite shear viscosity, Pa·s
$[\eta]$	Intrinsic viscosity, Pa·s
θ	Contact angle/cone angle, °
κ	Ratio of droplet size
λ	Time constant, s
λ_{eff}	Effective relaxation time, s
λ_Z	Longest relaxation time, s
ρ	Density, $kg \cdot m^{-3}$
σ	Electrical conductivity, $S \cdot m^{-1}$
τ	Viscocapillary time, s
φ	Volume fraction
χ	Ratio of droplet velocity
ψ	Cone angle, °

Dimensionless groups

Ca	Capillary number, $Ca = u\eta / \gamma$
Ec	Elasto-capillary number, $Ec = \lambda_{\text{eff}} \gamma / \eta w$
El	Elasticity number, $El = \lambda \eta / \rho w^2$
Oh	Ohnesorge number, $Oh = \sqrt{\eta / \rho \gamma w}$
Re	Reynolds number, $Re = lu\rho / \eta$
We	Weber number, $We = \rho w u^2 / \gamma$

Abbreviations

AC	Alternating current
AFM	Atomic force microscopy
CMC	Carboxymethyl cellulose sodium
DC	Direct current
fps	Frames per second
MD	Molecular dynamics
PAAm	Polyacrylamide
PEO	Polyethylene oxide
PIV	Particle image velocimetry
PMMA	Polymethyl methacrylate
SEM	Scanning electron microscope
VOF	Volume of fluid

Publications

[1] Qindan Zhang, Xiaofeng Jiang, David Brunello, Taotao Fu, Chunying Zhu, Youguang Ma, and Huai Z. Li*. Initial coalescence of a drop at a planar liquid surface. Physical Review E, 2019, 100 (3): 033112.

[2] Qindan Zhang, Yining Wu, Youguang Ma, and Huai Z. Li*. Self-sustained coalescence-breakup cycles of ferrofluid drops under a magnetic field. Langmuir, 2019, 35 (37): 12028-12034.

[3] Qindan Zhang, Chunying Zhu, Wei Du, Cai Liu, Taotao Fu*, Youguang Ma, Huai Z. Li*. Formation dynamics of elastic droplets in a microfluidic T-junction. Chemical Engineering Research and Design, 2018, 139: 188-196.

[4] Qindan Zhang, Huajun Li, Chunying Zhu, Taotao Fu*, Youguang Ma*, Huai Z. Li. Micro-magnetofluidics of ferrofluid droplet formation in a T-junction. Colloids and Surfaces A, 2018, 537: 572-579.

Ecoulements polyphasiques et phénomènes interfaciaux à multi échelles

Les écoulements polyphasiques couplés aux phénomènes interfaciaux à différentes échelles ont été étudiés expérimentalement par des méthodes passives et actives dans cette thèse. Les écoulements diphasiques viscoélastiques dans les microfluidiques ont été d'abord étudiés. L'effet de l'élasticité du fluide et des débits diphasiques sur la dynamique de formation de gouttelettes a été quantifié. La coalescence initiale d'une goutte pendante à une surface liquide et l'étalement initial sur une surface solide ont été étudiés par trois techniques distinctes. Le dispositif électrique à courant continu ultra-rapide a permis de suivre la dynamique de la coalescence des gouttes dans les 10 µs. Les champs de vitesse lors de la coalescence et de l'étalement initiaux ont révélé la transformation de l'énergie surfacique en cinématique. De plus, la manipulation active de la goutte de ferrofluide a été réalisée en introduisant un champ magnétique externe. Les cycles de rupture et de coalescence auto-entretenus des gouttes de ferrofluide ont été observés pour la première fois en fonction de différents champs magnétiques.

Mots clés: Multiéchelle, Écoulements polyphasiques, Phénomènes interfaciaux, Dynamique, Goutte, Fluide non newtonien, Ferrofluide

Study on the multiphase flows and interfacial phenomena at multiscale

The multiphase flows and interfacial phenomena at multiscale were investigated experimentally by both passive and active methods in this thesis. Firstly, the flow behaviors of the elastic non-Newtonian two-phase flows in the microfluidic devices were investigated. The influences of both the fluid elasticity and the two-phase flow rates on the dynamics of droplet formation, stretching and breakup were studied. Subsequently, the initial coalescence of a pendant drop at a liquid surface and the initial spreading on a solid surface were investigated by three different techniques. The ultrahigh-speed DC electrical device allowed monitoring the dynamics of drop coalescence and spreading within 10 µs. The velocity fields during the initial coalescence and spreading revealed the transformation of surface energy to kinetic energy. In addition, the active manipulation of the ferrofluid drop was realized by introducing an external magnetic field. The dynamics of ferrofluid drop coalescence were investigated at various magnetic fields. The self-sustained coalescence-breakup cycles of ferrofluid drops were observed for the first time.

Keywords: Multiscale, Multiphase flows, Interfacial phenomena, Dynamics, Drop, Non-Newtonian fluid, Ferrofluid